Quantitative Ultrasound Imaging of Thermal Ablation Therapy in the Liver

by

Nicholas Rubert

A dissertation submitted in partial fulfillment of

the requirements for the degree of

Doctor of Philosophy

(Medical Physics)

at the

UNIVERSITY OF WISCONSIN-MADISON

2014

Date of final oral examination: 12/9/13

The dissertation is approved by the following members of the Final Oral Committee:

Tomy Varghese, Professor, Medical Physics

James Zagzebski, Professor Emeritus, Medical Physics

James Holden, Professor, Medical Physics

Jennifer Smilowitz, Associate Professor, Medical Physics

Christopher Brace, Associate Professor, Biomedical Engineering

Abstract

The purpose of this dissertation is to investigate methods for delineating the extent of the thermally coagulated region following thermal ablation therapy of malignant tumors in the liver. In this dissertation, we examine quasistatic elasticity imaging for delineating the extent of the treated region. Next, we characterize scattering in normal, untreated liver and thermally coagulated liver. Finally, we examine attenuation estimation with reference phantom methods in the liver.

It has been well established that the Young's modulus of thermally coagulated tissue is much larger than in untreated liver tissue, making elastographic imaging an attractive candidate for delineating the extent of thermal coagulation. In quasistatic elastographic imaging of superficial organs such as the breast, external compression may be performed with a compressor plate or the transducer itself. However, in abdominal imaging, external compression is not effective. In response, our laboratory has developed electrode displacement for strain and modulus imaging. In electrode displacement strain imaging, deformation is applied by displacing the end of the RF electrode or microwave antenna by a small amount following treatment. We present electrode displacement strain images of thermally coagulated regions in *in vivo* porcine animal models during open surgery. We show that cross-sectional areas of treated regions delineated on electrode displacement strain images correlate well with coagulated areas determined on optical photographs of ablated regions of the excised livers. Additionally, we present electrode displacement strain images of VX2 tumors in rabbit animal models prior to and following thermal ablation.

Next, we develop mean scatterer spacing (MSS) estimation in the liver. In the liver, it has been hypothesized that periodic scattering results from a unique arrangement of

microvasculature. Indeed, the liver is a unique organ because of its dual vascular supply from the hepatic artery and portal vein. We first show that utilizing a multi-taper spectral calculation results in a lower mean square error in MSS estimates using simulations of periodic tissue. Next, we show that average spectral coherence decreases in thermally coagulated liver compared with untreated liver in a small number of *ex vivo* RF ablations. Finally, we demonstrate that thermally coagulated regions are best modeled by aperiodic collections of scatterers, while normal liver exhibits periodicity.

In the final section of the dissertation we consider attenuation estimation. This is an attractive area of research because the attenuation coefficient is approximately doubles in the liver following thermal ablation. In past works, authors have developed attenuation algorithms with the assumption that the tissue being imaged may be modeled by a collection of a large number of randomly distributed scatterers. We show that in *ex vivo* bovine liver the scatterer number density is small. We demonstrate that the effect this has on attenuation estimation is to significantly increase the variance in attenuation estimation relative to tissue that may be modeled with a large scatterer number density. Using computer simulation and phantom experiments we show that when the scatterer number density is sufficiently large it is possible to achieve low variance, high resolution attenuation estimates. However, as the scatterer number density decreases either spatial resolution in the attenuation estimate must be sacrificed or attenuation estimate variance will increase. We find a linear attenuation coefficient in thermally coagulated liver that is approximately double the attenuation coefficient of normal, untreated liver. However, we also find a low scatterer number density in these tissues and a correspondingly high attenuation estimation variance.

Acknowledgements

I am grateful for the time I have been in Madison as a part of such a fantastic department. Above all, I would like to thank my advisor Tomy Varghese for his optimism and enthusiasm. His support has been invaluable for helping to guide and spur me on throughout my graduate career. He has been a constant impetus towards new directions when I feel like my research is stuck in place.

I'd like to thank Gary Frank and Ernest Madsen with their assistance in experimental work and for the phantoms they made for me. I'd like to thank Dr. Zagzebski for his guidance and encouragement while I've been a student here. I'd also like to thank him for the conversations about simulation programs and quantitative ultrasound. This thesis has also been made possible by helpful discussions and advice from many of the other graduate students and post-docs that have come and gone or are still here: Jingfeng Jiang, Ryan DeWall, Matthew McCormick, Kibo Nam, Haiyan Xu, Atul Ingle, Ted Fisher, Eenas Omari, Ivan Rosado-Mendez, Eric Nordberg, Chi Ma, Xiao Wang, and Shyam Bharat.

I'd like to thank the other members of my thesis committee Jim Holden, Chris Brace, and Jennifer Smilowitz. They have devoted a substantial amount of time and energy to reviewing my work during my preliminary and final examinations, and I am grateful for their feedback and constructive criticism.

I'd also like to thank my parents and brothers for their love and support over the years. Finally, I'd like to thank Samantha for her love, for making my time in Madison that much better, and for listening to me talk about liver so much.

Contents

List of Figures

List of Tables

Chapter 1. Introduction

1.1. Motivation

As of 1999, cancer became the leading cause of death in the United States for people aged 85 and younger [1]. In 2011, the International Agency for Research on Cancer declared the disease to still be the leading cause of death in economically developed countries [2]. In particular, it was projected by the American Cancer Society that 2013 would see 30,640 new cases of liver cancer with 21,670 deaths [3]. This mortality rate represents an extremely poor outcome. Despite these dismal statistics, treatment of liver cancer has been steadily improving through the development of innovative treatment strategies. Among newer treatments, thermal ablation therapy is a promising technique for curative treatment of liver tumors in some patients. Currently, thermal ablation therapy is hindered by a lack of methods to reliably image the extent of the treated region immediately following treatment. Ultrasound (US) imaging is a low-cost, portable imaging modality capable of real-time monitoring of thermal ablation treatment. Therefore, it is the goal of this dissertation to explore novel techniques for imaging the extent of thermal ablation using parametric ultrasound imaging techniques.

1.2. Anatomy of the Liver

In an adult human, the liver occupies the majority of the upper right abdominal cavity. The liver is one of the largest organs of the body, weighing 1.2 to 1.8 kg, and occupying 1.8 to 3.1% of an adult's total body weight [4]. At any moment, the liver contains a volume of blood equivalent to approximately 25% of the cardiac output [5]. This blood is received from a dual vascular supply consisting of the portal vein and hepatic artery. The majority of blood volume is

supplied by the portal vein, while the liver receives the majority of its oxygen from the hepatic artery [5]. In addition to having a dual vascular supply, the liver also has dual outflow tracts. Blood is drained from the liver by the hepatic vein, and bile produced in the liver is removed by the biliary system [4]. Anatomically, the liver may be divided into four lobes: right, left, quadrate, and caudate [4]. The liver may also be divided into nine segments based on the branching pattern of its vasculature [5].

The bulk of the liver consists of hepatocytes, which comprise 4/5'th of the volume of the normal liver [4]. These cells are generally 25-40 microns in diameter with a polyhedral shape. The hepatocytes of the liver are arranged individually along curves called cords, and the spaces between these cords are referred to as sinusoids. These sinusoids are lined primarily by two types of cells, Kupffer cells and endothelial cells [4]. Kupffer cells are cells of the immune system which act as macrophages, and measure up to 9 microns in length [4]. Endothelial cells have sizes ranging from 50-80 nm and occupy approximately half the volume of the liver sinusoids [4]. Their primary function is to filter macromolecules from the sinusoidal blood [4].

On a microscopic level, the liver is often divided into a series of functional units called liver lobules. Though the three-dimensional architecture of the liver is complex, it is a remarkable fact that no matter how the liver is sliced it has the same appearance on histology slides [5]. When examining the liver on any given histology slide, it presents as a collection of lobules. Each of these lobules consists of liver parenchyma and 4-6 portal tracts each surrounding a central vein [5]. The portal tracts are collections of a slightly variable number of vessels. A single portal tract may contain one or two interlobular bile ducts, a hepatic arteriole, and a hepatic venule [5]. A portal tract is sometimes referred to as a portal triad.

While the two-dimensional appearance of the liver on histology is settled, the basic functional unit of the liver is still a matter for debate. The classic liver lobule, consisting of a hexagonal arrangement of portal tracts surrounding a central vein, was described in 1833 by Kiernan [5]. However in 1954, Rapaport proposed the acinus as the basic functional unit of the liver [5]. The acinus is based on the distance of sinusoids from arterial blood supplies, and it lies between two central veins [5]. The primary liver lobule was proposed in 1979 by Matsumoto for the basic functional unit of the liver [5]. This construction attempts to take into account the three dimensional micro-architecture of the liver. This model for the basic functional unit of the liver has the appealing characteristic that it has a correspondence to the classical liver lobule. Six to eight Matsumoto primary liver lobules in a hexagonal array corresponds to the classic liver lobule [5].

The vasculature of the liver is arranged across a wide range of size scales. In ultrasound measurements across 107 patients aged 21-40, a mean diameter of 11 mm was measured for the portal vein [6]. This large vessel undergoes extensive branching into interlobar, segmental, interlobular, pre-terminal, and terminal portal venules measuring 20-30 microns in diameter[4]. The branches of the hepatic artery accompany the branching of the portal vein until within the portal tract. Here the hepatic arterial circulation branches into two segments: the periportal plexus, and peribiliary plexus. The periportal plexus drains into the liver sinusoids and the peribiliary plexus drains into the interlobular bile ducts. Meanwhile, the smallest component of the biliary tract is the biliary canaliculi. These microvessels range in size from 0.5 to 1 micron in diameter and are located in the intercellular spaces between hepatocytes. As the canaliculi enter the portal tracts they become the canals of Hering, which feed into the interlobular bile ducts (15

to 20 micron diameter), which feed into the septal ducts (100 micron diameter), which lead to the segmental ducts (800 micron diameter), and finally the hilar ducts (1.5 mm diameter) [4].

1.3. Liver Cancer

The most common type of primary liver cancer is hepatocellular carcinoma (HCC), which accounts for 83% of all cases of primary liver cancer [7]. Intrahepatic cholangiocarcinoma (ICC) is the second most common primary tumor of the liver. In the United States, ICC accounts for approximately 15% of all primary liver cancer cases [8]. Hepatocellular carcinoma is currently theorized to arise in either mature hepatocytes, liver stem cells, or a combination of these cells [7]. Cholangiocarcinoma originates from malignant transformation of cholangiocytes, the epithelial cells of the bile ducts[8].

The etiology of HCC is well established. Between 75% and 80% of all cases of primary liver cancer are attributable to persistent viral infection by either the hepatitis B virus (HBV) or the hepatitis C virus (HCV) [9]. In developed countries, viral infections are typically acquired in adolescence or later in life through sexual contact, blood transfusion, or other invasive procedures under non-sterile conditions [9]. Other factors may influence the risk of primary liver cancer and increase the potency of HBV and HCV with respect to their ability to create primary liver tumors [9]. Both alcohol use and dietary aflatoxin exposure have been linked to elevated risk of developing primary liver cancers in individuals carrying HBV or HCV antigens [9]. In southeast Asia, the primary cause of intrahepatic choloangiocarcinoma has been identified as chronic biliary tract infestation with parasitic liver flukes, *Opisthorchis viverrini* and *Clonorchis Sinensis*. The incidence of ICC in the United States has been rising, and risk factors for this disease include liver cirrhosis, HCV infection, and diabetes [8].

In the U.S. and Europe, metastatic liver tumors are far more common than primary liver tumors. The liver is a frequent site of metastasis, accounting for 25% of all metastases from solid organs [10]. Carcinomas are the most common metastasis, and most of these are adenocarcinomas [10]. The most common organ of origin for metastasis is the lung, followed by the colon [10]. Typically, treatment of metastases to the liver from the lung are strictly palliative. Meanwhile, local treatment of colorectal metastases has been shown to prolong survival or potentially provide a cure for some patients[11].

In addition to malignant liver tumors, benign hemangiomas frequently arise in the liver. A hemangioma is a solid tumor of the liver occurring mostly in middle-aged women [12]. A benign hemangioma merits no treatment unless it becomes giant (having a diameter greater than 5 cm) [13]. This type of tumor is almost always asymptomatic, and is usually only incidentally detected when performing abdominal examinations on patients with other disease [12].

1.4. Treatment of Liver Tumors

Treatment options for liver cancer include surgical resection, chemotherapy, radiotherapy, ablation therapy, or a combination of these techniques. Surgical resection has been recommended to treat solitary HCC tumors less than 2 cm in diameter [14]. However, five year recurrence rates following surgical resection of HCC have been found to approach 100% [15]. A 2010 study of hospitals across England examined surgical resection for treatment of metastases to the liver, and it found a five year survival rate of 44.2% [16]. The study indicated that patients that underwent surgical resection for metastases had a survival rate comparable to patients who only had stage III disease [16].

Following surgical resection, the liver itself is the most common site of tumor recurrence, with 50% of cases presenting here [17]. The lung makes up another 25% of cases, and the colon or rectum another 10-20% [17]. When examining 10 year survivors after surgical resection, one report found that approximately half of these patients required a second hepatectomy to treat recurrences [17]. The most powerful predictor of tumor recurrence is a positive surgical margin [17]. A positive surgical margin means that tumor cells are found out to the edges of the excised tissue, indicating that all malignant cells have likely not been removed from a patient. The regional lymph node involvement is also a powerful predictor of tumor recurrence [17].

Chemotherapy is often used in conjunction with surgical resection to treat liver tumors. Chemotherapy is also used to reduce a patient's tumor burden and to upgrade their status from having unresectable colorectal cancer (CRC) liver metastases to being candidates for surgery [18]. Even in patients presenting with CRC liver metastases that are initially eligible for surgery, it has been shown that perioperative chemotherapy confers a survival benefit to patients [18].

Radiotherapy is frequently avoided in treating liver tumors because the liver has a limited tolerance for radiation. Radiation induced liver disease occurs in 5% of patients at doses as low as 30-35 Gy to the whole liver [19]. Radiation induced liver disease is marked by severe congestion of the liver sinusoids and foci of necrosis within the liver [19]. This typically occurs 4-8 weeks after completing therapy [19]. Highly conformal radiotherapy treatments may have some utility for treating liver tumors, and phase I and phase II studies have been undertaken for treatment of liver metastases using stereotactic body radiotherapy [20].

Ablation therapy has long been recognized as an attractive treatment option for patients with inoperable liver tumors, dating back to Livraghi *et al*.'s 1995 study of percutaneous ethanol injection treatments of patients with HCC tumors [21]. There are numerous ablation treatments

developed and under development. These treatments may be categorized as either chemical or thermal ablation. Chemical ablation with absolute ethanol or acetic acid has been used to treat HCC, but it has not shown promise in treating CRC metastases [17]. HCC is a soft tumor usually occurring in a stiff, cirrhotic liver. Meanwhile, CRC metastases are firm or stiffer tumors, usually occurring in a soft liver. This makes injection of chemicals into colorectal metastases difficult [17].

Thermal ablation therapy includes both cryoablation and hyperthermic therapy. In cryoablation, liquid nitrogen and argon gas under high pressure are commonly applied to cryoablate tumors [22]. Temperatures less than -50° C are considered lethal to cells, though the exact temperature is debatable [22]. Multiple mechanisms for cell death exist depending on the temperature achieved. Cooling to temperatures less than 50° C is known to create lethal ice crystals within cells [22]. In slightly warmer, peripheral regions of the frozen tissue extracellular fluid freezes, and cells are dehydrated due to osmotic pressure [22]. In hyperthermic thermal ablation, tissue heating leads to immediate protein denaturation of cytosolic and mitochondrial enzymes and DNA-histone proteins [23]. These denatured proteins coagulate, which is to say that they bind together and form functionless complexes [23]. This damage results in cellular death over several days and is referred to as coagulative necrosis [23]. At tissue temperatures of 50° C, it may take several minutes to achieve coagulative necrosis [24]. At temperatures of 60° C, cell necrosis takes only seconds [24]. A wide variety of hyperthermic thermal ablation techniques have been developed including radiofrequency (RF) ablation, laser interstitial thermotherapy (LITT), high intensity focused ultrasound (HIFU), and microwave ablation (MWA).

In RF ablation, an alternating current with a frequency from 200-1200 MHz is applied. Current is applied by placing an exposed electrode directly into the target tumor. RF ablation was first demonstrated to be effective by Rossi *et al*. in a trial involving patients with inoperable HCC in a paper published in 1995 [25]. HCC is an easier tumor to treat with hyperthermic thermal ablation than metastatic tumors. Cirrhotic livers in which HCC occurs typically act as insulators, allowing more heat to be deposited within the tumor volume. Extensive research has been performed with regards to RFA of liver tumors. Solbiati *et al.* performed RF ablation on 29 patients with 44 hepatic metastases using cool-tip RF electrodes [26]. They confirmed complete necrosis of 66% of all treated tumors 3-6 months following treatment using CT and MR imaging [26]. Guglielmi *et al*. examined 98 patients treated by RF ablation for 145 HCC. They found complete ablation was achieved in 85.5% of tumors [27]. They also found median survival was 38 months for patients exhibiting alpha-fetoprotein levels below 100 ng/ml, complete ablation, and Child-Pugh class A cirrhosis [27].

In LITT, laser light energy is converted to heat. The most common laser in use is neodymium:yttrium-aluminum-garnet (Nd:YAG), with a wavelength of 1064 nm [28]. At this wavelength, Nd:YAG lasers exhibit a tissue penetration depth of up to 10 mm [28]. In LITT, photons are absorbed depending on the optical characteristics of the target tissue, and there is a corresponding temperature rise [28]. In HIFU, a low frequency high amplitude ultrasound pulse causes heating and cavitation in the target tissue [29]. In HIFU treatment of the liver, an extracorporeal device operating at a frequency near 1 MHz is typically used [29]. A single HIFU exposure typically creates a small, rice kernel-shaped lesion 1-3 mm wide and 8-15 mm long (along the beam axis) [30]. In a HIFU treatment of a tumor, multiple HIFU exposures are used to paint out the entire tumor target volume [30].

In MWA, a 14.5 gauge partially insulated microwave antenna is placed directly into the tumor. Electromagnetic (EM) waves are emitted through a non-insulated portion of the antenna, causing vibration of water molecules in the target tumor. This creates dielectric heating and leads to thermal coagulation. MWA antennas operate at frequencies of 0.9 to 2.45 GHz. MWA has several advantages over RF ablation, LITT, and HIFU. MWA has an active heating zone of up to 2 cm [31]. Meanwhile, RF ablation and LITT rely on thermal conduction to heat tissue over this large a volume [31]. This gives MWA a strong advantage when the target tumor is abutting a large blood vessel. Flowing blood in large vessels helps to protect the vascular endothelium if a vessel is abutting a tumor. However, a vessel abutting a tumor could also act as a heat sink during the ablation process and limit the size of the ablation zone when heating is largely achieved by thermal conduction. Additionally, microwaves are able to propagate through water vapor and dehydrated, charred, and desiccated tissues which all may be produced over the course of an ablation procedure [31]. All these tissue types are known to hamper the transmission of energy through RF ablation, HIFU, and LITT [31].

1.5. Imaging of the Treated Region Following Thermal Ablation

Research on monitoring thermal ablation treatment has proceeded along two complementary tracks: monitoring temperature rise during treatment, and monitoring the extent of tissue coagulation following treatment. Ultrasound (US), magnetic resonance imaging (MRI), and X-ray computed tomography (CT) imaging have all been utilized to delineate the extent of the thermal ablation in some way. Relative to ultrasound, MRI has the disadvantage of its high cost. Meanwhile, CT imaging has the disadvantage of exposing patients to ionizing radiation.

Magnetic resonance imaging is the most sensitive imaging technique, and it can be used to detect small tumors that may not be visible on other imaging modalities [32]. Additionally, MR imaging has the advantage of being able to track temperature changes in tissue up to very high temperatures with an accuracy of 1° C [33]. In current clinical practice, the standard of care for patients is to undergo a follow up contrast enhanced CT or MR imaging examination 4-6 weeks following ablation treatment [34]. The ablated region will then appear as a non-enhancing region on contrast enhanced CT or MR images [34]. An irregularly shaped enhancing region in the periphery of the treated region would indicate that an ablation procedure failed to treat the entire tumor [34].

Contrast enhanced ultrasound (CEUS) has also demonstrated potential for monitoring the extent of thermal ablation treatment. In one study, Solbiati *et al.* imaged the treated region with ultrasound following RF ablation and injection of sulfur hexafluoride microbubbles [35]. They treated 109 patients with 192 HCC lesions and 53 patients with 97 liver metastases, and they detected residual tumor with CEUS at almost the same rate as with contrast enhanced helical CT [35]. Another study compared the performance of residual tumor detection between CEUS performed immediately after treatment, CEUS performed 24 hours after treatment, and contrast enhanced CT performed 24 hours after treatment [36]. All three imaging tasks performed comparably. However, both CEUS and contrast enhanced CT tended to exhibit a high number of false negatives and a correspondingly low sensitivity [36]. When performing contrast enhanced imaging, a hyperemic reactive halo around the ablation zone has been found for weeks following treatment [36]. This hyperemic region makes it difficult to ascertain whether or not viable tissue that needs to be treated remains at the edge of the ablated region. It is this phenomenon that is responsible for the false negatives exhibited with contrast enhanced imaging.

1.6. Organization of the Dissertation

While contrast enhanced imaging has demonstrated its utility for follow-up imaging of thermal ablations, this dissertation focuses on fundamental tissue properties which may be estimated and imaged using ultrasound without contrast enhancement. This dissertation investigates bulk mechanical and acoustic properties of liver and thermal ablations that may be exploited to produce parametric images of the treated region following thermal ablation.

In Chapter 2, we provide an overview of elasticity imaging techniques and a review of their application to imaging thermal ablation. We then describe electrode displacement strain imaging for monitoring RF ablation of liver tumors. The block matching algorithm utilized to produce displacement fields used in quasi-static axial strain imaging is then discussed.

In Chapter 3, we apply electrode displacement imaging to the problem of imaging thermal ablations in an open surgery *in vivo* porcine animal model. We then apply electrode displacement strain imaging to the problem of imaging thermal ablations in a percutaneous treatment of a VX2 tumor bearing rabbit animal model.

In Chapter 4, we present scattering models utilized in ultrasound imaging. We discuss periodic scattering models in the liver and extend frequency domain ultrasound simulations developed at UW-Madison to the case of quasi-periodic scattering. We also review methods for estimating the mean scatterer spacing (MSS) in quasi-periodic scattering models. Finally, we discuss the multi-taper method of David Thomson, and we apply multi-taper spectral calculations to computing MSS in computer simulations.

In Chapter 5, we examine spectral coherence in simulated models of tissue, and we compare simulation results with measurements made in bovine liver *ex vivo*. We also examine spectral coherence measurements in thermally coagulated bovine liver *ex vivo*. We demonstrate

that while normal liver may be modeled as a combination of aperiodic and quasi-periodic scatterers, thermally coagulated tissue is better modeled as a collection of strictly aperiodic scatterers.

In Chapter 6, we examine reference phantom measurements of attenuation. We then investigate the theoretical performance of reference phantom attenuation in simulations and tissue-mimicking (TM) phantoms with low, variable scatterer number densities. Finally, we examine the performance of attenuation estimation in the liver and thermally coagulated liver with measurements made in *ex vivo* bovine liver.

Finally, in Chapter 7, we summarize our results and discuss future directions for imaging thermal ablations with ultrasound.

Chapter 2. Elastographic Imaging of Thermal Ablations

2.1. Linear Elasticity

In this chapter, we discuss linear elasticity. While reconstruction of non-linear elastic properties of tissue has been demonstrated [37], non-linear elasticity parameters have largely been used to distinguish between different types of breast tumors rather than used to delineate the extent of thermal ablation [38]. Producing images representing bulk mechanical properties of linear, elastic tissue is frequently referred to as elastography. The use of the term "elastography" for strain and modulus imaging originated from a 1991 paper by Jonathan Ophir *et al* [39]. In this paper, Ophir *et al.* demonstrated that a strain distribution could be estimated in tissue using a one-dimensional cross-correlation technique applied between pre-compression and post-compression RF data frames. If the stress distribution within tissue is known, then an elastic modulus image may be produced from a strain image [39]. In elastography of the liver, tissue is often imaged when subjected to only a small deformation [40]–[42]. In this regime, tissue is often modeled by a linear, elastic solid [43]–[46]. There are five parameters commonly used to describe a linearly elastic solid: Bulk modulus (denoted K), Young's modulus (denoted E), Lamè's first parameter (denoted λ), the shear modulus (denoted μ), and Poisson's ratio (denoted ν). Tissue is frequently modeled as incompressible [47]–[49] or nearly incompressible [44], [50], [51], which means that a Poisson's ratio of 1/2 or a Poisson's ratio close to 1/2 is used to model tissue. There have been limited attempts to create images of estimates of Poisson's ratio by plotting axial versus lateral strain [52], [53]. Estimates of Poisson's ratio in tissue have also been

inferred from measurements of the shear modulus and bulk modulus [54], [55]. Poisson's ratio may be computed from the bulk modulus and shear modulus according to:

$$\nu = \frac{3K - 2\mu}{2(3K + \mu)} \tag{2.1}$$

In the limit of K being much larger than μ, ν approaches the value of 1/2. An approximate value for the bulk modulus may be estimated from the relationship between sound speed, density, and bulk modulus:

$$c = \sqrt{\frac{K}{\rho}} \tag{2.2}$$

Assuming a sound speed of 1540 m/s and a tissue density of 1.0 g/cm^3, tissue bulk modulus may be assumed to be 3.27 GPa. Meanwhile, shear modulus estimates in the livers of patients with different degrees of liver fibrosis using Fibroscan technology yield values of only 5-100 KPa [56]. The values much larger than 5 KPa in this study were all due to patients with liver fibrosis [56]. Therefore in a healthy liver, the shear modulus is as low as 1.6×10^{-4}% the value of the bulk modulus, and Poisson's ratio would only deviate from 1/2 by 1.5×10^{-4}% if we assume these values for the bulk modulus and the shear modulus.

In elasticity imaging, it is the shear modulus or the Young's modulus that is typically sought. However in quasi-static elastography, the image that is often computed is the magnitude of the axial strain component of the Cauchy strain tensor [39], [41], [57]–[61]. The Cauchy strain tensor is given by a sum of partial derivatives of displacement fields:

$$\epsilon_{ij} = \frac{1}{2}(\partial_i u_j + \partial_j u_i) \tag{2.3}$$

In equation 2.3, u_j and u_i are the i^{th} and j^{th} component of a vector displacement field in a Cartesian coordinate system. ∂_i and ∂_j are partial derivative operators, components of the gradient

operator in the i^{th} and j^{th} coordinates of a three-dimensional Cartesian coordinate system. For a linear, elastic solid there is a linear relationship between the Cauchy strain tensor and the stress tensor. In its simplest form, the stress-strain relationship may be written in terms of Lamé's first parameter and the shear modulus:

$$\sigma_{ij} = \epsilon_{kk}\lambda\delta_{ij} + 2\mu\epsilon_{ij} \quad \textbf{(2.4)}$$

In equation 2.4, the symbol δ_{ij} is the Kronecker-delta function. It is 1 when $i=j$ and 0 otherwise. A summation is taken over the repeated indices on the first term. This relationship may also be written using Poisson's ratio and the Young's modulus:

$$\sigma_{ij} = \frac{E\nu}{(1+\nu)(1-2\nu)}\epsilon_{kk}\delta_{ij} + \frac{E}{(1+\nu)}\epsilon_{ij} \quad \textbf{(2.5)}$$

The stress-strain relationship in equation 2.5 may be inverted:

$$\epsilon_{ij} = \frac{1}{E}(\sigma_{ij}(1+\nu) - \nu\sigma_{kk}\delta_{ij}) \quad \textbf{(2.6)}$$

In quasi-static elasticity imaging, it is assumed that tissue is compressed at a slow enough rate that acceleration of the particles is negligible [44]. If we neglect the influence of gravity, then for a quasi-static situation a linear elastic material must satisfy the following three differential equations expressed in indicial notation:

$$\frac{\partial\sigma_{ij}}{\partial x_j} = 0 \quad \textbf{(2.7)}$$

Solving equation 2.7 in combination with displacement or traction boundary conditions to yield displacement and strain fields within a material is known as the forward problem of elastography [62]. In Ophir's paper on elastography [39], it was a strain distribution that was actually estimated within tissue using cross-correlation techniques. In order to convert a strain image into a modulus image or interpret a strain image as a modulus image, a common assumption made is

that stress is uniform throughout an image [51]. Specifically, if we assume σ_{xx}, σ_{yy}, σ_{zz}, and the Poisson's ratio are constant throughout an image, then from equation 2.6**,** $\varepsilon_{zz}=1/E\ (\sigma_{zz} - \nu\ (\sigma_{xx} + \sigma_{yy}\ )\ )$, and the axial component of the strain tensor is inversely proportional to the Young's modulus.

Much effort has been devoted to determining a Young's modulus or shear modulus distribution within tissue, given displacement fields estimated within tissue following a deformation. Determining an unknown modulus distribution given a displacement field within a body and boundary conditions is known as the inverse problem of elastography. Methods for solving the inverse problem are typically labeled as either direct [62]–[64] or iterative [44], [46], [65], [66] approaches, with iterative approaches being more commonly employed because of the stability of this method with respect to noise. In an iterative approach to modulus reconstruction, a finite element model is iteratively updated until a displacement field predicted by this model matches with a measured displacement field obtained from ultrasound images. The choice of constitutive equations and boundary conditions is an important question, and the uniqueness of solutions in modulus imaging for compressible and incompressible material models has been explored [49], [67].

In addition to quasi-static elastography, many other methods have been proposed for creating images of the Young's modulus or shear modulus of tissue. These methods include dynamic deformation methods such as acoustic radiation force based imaging (ARFI) [68] and shear wave based imaging methods [69]–[74]. During ARFI, focused ultrasound is used to apply localized displacements to small tissue volumes through radiation force. Tissue displacement results from momentum transfer to particles within tissue through absorption of energy in the acoustic wave [68]. Correlation based methods are then used to track the resulting displacements,

and the magnitude of the resulting displacements in the axial direction can be shown to be inversely proportional to the Young's modulus of tissue [68].

In shear wave imaging, low frequency mechanical excitations are applied to tissue, and the displacements caused by the resulting shear waves are estimated [56], [71]. Multiple methods have been proposed for generating shear waves and performing the subsequent signal processing. In [71], Sandrin *et al.* proposed using a low-frequency vibrating device surrounding the active elements of a clinical array transducer to generate shear waves within tissues. They then proposed tracking the resulting displacements using high frame rate ultrasound and solving a simplified wave equation for the shear modulus [71]. In [72], Gao *et al.* proposed sonoelastography. In sonoelastography, a sinusoidal excitation (amplitude < 50 microns and frequency < 1 kHz) is externally applied to the tissue of interest through a device such as a speaker. The external source generates shear waves within tissues, and regions with a high shear modulus exhibit a lower displacement amplitude than regions with a low shear modulus [72].

In supersonic shear imaging, the ultrasound beam is focused to a point to generate a shear wave source through radiation force [70]. This source is moved along a column in the axial direction generating a plane shear wave propagating in the lateral direction [70]. Motion tracking at a high frame rate is performed, and the shear modulus is then recovered by inverting the wave equation [70]. MR elastography has also been utilized to track shear waves generated in tissue [73]. In magnetic resonance elastography, an external vibration source coupled to a patient's skin creates shear waves within tissue. Displacement throughout a tissue volume is tracked by phase encoding MR imaging methods [74]. The wave equation may be inverted locally to arrive at an estimate of the shear modulus in a region [74].

2.2. Elastographic Imaging of Thermal Ablations

Following radiofrequency (RF) ablation, the coagulation zone that is created has been shown to have a much larger Young's modulus than healthy liver tissue [75]. Specifically, Bharat *et al.* found a Young's modulus ranging from 5.0 kPa to 25.0 kPa in *ex vivo* canine tissue undergoing RF ablation at temperatures from 60° to 90° C [75]. Thus, imaging tissue mechanical properties seems to be a promising avenue for monitoring the progress of thermal ablations. Quasi-static elastography and its ability to image the extent of RF ablation zones has been extensively studied by our group. One of the difficulties associated with this technique in abdominal organs is the non-uniform deformation that results from pushing the transducer or an external compressor plate against the abdomen [76]. Diaphragmatic and cardiovascular motion has also been used as a deformation approach in the liver [76], though the compressions resulting from physiological motion may not be controlled and reproducible, as necessary for solving the inverse problem for elastography. As a solution to this, our laboratory has developed electrode displacement elastography (EDE). In electrode displacement elastography, the mechanical stimulus is applied by displacing the RF ablation electrode, which is firmly bonded to the thermal ablation. The feasibility of this method has been demonstrated in finite element simulations [77], phantom studies [41], *ex vivo* [42] and *in vivo* animal models [78].

Both axial strain imaging and modulus reconstruction have been used extensively in our laboratory to delineate the extent of ablation zones. Work on imaging and delineating ablation zones began by our group in 2001, with initial results published in 2002 [61]. In 2002, our laboratory demonstrated both *ex vivo* and *in vivo*, that high contrast axial strain images of thermal ablations could be produced [61]. Our laboratory initially introduced the concept of electrode displacement elastography (EDE), by using a stepper motor to apply sub-millimeter

displacements to an ablation electrode after performing RF ablation on a porcine animal model [61]. The following year, 2003, the accuracy of axial strain imaging for depicting the extent of ablation zones was demonstrated by producing axial strain images of 40 thermal ablations *ex vivo* and comparing pathological areas and volumes with areas and volumes measured in axial strain images [42]. Following this, it was shown by our laboratory group that elastographic imaging has the potential to provide better contrast between ablated and unablated liver tissue than x-ray CT imaging without contrast [79]. It was also demonstrated by our group that though gas bubbles formed during RF ablation procedures and degrade axial strain image quality somewhat, the extent of the coagulation zone may still be visualized before these gas bubbles fully disperse [80].

Next, our laboratory investigated the effects of the duration and intensity of the RF ablation on the resulting ablation stiffness [75]. It was found that different tissue stiffnesses were produced by ablating liver tissue at different temperatures, though there was not a monotonically increasing relation between tissue stiffness and ablation temperature. An interesting observation by our group in regards to EDE was made in 2006. Using FEA simulations, it was demonstrated that due to the particular mechanical boundary conditions of EDE the contrast on strain images is potentially higher than the underlying modulus contrast of the tissue being imaged [81].

The next several experiments published by our laboratory, from 2007-2008 were finite element and phantom experiments validating the feasibility of EDE [41], [77], [82]. Most notably, 2008 marks our group's first publication demonstrating three-dimensional axial strain reconstructions of an EDE TM-phantom acquired using a mechanically rocked array transducer [82]. In 2009, our group began investigating modulus imaging for the display of tissue stiffness during RF ablation. A phantom study was published demonstrating the feasibility of solving the

inverse problem during quasi-static strain imaging and using the resulting image to depict the extent of the ablation zone [40]. A comparison between axial strain and modulus images of thermal ablations in an open surgery RF ablation procedure was published following this [83]. Preliminary results suggest that modulus images may provide more easily segmentable depictions of ablation zones than axial strain images [83].

In addition to quasi-static elastography, our group has also conducted considerable work on shear wave imaging for depicting the extent of thermal ablations [84]–[87]. In [86], Bharat *et al.* determined shear wave velocities in computer simulations where a half sinusoid axial displacement was applied to the tissue bonded electrode following RFA [86]. The shear wave velocity was then related to the time until the maximum displacement at a point lateral to the electrode [86]. Shear wave velocity images of TM phantoms and thermal coagulations in *ex vivo* bovine liver were presented by DeWall *et al.* in [85]. In [87], DeWall *et al.* compared cross-sectional areas from shear wave velocity images with cross-sectional areas measured on optical images of *ex vivo* thermal lesions in bovine livers and found good agreement.

Several other groups have demonstrated promising elasticity imaging results with regard to imaging of thermal ablations. The possibility of using ARFI to delineate the extent of the thermal ablation zone has been investigated [88]–[91]. In [88], Fahey *et al.* utilized ARFI imaging to delineate the extent of chemically and thermally induced lesions in *ex vivo* bovine liver. In [89], ARFI was used to monitor RF ablation procedures in ovine (sheep) cardiac tissue. In [90], *in vivo* ARFI images of thermally ablated regions in ovine liver were presented. A small trial of 5 patients presenting 5 liver tumors was presented in [91].

Supersonic shear wave imaging (SSI) has also been used to delineate the extent of thermal ablations [92], [93]. In [92], Bercoff *et al.* used SSI to delineate the extent of HIFU

lesions created in *ex vivo* tissue. In [93], Arnal *et al.* used a confocal arrangement of an 8 MHz linear array ultrasound probe and a HIFU device to monitor the formation of thermal lesions in *ex vivo* porcine muscle in real-time. Sonoelastography has also been applied to elasticity imaging of thermal ablations. In [94], sonoelastography was used to visualize the extent of thermal coagulations produced with RF ablation and HIFU in porcine animal models. To a limited extent, Magnetic resonance elastography has also been used to determine the extent of the treated region following thermal ablation therapy [95], [96]. Wu *et al.* demonstrated MRE images of thermal ablations produced in *ex vivo* porcine muscle [95]. Chen *et al*. performed *in vivo* experiments demonstrating MRE images of thermal ablations created with LITT in pig liver [96] .

2.3. Displacement and Strain Estimation

Almost all elasticity imaging techniques have as their first processing step examination of a time series of ultrasound images prior to and following a mechanical excitation or deformation and estimating the displacement field within tissue. In Ophir's original paper, displacement fields were estimated by a simple one-dimensional cross-correlation based analysis [39]. Other similarity metrics have been utilized for computing time delays in ultrasound motion tracking including sum of squared differences (SSD), sum of absolute differences (SAD), non-normalized cross correlation, and normalized cross-correlation [97]. Selecting a similarity metric is a trade-off between computational efficiency and displacement estimation performance.

With a simple exhaustive cross-correlation search, large errors in motion tracking on the order of half a wavelength or more may occur (154 microns or more for a sound speed of 1540 m/s and a frequency of 5 MHz). Large errors can be a result of signal decorrelation introducing peak hopping errors in cross-correlation based algorithms. In a peak hopping error situation, an

inaccurate displacement is found because the signal may provide a large correlation coefficient value on a secondary peak rather than the primary peak near zero-lag [98]. Peak hopping errors are typically worse for RF data than they are for the envelope of echo signals [98]. Signal decorrelation can result from out-of-plane motion of scatterers, non-uniform motion of scatterers within a resolution cell, and even from the tissue deformation itself [59]. Decorrelation errors are the greatest at large strains, approaching 10% [59].

These large motion tracking errors are typically handled in elastography by introducing block matching algorithms that contain a continuity constraint in addition to the cross-correlation technique. One form of continuity constraint is to employ a guided search in the block matching algorithm [99]–[101]. In [100], Zhu *et al.* utilized an axially adjacent displacement estimate as an initial guess for a subsequent sum of squared difference calculation with a restricted search range. In [101], Pesavento *et al.* used a phase-zero algorithm. In a phase-zero algorithm, a complex correlation coefficient is computed from the analytic pre and post-compression signals. The time shift yielding zero-phase for the complex correlation is the desired time shift. In [101], Pesavento *et al.* minimized the phase of the complex correlation with a Newton search. Pesavento's algorithm was a predictive algorithm because for each estimated displacement the initial value for the Newton search minimization was the time shift estimated at the axial neighbor of the current location. Chen *et al.* developed a predictive search algorithm which automatically divided the image into arbitrarily shaped, disjoint regions having continuous displacement fields [99]. In the algorithm of Chen *et al.*, an initial grid of displacement candidates is selected and these starting displacements are referred to as seeds. The seed with the largest value for cross correlation is propagated as an initial guess for neighboring cross correlation searches whose range is only a few pixels [99]. If the cross-correlation values drop

within one region, a new seed is selected and a new region in the displacement image is grown [99]. This process repeats until an entire image is formed. In Chen's algorithm, the predictive search is free to grow in either direction: laterally or axially [99].

Another form of continuity constraint is to introduce an explicit cost function containing a term for image similarity and a second term for displacement continuity [102], [103]. It has been shown that such a cost function may be efficiently solved using a Viterbi algorithm [102], [103]. In [102], Jiang *et al.* implemented two algorithms utilizing a cost function to enforce motion continuity over small regions in a displacement image and two different predictive search strategies to reduce the possible number of displacements allowed at each point. In [103], Rivaz *et al.* developed a similar dynamic programming algorithm in which they enforced continuity along an A-line and between adjacent A-lines and minimized the resulting cost function with the Viterbi algorithm.

Multi-level strategies are also commonly used to enforce motion continuity constraints [104]–[107]. In a multi-level block matching algorithm, a large block size is used to estimate an initial low-resolution displacement image. This coarse displacement image is used to initialize restricted block-matching search regions to form a higher resolution displacement image. The process of searching smaller regions for block matching and initializing the search with a lower resolution image is repeated until a desired resolution is achieved. In [106], Yeung *et al.* utilized a four-level block matching algorithm where the axial length of the blocks were reduced in half at each level. Correlation was performed on fully sampled data at all levels, and a smoothness constraint was introduced at each level of block matching [106]. In [107], the authors also utilize a multi-level model with smoothness constraints, although they impose no smoothness constraint on the top level of their algorithm. In [105], Chen *et al.* utilize a two-step method where they

perform normalized cross-correlation with a 20 wavelength long block in the first step and a smaller block in the second step. Shi and Varghese extended this method to a multiple level algorithm where a combination of envelope and RF data was used in the block matching [104]

A significant number of peer-reviewed journal papers have been devoted to the problem of estimating displacement with sub-sample precision [108]–[112]. When computing a cross-correlation function, a discrete array of RF data is used for the calculation. However, to perform accurate motion tracking it's necessary to estimate displacement with a precision finer than the typical pixel spacing in ultrasound (19.25 microns assuming a sound speed of 1540 m/s and a sampling rate of 40 MHz). To compute displacements with sub-sample precision an interpolation scheme is necessary for the cross-correlation function in the region of the peak. Cespedes compared curve fitting with a parabola and cosine function, frequency domain zero-padding, sinc interpolation, and iterative reconstructive filtering for sub-sample precision estimates in one dimension [108]. In two dimensions, McCormick *et al.* utilized windowed sinc interpolation with a variety of window functions for sub-sample interpolation [109]. In one dimension, Viola and Walker proposed spline fitting both pre and post-compression signal and finding the continuous time delay which yielded the minimum sum of squared errors [113]. Their algorithm was later extended to two dimensional kernels [112].

With an axial displacement field computed, many elasticity algorithms estimate and display the magnitude of the axial strain as their final step. In order to estimate axial strain a gradient operation must be performed on the axial displacement field, which amplifies noise in the displacement image. The most commonly used estimator for axial strain is a linear least squares fit to the displacements [60]. Using a least squares strain estimator, a small kernel of displacement points, typically spanning 2 to 3 mm [40], is fit to a line with a least squares fit and

the axial strain is the slope of that line [60]. The least squares strain estimator, along with several other commonly used strain estimators, have been shown to be equivalent to a linear filtering operation to smooth the displacement data followed by differentiation of the smoothed displacement field [114]. The axial strain imaging algorithms discussed so far are two-step algorithms, where a displacement field is estimated in step one and then differentiated in step two to yield a strain field. In addition to two-step strain imaging algorithms, strain imaging algorithms have been proposed where strain is estimated by examining the power spectrum without an intermediate block matching step [58], [115], [116]. Images formed this way are referred to as spectral strain images [58], [115], [116]. In spectral strain imaging, the difference in the centroid of the power spectrum before and after compression is estimated and related to the applied strain [58], [115], [116].

In this dissertation, we form elastographic images of thermal ablations through electrode displacement elastography. We estimate and display the magnitude of the axial strain following displacement of the RF electrode in the case of RF ablation and displacement of the microwave antenna in the case of microwave ablation. We refer to both devices as the applicator. We estimate an axial displacement field between pre and post-compression RF data using two algorithms. In the following chapter, we form EDE strain images of thermal ablations in open surgery *ex vivo* porcine liver models. We utilize the multi-level algorithm of Shi and Varghese to estimate an axial displacement field with RF data from this study [104]. Additionally, we examine EDE strain images in VX2 tumor bearing rabbit models prior to and following thermal ablation. We utilize the quality guided block matching algorithm of Chen *et al.* when estimating displacement fields from RF data acquired from the rabbit models [99]. In both cases we estimate axial strain from axial displacements with the widely utilized linear least squares

estimator [60]. To achieve sub-sample displacement estimation, we perform sub-sample fitting with a parabola [108].

Chapter 3. *In Vivo* Strain Imaging in Animal Models

3.1. Introduction

In this chapter, we discuss results of electrode displacement strain imaging experiment in *in vivo* porcine livers and in a rabbit model of VX2 tumors. Healthy porcine livers were imaged following thermal ablation with a commercial RF ablation system. Additionally, we present electrode displacement strain images of VX2 tumors in rabbit animal models prior to and following microwave ablation. Some of the results presented in this chapter were previously presented in [78].

3.2 RF Data Acquisition of Porcine Thermal Ablations

Four female domestic swine were used for this study. The study was approved by the research animal care and use committee of the University of Wisconsin-Madison. Animal husbandry and experimental studies were compliant with the NIH Guide for Care and Use of Laboratory Animals (http://oacu.od.nih.gov/regs/guide/guidex.htm). General anesthesia was induced initially with an intramuscular injection of teletamine and zolazepam (Telazol, Fort Dodge Laboratories, Fort Dodge, IA) and xylazine (Rompun, Bayer Corporation, Shawnee Mission, KS) and maintained with 1%–3% inhaled isoflurane. The anesthetized pigs were placed in a supine position and the liver exposed through a midline incision. Thirteen RF ablations were created in the normal liver parenchyma, and electrode displacement utilized for strain imaging. RF ablations were performed in any of the four lobes of the liver. The only criterion for the selection was whether the thickness of the lobe could support the formation of an ablation zone, leaving ~1–3 cm of normal tissue from the liver surface to the ablated region. RF ablation

procedures were performed using a Cooltip™ RF ablation system (Valleylab, Boulder, CO). The RF electrodes were 17 gauge (1.5 mm in diameter) with a 3.0 cm exposed tip. Ablation zones were created by applying power for 10 min per ablation using an impedance-controlled power pulsing algorithm. This duration was chosen since it provides a sufficient ablation zone size for ultrasound B-mode and strain imaging, as the ablated region remains within the transducer field of view. After the ablation procedures, electrode displacement elastography was performed on the thermally ablated regions. Radiofrequency data were acquired within 10–15 min of the end of the ablation procedure for all the ablated regions.

The ultrasound system utilized to guide ablation applicator placement was a Siemens Antares (Siemens Medical Solutions, USA Inc., Issaquah, WA) real-time scanner equipped with a 10 MHz center frequency linear-array transducer (VFX 13–5) with a bandwidth of approximately 60%. After the ablation procedure, the scanner was also used to collect radiofrequency data loops during freehand perturbation of the ablation electrode for electrode displacement elastography. Pairs of these radiofrequency data frames were analyzed using a two-dimensional (2D) multistep method for displacement estimation, followed by a linear least-squares strain computation algorithm [104]. Following electrode displacement-based strain imaging, the liver was excised and the ablation zone exposed for gross-pathology measurements by slicing along the ultrasound and elastographic imaging plane using a commercially available meat slicer.

3.3 Strain Images and Observer Segmentations

B-mode and strain images were segmented by three observers and an automated segmentation algorithm. The three observers included myself and two other graduate students

(Ryan DeWall and Shyam Bharat). All three observers' roles in the field of elastography were that of graduate researchers in Medical Physics and Engineering disciplines. At the time of the segmentations, Ryan DeWall and myself had less than one year of experience working in the field of strain imaging and Shyam Bharat had multiple years of experience working in the field of elastography. All image segmentations were performed using a polygon fitting tool from ImageJ (public domain software developed at the NIH) for segmentation. The observers, indicated by their initials, (A (NR), B (RD), and C (SB)) were blinded to both the ultrasound B-mode and pathology image prior to lesion segmentation on the strain images of the thermal ablation zones, which were also randomized for each observer. The only guidance provided to the observers was to delineate the stiffer or darker region on the strain image from the surrounding softer or lighter background liver tissue. The strain images were also segmented using an automated segmentation algorithm developed in our laboratory. These automated segmentations were also compared to pathology measurements using linear regression. The segmentation algorithm consisted of a series of basic morphological image processing steps, such as dilation and opening. First, a 3 by 3 pixel averaging filter was applied to smooth the image. A binary image was created by thresholding at a value adjusted for the amount of strain present in the image. Next, a mask was created that removed all "holes" in image objects through a process of iterative dilation and masking with the background. Morphological opening was performed with a disk structural element with radius 30% of the size of the largest object in the image, where size is defined to be the radius of the largest circle that would fit inside objects in the image. The opening was performed to isolate large, nearly convex masses. The ablation zone was assumed to be the mass lying near the center of the image, isolated through iterative dilation and masking. Dilation with a structural element 50% the size of the opening structural element

and masking with the original threshold image restored the outer mass of the ablation zone. Finally, morphological closing with a structural element 65% of the opening structural element's size ensured a realistic shape. For two thermal ablations (ablations 12 and 13), it was necessary to replace the high strain region in the center of the manually segmented ablated region using uniformly distributed random numbers corresponding to strains between 0% and 0.2% in order to achieve proper automated segmentation. In the gross-pathology photographs of the corresponding ultrasound imaging plane (marked on the liver surface), the extent of the ablation zone was delineated manually, based on the transition between white and pink tissue regions. The ultrasound scan plane was identified by marking the position of the linear-array transducer on the liver surface. This mark recorded the orientation of the transducer relative to the ablation electrode; the needle track from the RF ablation was used to obtain the imaging plane for pathology measurements. No fiducial markers were introduced into the scan plane, so comparison of the elastographic segmentations to the pathology were made manually based on the shape of the region depicted. This section presents B-mode images, strain images, pathology images, and the corresponding segmentations chosen by all human observers. In the images, red segmentations correspond to observer NR, green to observer RD, and blue to observer SB.

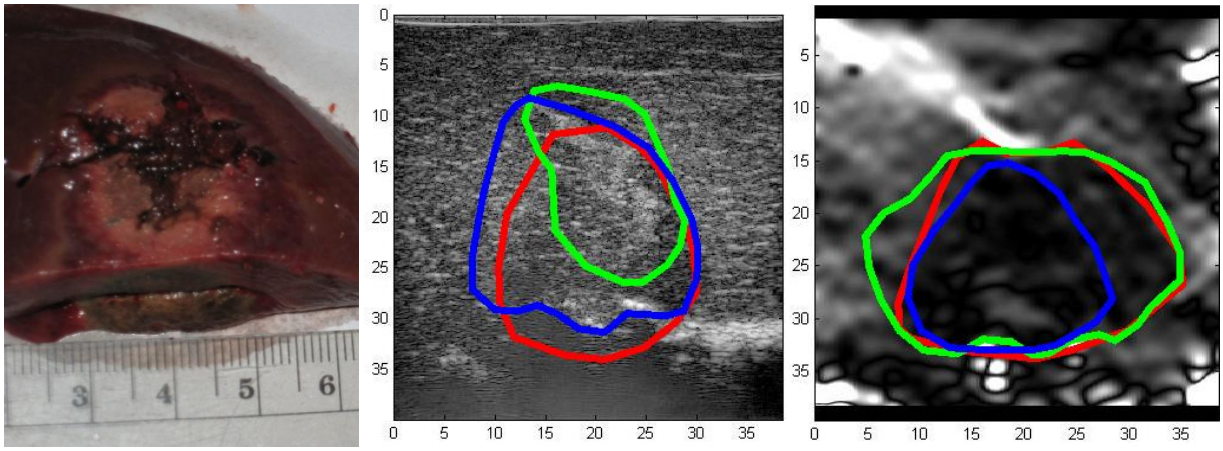

(A) (B) (C)

Figure 3.1. Ablation 1. Figures 3.1 through 3.13 present the following three images for each ablated region: **(A)** Pathology image, **(B)** B-mode image, and **(C)** strain image. The B-mode images are displayed with a dynamic range of 60 decibels. The strain images have a dynamic range of zero to 2% except ablations 3,5,9, and 10 where dynamic range is reduced. The axis tick labels on the B-mode and strain images are in mm. The red, green, and blue contours are manual segmentations selected by the different observers.

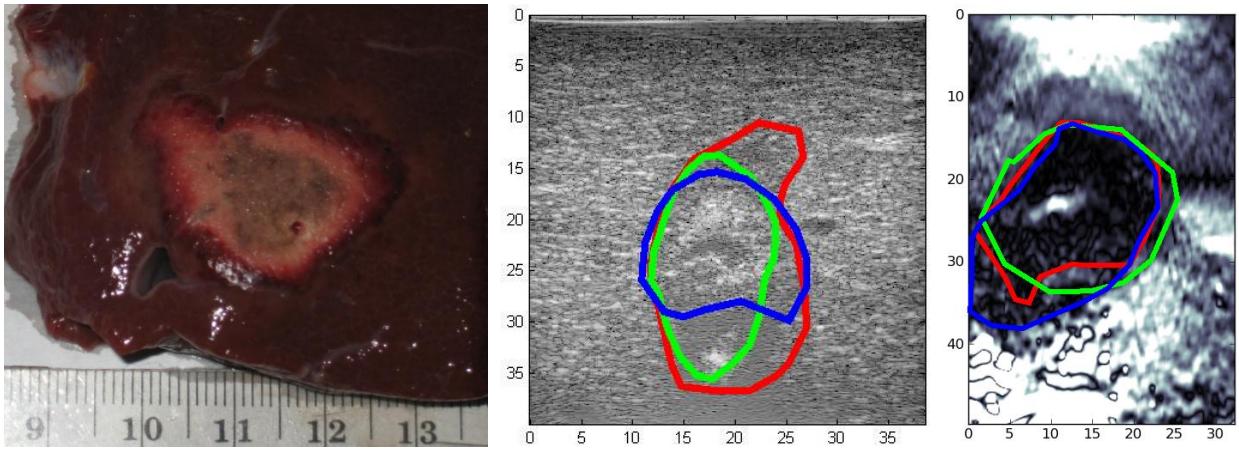

(A) **(B)** **(C)**

Figure 3.2. Ablation 2.

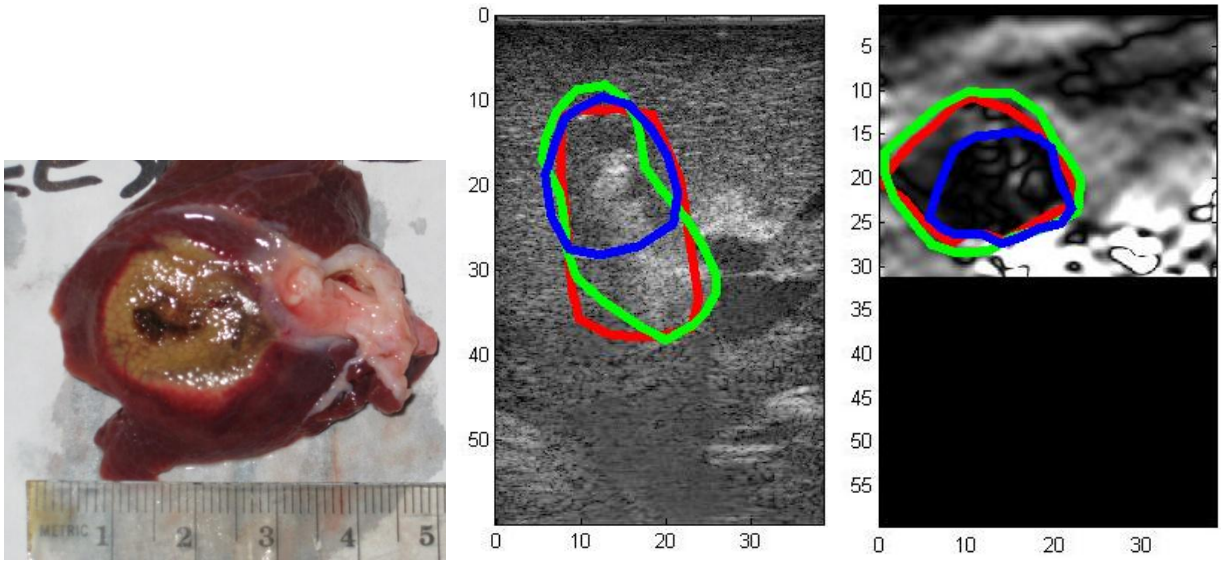

(A) (B) (C)

Figure 3.3. Ablation 3. The scale of the strain image (C) is from 0 to 1%.

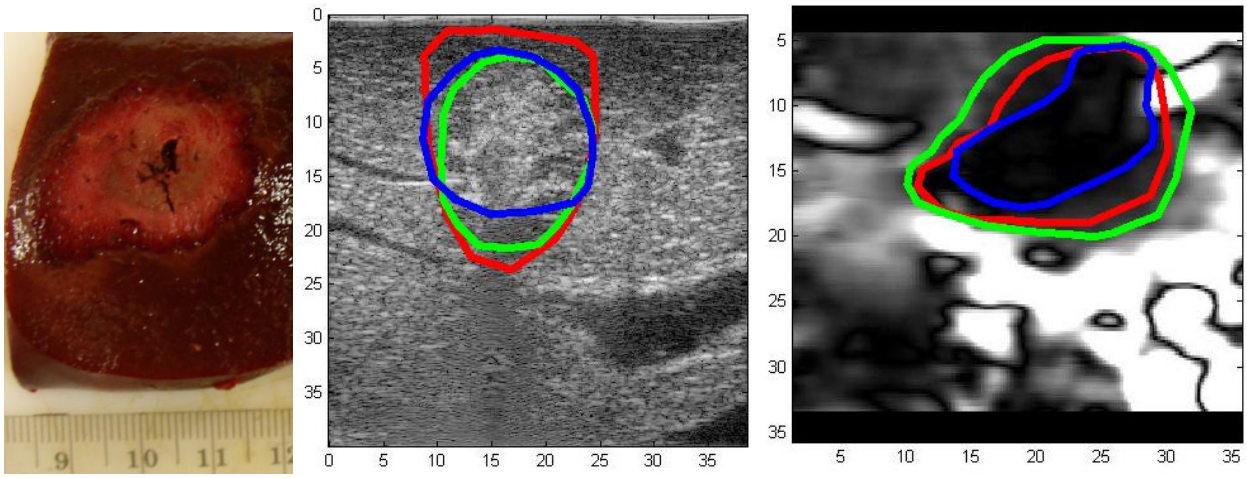

(A) **(B)** **(C)**

Figure 3.4. Ablation 4.

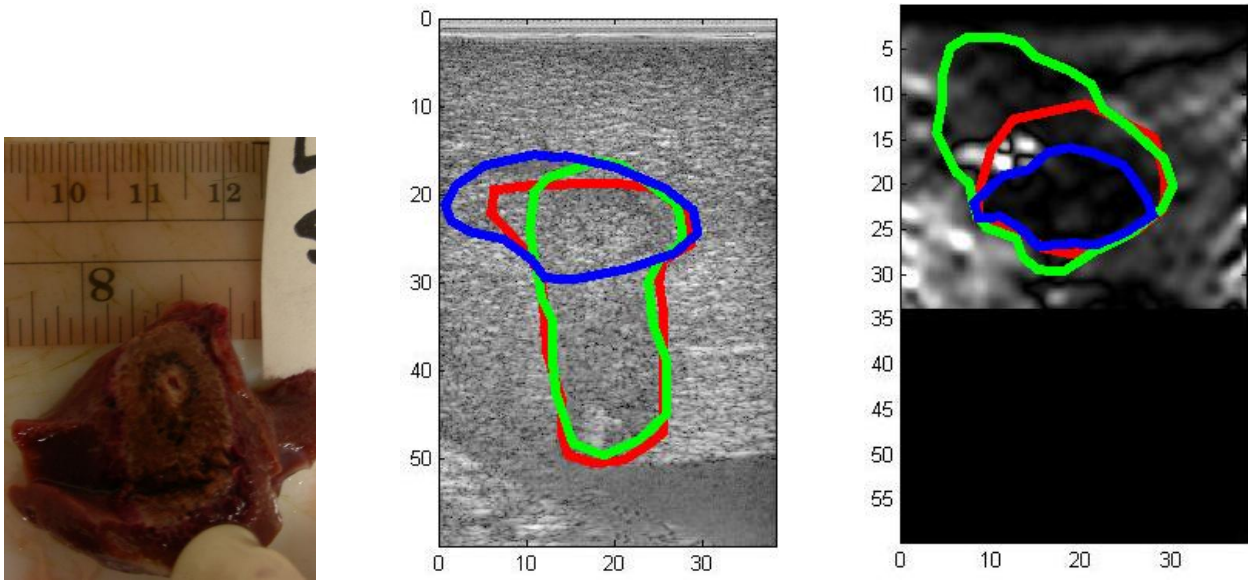

(A) **(B)** **(C)**

Figure 3.5. Ablation 5. The scale of the strain image (C) is from 0 to 1%.

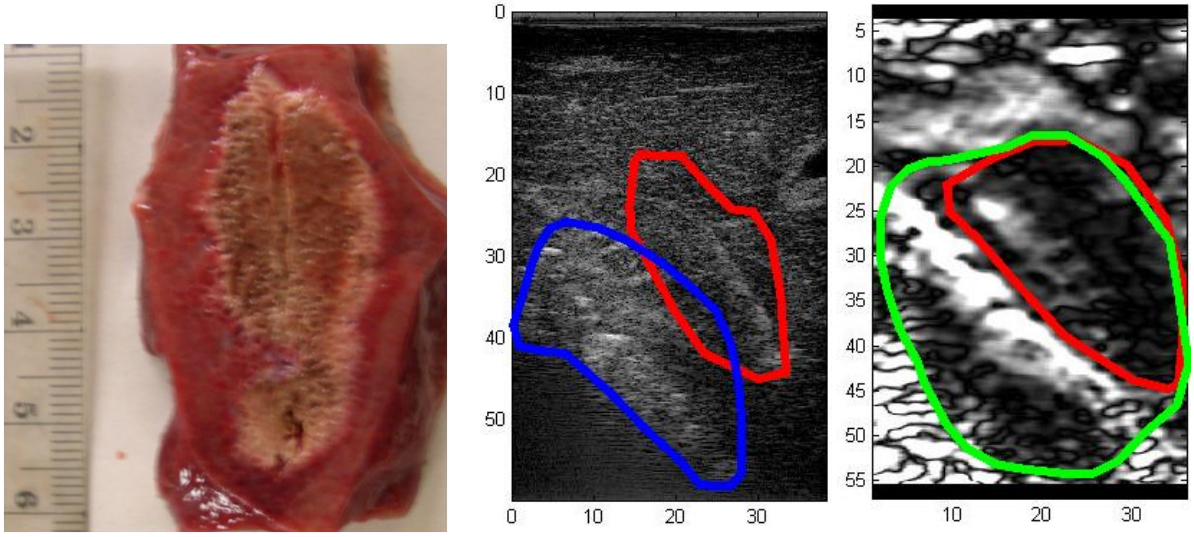

(A) **(B)** **(C)**

Figure 3.6. Ablation 6.

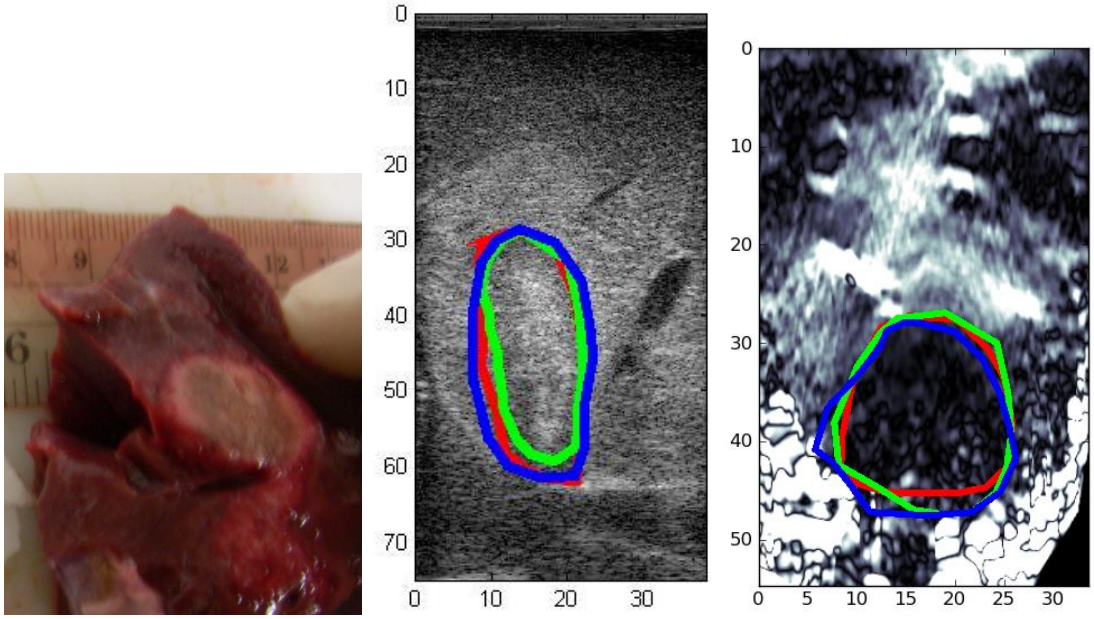

(A) **(B)** **(C)**

Figure 3.7. Ablation 7.

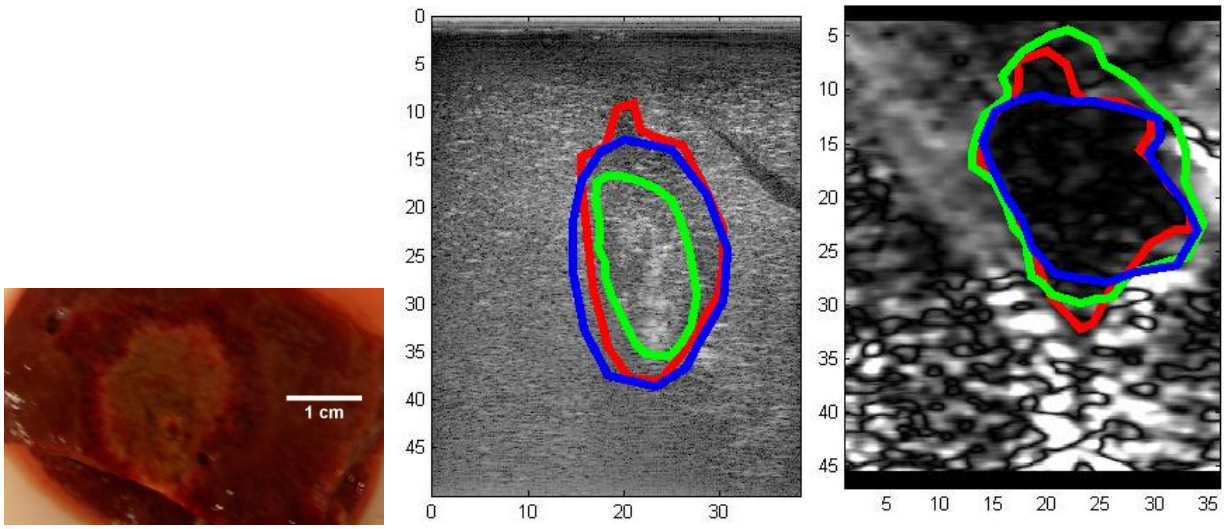

(A) **(B)** **(C)**

Figure 3.8. Ablation 8.

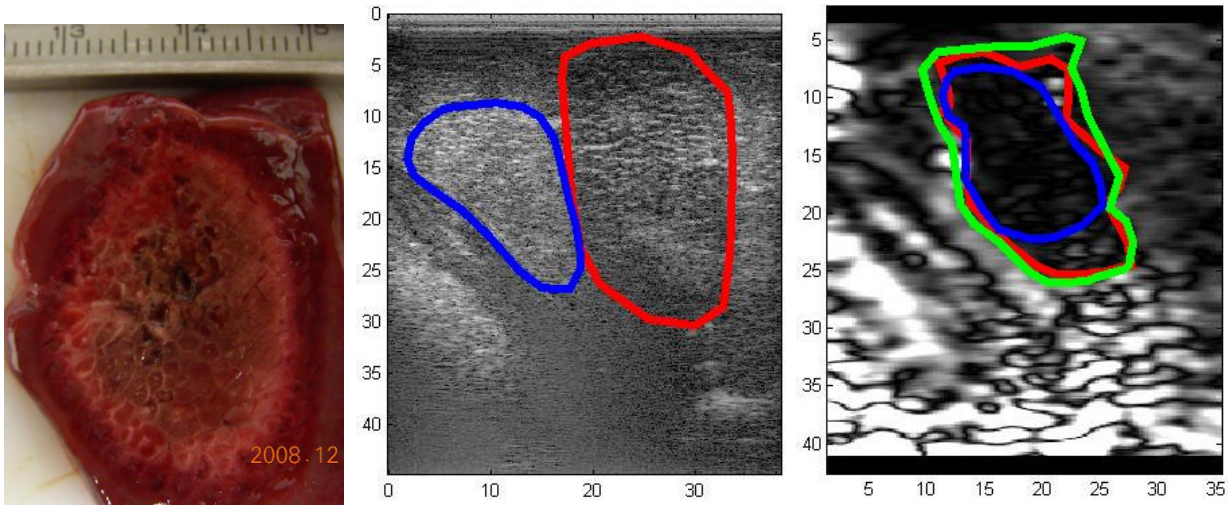

(A) **(B)** **(C)**

Figure 3.9. Ablation 9. The scale of the strain image (C) is from 0 to 0.5%.

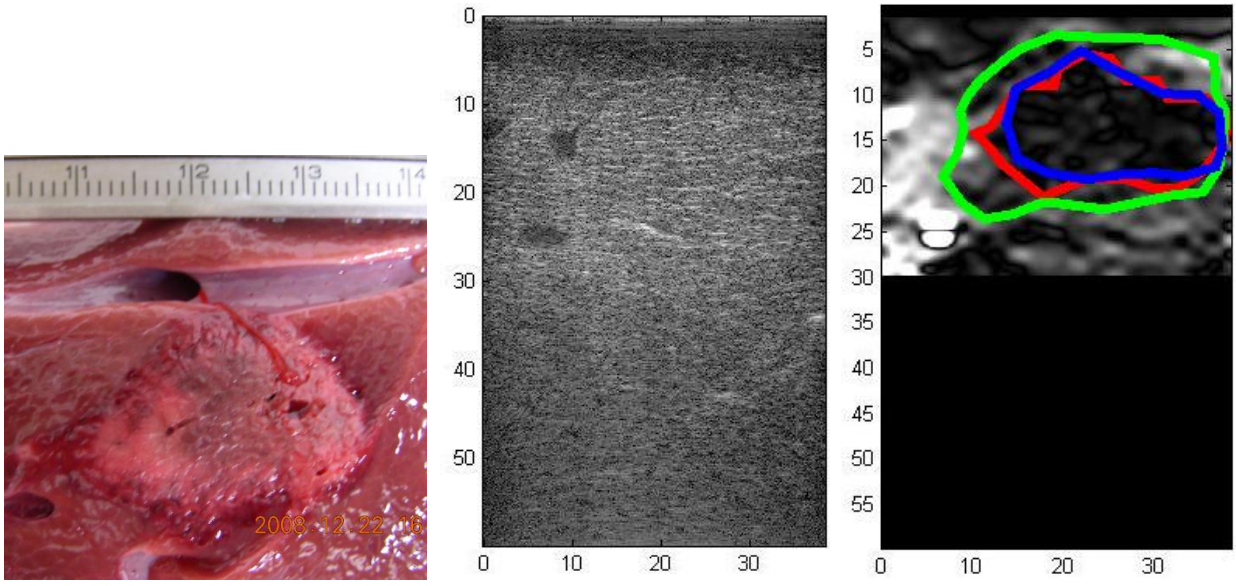

(A) **(B)** **(C)**

Figure 3.10. Ablation 10. The scale of the strain image (C) is from 0 to 1%.

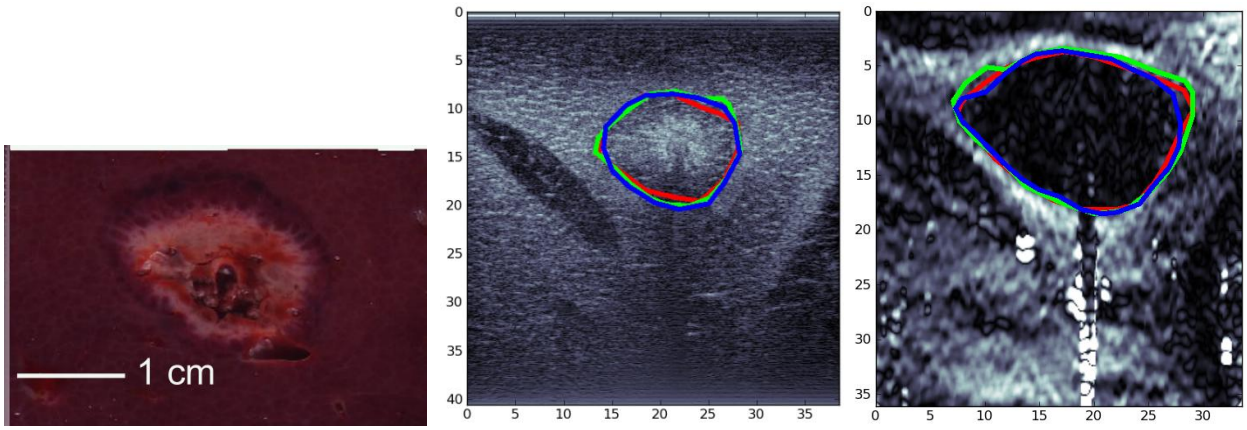

(A) **(B)** **(C)**

Figure 3.11. Ablation 11.

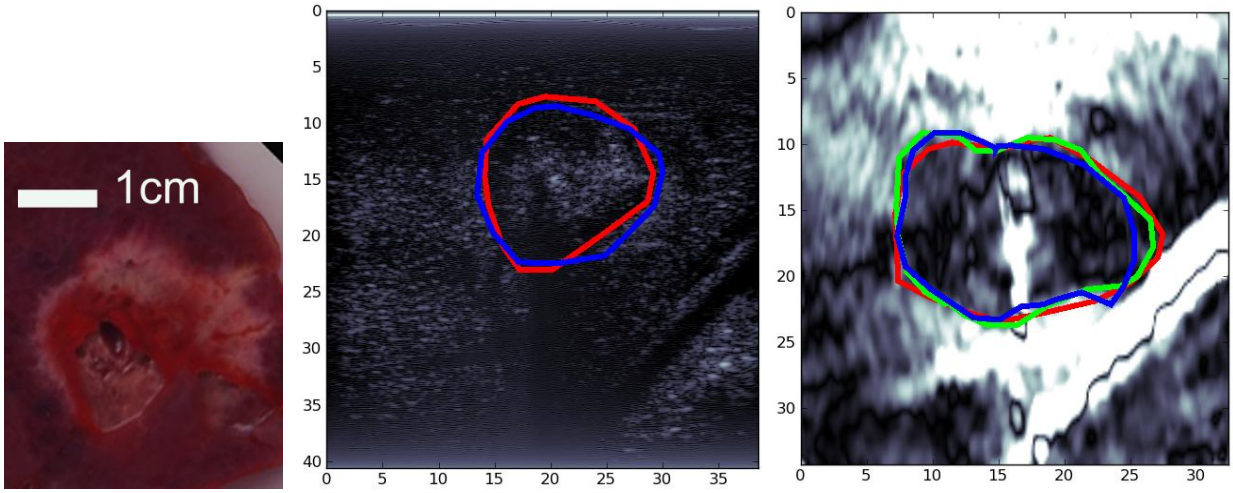

(A) **(B)** **(C)**

Figure 3.12. Ablation 12.

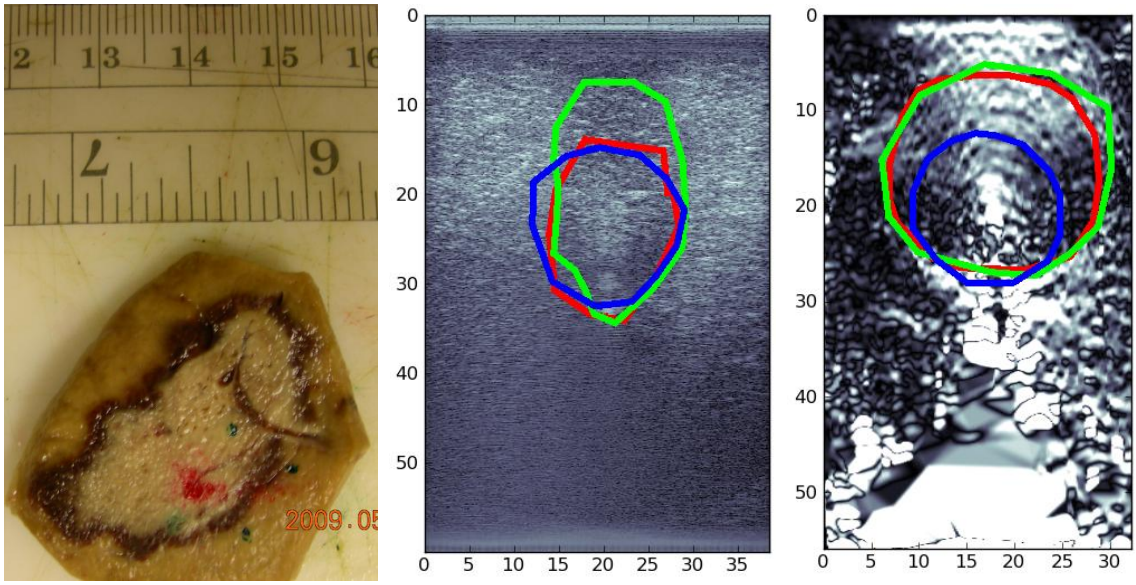

(A) **(B)** **(C)**

Figure 3.13. Ablation 13.

3.4 Pathological Correlation: Porcine Liver Ablations

In this section, areas measured on gross-pathology images of the ultrasound scan plane were compared with areas measured on strain images generated for the 13 separate ablation zones. Area measurements were performed without registration performed between the pathology and strain images. Segmentation by each observer resulted in the creation of a mask image, where the pixels belonging to the thermal ablation zone were identified. The area of the thermal ablation in the B-mode or strain image was then calculated as the sum of the areas of all the pixels identified as belonging to the thermal ablation zone. A linear fit was performed between gross-pathology and strain area measurements for each individual observer and the results are presented in table 3.1 and figure 3.3. A linear fit was also performed between the mean values of the strain measurements of the three observers to determine the correlation between the two measurements. In one of the cases, an observer was unable to delineate ablation zone boundaries in the strain images. For this case only, the values from two observers were averaged. In addition, discrepancies in boundary delineation were also evaluated based on the differences between the gross-pathology boundary and boundary segmented by the observers, with the mean and standard deviation presented in Table 3.2. These measurements were made after aligning the centroids of the pathology and observer segmentations and accounting for ablation zone shape. The differences between a straight line passing through this common centroid and the two boundaries at 36 locations were estimated to compute the boundary discrepancy. The results depict the possible errors with the visualization of each of the ablation zones for all three observers and for the automated segmentation results in Table 3.2.

When cross-sectional areas were determined according to image segmentation, no attempt was made to perform principal axis measurements for pathological correlation. This is

justifiable due to the highly irregular geometries demonstrated in the strain images. Ablation numbers 2,4, and 5 demonstrates the irregular nature of the boundaries of an RF ablation in particular. Presented with the strain images in this experiment it was deemed too difficult to consistently define principal axes among different observers. However, in some of the RF ablation procedures we do obtain ablation zones that are elliptical. Ablations 3, 10, and 11 have a particularly round shape in the strain images. The results of the correlation between the multireader segmentation and pathology area measurements are summarized in figure 3.3 and Table 3.1. On one of the strain images, one observer was unable to identify ablation zone boundaries. This is far better performance than was seen with the B-mode images. In two cases, two of the three observers were unable to delineate ablation zone boundaries on the B-mode images. In one case, where the thermal ablation zone was isoechoic, none of the observers were able to identify ablation zone boundaries on the B-mode image.

For the strain images, the correlation coefficient between areas measured on pathology and mean areas measured on strain images was found to be r=0.894 (p=0.001). The error bars shown for each point are equal to one standard deviation of the three or two area measurements, respectively. We neglected to display the results of correlation between cross-sectional area measurements on B-mode images and pathology images. This is because an attempt to perform a linear regression on a plot of gross-pathology areas versus the ultrasound B-mode areas yielded a nearly horizontal line with a slope of 0.29, and a correlation coefficient of r=0.33.

While strain imaging outperformed B-mode imaging, there was considerable interobserver variability on the noisier, less obvious strain images. This being the case, a linear regression was performed between elastographic area measurements for each observer and pathology measurements. It was found that two of the three observers showed a fairly high

correlation coefficient between cross-sectional area segmented on pathology and cross-sectional area segmented on strain imaging, while the value for the third observer was considerably lower. As illustrated in figure 3.1, considerable differences between observers exist for segmentations on the same ablation zone in ablation 5,6, and 13. The result of segmenting ablation 12 is interesting though. There is considerable strain within the region that all three observers have declared to be the ablation zone, yet there is very little discrepancy on the boundary delineation.

The results of the automated segmentation, shown in figure 3.4, were comparable to the result of segmentation by the human observers, though the automated segmentation performed slightly worse. The reason for this is probably that some of the images were quite noisy, and a human observer was better able to draw realistic boundaries on a noisy image than the automated segmentation routine was able to produce. Ablation zone number 13 is the worst offender in this case. A linear regression was also performed for the automated segmentation, and the linear fit was found to have a correlation coefficient r=0.828 (p=0.001).

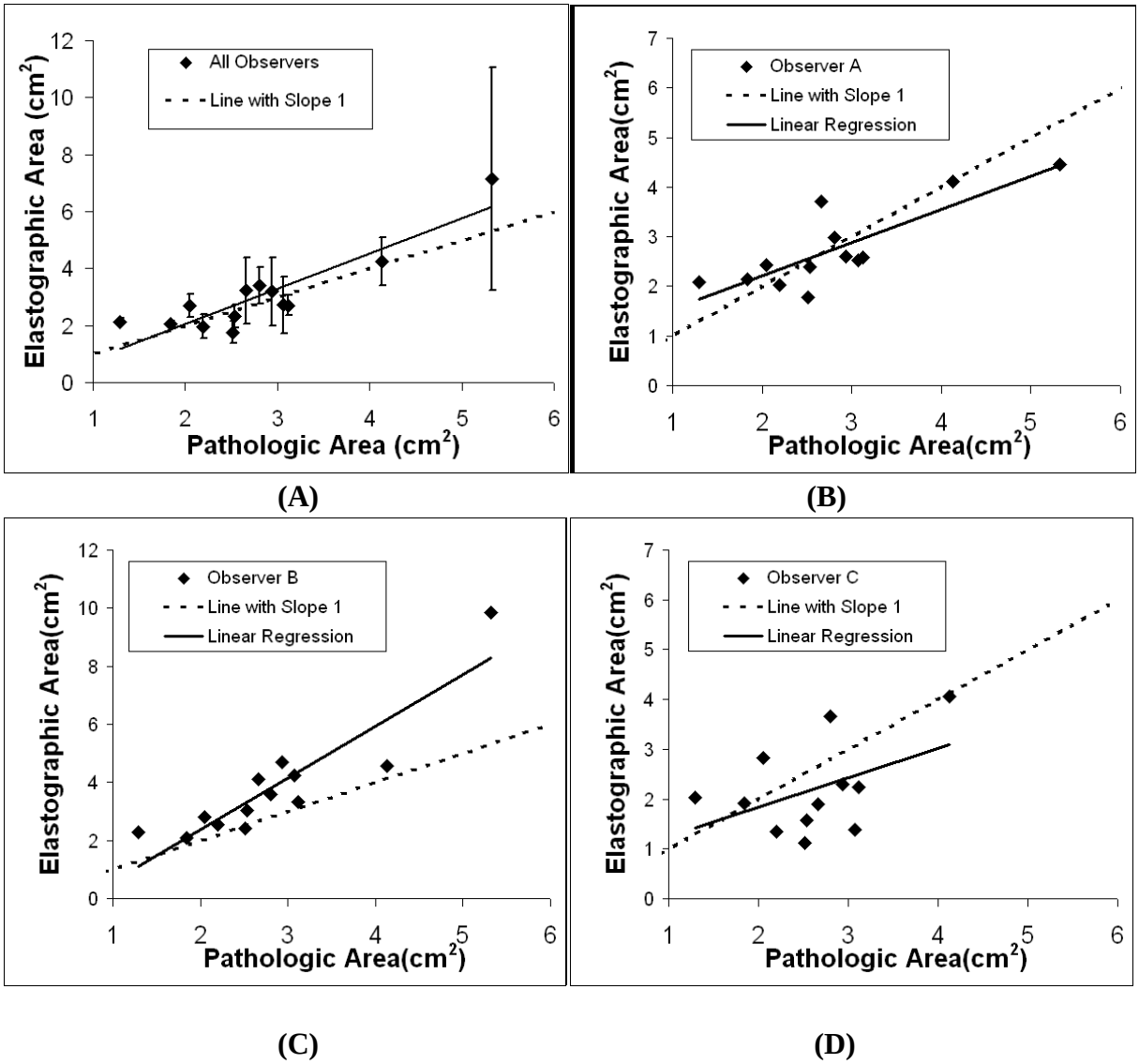

Figure 3.14. Comparison of the areas of thermal ablation zones between strain images, manually segmented by three observers and gross-pathology images. A linear fit using the area estimated from the gross-pathology photographs was performed for each observer [A (NR), B (RD), and C (SB)]. (D) The area measurements were also averaged, and the linear fit performed. The dashed line has a slope of 1 and an intercept of 0 and corresponds to an exact match between areas measured on pathology and areas measured on strain images. Error bars in (D) indicate one standard deviation of the area measurements estimated by the observers.

Table 3.1 Regression coefficient and linear fits to the data presented in figure 3.2.

Observer	r	Linear fit
NR	0.824	0.67x+0.876
RD	0.901	1.78x-1.17
SB	0.465	0.59x+0.67
Mean	0.894	1.23x-0.42

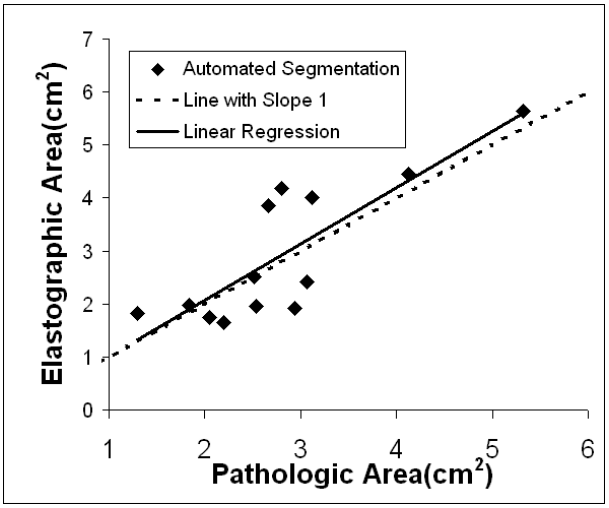

Figure 3.15. Comparison of the areas of thermal ablation zones in the marked imaging plane using automated segmentation of strain images. The dashed line has a slope of 1 and an intercept of 0 and corresponds to an exact match between areas measured on pathology and areas measured on strain images. The linear regression between the pathology area and the strain area shows a correlation coefficient, r=0.828 (p=0.001).

Table 3.2. Boundary discrepancies between gross-pathology and the observer and automated segmentations of strain images (mm).

Ablation No.	Observer A (NR)	Observer B (RD)	Observer C (SB)	Automated
1	1.47 ± 0.80	1.77 ± 0.96	3.50 ± 0.82	2.10 ± 1.30
2	1.58 ± 0.93	1.84 ± 0.97	2.22 ± 1.33	2.61 ± 1.19
3	1.47 ± 0.76	0.93 ± 0.66	3.13 ± 1.09	1.58 ± 0.79
4	4.31 ± 1.44	2.91 ± 1.44	4.64 ± 2.12	2.93 ± 1.44
5	2.39 ± 0.004	2.67 ± 0.007	6.08 ± 1.56	2.94 ± 0.01
6	2.72 ± 0.06	5.31 ± 1.25	NA	5.31 ± 1.25
7	1.58 ± 1.24	2.31 ± 1.33	1.19 ± 1.13	2.57 ± 1.54
8	1.13 ± 0.001	0.66 ± 0.001	0.72 ± .001	0.98 ± 0.003
9	3.17 ± 0.98	2.12 ± 1.04	4.61 ± 1.20	4.02 ± 0.86
10	2.44 ± 0.07	7.61 ± 0.15	2.03 ± 1.38	2.60 ± 0.06
11	1.23 ± 0.54	1.57 ± 0.59	1.14 ± 0.435	1.46 ± 0.81
12	1.75 ± 0.05	2.02 ± 0.058	2.57 ± 0.33	0.02 ± 0.05
13	3.03 ± 0.57	3.03 ± 0.57	0.59 ± 0.22	10.74 ± .06

3.5 Mechanical Boundary Conditions and Blood Vessels

An interesting phenomenon worth noting on the strain images produced during this study is presented in figure 3.4. Ultrasound imaging has long been used to image blood vessels, and strain images generated during this study show that strain imaging preserves this functionality. In figure 3.4, the B-mode image of an ablation zone (figure 3.4 (A)) illustrates the presence of a blood vessel, possibly above the ablation zone. In the strain image, the blood vessel manifests as a bright artifact in the image. The strain image (figure 3.4 (C)) confirms the presence of the blood vessel cutting across the ablation zone, where it manifests as a bright decorrelation artifact in the image. The pathology image also shows this blood vessel. For this particular ablation, we were unable to expose the imaging plane when cutting through the ablation zone, and the pathology photograph shows a cross-section of the ablation zone perpendicular to the needle

track. In the gross pathology photograph, the two holes visible on either side of the ablation zone indicate the presence of the blood vessel. Reliably imaging blood vessels during RF ablation is particularly important because blood vessels act as heat sinks during ablation procedures and reduce the efficiency of the procedure. In addition, the stiffer region in the strain image appears to encompass the entire image. If the entire dark region is assumed to be the thermal ablation zone, this yields a cross-sectional area of approximately 9 cm^2, an unrealistically large value for the ablated area. This is possibly an artifact due to the presence of the blood vessel. It is possible that the displacement of the ablation electrode was not transmitted above the blood vessel leading to reduced or no deformation on the other side of the blood vessel. The displacement image in figure 3.4 (c) supports this hypothesis, as the displacements on the side of the blood vessel closer to the transducer are very small compared to the local displacement distal to the blood vessel. Thus the lower strain values in the image may be attributed to mechanical boundary conditions rather than an underlying modulus contrast, leading to the overestimation of the ablation zone. One approach to overcome artifacts due to interpreting a strain image as a modulus image is to perform iterative modulus reconstruction as described in [83]. However, this would not have entirely solved the problem presented in figure 3.4. In modulus reconstruction, it is assumed that the tissue being imaged is a single continuum, a nearly incompressible solid body [83]. The presence of a blood vessel in the strain image violates this very basic assumption, introducing blood flow (a fluid disconnected from the single solid body of the liver) into the middle of the deformation field.

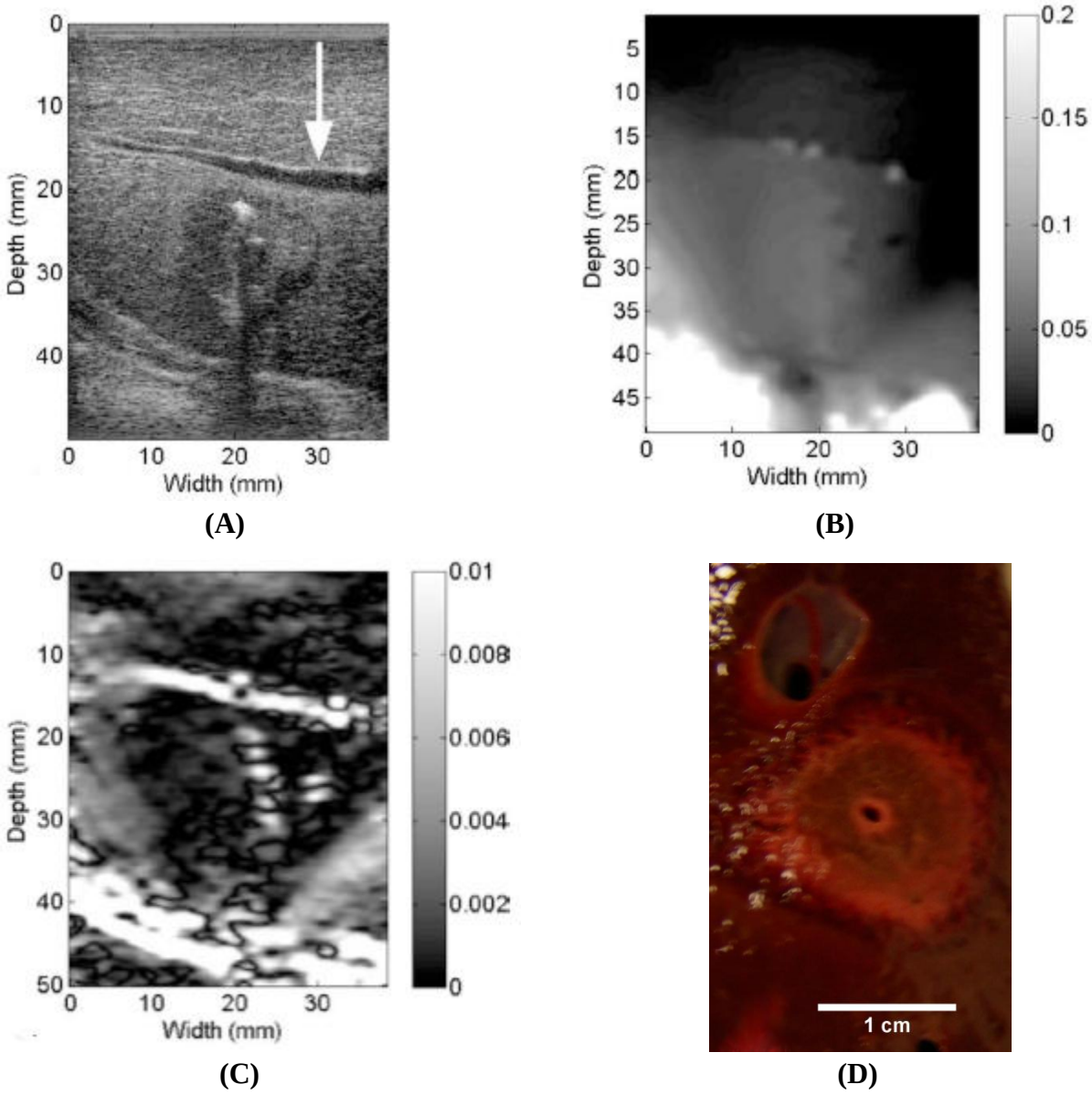

Figure 3.16. Images illustrating an interesting case with an RF ablation procedure. The location of the blood vessel is indicated by the arrow in **(A)** the ultrasound B-mode image. **(B)** The corresponding local displacement image where the units for displacement are in mm. Corresponding **(C)** electrode displacement strain image and **(D)** gross-pathology image are also shown. Notice the presence of a blood vessel which manifests itself as a bright decorrelation streak through the ablation zone in the strain image.

3.6 RF Data Acquisition of Rabbit VX2 Thermal Ablations

Ten rabbits were surgically implanted with VX2 tumor aliquots to create a single tumor per animal. The tumor growth times ranged from 3 to 5 weeks. At the end of the tumor growth period, each rabbit was anaesthetized and ultrasound imaging was performed with a Siemens S2000 scanner. Images were acquired with both VFX 9L4 transducers and VF 18L6 transducers. Initially, ultrasound B-mode imaging was used by a sonographer to locate the tumor and guide percutaneous insertion of a microwave applicator into the VX2 tumor. The microwave system used was a Neuwave Medical Certus 140 (Madison,WI) operating at 2.45 GHz. An initial set of RF data was recorded for each rabbit depicting the VX2 tumor prior to treatment. When this initial data set was recorded, a cryolock option was activated on the thermal ablation system to bond the microwave applicator to the tumor prior to treatment. The cryolock option released a small amount of liquid carbon dioxide from the active region of the applicator. Small deformations were manually induced in the tumor through the bonded applicator prior to treatment, and RF data acquisition occurred during this deformation. Microwave energy was then delivered to the tumor. For treatment, 50 W were applied for a period of 5 minutes. Following treatment, bonding between tissue and the microwave applicator was again ensured by activating cryolock. Post treatment RF data was acquired during electrode displacement elastography. To form EDE images prior to thermal ablation treatment and following thermal ablation treatment, block matching was performed using the quality guided block matching algorithm of Chen *et al.* [99]. A block size of 0.75 mm axially and 2.5 mm laterally with an axial overlap of 65% was used for the displacement estimation. The size of the strain kernel was 4.0 mm.

3.7 B-mode and Strain Images of VX2 Tumors Prior to and After Microwave Ablation

B-mode and strain images were segmented by four observers (Tomy Varghese, Atul ingle, Chris Brace, and Sarah Kohn). Tomy Varghese is a professor of medical physics and biomedical engineering with multiple decades of experience in the field of strain imaging. Chris Brace is a professor of biomedical engineering with experience in the field of thermal ablation. Sarah Kohn is an ultrasonographer, and Atul Ingle is a graduate student with one year of experience in elasticity imaging of thermal ablations. As in the previous section, all image segmentations were performed using the ImageJ polygon fitting tool. The observers were presented with four images for each ablation in the following order:

1) B-mode image of the VX2 tumor prior to ablation

2) Strain and B-mode images of the VX2 tumor prior to ablation

3) B-mode image of the tumor following ablation

4) B-mode and strain images of the VX2 tumor following ablation

Each observer was asked to segment the VX2 tumor prior to ablation on the B-mode image then on the strain image. After segmenting the pre-ablation images, each observer was also asked to segment the treated region on the B-mode image and on the strain image following thermal ablation. Observers were blinded to pathology image prior to segmentation of B-mode and strain images.

The only guidance provided to the observers was to delineate the stiffer or darker region on the strain image from the surrounding softer or lighter background liver tissue. This section presents B-mode, strain, and pathology images and the corresponding segmentations chosen by all human observers. In the strain and B-mode images, red segmentations correspond to Atul

Ingle, blue to Chris Brace, green to Sarah Kohn, and yellow to Tomy Varghese. With the exception of rabbit one, all pathology photographs are presented following a period of preservation in formaldehyde.

From pathology photographs, it appears complete ablation can be confirmed in 6 out of the 10 tumors. In pathology photographs for rabbits 2, 3, 4, 5, and 10 the tumor is surrounded on all sides by a white, thermally coagulated margin of liver. Tumors 6 and 9 were too large and were only partially ablated. Margins around these tumors are not visible in pathology photographs. Tumor 6 presents a cross-section at least 100 mm^2 larger than the next largest tumor. Tumor 9 was even larger than tumor 6. Tumors 1 and 7 were small enough to have been fully ablated though a consistent margin of thermally coagulated liver is not visible around all tumor borders. Tumor sizes and ablation status are summarized in table 3.1. We provide boundaries indicating thermal coagulation based on the assumption that all tumors were fully treated.

We computed Dice's coefficient between the segmentations chosen by different observers. These results are presented in are given in Table 3.2. Dice's coefficient is given by:

$$D = \frac{S_{AI} \cap S_{CB} \cap S_{SK} \cap S_{TV}}{S_{AI} \cup S_{CB} \cup S_{SK} \cup S_{TV}} \quad \textbf{(3.2)}$$

In equation 3.1, the numerator represents the area of the image region segmented by all four observers. The denominator is given by the total area of the image region segmented by any of the four observers. Averaged among the ten subjects, the Dice's coefficient is highest among the four imaging situations when comparing post ablation strain imaging segmentations. The addition of strain imaging also increases the Dice's coefficient. For post-ablation strain imaging, the highest Dice's coefficient was obtained in VX2 tumor number 4. In this rabbit, the proximal borders of the treated region are nicely visualized by a high strain region. The distal border of

this treated region is agreed upon by an imaging artifact. The distal region shows a high strain border, although the high strain is due to the loss of signal in the distal portion of the image. The signal loss could be due to either attenuation, or the fact that this is the true boundary of the tumor-bearing liver. Dice's coefficient was also high on strain imaging in tumors 6 and 7 prior to ablation. Tumor 7 is interesting because this elastogram indicates that VX2 tumors are stiff compared to the surrounding liver tissue. The only strain within the tumor seems to be due to image shadowing from the ablation electrode, which is out-of-plane for this case.

Table 3.3. Cross-sectional areas of VX2 tumors estimated from pathology photographs and cross-sectional areas of thermally coagulated regions estimated from pathology photographs.

Subject Number	Tumor cross-sectional area (mm^2)	Thermal coagulation cross-sectional area (mm^2)	Full Ablation?
1	129	493.0	Possible
2	280	389.0	Yes
3	336	606.0	Yes
4	355	761.0	Yes
5	112	663.0	Yes
6	472	688.0	No
7	292	825.0	Possible
8	33	600.0	Yes
9	1418	1418.0	No
10	185	591.0	Yes

Table 3.4. Dice's coefficient computed between all observers for B-mode imaging alone and B-mode plus strain imaging prior to and following ablation.

Subject Number	Pre Ablation B-mode	Pre Ablation strain	Post Ablation B-mode	Post Ablation strain
1	0	0	0.19	0.36
2	0	0.01	0.03	0.37
3	0.04	0	0.04	0.51
4	0.23	0.40	0.49	0.68
5	0.19	0.20	0.28	0.12
6	0.68	0.84	0.77	0.26
7	0.48	0.65	0.21	0.36
8	0.19	0.27	0.07	0.28
9	0.39	0.30	0.39	0.51
10	0.37	0.53	0.52	0.49
Mean	0.26	0.32	0.30	0.39

Table 3.5. Relative error in cross-sectional area measurements between pre-ablation cross-sectional areas segmented on B-mode and strain images and areas segmented on pathology images for all observers. Errors are given in units of mm^2, and as a percentage of the cross-sectional area on pathology. A positive error corresponds to an overestimate of the VX2 tumor area and a negative error corresponds to an underestimate of the VX2 tumor area.

#	AI B-mode Error	AI Strain Error	CB B-mode Error	CB Strain Error	SK B-mode Error	SK Strain Error	TV B-mode Error	TV Strain Error
1	105 (21%)	51 (40%)	248 (50%)	188 (145%)	313 (64%)	67 (52%)	523 (106%)	-67 (-52%)
2	90 (23%)	-6 (-2%)	19 (5%)	-140 (-50%)	358 (92%)	374 (134%)	51 (13%)	228 (81%)
3	-119 (-19%)	-164 (-49%)	-208 (-34%)	-59 (-18%)	-192 (-32%)	-152 (-45%)	284 (47%)	-77 (-23%)
4	9 (1%)	120 (34%)	29 (4%)	178 (50%)	532 (70%)	234 (66%)	291 (38%)	559 (158%)
5	458 (69%)	369 (330%)	430 (65%)	398 (355%)	130 (20%)	416 (371%)	307 (46%)	175 (156%)
6	86 (13%)	0 (0%)	202 (29%)	64 (14%)	113 (16%)	45 (10%)	201 (29%)	15 (3%)
7	-77 (-9%)	-58 (-20%)	78.0 (10%)	-47 (-16%)	-104 (-13%)	-101 (-35%)	-95 (-12%)	-50 (-17%)
8	282 (47%)	350 (1061%)	295 (49%)	453 (1373%)	492 (82%)	603 (1827%)	170 (28%)	571 (1730%)
9	67 (5%)	-489 (-35%)	-699 (-49%)	-754 (-53%)	367 (26%)	107 (8%)	151 (11%)	505 (36%)
10	102 (17%)	204 (110%)	125 (21%)	338 (183%)	375 (64%)	393 (212%)	32 (5%)	516 (279%)

Table 3.6. Relative error in cross-sectional area measurements between post-ablation cross-sectional areas segmented on B-mode and strain images and thermally coagulated areas segmented on pathology images for all observers. Errors are given in units of mm^2, and as a percentage of the cross-sectional area on pathology. A positive error corresponds to an overestimate of the thermally coagulated region and a negative error corresponds to an underestimate of the thermally coagulated region.

#	AI B-mode Error	AI Strain Error	CB B-mode Error	CB Strain Error	SK B-mode Error	SK Strain Error	TV B-mode Error	TV Strain Error
1	-216 (-44%)	-250 (-51%)	-240 (-49%)	92 (19%)	-212 (-43%)	-156 (-32%)	132 (27%)	-95 (-19%)
2	120 (31%)	96 (25%)	-281 (-72%)	28 (7%)	57 (15%)	86 (22%)	99 (25%)	234 (60%)
3	-182 (-30%)	-86 (-14%)	-403 (-67%)	-176 (-29%)	-53 (-9%)	-99 (-16%)	152 (25%)	126 (21%)
4	-176 (-23%)	-307 (-40%)	-277 (-36%)	-268 (-35%)	-254 (-33%)	-236 (-31%)	23 (3%)	-137 (-18%)
5	-88 (-13%)	-218 (-33%)	-79 (-12%)	215 (32%)	-145 (-22%)	54 (8%)	-238 (-36%)	95 (14%)
6	72 (11%)	-124 (-18%)	78 (11%)	11 (2%)	31 (5%)	-220 (-32%)	90 (13%)	1015 (148%)
7	-265 (-32%)	-324 (-39%)	-486 (-59%)	-480 (-58%)	270 (33%)	-165 (-20%)	-8 (-1%)	47 (6%)
8	-276 (-46%)	-352 (-59%)	-378 (-63%)	-199 (-33%)	-194 (-32%)	-371 (-62%)	-246 (-41%)	-331 (-55%)
9	-228 (-16%)	-414 (-29%)	-568 (-40%)	-177 (-13%)	-272 (-19%)	51 (4%)	234 (17%)	482 (34%)
10	-204 (-35%)	-222 (-38%)	106 (18%)	-48 (-8%)	22 (4%)	-196 (-33%)	-64 (-11%)	91 (15%)

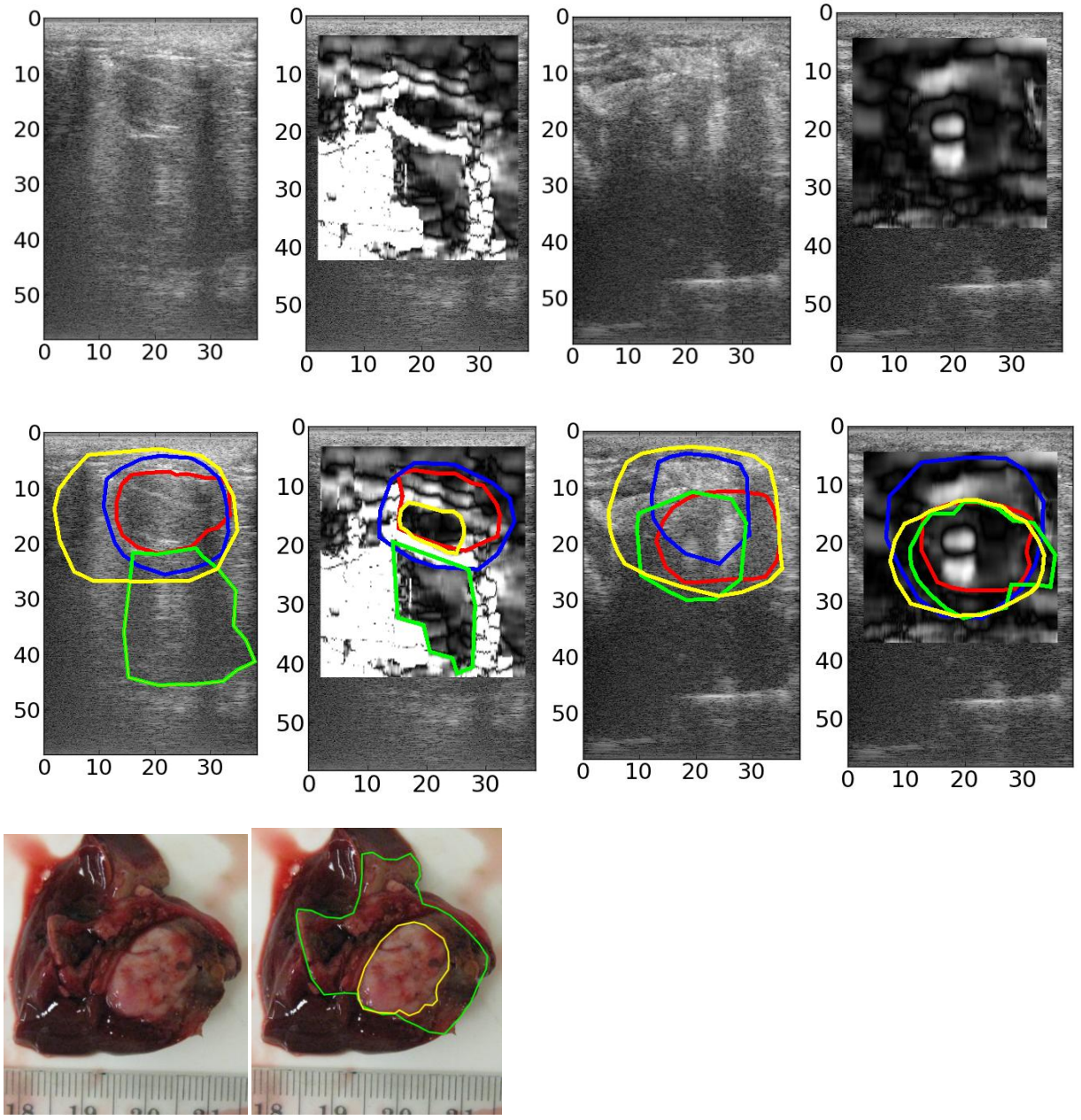

Figure 3.17. VX2 Tumor 1. Nine images are presented for each tumor bearing VX2 rabbit. The images are presented in the following order from left to right: **1)** B-mode image of VX2 tumor prior to ablation. **2)** Strain image of VX2 tumor prior to ablation. **3)** B-mode image of thermally ablated region following treatment. **4)** Strain image of thermally ablated region following treatment. **(5-8)** Segmented versions of images **(1-4). 9)** Pathology images of thermally coagulated VX2 tumor. All B-mode images are displayed with a dynamic range of 60 decibels,

and all strain images have a dynamic range of zero to 2%. In strain and B-mode images red segmentation corresponds to observer AI, blue to observer CB, green to observer SK, and yellow to observer TV. In pathology images yellow segmentation corresponds to tumor and green segmentation corresponds to thermally coagulated region.

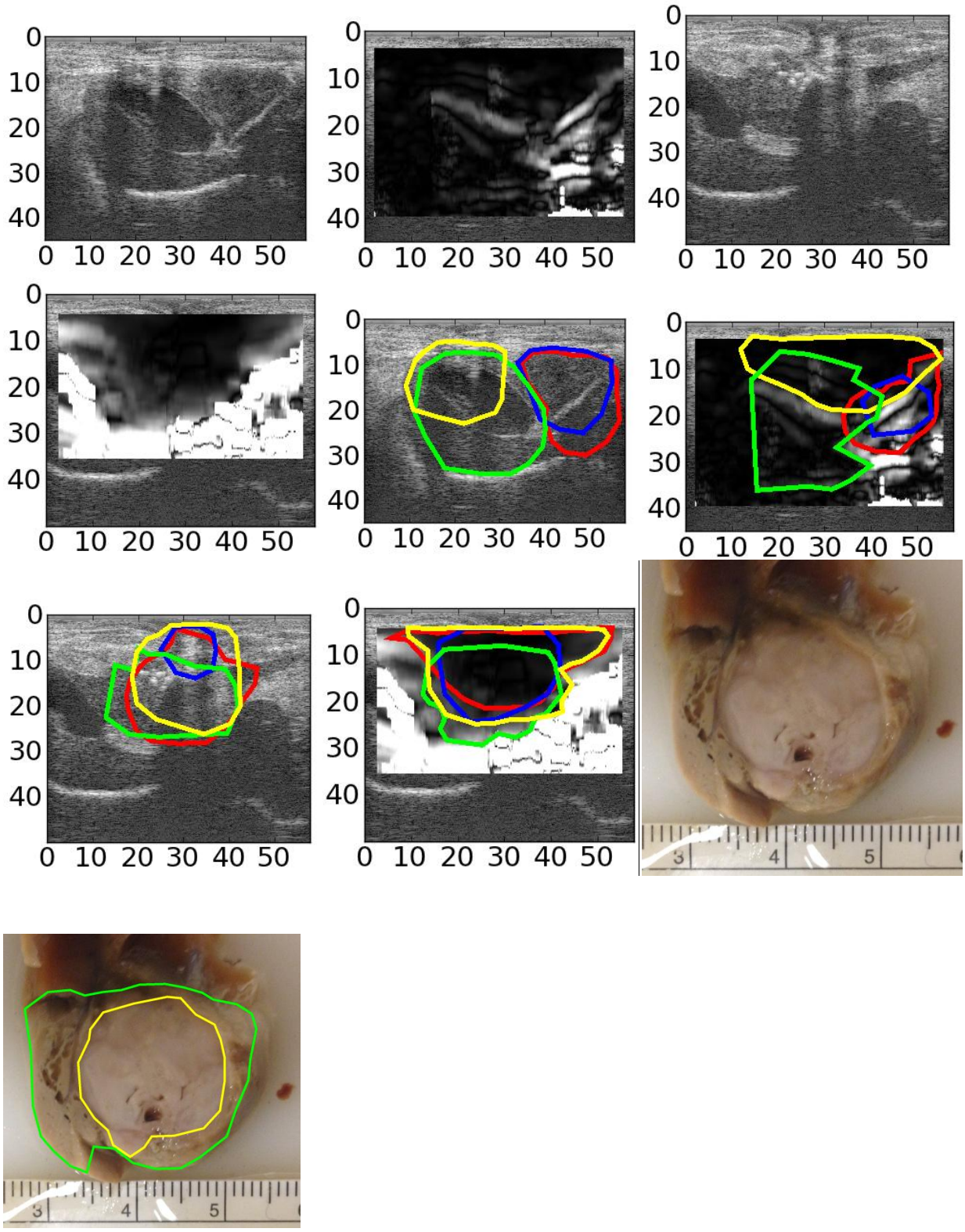

Figure 3.18. VX2 Tumor 2.

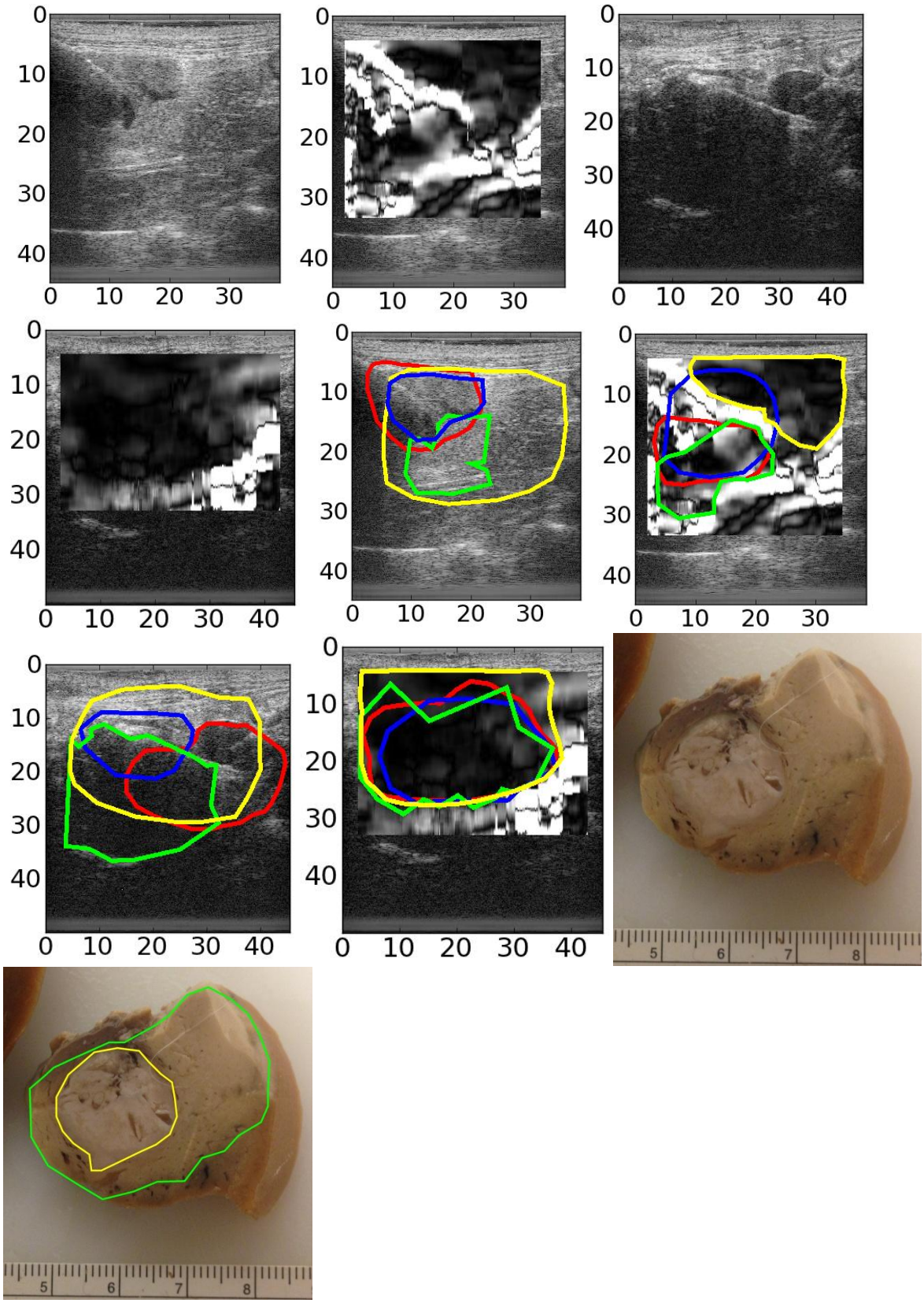

Figure 3.19. VX2 Tumor 3.

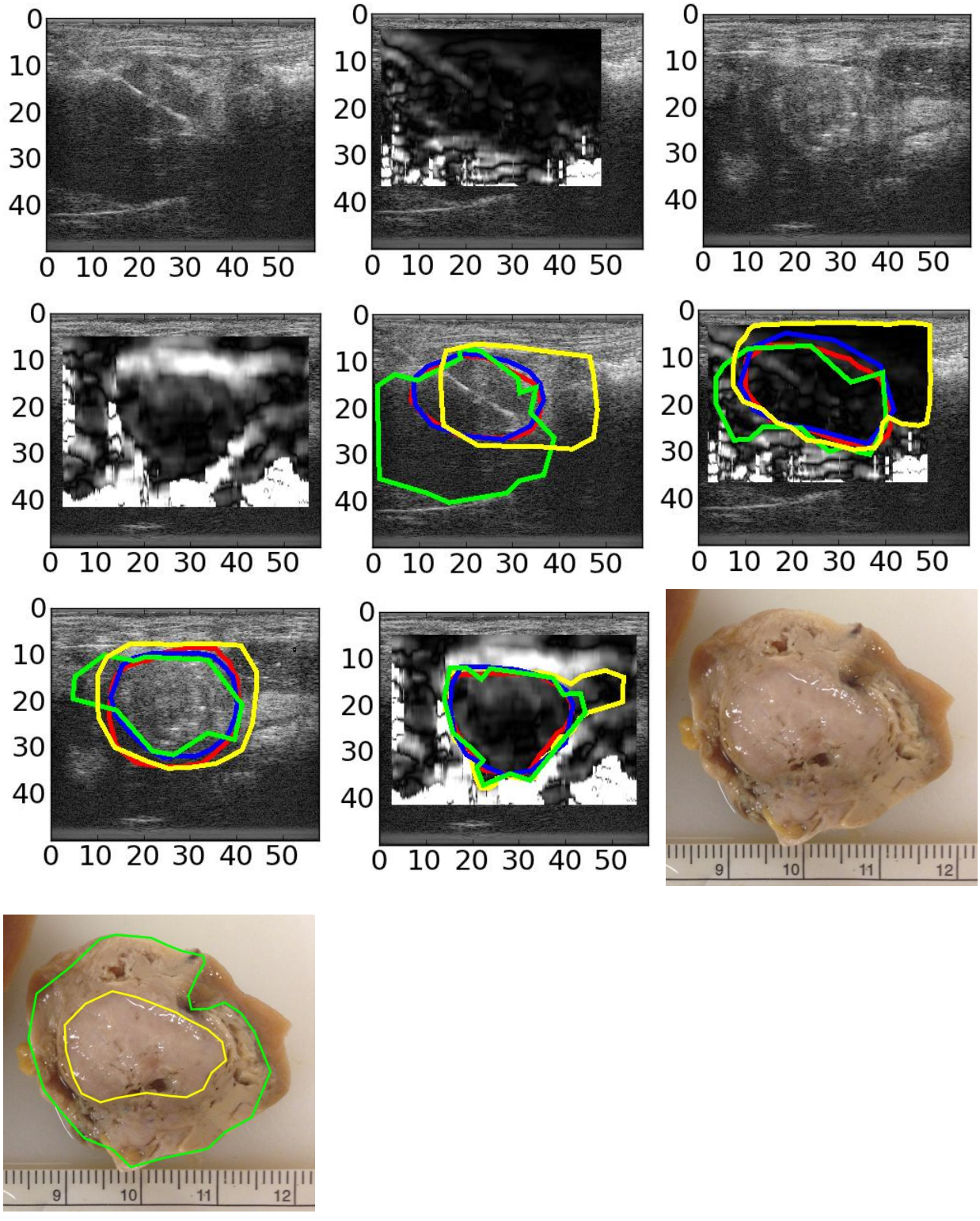

Figure 3.20. VX2 Tumor 4.

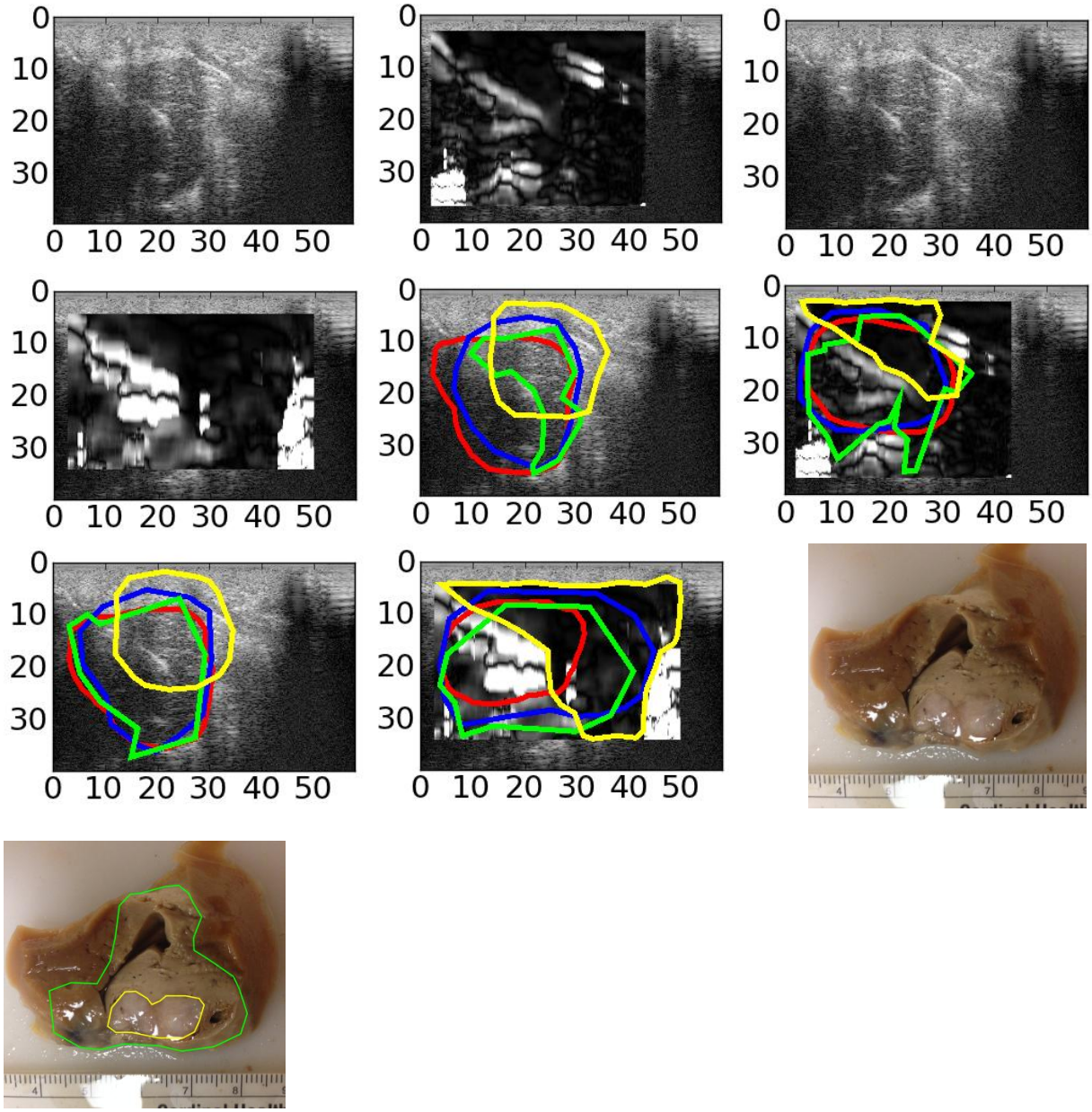

Figure 3.21. VX2 Tumor 5.

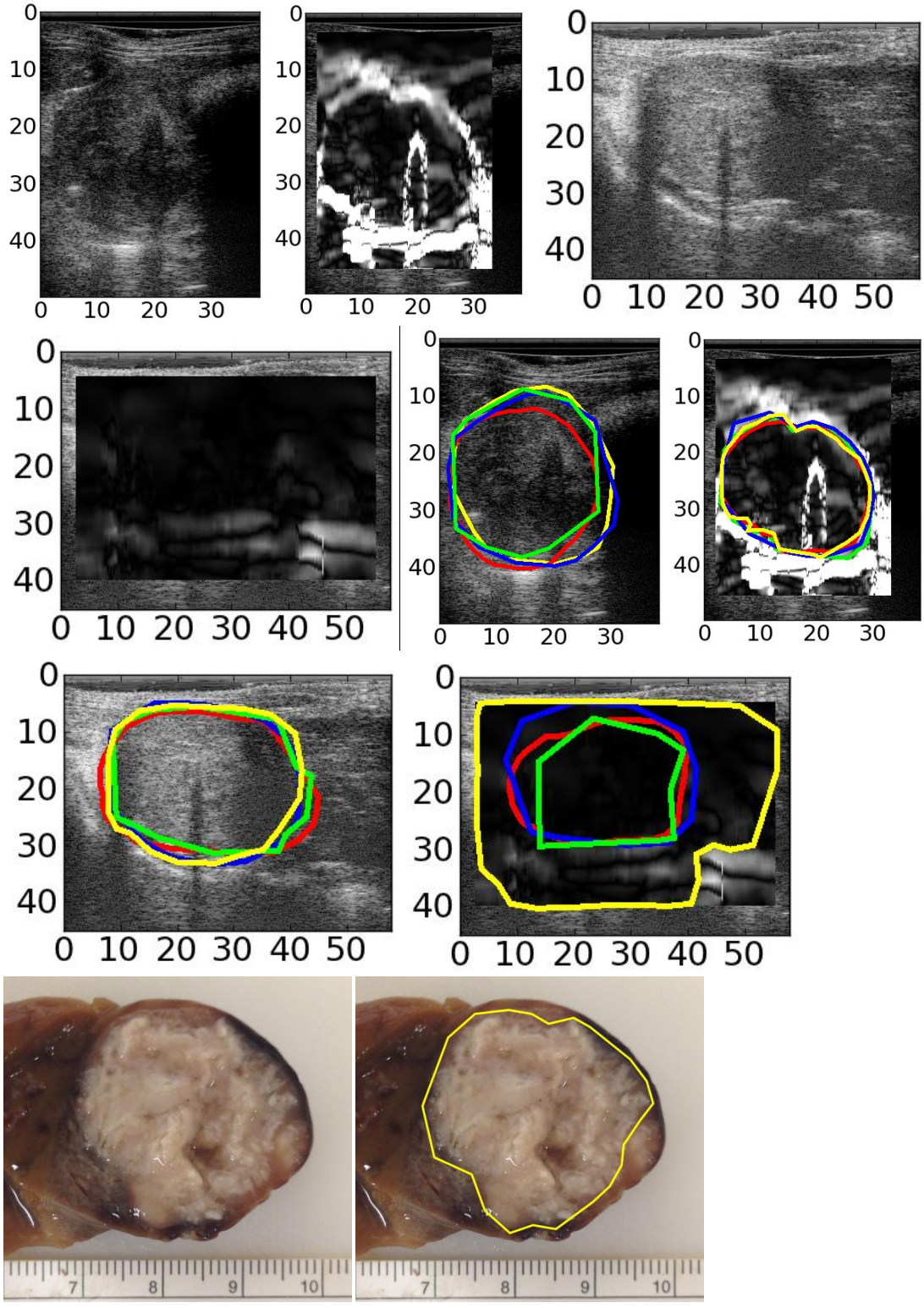

Figure 3.22. VX2 Tumor 6. Only VX2 tumor is segmented in pathology image.

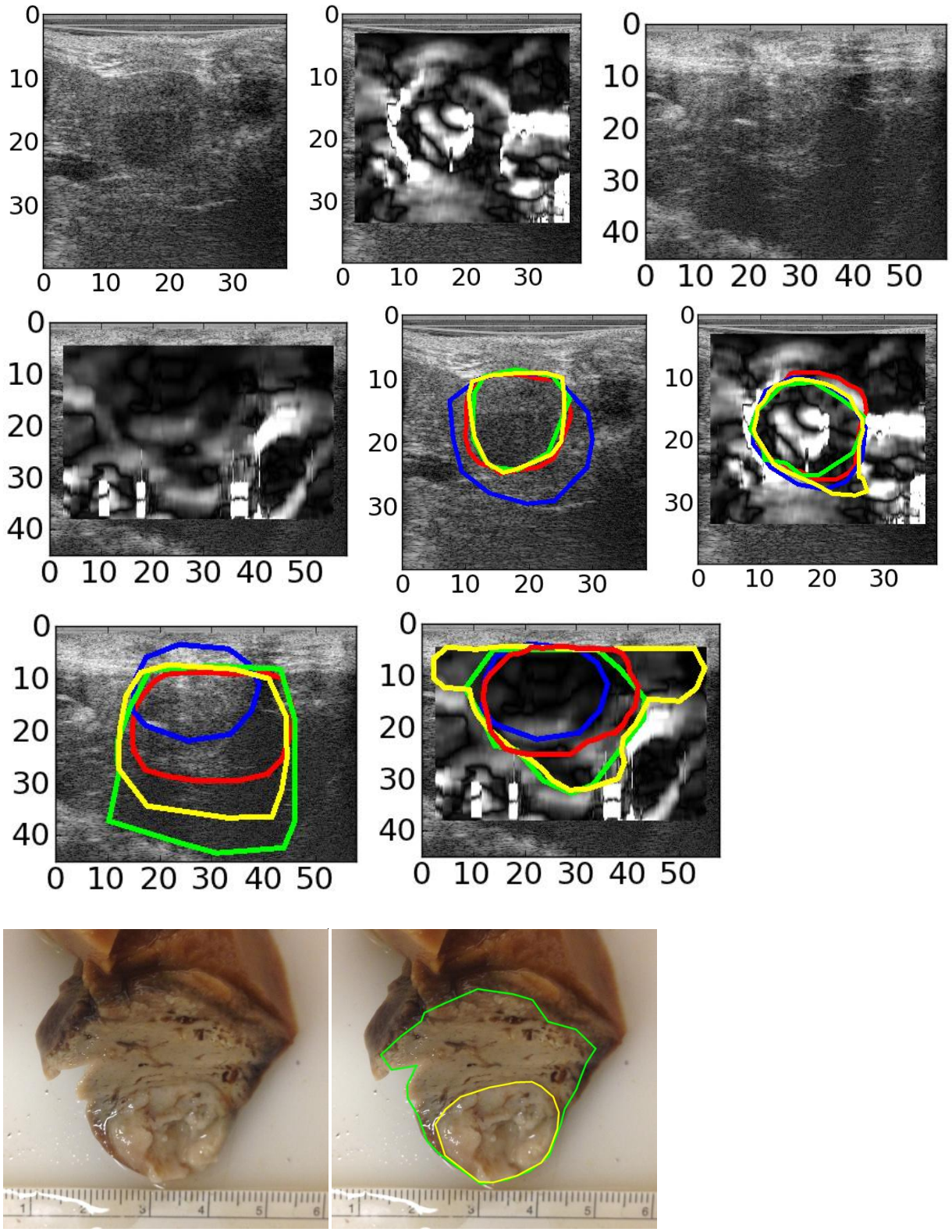

Figure 3.23. VX2 Tumor 7.

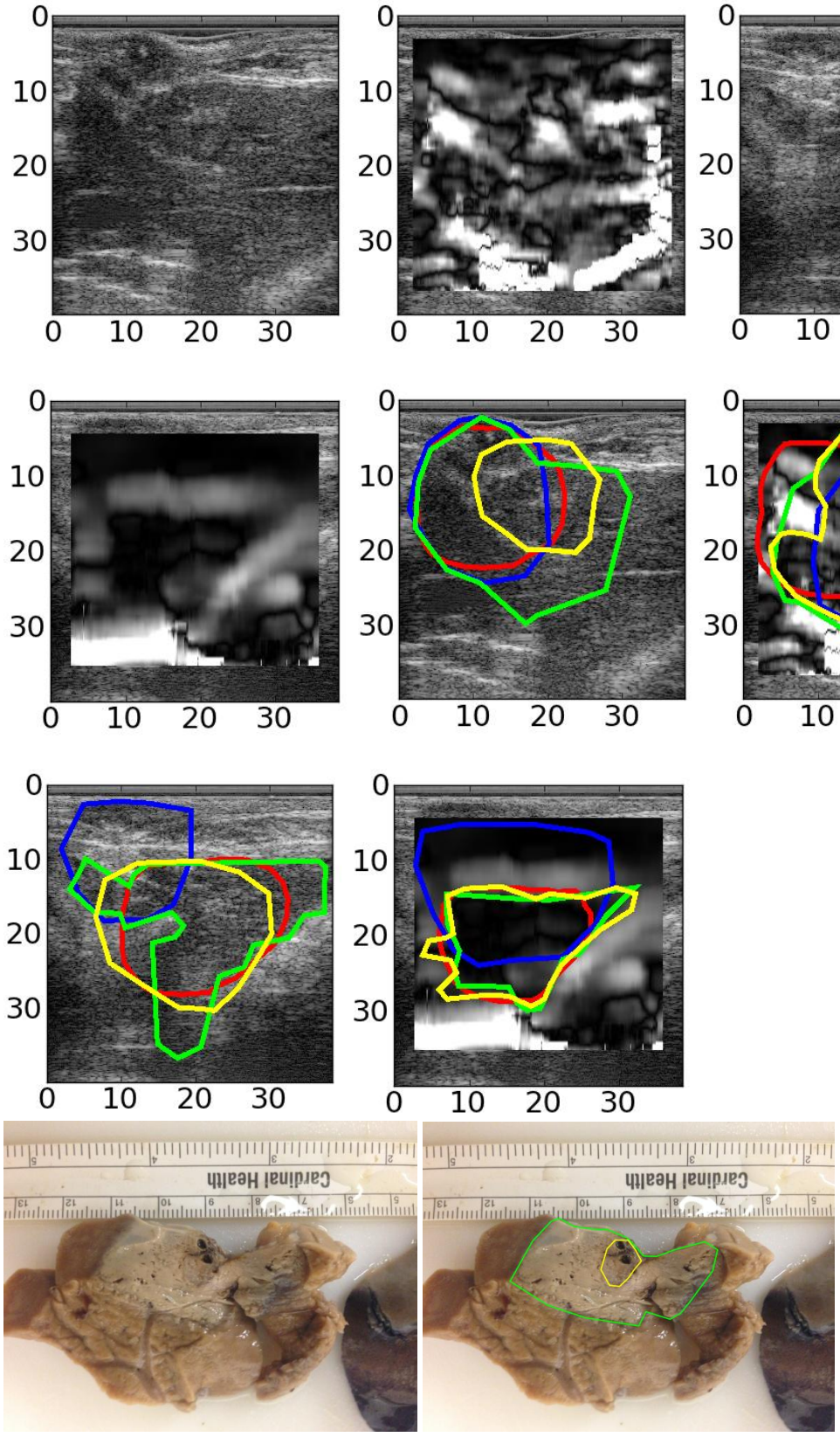

Figure 3.24. VX2 Tumor 8.

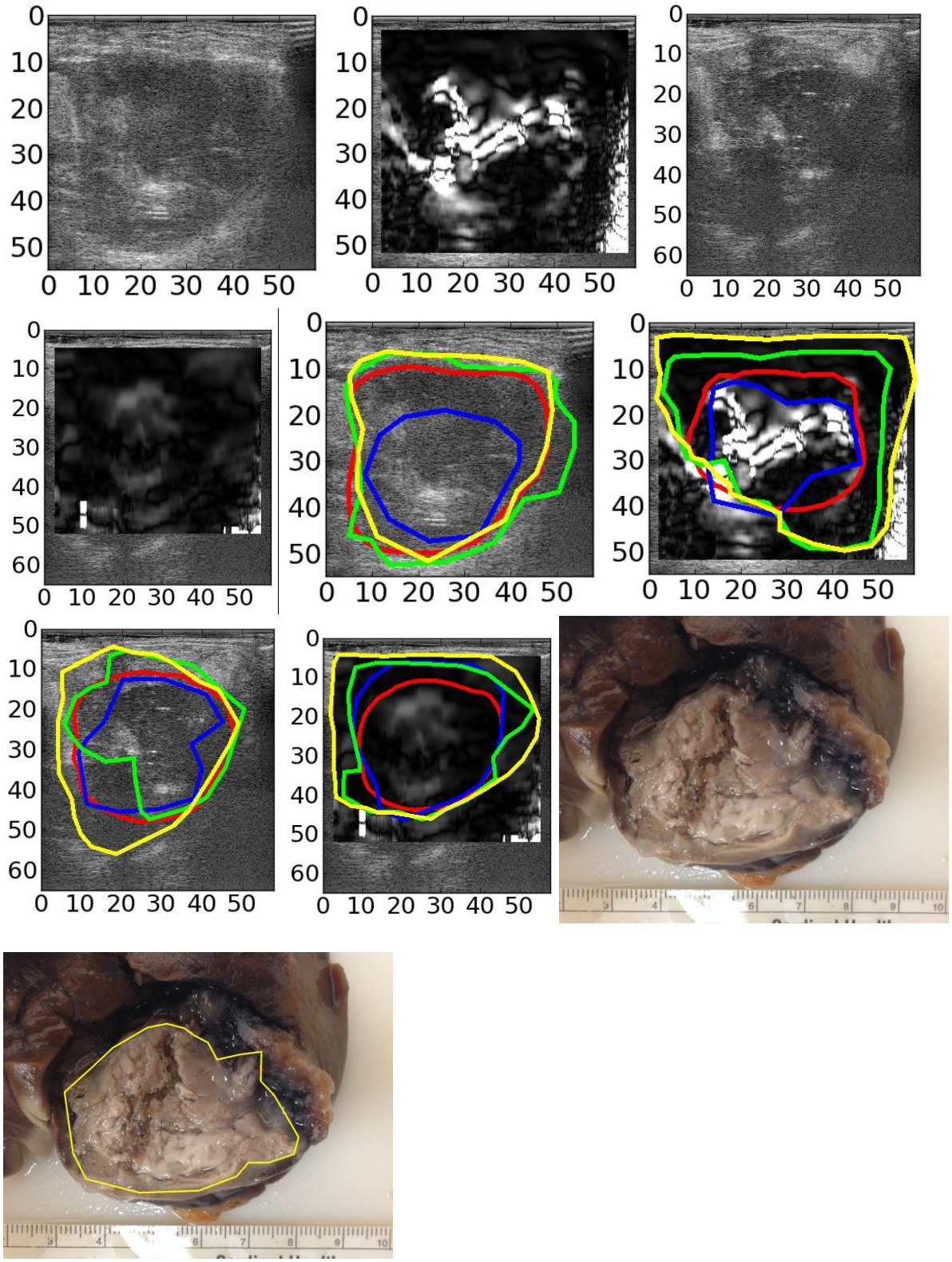

Figure 3.25. VX2 Tumor 9. Only VX2 tumors is segmented in pathology image.

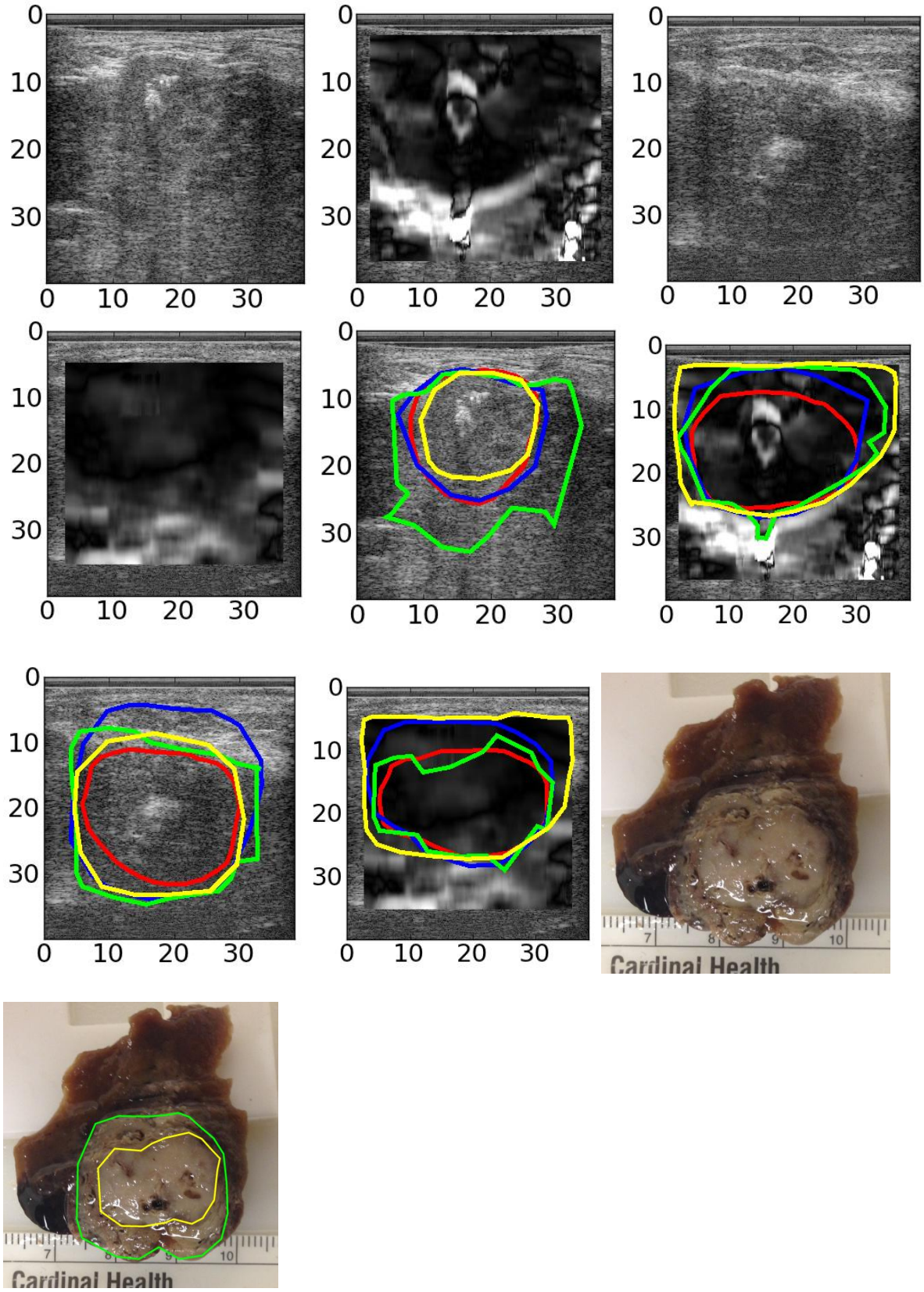

Figure 3.26. VX2 Tumor 10.

3.8. Discussion

Previous phantom and *ex vivo* experiments have demonstrated the accuracy of strain imaging for measuring the extent of tissue necrosis following RF ablation[41], [42]. In previous *ex vivo* porcine studies, the correlation between pathology and strain imaging for cross-sectional imaging was found to be as high as 0.9371 (p=0.000 01) for a sample of 40 thermal ablation zones [42]. In our *in vivo* open surgery porcine study, electrode displacement elastography was performed on normal porcine liver parenchyma after RF ablation to create the thermally coagulated regions, and imaging was performed with the transducer in direct contact with the liver. A smaller sample size of 13 ablation zones was used and three human observers manually segmented the ablation zones obtained from strain images. A linear regression between elastographic and pathologic areas yielded a correlation coefficient of 0.894 (p=0.0001). For the case of automated segmentation, a linear regression between elastographic and pathologic area measurements yielded a correlation coefficient of 0.828 (p=0.001). The strain images illustrated in the *ex vivo* porcine study indicate that thermally ablated liver tissue may be differentiated from healthy liver parenchyma in an *in vivo* animal model. Comparison of the ablated areas between gross-pathology and strain images was performed using boundary contour delineation, which results in reasonably good agreement between strain and gross-pathology measurements. This was shown for the case with multiple human observers and using automated segmentation based on morphological operators. The automated segmentation algorithm can be improved or augmented using manual interventions to improve the segmentation performance.

Although several of the segmentations of the porcine ablations show good agreement with pathology, some of the manual segmentations presented in Table 3.2 show some discrepancy with pathology. This is probably due to the alignment of the ultrasound imaging

plane to the 2D slice utilized for the gross pathology measurements. As previously mentioned, no fiducial markers were introduced into the scan plan to indicate the exact plane for gross-pathology measurements. Coregistration was performed based on the shape of the respective gross-pathology and strain contours for the scan plane identified based on a line burned onto the porcine liver parenchyma after the ablation procedure. Clinicians generally treat a normal tissue margin of approximately 1 cm beyond the tumor boundary to ensure that the entire tumor has been treated. Results reported in the literature indicate that an ablative margin of at least 5 mm or larger is necessary to reduce local tumor recurrence[117]. Note that the boundary discrepancies shown in Table 3.2 are still less than the 5 mm safety margin. We anticipate that with accurate registration the boundary discrepancies between strain imaging and gross-pathology would be minimized further.

These results also demonstrate the need for 3D strain imaging for complete tracking and measurement of the lesion volume [82]. Volume imaging of the ablation zone will reduce errors associated with area measurements [82]. The other limitations of this study include the use of high transducer center frequencies, which are not feasible for imaging human patients during a percutaneous procedure. Ultrasound imaging was performed using an open-chest preparation with the transducer placed directly on the liver surface. This study, therefore, does not evaluate the impact of attenuation introduced by overlying tissue encountered with percutaneous procedures. As demonstrated by the image of the ablation near the blood vessel in figure 3.4, the mechanical boundary conditions also impact the information depicted on the strain image. Note that the quality of the strain images presented in this paper can be significantly improved with the implementation of the strain estimation algorithm in real-time to enable assessment of the mechanical boundary conditions and the corresponding impact on the strain images during data

acquisition. Future works will assess the viability of this technique in more realistic percutaneous animal models, using 3D volume imaging [82] along with improved registration between pathological and imaging planes. Tumor models in animals will also be used to evaluate the ability of electrode displacement elastography to delineate and differentiate the volume treated from the volume to be treated. If successful, these results would enable the use of this technology for clinical applications.

Chapter 4. Mean Scatterer Spacing Estimation

4.1. Introduction

In this chapter we discuss ultrasound scattering models and in particular quasi-periodic scattering in the liver. We then proceed to discuss algorithms for analyzing quasi-periodic ultrasound signals. We discuss the generalized spectrum and its role in ultrasound. Finally, we show simulation results demonstrating the improvement obtained with Thomson's multi-taper algorithm for spectral calculation when the quasi-periodic component of the ultrasound RF signal is weak. The results presented in this chapter have been previously published in [118].

4.2 Review of MSS Estimation Methods

As an acoustic wave propagates through the liver, most of the wave energy is absorbed and converted to heat [119]. A small fraction of the incident acoustic energy is re-radiated by spatial fluctuations in compressibility and density in a process referred to as acoustic scattering [120]. Campbell and Waag estimated that the total scattering loss component of acoustic attenuation over all scattering angles is only 2% in *ex vivo* calf liver [121]. Typically, it is assumed that acoustic scattering results from fluctuations in compressibility rather than fluctuations in density [122]. Compressibility scattering is monopolar in nature, and monopole scattering makes the scattering intensity independent of scattering angle. In addition to simplifying measurements and simulations, the angular independence of scattering agrees well with experimentally measured data in the liver [123]. Specifically Nassiri and Hill found the ratio of fractional fluctuations in density to fractional fluctuations in compressibility, $\gamma_\rho/\gamma_\kappa$, to be in the

range from 12 to 20% or 3 to 8% in the frequency range of 4 to 7 MHz, depending on the correlation model used in the calculations [123].

Diffuse scattering is often assumed for tissue [122], [124]–[129]. Diffuse scattering means that there are a large number of scatterers, greater than 10, contained within an ultrasound resolution cell. Diffuse scattering also assumes that the positions of these scatterers are randomly and spatially uniformly distributed. Diffuse scattering results in speckle, and it has been demonstrated that the random signal received from such a collection of scatterers has an envelope whose values are distributed according to a Rayleigh probability density function [130]. However, in the liver it has been shown that a two component scattering model may be more appropriate for modeling the distribution of scatterers [131]–[133]. This two-component model contains pseudo-periodically arranged scatterers and diffuse scatterers with a uniform spacing distribution [131]–[133]**.** The pseudo-periodically arranged scatterers are hypothesized to correspond to the portal triads, which have a spacing of approximately 1 mm on the average, and encircle the periphery of the liver lobule [131]. The mean scatterer spacing (MSS) of these pseudo-periodically arranged scatterers has been proposed as an useful biomarker to evaluate pathological changes in the liver, such as cirrhosis [131], [132], [134], or infiltration of primary or secondary liver tumors [135].

One of the earliest attempts to characterize liver tissue in terms of an MSS was by Fellingham and Sommer [131]. For a regular array of scatterers with a separation of d, Fellingham and Sommer demonstrated that peaks in the power spectrum would occur at frequency intervals, $\Delta f = c/2d$, where c is the sound speed of the medium [131]. They performed peak detection using the autocorrelation of the power spectrum and made MSS measurements in healthy and cirrhotic livers of human subjects [131]. With a 5 MHz broadband transducer, they

found an MSS of 1.07 ± 0.16 mm across 14 healthy livers and an MSS of 1.48 ± 0.24 mm across 15 cirrhotic livers [131]. The cepstrum has also been used for estimating MSS because it transforms the multiplicative relationship between the system response and tissue response to an additive relationship [133], [136]. Kuc showed that the maximum value of the cepstrum was related to the most probable spacing of a unimodal scatterer spacing distribution [136].

The generalized spectrum (GS), referred to as spectral autocorrelation initially, was introduced by Varghese and Donohue in order to measure MSS [137], [138], and as a QUS biomarker. In [137], using computer simulations, they compared MSS measurements from the GS with MSS measurements from the cepstrum. In their simulations, two types of point-like scatterers were randomly incorporated: uniformly distributed scatterers, referred to as diffuse scatterers, and Gamma distributed scatterers, referred to as quasi-periodic scatterers. The Gamma distribution was selected in this study because it is frequently used to model the arrangement of randomly but regularly spaced scatterers in one dimension. The first use of the Gamma distribution for modeling scatterer spacing can be attributed to Landini and Verrazini [132].

In Varghese and Donohue's simulations [137], the randomly placed scatterers were convolved with a point spread function representing tissue attenuation and an ultrasound imaging system. It was shown that peaks in the GS predict MSS more reliably than peaks in the cepstrum as the concentration of diffuse scatterers increases or the regularity of the coherent scatterers decreases [137]. Additionally, the GS offers the theoretical advantage that when considering expectations computed over many realizations of the scattering process, the energy from diffuse scattering and the energy from periodic scattering appear in different regions of the GS [137]. Concerning separation of tissue properties from the imaging device, a normalization has been proposed to remove the effects of the imaging device from the measurement of the GS [137].

In addition to frequency domain techniques, MSS may be measured through time domain measurements of the autocovariance function. Using singular spectrum analysis (SSA), Pereira *et al.* have decomposed the autocovariance of the RF echo envelope into a component due to diffuse scattering and a component due to periodic scattering [139], [140]. In SSA, the covariance matrix of the signal is diagonalized. Pairs of eigenvalues are identified whose eigenvectors have a normalized correlation coefficient above a threshold and whose eigenvectors have frequency content with sufficiently close peaks. These eigenvectors are deemed to be due to a periodic component in the signal. The MSS associated with the periodic component of the signal can then be found by examining the spectrum of the periodic basis vectors.

Rather than model the signal as non-stationary in its second moment, some authors have tried to model the ultrasound signal as a wide-sense stationary (WSS) signal and attribute coherent scattering to its higher order moments [141]–[144]. In [141]–[143], the authors use the Wold decomposition theorem to separate the RF echo signal into a sum of a coherent and a diffuse component. In [141]–[143], the diffuse component of the signal is modeled as a zero-mean autoregressive process driven by a zero-mean white noise sequence. In [141], the coherent component is modeled as a quasi-periodic sequence; the authors use this model to measure an MSS of approximately 1 mm in the liver of three healthy subjects using a clinical transducer with a center frequency of 3.5 MHz. Meanwhile in 3 other volunteers with liver tumors, an average MSS of 1.5 mm was estimated within their tumors using the same computational model and ultrasound system. In [144], Abeyratne *et al.* also measured an MSS of approximately 1 mm in the liver of two subjects based on higher order statistics of the RF signal from a 3.5 MHz clinical array transducer.

Very recently MSS estimation has been applied to imaging thermal ablations in an *ex vivo* context [145]. In the context of thermal ablation, a wavelet-based MSS detection algorithm similar to that of Abeyratne and Tang has recently been applied to the task of distinguishing between ablated and unablated liver tissue [145]. Zhou *et al*. estimated MSS in 20 liver tissue samples heated in a water bath and 18 cases of microwave ablation of fresh *ex vivo* porcine liver samples. They found an MSS of 1.15 ± 0.12 mm in normal porcine liver and an MSS of 0.93 ± 0.07 mm in coagulated porcine liver tissue.

4.3. Ultrasound Scattering Model in the Liver

We assume the ultrasound RF echo signal is produced by a large number of monopole scatterers. Following the work of Donohue *et al.* [146], we divide these monopole scatterers into three groups: diffuse, periodic, and sparse. Diffuse scatterers are a large number of spatially uniformly distributed microscopic fluctuations in compressibility. Periodic scatterers are scatterers arranged in a quasi-regular pattern with a characteristic spacing, *d*. While the three-dimensional structure of periodic scatterers in the liver is debatable, the position of periodic scatterers in one dimension may be modeled by generating the inter-scatterer spacing from a Gamma distribution [138]. Finally, sparse scatterers are a very small number of aperiodic dominant scatterers lying within the A-line, or a specular surface running through the A-line. Our signal model can therefore be written as:

$$\begin{aligned} x(t) = & \sum_{i=1}^{N_D} \int d_i(\lambda - \tau_i) h(t - \lambda; \tau_i) d\lambda + \\ & \sum_{j=1}^{N_P} \int p_j(\lambda - \tau_j) h(t - \lambda; \tau_j) d\lambda + \\ & \sum_{k=1}^{N_S} \int s_k(\lambda - \tau_k) h(t - \lambda; \tau_k) d\lambda \end{aligned} \qquad \textbf{(4.1)}$$

In equation 4.1, h is a time-varying system response function which characterizes overlying tissue attenuation and beamforming. d_i is a scattering function for the i^{th} diffuse scatterer, p_j is a scattering function for the j^{th} periodic scatterer, and s_k is a scattering function for the k^{th} sparse scatterer. In equation 4.1, the integral signs imply that the ultrasound signal is a continuous function of time. Yet on a modern ultrasound scanner, all the data we process is digitized and the signals are discrete. For the remainder of this chapter, we let t denote a discrete-time variable having integer values, and we utilize the same symbol $x(t)$ to denote a discrete-time sequence of RF data. Since the ultrasound RF signal is modeled as a real-valued random time series, the set of variables $x(1)$, $x(2)$, and $x(3)$ then represent three distinct random variables at time points $t = 1$, $t = 2$, and $t = 3$.

4.4. The Loève Spectrum and MSS

For a zero-mean signal, the expected value of the correlation between the signal at two arbitrary time points is given by the autocovariance function, $\Gamma_L(t_1,t_2)$. The two time points, t_1 and t_2, are any two arbitrary points from the time axis, such that $\Gamma_L(t_1 = 3, t_2 = 5)$ is the correlation between the two random variables $x(3)$ and $x(5)$. Symbolically, for a zero-mean random signal, the autocovariance function is given by:

$$\Gamma_L(t_1,t_2) = E[x(t_1)x(t_2)] \qquad \textbf{(4.2)}$$

The operator $E[\ ]$ denotes expectation. We note that in the definition of the autocovariance function the random variables $x(t_1)$ and $x(t_2)$ are interchangeable so that $\Gamma_L(t_1,t_2) = \Gamma_L(t_2,t_1)$.

For a stationary process, the statistics of the signal do not change over the entire time axis. Specifically, in the case of a stationary process, for any two points located at arbitrary time

points t_1 and t_2, the correlation between $x(t_1)$ and $x(t_2)$ depends only on the difference between t_1 and t_2, τ, and not the average time, t_0.

$$\begin{aligned} \tau &= t_2 - t_1 \\ t_0 &= (t_2 + t_1)/2 \end{aligned} \qquad \textbf{(4.3)}$$

In ultrasound, a strictly stationary signal would correspond to the following unachievable situation: strictly diffuse scattering, an object infinite in extent being imaged, and the influence of attenuation and diffraction being negligible. For a stationary signal, the autocovariance function becomes a function of just the single variable τ, and is symmetric about $\tau = 0$.

It is also possible to characterize random signals in the frequency domain. For a time domain random process, *x(t),* a frequency domain random process Z*(f)* may be associated. This frequency domain representation of the signal is a complex-valued random weighting function for decomposition of the signal into complex exponential functions. The representation of a signal by random amplitude, random phase complex exponentials was developed by Cramèr [147]:

$$x(t) = \int_{-1/2}^{1/2} \exp(i2\pi ft)dZ(f) \qquad \textbf{(4.4)}$$

The integral in equation 4.4 is interpreted as a Riemann-Stieltjes integral. Frequently, random processes are described in terms of their increments. An increment of a random process is given by:

$$dZ(f) = \lim_{h \to 0} Z(f) - Z(f+h) \qquad \textbf{(4.5)}$$

We note that the increment process is generally non-zero because *Z(f)* is generally discontinuous over the band-width of interest. For a stationary process, the associated frequency domain process has uncorrelated increments. This is often written as:

$$E[dZ(f_1)dZ^*(f_2)] = 0 \text{ if } f_1 \neq f_2 \qquad \textbf{(4.6)}$$

In equation 4.6, the variables f_1 and f_2 are similar to the variables t_1 and t_2 of equations 4.2 and 4.3. When they are not equal, f_1 and f_2 indicate two distinct points along the frequency axis. When f_1 and f_2 are equal, the quantity on the left hand side of equation 4.6 is the power spectrum. The power spectrum is defined in terms of the increment process by the following equation.

$$S(f) = E[|\, dZ(f)\,|^2] \tag{4.7}$$

Historically, a widely used estimator for the power spectrum was to compute the magnitude squared of a discrete Fourier transform of a finite length of a signal [148]. This is referred to as a periodogram [148]. The power spectrum is related to the autocovariance function of a stationary signal through the Wiener-Khintchine theorem [147].

$$\Gamma_L(t_1, t_2) = \int \exp(i2\pi f(t_1 - t_2))S(f)df \tag{4.8}$$

In the case of periodic and sparse scattering, even if the effects of diffraction and attenuation can be neglected the signal statistics would still depend not just on the time lag τ, but also on the average time t_0. This can also be expressed in the frequency domain by introducing non-zero correlations in the signal between distinct frequencies. The Cramèr representation and the Wiener-Khintchine theorem have been extended to non-stationary signals by Michel Loève [149]. A non-stationary signal with a Cramèr representation is referred to as a harmonizable process [150]. Harmonizable processes are a very general class of random functions which includes stationary time series, periodically correlated time series, and other types of time series [150]. For a zero-mean, harmonizable process the autocovariance function is related to the Loève spectrum, $\gamma_{L,}$ through a rotation and a Fourier transform:

$$\Gamma_L(t_1, t_2) = \int_{-\infty}^{\infty} exp(i2\pi(t_1 f_1 - t_2 f_2))\gamma_L(f_1, f_2)df_1 df_2 \tag{4.9}$$

In the field of ultrasound tissue characterization, the Loève spectrum has been referred to as the spectral autocorrelation [137], [151] or the GS [146], [152], [153]. The Loève spectrum may also be defined in terms of the increment process [154], as:

$$\gamma_L(f_1, f_2)df_1df_2 = E[dZ(f_1)dZ^*(f_2)] \tag{4.10}$$

Equation 4.10 indicates that the Loève spectrum may be interpreted as a correlation between different frequency components of the random signal. As demonstrated by Haykin in [155], it is easier to interpret the frequency and time variables if the coordinate system is rotated by 45 degrees. We define an average frequency *f* and a frequency difference *g* by:

$$\begin{aligned} f &= (f_1 + f_2)/2 \\ g &= f_1 - f_2 \end{aligned} \tag{4.11}$$

Doing this, the autocovariance and the Loève spectrum may be rewritten in terms of the rotated time and frequency variables, yielding:

$$\Gamma(t_0, \tau) = \int_{-\infty}^{\infty}\int_{-\infty}^{\infty} exp(i2\pi(\tau f + \mathrm{t}_0 g))\gamma(f, g)dfdg \tag{4.12}$$

With this equation, the rotated Loève spectrum, γ, is the Fourier transform of the rotated autocovariance function, Γ; the time lag and average frequency may be considered conjugate variables; and the average time and frequency difference may be considered conjugate variables. Along the line *g=0*, the GS is identical to the power spectrum. Any energy outside the line *g*=0 is an indication that a time series is not stationary.

Since the signal undergoes frequency-dependent attenuation and at any given depth, depending on the location of the focus, the beam is either becoming more narrow or progressively diverging, the Loève spectrum depends on the overlying attenuation, the beamforming, and the scattering properties of tissue. In the signal model of equation 4.1, it was assumed that the signal itself was a time varying convolution between a scattering function and a

point spread function representing diffraction and attenuation. However, when characterizing tissue we are only interested in signal non-stationarity due to scattering. Donohue *et al.* have shown that if the ultrasound RF signal can be modeled by the time-varying convolution of equation 4.1, then the spectrum of a gated RF data segment may be regarded as a product of a scattering function and a function encompassing diffraction and overlying attenuation effects [146]. Donohue *et al*. further showed that if spectral coherence is computed instead of the Loève spectrum, then spectral coherence depends only on the phase relationship between the scatterers [146]. Spectral coherence may be computed using:

$$C(f_1, f_2) = \gamma_L(f_1, f_2) / \sqrt{\gamma_L(f_1, f_1)\gamma_L(f_2, f_2)} \quad \textbf{(4.13)}$$

Dividing the Loève spectrum by the magnitude of the diagonal components reduces the dependence of the Loève spectrum to only the phase relationships between the scatterers. Spectral coherence is a more useful quantity for analyzing periodicity than the Loève spectrum, as this doesn't give additional weight to the larger spacing's near the power spectrum. Spectral coherence has been referred to as a system-normalized GS in prior works[137], [146], [151], [153].

Once the spectral coherence function was calculated, MSS can be computed in two ways. In this chapter, we compute MSS by finding the collapsed average of the spectral coherence function. The collapsed average is an average along diagonal lines of constant scatterer spacing. It may be regarded as an extension of the diagonal smoothing performed on the spectral coherence through multi-tapering or convolutional smoothing [151]. The collapsed average is given by:

$$C_A(\Delta f) = \frac{1}{M(\Delta f)} \sum_{|f_1 - f_2| = \Delta f} |C(f_1, f_2)| \quad \textbf{(4.14)}$$

In equation 4.14, M is a normalization constant that depends on the number of discrete entries in a diagonal line of constant frequency difference. Alternatively, MSS may be found by increasing the amount of diagonal smoothing in the spectral coherence calculation by increasing W. MSS may then be directly estimated from a local maximum in the magnitude of spectral coherence. We follow this approach in chapter 5. Any region in the bifrequency plane, or along the collapsed average, where the frequency difference, f_1-f_2, corresponds to half the gate length or more was set equal to zero to avoid erroneous local maxima detection near the power spectrum when computing MSS. We denote the frequency difference yielding the maximum value of either spectral coherence magnitude or collapsed average by Δf_{max}. MSS was computed according to:

$$MSS = \frac{c}{2 * \Delta f_{max}} \tag{4.15}$$

4.5. Single-taper Estimation of the Loève Spectrum

To date in ultrasound, the most commonly employed estimator for the GS is a synchronized, Welch-Bartlett time-averaged power spectral estimate [137], [146], [153], [156]:

$$\hat{\gamma}_{WB,i}(f_1, f_2) = \frac{1}{N_S}\sum_{i=1}^{N_S} Y_i(f_1)\phi_i(f_1)Y_i^*(f_2)\phi_i^*(f_2)$$
$$\gamma_{WB}(f_1, f_2) = \frac{1}{N_A}\sum_{i=1}^{N_A} \hat{\gamma}_{WB,i}(f_1, f_2) \tag{4.16}$$

The Y_i in the above equation refer to windowed DFTs of RF A-lines. For Welch-Bartlett averaging, each of these A-lines is broken up into N_S overlapping segments, where typically N_S=3 [137]. The $\varphi_i(f)$ are phase factors that account for the fact that arbitrarily dividing a segment into different sections produces phase offsets between those segments. The phase factor

for a segment is given by $\varphi(f) = exp(j2\pi f\tau_i)$, where τ_i is the time delay between the beginning of the A-scan segment and the position of the dominant periodic scatterer [153]. This is typically approximated as the location of the maximum value of the envelope of the RF data. The averages across overlapped A-line segments are then averaged over N_A A-lines. This type of estimate for the GS effectively decreases the resolution of the estimate to decrease the estimation variance.

In addition to a Welch-Bartlett average for the GS, a diagonally smoothed estimate has been proposed by Varghese and Donohue [151]. The diagonal smoothing exploits the fact that for a signal with periodically correlated frequency components we expect the GS to be continuous along lines corresponding to a constant scatterer spacing and experience more rapid fluctuations along lines perpendicular to this. A diagonally smoothed GS estimate is given by:

$$\hat{\gamma}_{ST,i}(f_1, f_2) = \sum_{f_1'=-R}^{f_1'=R} \sum_{f_2'=-R}^{f_2'=R} Y(f_1 - f_1')Y_i^*(f_2 - f_2')H(f_1', f_2')$$
$$\hat{\gamma}_{ST}(f_1, f_2) = \frac{1}{N}\sum_{i=1}^{N_A} \hat{\gamma}_{ST,i}(f_1, f_2)\phi(f_1)\phi^*(f_2) \quad \textbf{(4.17)}$$

In the equation above, R is the radius of non-zero elements of the smoothing kernel, H, and i indexes individual A-lines. Diagonal smoothing is implemented by allowing $H(f_1,f_2) = \delta(f_1 - f_2)$.

4.6. Multi-taper (MT) Estimation of the Loève Spectrum

To discuss the MT method, we begin by substituting the Cramèr representation for a discrete time process into the equation for a discrete Fourier transform. Using the convention that the sampling frequency is equal to one, a discrete Fourier transform computed using only N discrete time samples is given by:

$$y(f) = \sum_{t=0}^{N-1} x(t)exp(-i2\pi ft) \quad \textbf{(4.18)}$$

Inserting the Cramèr representation for a stochastic process into this equation, after some manipulation, yields:

$$y(f) = \int_{-1/2}^{1/2} K_N(f - f')dZ(f')$$
$$K_N(f) = \frac{sin(N\pi f)}{sin(\pi f)} exp(-i2\pi f(N-1)/2) \quad \textbf{(4.19)}$$

This equation is derived in [148] and is often referred to as the fundamental equation for spectral estimation. It describes the blurring in the frequency domain that results from using a discrete Fourier transform with only a finite number of time samples. The integral kernel K_N is similar to a sinc function and is known as the Dirichlet kernel. This equation shows that due to the implicit application of a rectangular window function to a time series prior to computing it's discrete Fourier transform, the result will be blurred by convolution with a sinc-like function.

Estimating the statistical properties of *Z(f)* could be considered an inverse problem. The corresponding forward problem would be to take a known random process, *Z(f)*, and blur it with the Dirichlet kernel, K_N, given in equation 4.19. To solve the inverse problem where *Z(f)* is unknown, Thomson advocated the use of a local least-squares eigenfunction approximation to the solution of the fundamental equation of spectrum estimation [148]. An eigenfunction approximation is possible because the eigenfunctions of the Dirichlet kernel are well known. They are the discrete prolate spheroidal sequences (DPSS). We will denote the k^{th} DPSS by $v_k(t)$ and the Fourier transforms of the DPSS as $V_k(f)$, while the eigenvalue of the k^{th} DPSS will be denoted λ_k. Note that the DPSS are also known as the Slepian sequences. An N-point Slepian sequence is defined as the inverse Fourier transform of the frequency domain function satisfying the following eigenvalue equation:

$$\int_{-W}^{W} \frac{\sin(N\pi(f - f'))}{\sin(\pi(f - f'))} U_k(N,W;f')df' = \lambda_k(N,W)U_k(N,W;f) \quad \textbf{(4.20)}$$

The parameter *W* is a user selected parameter, and the majority of the energy of the eigenfunctions is concentrated in a band from -*W* to *W*. An approximate solution for *Z(f)* in the integral equation in 4.14 could be created by projecting *Z* onto the DPSS over the bandwidth -*W* to *W*. The projection operation would yield Z_k, where Z_k are the unobservable, ideal eigencoefficients for the expansion. They are given by:

$$Z_k(f) = \frac{1}{\sqrt{\lambda_k}} \int_{-W}^{W} U_k(f') dZ(f - f') \tag{4.21}$$

The Z_k in the above equation are unobtainable with the data. However, Thomson demonstrated a useful relationship between time series data windowed by the DPSS and the ideal expansion coefficients in equation 4.21. Before providing that relationship we present a definition. Thomson referred to windowed discrete Fourier transforms of data as estimated eigencoefficients in his seminal paper on MT estimation [148], and we denote these eigencoefficients by $y_k(f)$:

$$y_k(f) = \sum_{t=0}^{N-1} exp(-i2\pi fn) v_k(n) x(n) \tag{4.22}$$

Utilizing the fact that the DPSS are eigenfunctions for the Dirichlet kernel, Thomson derived the following relationship between the estimated eigencoefficients and the ideal eigencoefficients [148]:

$$y_k(f) = \int_{-1/2}^{1/2} U_k(f') dZ(f - f') \tag{4.23}$$

Equation 4.23 demonstrates two concepts. First, the eigencoefficients can be approximated by the DFT of the data segment windowed with one of the DPSS. Second, the difference between the ideal eigencoefficients and the estimated eigencoefficients is given by the integral outside the bandwidth (-*W*, *W*). This difference between the ideal and estimated

eigencoefficients can introduce bias in the spectral estimate. We define the bias for the estimate of the k^{th} eigencoefficient, $b_k(f)$, as:

$$b_k(f) = \int_{-1/2}^{1/2} V_k(f')dZ(f-f') - \int_{-W}^{W} V_k(f')dZ(f-f') \qquad \textbf{(4.24)}$$

In Thomson's derivation of the multi-taper algorithm, an adaptive weighting scheme was developed in order to reduce the out of band bias from multi-tapering, given by equation 4.24. The data adaptive weights essentially function to decrease the contribution to the spectral estimate from the higher order tapers in regions where the spectrum is rapidly changing. We found that the data adaptive weights made little difference in our own calculations and will not discuss them further in this dissertation.

In the case of power spectrum estimation for a stationary process, one computes the power spectrum by squaring the approximate eigencoefficients, $y_k(f)$, and averaging the result over $2NW$-1 tapers. In order to compute the Loève spectrum, one finds the correlation between the approximate eigencoefficients at different frequencies and averages that result over $2NW$-1 tapers. A multi-taper estimate of the Loève spectrum using a single RF data segment, $x_i(t)$, having approximate eigencoefficients, $y_{i,k}$, is given by:

$$\hat{\gamma}_{MT,i}(f_1, f_2) = \sum_k y_{i,k}(f_1) y_{i,k}^*(f_2) \qquad \textbf{(4.25)}$$

Due to the properties of the Slepian sequences, this estimator for the Loève spectrum performs diagonal smoothing along lines of width $2W$ [154]. The estimator for the Loève spectrum in equation 4.25 has been employed in the field of geophysics prior to being used in ultrasound signal processing [157]. To compute a multi-taper estimate over a block of ultrasound data containing N_A A-lines, we multiplied estimates along each A-line by the appropriate phase factor $\varphi_i(f)$ and averaged them, to obtain:

$$\hat{\gamma}_{MT}(f_1, f_2) = \frac{1}{N_A} \sum_i \hat{\gamma}_{MT,i}(f_1, f_2) \phi_i(f_1) \phi_i^*(f_2) \tag{4.26}$$

4.7. Spectral Windows

The analytical formulas for the three single tapers used in this dissertation are illustrated in table 4.1. For computing the Slepian sequences, the algorithm utilized was a Python wrapper on a Fortran library developed by Prieto *et al.* [158]. In this code, the Slepian sequences are found according to an algorithm given by Thomson in appendix B of [159]. We display plots of the first three Slepian sequences when N=100 and NW=5 in figure 4.1 (a). The lowest order Slepian sequence bears a close resemblance to a Gaussian, and higher order sequences possess an increasing number of zero-crossings. The lowest order taper has the smallest side lobes if the Fourier transform is examined. The higher order tapers are able to recover information from the window edges that are lost in using only the lower order taper. However, using an increasing number of tapers to recover this information comes at a price of increasing side lobes. We note that the lowest order DPSS closely resembles the Hann, Hamming, and Blackman-Harris windows shown in figure 4.1 (b). However, the lowest order DPSS is narrower than any of the single tapers. We note from figure 4.2 that the lowest order DPSS has much lower side lobes than any of the single tapers considered.

Table 4.1. Analytical formulae for windows used in single taper (ST) GS calculations

Window	Formula
Hann	$W(n) = 0.5\,(1 - \cos(2\pi n / (N - 1)))$
Hamming	$W(n) = .54 - .46 \cos(2\pi n / (N-1))$
Blackman-Harris	$W(n) = a_0 - a_1 \cos(2\pi n / (N-1)) + a_2 \cos(4\pi n / (N-1)) - a_3 \cos(6\pi n /(N-1))$; $a_0 = 0.3635819$; $a_1 = 0.4891775$; $a_2 = 0.1365995$; $a_3 = 0.0106411$

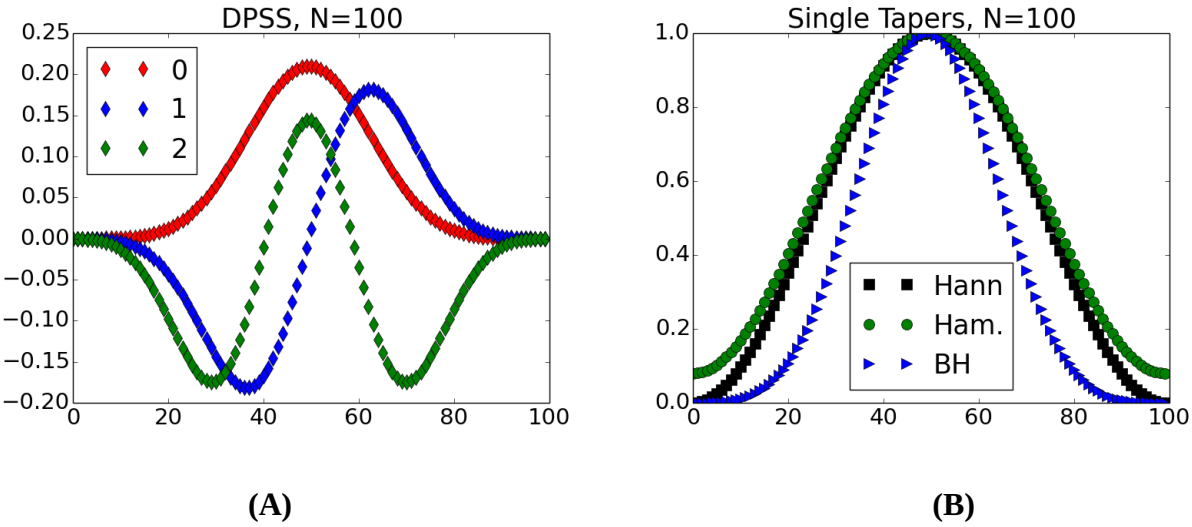

Figure 4.1. (A) First three Slepian sequences when N=100 and NW=5. The legend stands for the order 0, order 1, and order 2 taper. **(B)** Plot of Hann, Hamming (Ham. in legend), and Blackman-Harris (BH in legend) windows for N=100.

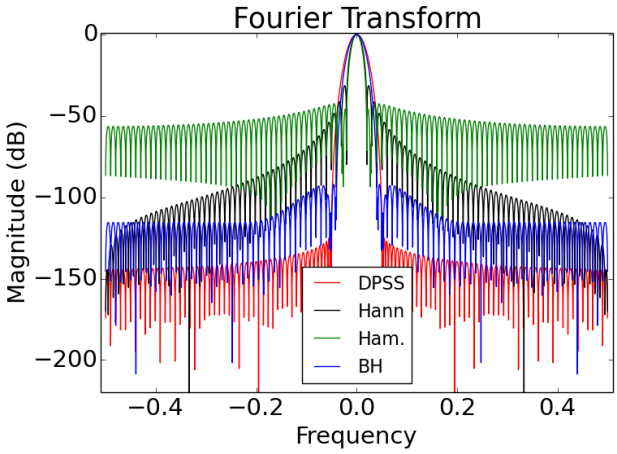

Figure 4.2. Plot demonstrating spectral concentration and side lobes of lowest order DPSS. In the figure above the magnitude of the Fourier transform of the lowest order DPSS, Hann, Hamming, and Blackman-Harris tapers are displayed. Each 100-point window sequence was zero-padded with 5,000 additional points prior to computing the discrete Fourier transform.

4.8 Simulations: Pressure Field Calculation

Simulations were performed by computing the pressure field in the frequency domain as described by Li and Zagzebski [160]. We summarize the salient features of the simulation in the following paragraphs. The pressure at field point ***r*** emitted from a single rectangular element of a linear array transducer, vibrating so that the velocity of the surface is $v(t) = u(\omega)exp(i\omega t)$, is given by:

$$p_i(\mathbf{r},\omega) = -\frac{i\rho kcu(\omega)}{4\pi} A_0(\mathbf{r},\omega)$$
$$A_0(\mathbf{r},\omega) = \int_{-b/2}^{b/2}\int_{-a/2}^{a/2} \frac{exp(ik\,|\,\mathbf{r}-\mathbf{r}'\,|)}{|\,\mathbf{r}-\mathbf{r}'\,|} dx'dy' \qquad \textbf{(4.27)}$$

In the equation above, c is the speed of sound in the medium, ρ is the density of the medium, k is the wavenumber, and $\boldsymbol{r}'$ is the field point on the surface of the transducer. The width of the element laterally is b, and elevationally is a. Accurate approximation of this integral by truncating a Taylor series expansion for the term $|\boldsymbol{r} - \boldsymbol{r}'|$ is discussed in [160]. Attenuation was taken into account by letting the wave number be a complex variable with an imaginary part equal to the attenuation. Linear attenuation with frequency was used for these simulations, with an attenuation coefficient equal to 0.65 dB/cm MHz.

For a focused, linear array transducer, the field from each element is summed and appropriate time-delays are applied to achieve a focused ultrasound beam. A 128 element array with element sizes of 0.15 mm laterally and 10 mm elevationally was simulated. Approximation of the time delays is discussed in [160]. The simulated transducer had an *F/#* of 2. The simulations assume the Born approximation of weak scattering, which means that there is no multiple scattering, and that locally the incident pressure wave looks planar. Under these assumptions, the scattered pressure at a point $\boldsymbol{r}''$ from a single scatterer is given by:

$$p_s(\mathbf{r}'', \omega) = p_i(\mathbf{r}, \omega) \frac{exp(ik|\mathbf{r} - \mathbf{r}''|)}{\mathbf{r} - \mathbf{r}''} \Phi(\omega, \theta) \quad \textbf{(4.28)}$$

The quantity $\varphi(\omega,\theta)$ denotes the scattering amplitude in the azimuthal direction. It describes the angular distribution of the scattered sound energy, and is discussed in Morse and Ingard [161].

The force on the face of the transducer due to a single scatterer was given by integrating over the face of the transducer and assuming that the scattering amplitude was constant over all scattering angles. This is equivalent to the assumption that the scatterers are monopolar, as discussed in section 4.3. We summed the contributions from all the scatterers, and assumed a uniform force to voltage transfer function for the transducer. The time domain signal was generated by multiplying the scattered pressure in the frequency domain by a bandpass filter corresponding to a transducer with a particular bandwidth, *BW*, and center frequency, f_c; then, performing the inverse Fourier transform.

$$V(t) = \int_0^\infty V(\omega) exp(-\frac{(f - f_c)^2}{(f_c BW)^2}) exp(-i\omega t) d\omega \quad \textbf{(4.29)}$$

A center frequency of 3.5 MHz with a fractional bandwidth of 70% was used in the simulations in this chapter. The pressure field was calculated over a discrete grid with a spacing of Δx = 0.2 mm, Δy = 0.2mm, and Δz = 0.01 mm. We use the same convention as in [160] for our coordinate system, where *x* is the elevational direction, *y* is the lateral direction, and *z* is the axial direction. The pressure from scatterers located at arbitrary locations was found by multiplying the pressure at the closest grid point by a phase factor, φ, that accounted for the difference in phase and attenuation:

$$\phi(\Delta z) = exp(i2\pi(2\Delta z)k) \quad \textbf{(4.30)}$$

4.9 Simulations: Scatterer Distributions

In figure 4.3 (a) we show a schematic approximation of the liver tissue model containing multiple lobules. In the model, a lobule is made up of 7 periodic scatterers corresponding to 6 hexagonally arranged portal triads and the central vein, along with a collection of diffuse scatterers. In simulation, each A-line was a signal generated by an independent realization of a medium containing randomly placed scatterers. The simulated medium had dimensions of 44 mm axially, 5 mm laterally, and 10 mm elevationally. Two types of scatterers were created in each computational phantom: diffuse and periodic. They differed in the intensity of the reflected sound wave and their spatial arrangement. Diffuse scatterers were simulated by creating uniformly randomly distributed scatterers with a number density of $10/mm^3$. To ensure sufficient signal intensity, periodic scatterers were placed in the center of the beam laterally and elevationally and any reflected pressure from a periodic scatterer was amplified by a factor of 5. Axially, we used an MSS of 1 mm, or (2.27 wavelengths relative to the center frequency), for each column of periodic scatterers. However, from one beamline to the next we allowed a random offset between the start of each series of periodic scatterers. This was captured in the simulations by drawing the position of the first periodic scatterer from a uniform distribution with a maximum value of 1 mm. Subsequent periodic scatterers were arranged according to a Gamma distribution. A diagram of a computational phantom is shown in figure 4.3 (b).

To calculate the scattering amplitude at 180^0, we modeled the diffuse scatterers as glass beads 45 microns in diameter and the periodic scatterers as glass beads 85 microns in diameter. This was done because the scattering amplitude of glass beads is easily calculated based on Faran theory [162]. The medium was assumed to be tissue equivalent with a sound speed of 1540

m/s and a density of 1.02 g/cm^3. The glass beads were assumed to have a sound speed of 5,570 m/s, a shear wave speed of 3,375 m/s and a density of 2.54 g/cm^3.

The Gamma distribution is typically defined in terms of a shape parameter, k, and a scale parameter, θ. The distribution, $f(x;k,\theta)$ is given by:

$$f(x;k,\theta) = \frac{x^{k-1} exp(x/\theta)}{\theta^k \Gamma(k)} \tag{4.31}$$

The symbol Γ denotes the Gamma function in this context. For our purposes we discuss results in terms of the MSS, μ, the variance of the distribution, σ^2, and the fractional standard deviation of the scatterer spacing, $\eta = \sigma/\mu$. The mean and the variance are related to the shape and scale by $\mu=k\theta$ and $\sigma^2=k\theta^2$, respectively.

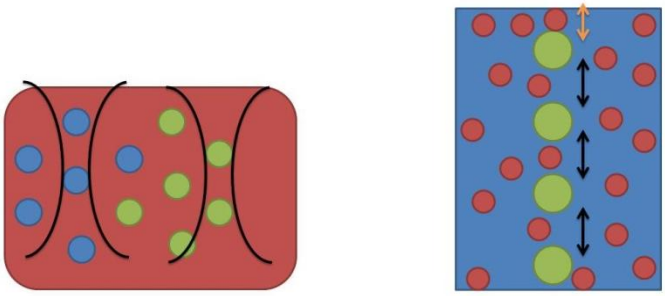

(A) **(B)**

Figure 4.3. (A) Diagram showing idealized liver tissue insonified by two focused ultrasound beams. **(B)** Simplified quasi-periodic and diffuse scattering model used in simulation of an A-line. Large green circles represent regularly spaced scatterers which had initial position determined by a uniform distribution (orange arrow) and subsequent spacing determined by a Gamma distribution (black arrow). Small red circles represent diffuse scatterers.

We point out now that the one-dimensional nature of our simulated periodic scattering distributions has consequences that do not necessary reflect the actual liver. In these simulations, as in reality, the ultrasound beam is diverging as one examines regions away from the focus. We have enhanced the periodic signal in our simulation by placing the periodic scatterers in the center of the ultrasound beam. Meanwhile, as the simulated ultrasound beam propagates through tissue, the resolution cell becomes larger. With an increase in the dimensions of the resolution cell, the ratio of diffuse signal energy to coherent signal energy increased. This is because the periodic scatterers were distributed in one dimension, along a column, while the diffuse scatterers were distributed three-dimensionally and uniformly throughout the volume. As a consequence of the beamforming and the scatterer placement, the periodic component of the simulated signal became weaker relative to the diffuse component with depth. This is clearly visualized in the example signal in figure 4.4. Notice the regular peaks becoming weaker relative to the background with increasing depth.

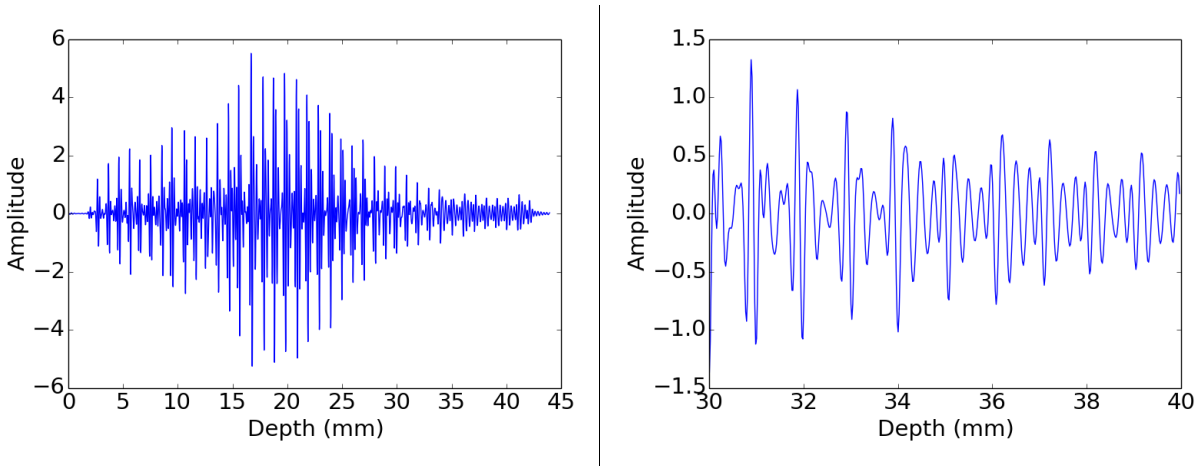

(A) **(B)**

Figure 4.4. Example simulated periodic signal. **(A)** Entire signal over full depth. **(B)** Signal gated from a depth of 30 mm to a depth of 40 mm. Notice that the quasi-periodic component of the signal is noticeably weakened away from the lateral and elevational focus at 20 mm.

4.10 Simulations: Results

For results presented in this section, all discrete Fourier transforms were computed using a standard FFT algorithm which is part of the scientific Python package [163]. Simulation results are presented for estimates of the GS for a specified number of gated A-line segments, gate length, and fractional standard deviation in spacing in figures 4.5 and 4.6. Monte Carlo simulations of MSS estimates for a variable number of A-lines or a variable gate length are shown in figures 4.7 and 4.8. In figures 4.5 and 4.6 the window that was used for the single taper method was the Hann window. When showing Monte Carlo simulation results in figures 4.7 and 4.8 we used several different windows, i.e. Hann, Hamming, and Blackman-Harris. All windows are given by the formulas in table 4.1. For all Monte Carlo simulations, 150 ensembles of independent A-lines were generated and gated. To compute the MSS, the maximum of the CA of the coherence was computed. The CA was filtered, such that any values within 0.5 MHz of the diagonal corresponding to the power spectrum were set to zero. MSS was computed from the maximum value of the filtered CA. For all results shown we fixed the smoothing bandwidth at 0.642 MHz, and gated the data starting at a depth of 25 mm. We examined gate lengths from 5 to 12 mm throughout these simulations so NW varied from 4 to 10 discrete points.

The simulation results shown in figure 4.5 (a) and (b) demonstrate a ST and MT calculation of the coherence for a large number of gated data segments in the ensemble (N=200) for phantoms with η = 5%, using a short gate length of 6 mm. Figure 4.5 (a) and (b) indicates that a multi-taper calculation of spectral coherence may offer a better resolution in the non-stationary direction. The location of the peak in the MT calculation was precise at a 6 mm gate length, with a maximum occurring along a single diagonal line. There is some blurring in the non-stationary direction visible in the MT calculation, but the peak is identified more precisely

for the MT calculation than the ST calculation. In the limiting case of a great many independent data segments in the ensemble, we can see from the figure that the peaks of the ST calculation are centered in the correct diagonal band of the coherence estimate. They are simply diagonally smeared across a broader region of the bi-frequency plane.

The effect of increasing the gate length on the coherence calculation under the particular conditions of our image formation and scattering model is shown in figure 4.5 (c) and (d). In this figure, a loss of the higher order peaks is visible in both MT and ST calculations. Peaks are visible across three diagonal lines corresponding to a 1 mm spacing, two times this frequency difference, and three times this frequency difference with a short gate length. With a longer gate length the third peak is no longer discernible, and the first two peaks in the bi-frequency plane have a reduced intensity. The reason for this is the variability of the periodic SNR over the depth of the simulated phantom.

In figure 4.5, a phenomenon that was observed for larger fractional standard deviations in the spacing is demonstrated. This figure shows coherence calculations for a small number of gated data segments and a large number of gated data segments when η is high (20%). At a high fractional standard deviation in the scatterer spacing, the sub-harmonic spacing peak in the coherence calculation starts to dominate over the peak corresponding to a spacing of 1 mm. This seems counter-intuitive, but it has also been observed by Huang *et al*. [152]. We can see, though, that the effect is less severe for the MT calculation than it is for the ST calculations.

The Monte Carlo results shown in figures 4.7 and 4.8 provide statistical confirmation of our inferences from the calculations in figures 4.4 and 4.5. For the parameters explored, the MT calculation outperforms any of the ST calculations in variance and bias simultaneously. For the GS calculated for a low fractional standard deviation in the spacing of 5%, the peak of the CA

for the MT calculation corresponds precisely to 1.0 mm, while there is some variance and bias in the ST calculation when the number of gated data segments averaged is smaller than 8. As η increases to 10% there is some variance and a small amount of bias in the MT calculation, but this rapidly falls off as more than 10 gated data segments are used in the calculation. At an η equal to15%, a large amount of bias is visible in the MSS estimate for a small number of gated A-lines, but considerably less for the MT calculation than that obtained for any of the ST calculations. The bias towards smaller MSS that is visible when η = 15% is a result of the prominence of the sub-harmonic spacing peak. Of the 3 ST estimators, the Hann and the Hamming windows appear to perform the best with the Blackman-Harris window exhibiting slightly poorer performance.

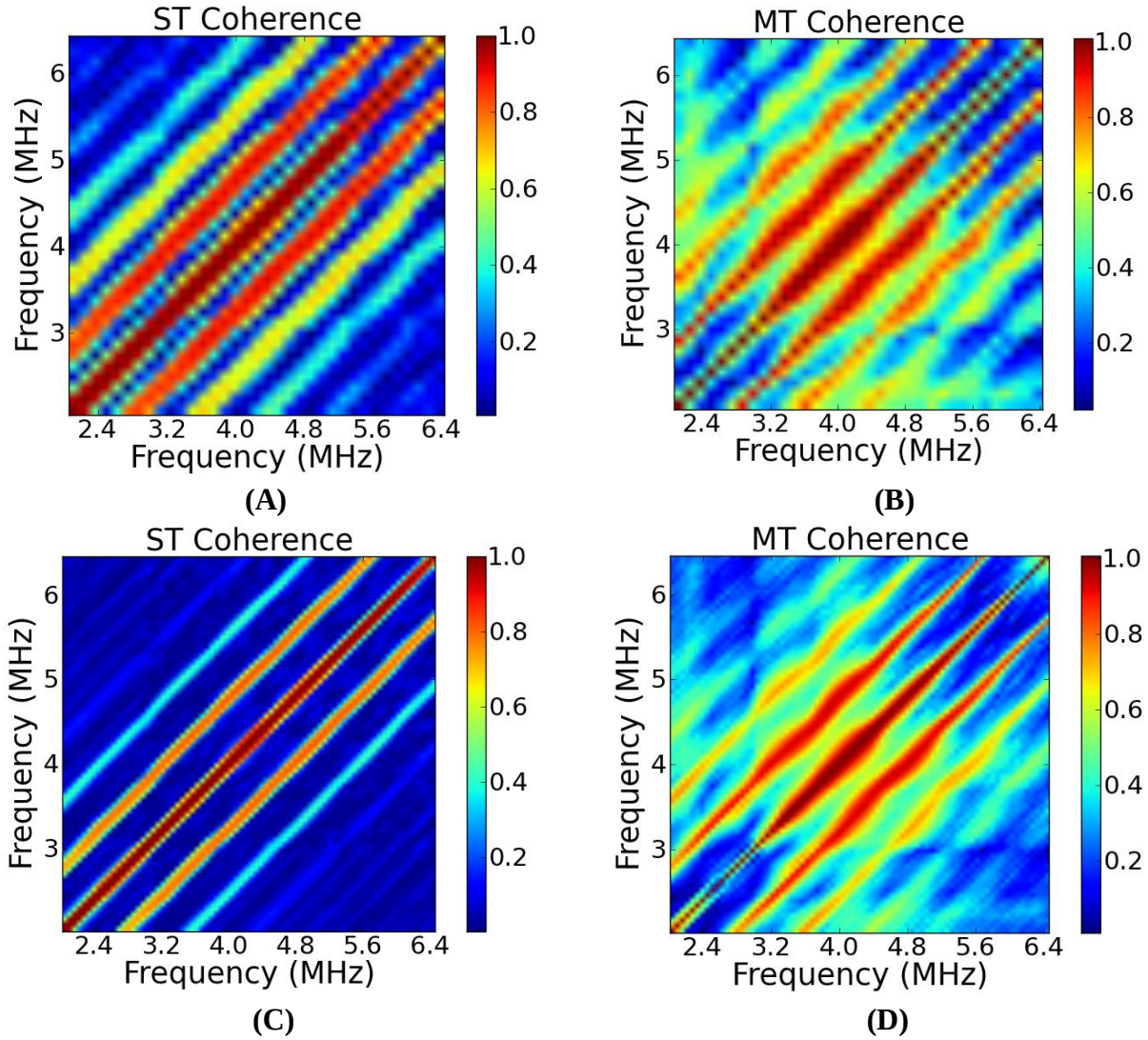

Figure 4.5. Single taper (ST) **(A, C)** and multi-taper (MT) **(B, D)** estimates of the coherence averaged over 200 data segments when η=5% and the gate length is either 6 mm **(A, B)** or **(C, D)** 13 mm.

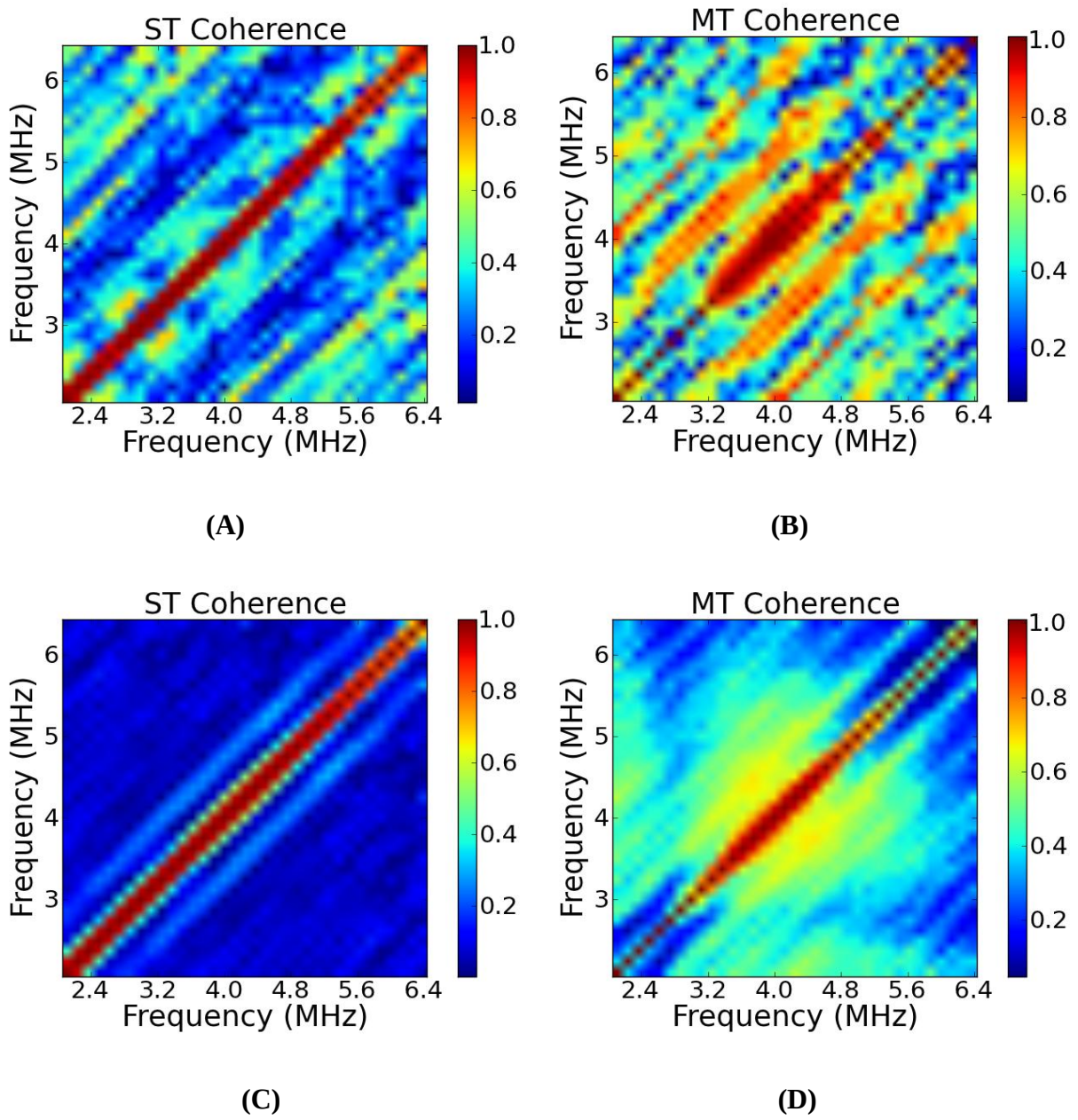

Figure 4.6. ST **(A, C)** and MT **(B, D)** estimates of the coherence with a gate length of 6 mm, η=20%, and averaged over **(A, B)** 10 or **(C, D)** 200 data segments.

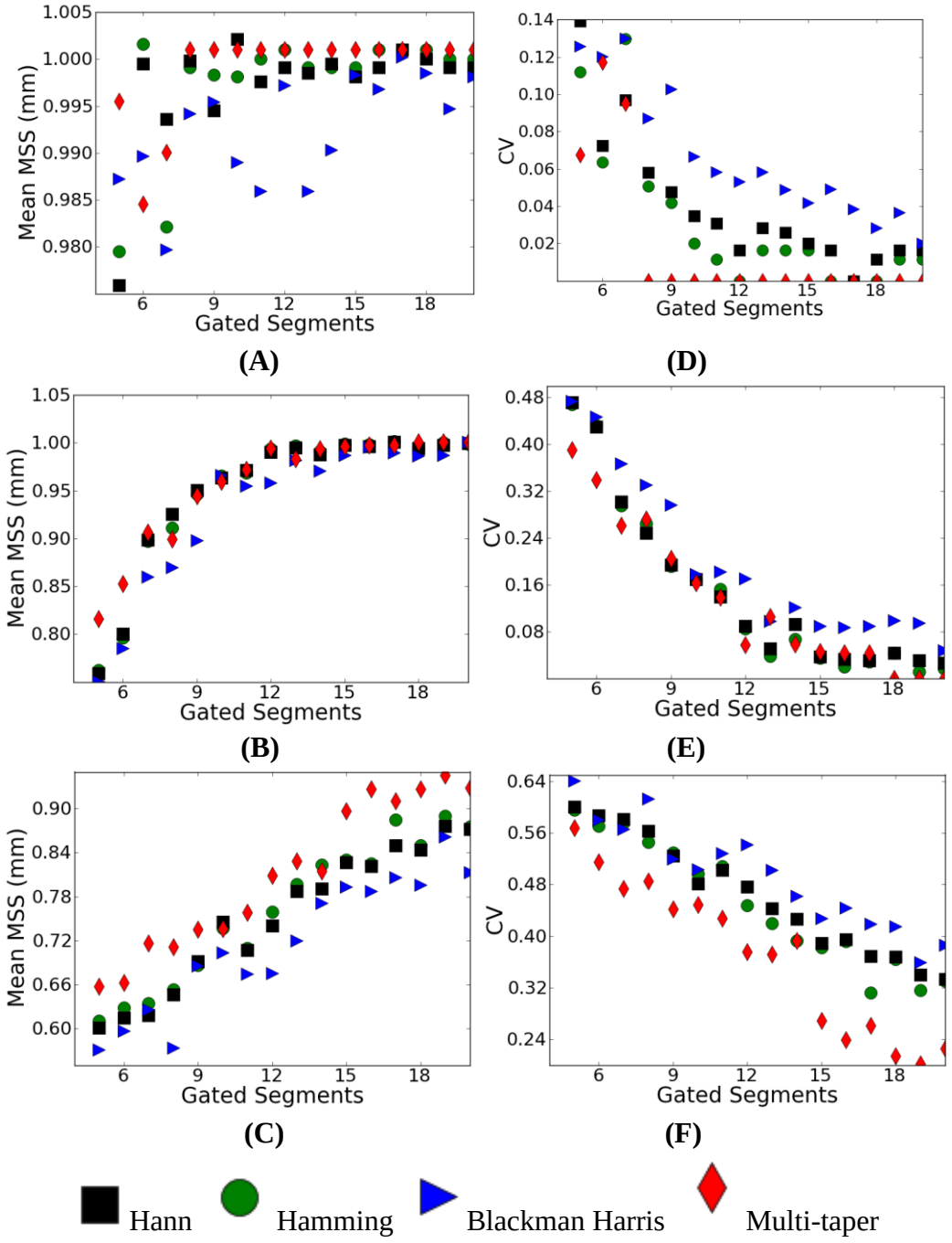

Figure 4. 7. Mean MSS estimates **(A, B, C)** and coefficient of variation **(D, E, F)** for a variable number of gated data segments in the estimate and a fixed gate length (6 mm). **(A, D)** η= 5% **(B, E)** η = 10% **(C, F)** η= 15%.

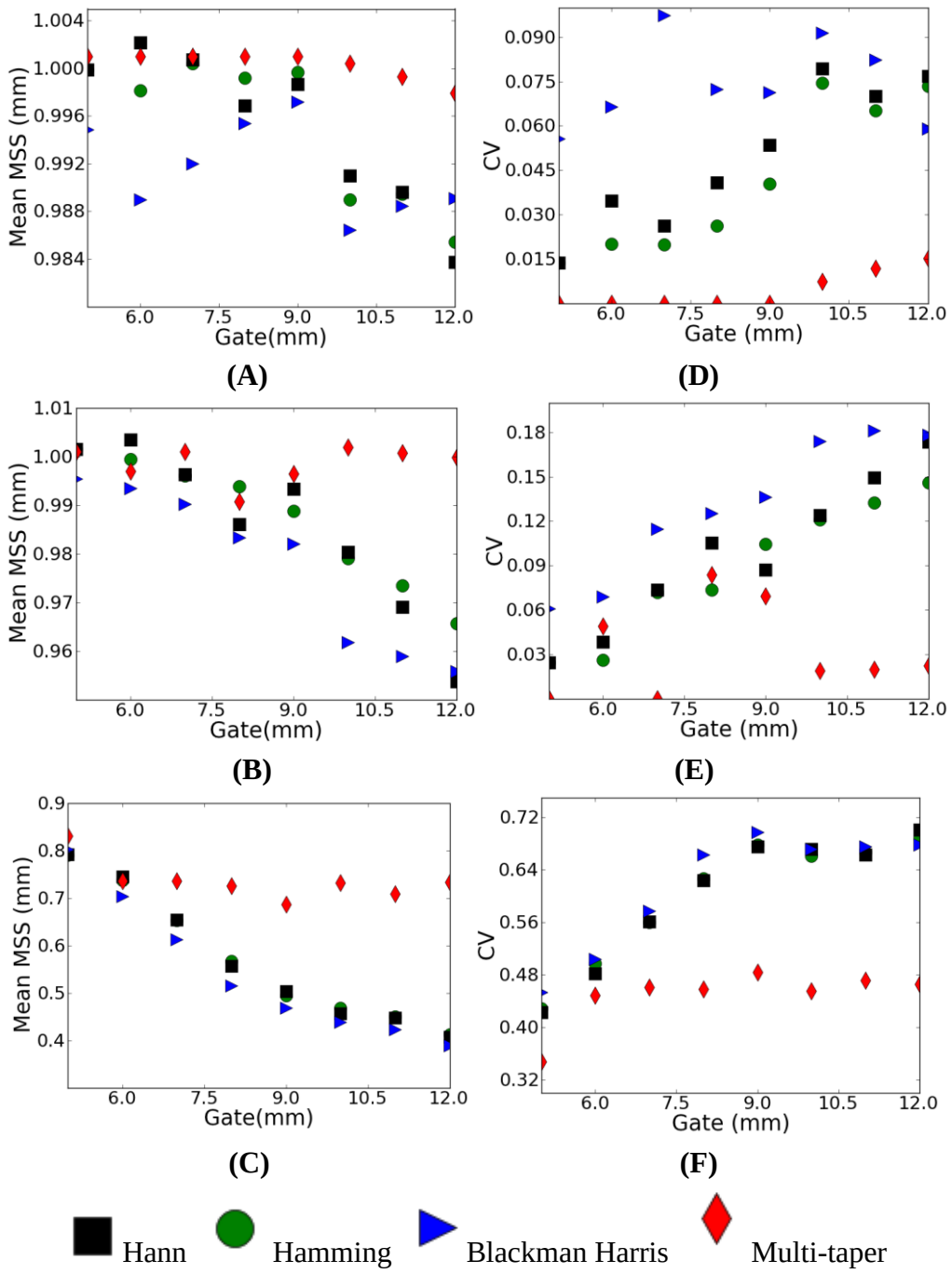

Figure 4.8. Mean MSS estimates (**A, B, C**) and coefficient of variation (**D, E, F**) for a variable gate length in the estimate and a fixed number of gated data segments (N=10) (**A,D**) η= 5% (**B,E**) η = 10% (**C,F**) η= 15%.

Chapter 5. Mean Scatterer Spacing Estimation in Normal and Thermally Coagulated Liver Tissue

5.1. Introduction

In this chapter, we continue the discussion presented in Chapter 4, with analysis and measurements of spectral coherence in *ex vivo* bovine liver before and after RF ablation. We assume a sound speed of 1540 m/s and apply both single-taper and multi-taper calculations. We also present water tank measurements of sound speed and the attenuation coefficient in *ex vivo* bovine liver and thermally coagulated *ex vivo* bovine liver. We then introduce sparse scattering ROI's into our simulations and incorporate the water tank measurements of sound speed and attenuation. Next, we examine MSS estimates in *ex vivo* bovine liver before and after thermal coagulation using saline bath heating. We compare features of the simulations with features of the *ex vivo* results. The data and many of the results in this chapter have been published in [118] and [164]

5.2. *Ex Vivo* RF Ablations: RF Data Acquisition

Five bovine livers were acquired from a slaughterhouse, and 23 tissue samples from among the five livers were excised for imaging. Samples were created by cutting a liver into small pieces approximately 3.5 × 6 × 6 cm. All procedures were performed within three days of acquiring the bovine liver. After preparation, a sample was placed on the holder shown in figure 5.1 (a) and immersed in physiological saline solution. Following this, the sample was placed in a vacuum chamber at a reduced pressure of 25 mm Hg for 15 minutes to remove any gas from the

tissue. After degassing, the tissue was placed in a water bath maintained at a constant temperature of 37° C for 30 minutes. An RF data set of the liver was then acquired.

The sample holder locked the specimen in place by allowing the insertion of two metal rods through the sample vertically. The sample holder also provided two openings for insertion of horizontal, staggered metal rods through its sides to ensure the imaging of the same plane, within the elevational resolution of the transducer. Each tissue sample was placed on top of a piece of rubber having a high absorption coefficient to avoid reverberations from the bottom of the container.

Following initial imaging of a sample, one RF ablated region was created in the imaging plane using an internally cooled CoolTip antenna with a 1 cm active region powered by a ValleyLab CoolTip RF generator. For each ablation, the power was set to 12 W for 8 minutes in a manual mode. These settings produced ablations that were roughly spherical and approximately 1-1.5 cm in diameter. Following ablation, the RF applicator was removed; tissue was again placed in physiological saline solution and degassed in a vacuum chamber at a pressure of 25 mm Hg for 15 minutes. Following the degassing, the sample holder was placed in the same water bath maintained at 37° C for 30 minutes. The samples remained in saline solution and a transducer was placed in a clamp and partially submersed in the saline solution while imaging was performed. The experimental set-up used is shown in figure 5.1 (b).

This procedure yielded 46 RF data sets. Twenty-three data sets were of the liver prior to RF ablation. The other 23 data sets were of identical imaging planes in the same sample of liver, but following RF ablation. One pair of ablated and unablated data sets was acquired from each bovine liver sample. Data sets were acquired using a clinical linear array transducer, the VFX

9L4, on the Siemens S2000 scanner (Siemens Ultrasound, Mountain View, CA, USA), at a transmit frequency of 6 MHz.

(A) **(B)**

Figure 5.1. (A) Tissue holder. **(B)** Tissue holder in water bath.

Identical imaging settings were used for each pair of data sets collected. In all data sets, the TGC was uniformly set to the minimum setting across the entire imaging depth. The focal depth was set such that the ablation was slightly deeper than the focus of the transducer. Across all cases this was a setting of 1 cm. The ablation was identified in B-mode imaging and registered by locating the fiducial markers. The presence of the ablation in the imaging plane was then also confirmed using acoustic radiation force imaging (ARFI), available on the ultrasound system, and gross pathology images.

5.3. *Ex Vivo* RF Ablations: Spectral Coherence

In this section we display the results of measurement of spectral coherence in the liver prior to and following RF ablation. We hypothesized that thermal ablation results in destruction of the portal triads and, therefore, a decrease in the periodic component of the ultrasound signal.

We also hypothesized that a MT estimator has the potential to detect coherent scattering more consistently than a ST estimator of coherence. In order to demonstrate this, we constructed a tissue classifier and performed an error rate analysis.

For the analysis, we selected an ROI from each of the 23 RF data sets before RF ablation and an ROI from each of the 23 RF data sets recorded following RF ablation. Figures 5.2a, 5.2b, 5.3a, and 5.3b demonstrate the selection of ROIs. The fiducial markers are clearly visible across the B-mode image as bright streaks. These markers were located prior to and following ablation within a sample. The ablation presented on the B-mode image as a slightly hyper-echogenic region showing a large amount of shadowing. In figure 5.2 (b) the shadowing is so extreme as to obscure the tip of the fiducial marker following ablation. We note that this indicates that attenuation is elevated to the point of obscuring the reflections that result from the huge impedance mismatch between the distal metal rod and the surrounding tissue. In addition to acoustic shadowing, we also confirmed the presence of the ablated region using ARFI and gross pathology, as delineation of the exact extent of the thermal ablation was difficult to determine from the B-mode image alone.

Analysis was performed for ROIs with two gate length dimensions: 5 mm axially by 5 mm laterally, and 7 mm axially by 5 mm laterally. The longer gate length was chosen as 7 mm because this was approaching the largest ROI that could be centered in an ablation having a diameter of 1 cm. The smaller ROI was chosen to be as small as possible while still containing several periodic scatterer pairs. At an assumed MSS of 1 mm, an axial ROI size of 5 mm is large enough to contain 5 scatterer pairs arranged in a column. Each ROI was selected such that for a pair of images obtained prior to and following ablation, the tissue region being analyzed was identical within the elevational width of an imaging plane and within the tissue volume changes

caused by the ablation procedure. The 5 mm long ROIs were manually selected, and the 7 mm long ROIs were obtained by extending the 5 mm ROIs by 1 mm on either side.

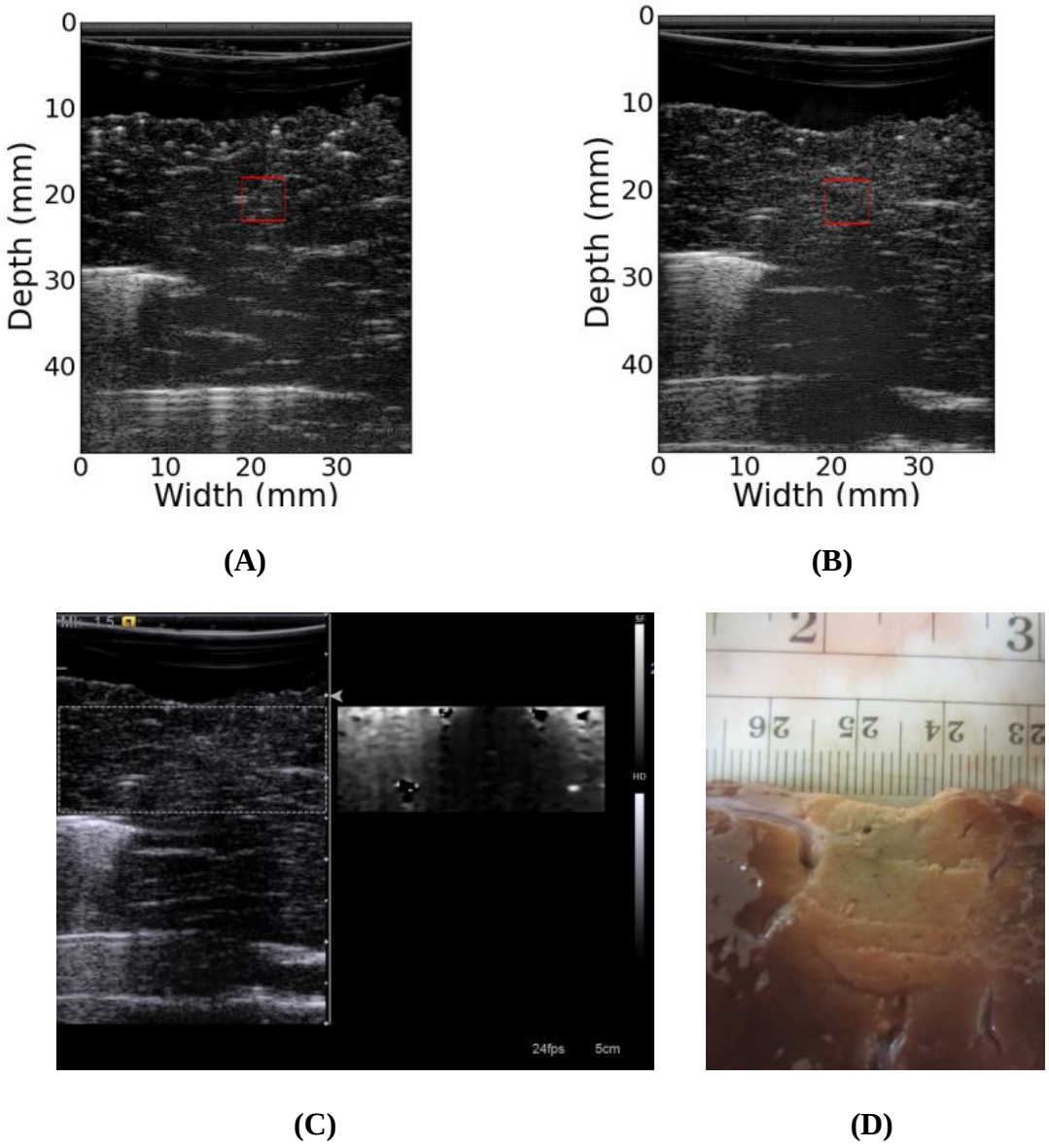

Figure 5.2. B-mode image of liver sample reconstructed from RF data prior to ablation (**A**) and following (**B**) ablation. Red box shows ROI used in calculations. (**C**) Clinical B-mode and ARFI image of thermal ablation (**D**) Optical (gross pathology) image of sample following thermal ablation.

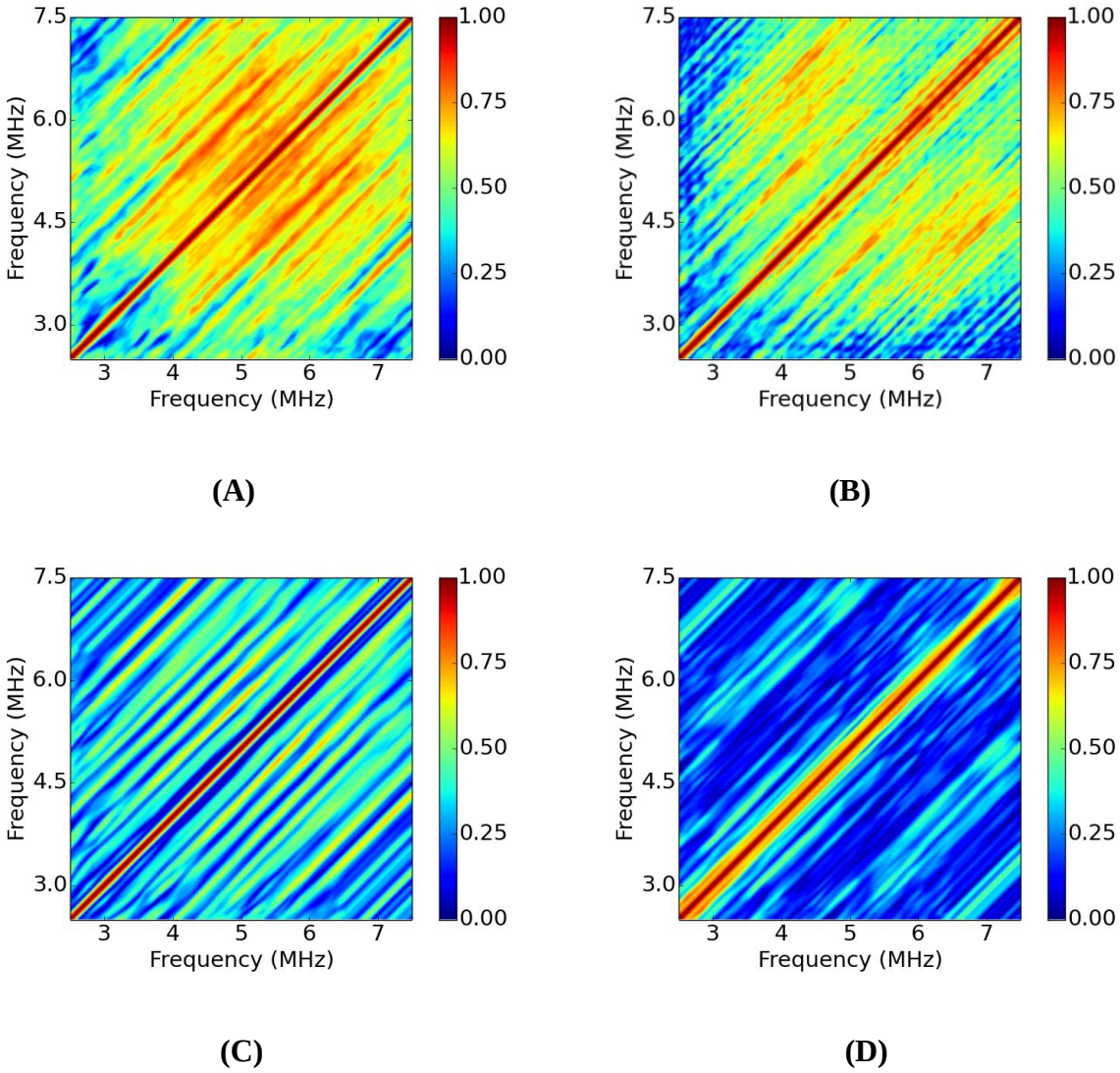

Figure 5.3. Coherence in ROI in figure 5.2 calculated using the MT method prior to (**A**) and following (**B**) ablation. Coherence obtained by the ST method using a Hann window prior to (**C**) and following (**D**) ablation.

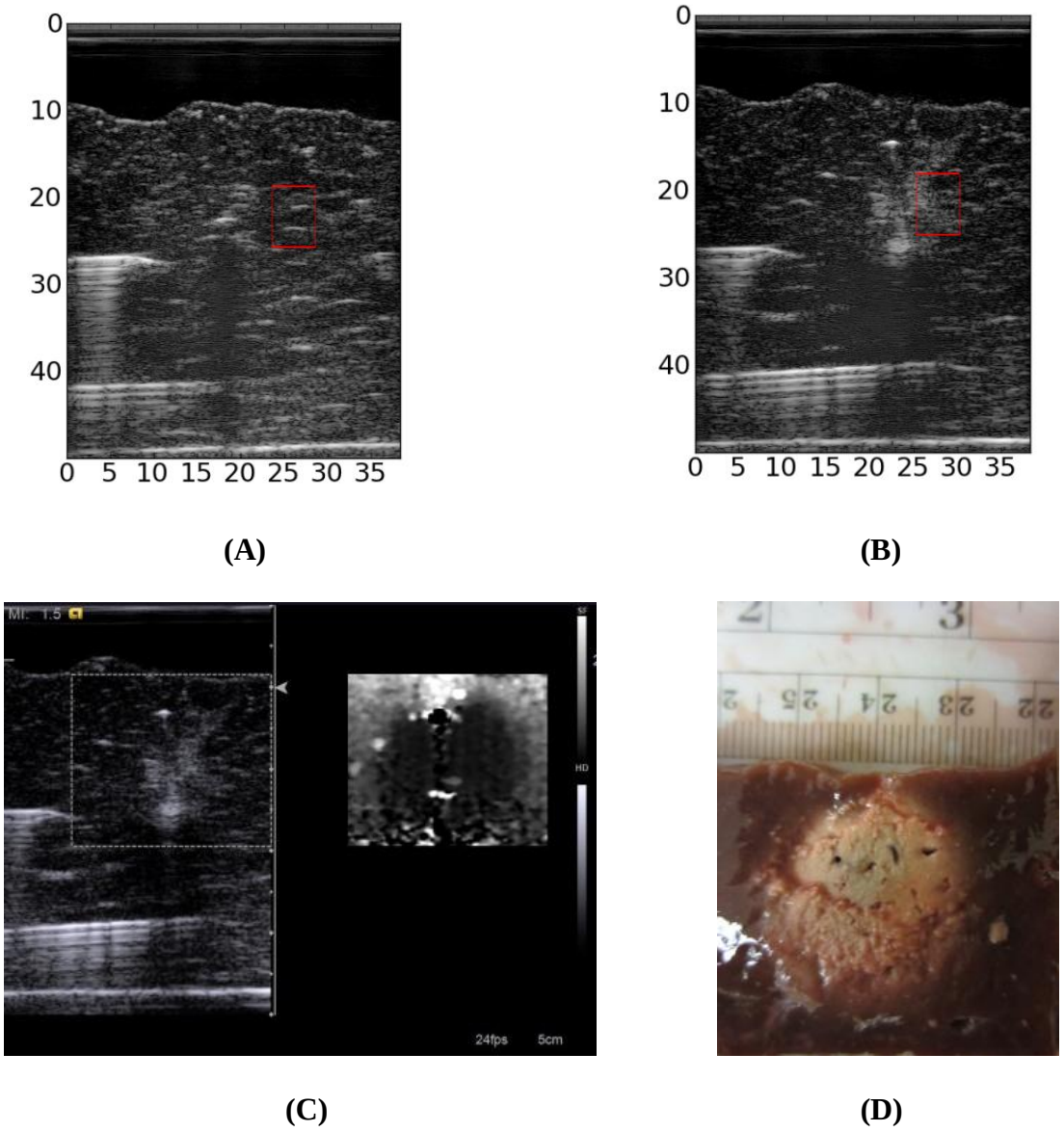

Figure 5.4. B-mode image of liver sample reconstructed from RF data prior to ablation (**A**) and following (**B**) ablation. Red box shows 7 mm long ROI used in calculations. (**C**) Clinical B-mode and ARFI image of thermal ablation (**D**) Optical image of sample following thermal ablation.

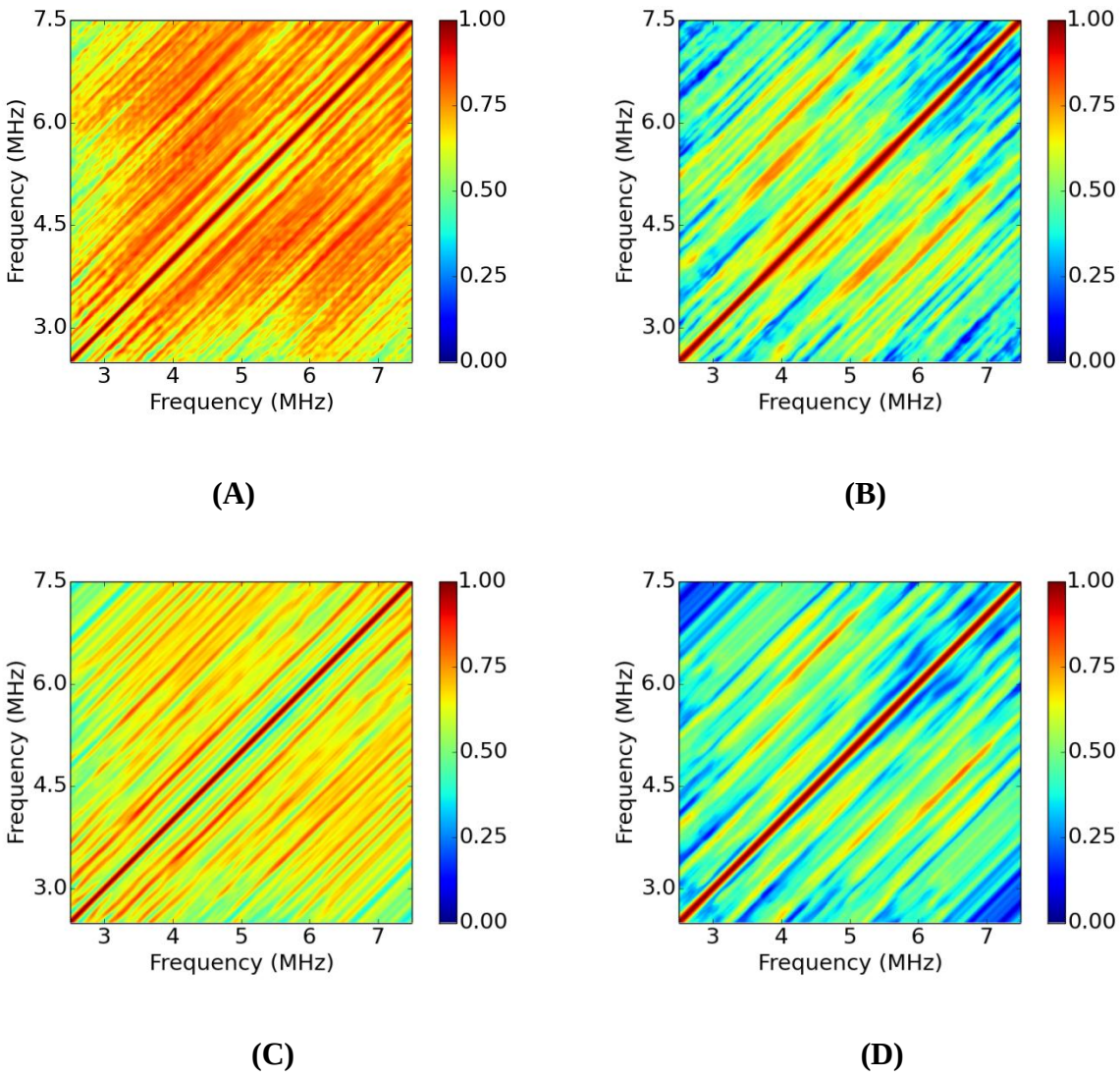

Figure 5.5. Coherence within the ROI in figure 5.4 calculated by the MT method prior to (**A**) and following (**B**) ablation. Coherence obtained by the ST method using a Hann window prior to (**C**) and following (**D**) ablation.

For each ROI, the center frequency of the received echoes was estimated by locating the maximum value of the power spectrum. At a 5 mm gate length, the mean estimated center frequency across all ROIs prior to ablation was 4.88 ± 0.34 MHz, and following ablation it was 4.66 ± 0.22 MHz. At a 7 mm gate length, the mean estimated center frequency across all ROIs

prior to ablation was 4.73 ± 0.23 MHz and 4.61 ± 0.21 MHz following ablation. The GS was calculated for each ROI over the frequency range of 2.5 to 7.5 MHz. This analysis bandwidth was chosen to fully capture the -20 dB bandwidth of each signal's power spectrum. We note that analyzing too large a region in the bifrequency plane isn't a significant issue, because spectral coherence tends to decrease as we move away from the zero frequency difference regions.

Coherence was computed within each of the ROIs prior to and following ablation. The pointwise mean and the pointwise standard deviation of coherence over all the ablated and unablated ROIs was computed in each frequency bin. The pointwise mean coherence prior to ablation was given by:

$$C_{pre}(f_1, f_2) = \frac{1}{N}\sum_{i=1}^{N} |C_i(f_1, f_2)| \tag{5.1}$$

In the equation above, N=23 was the number of ROIs, f_1 and f_2 ranged from 2.5 MHz to 7.5 MHz, and C_i is an estimate of coherence in the i^{th} ROI. The mean coherence following ablation was computed similarly and we denote it C_{post}. The standard deviation was computed according to:

$$C_{pre}(f_1, f_2) = \sqrt{\frac{1}{N-1}\sum_{i=1}^{N} (|C_i(f_1, f_2)| - C_{pre}(f_1, f_2))^2} \tag{5.2}$$

A tissue template was then constructed using Fisher's linear discriminant:

$$T = \frac{C_{pre} - C_{post}}{\sigma_{pre} + \sigma_{post}} \tag{5.3}$$

A score was then assigned to the speckle in each ROI by summing the coherence multiplied pointwise by the template. We display the templates that were created by each taper in Figures 5.6 and 5.7, respectively. Symbolically, for the i^{th} tissue sample we calculated the score S_i using:

$$S_i = \sum_{f_1=2.6}^{6.6} \sum_{f_2=2.6}^{6.6} |\gamma_i^c(f_1, f_2)| T(f_1, f_2) \quad \textbf{(5.4)}$$

We first discuss the claim that the received signal from ablated liver tends to exhibit a decreased coherent component relative to a signal from unablated liver. In figure 5.3 and figure 5.5 we show examples of coherence calculations corresponding to the ROIs shown in figure 5.2 and figure 5.4. Figure 5.3 demonstrates a calculation with a 5 mm ROI, while figure 5.5 demonstrates a calculation with a 7 mm ROI. In both figures, we show the coherence prior to ablation and following ablation. Across both ROIs shown, note that regardless of the calculation method the coherence decreases throughout the bi-frequency plane from its value prior to ablation. The tissue templates confirm this result across the ROIs investigated, as shown in figure 5.6 and figure 5.7. At this point, we remind the reader that if the ultrasound signal can be modeled as a linear time-varying system, then the effect of computing spectral coherence and not the Loève spectrum is to effectively deconvolve the dependence of attenuation and beamforming from the calculation. Across both gate lengths, all the calculated templates showed large positive values throughout the bi-frequency plane, indicating that the unablated liver tissue tended to exhibit either periodic scattering or sparse scattering.

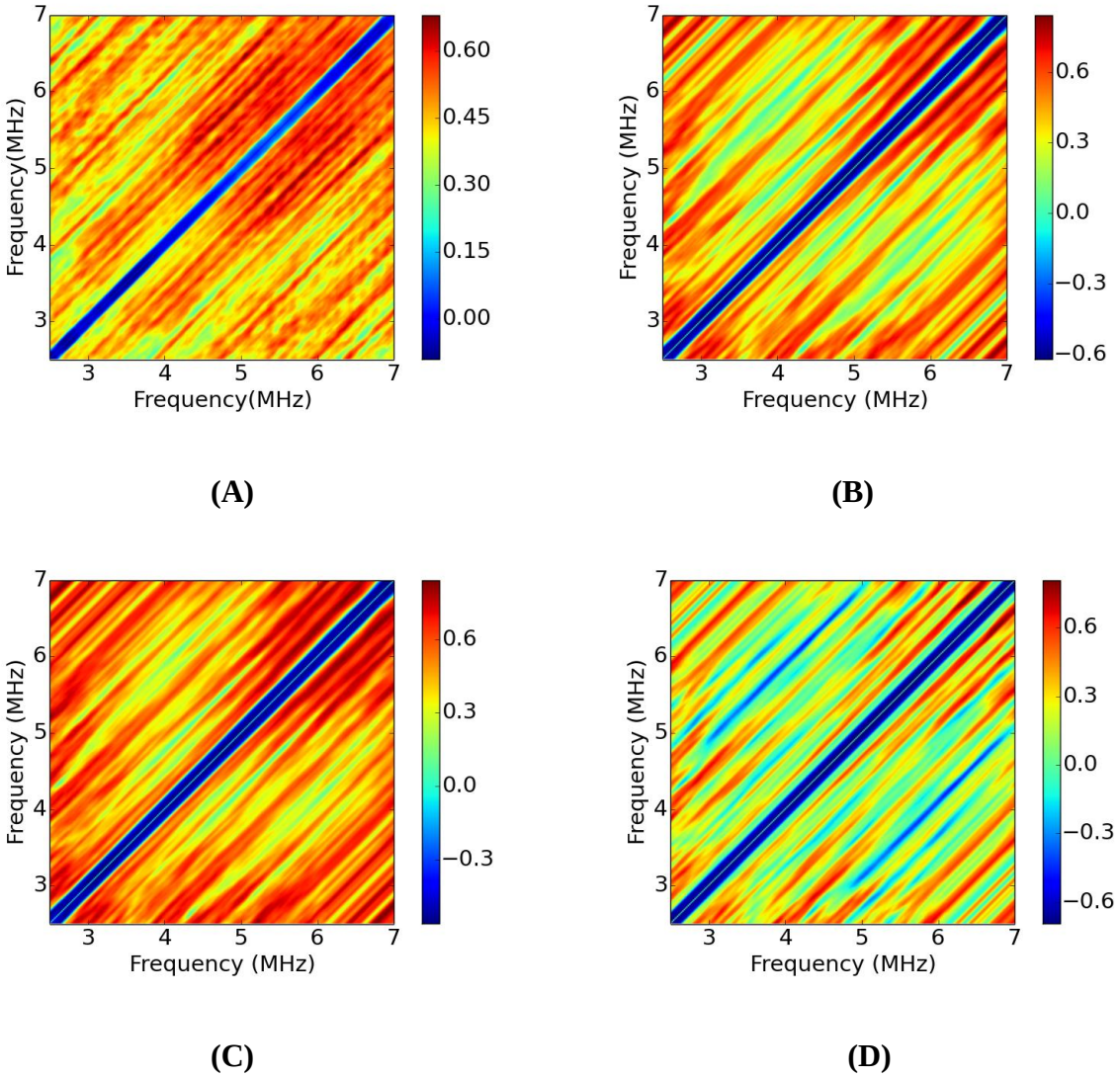

Figure 5.6. Templates created at a gate length of 5 mm by (**A**) MT method (**B**) Hann window (**C**) Hamming window (**D**) Blackman Harris window.

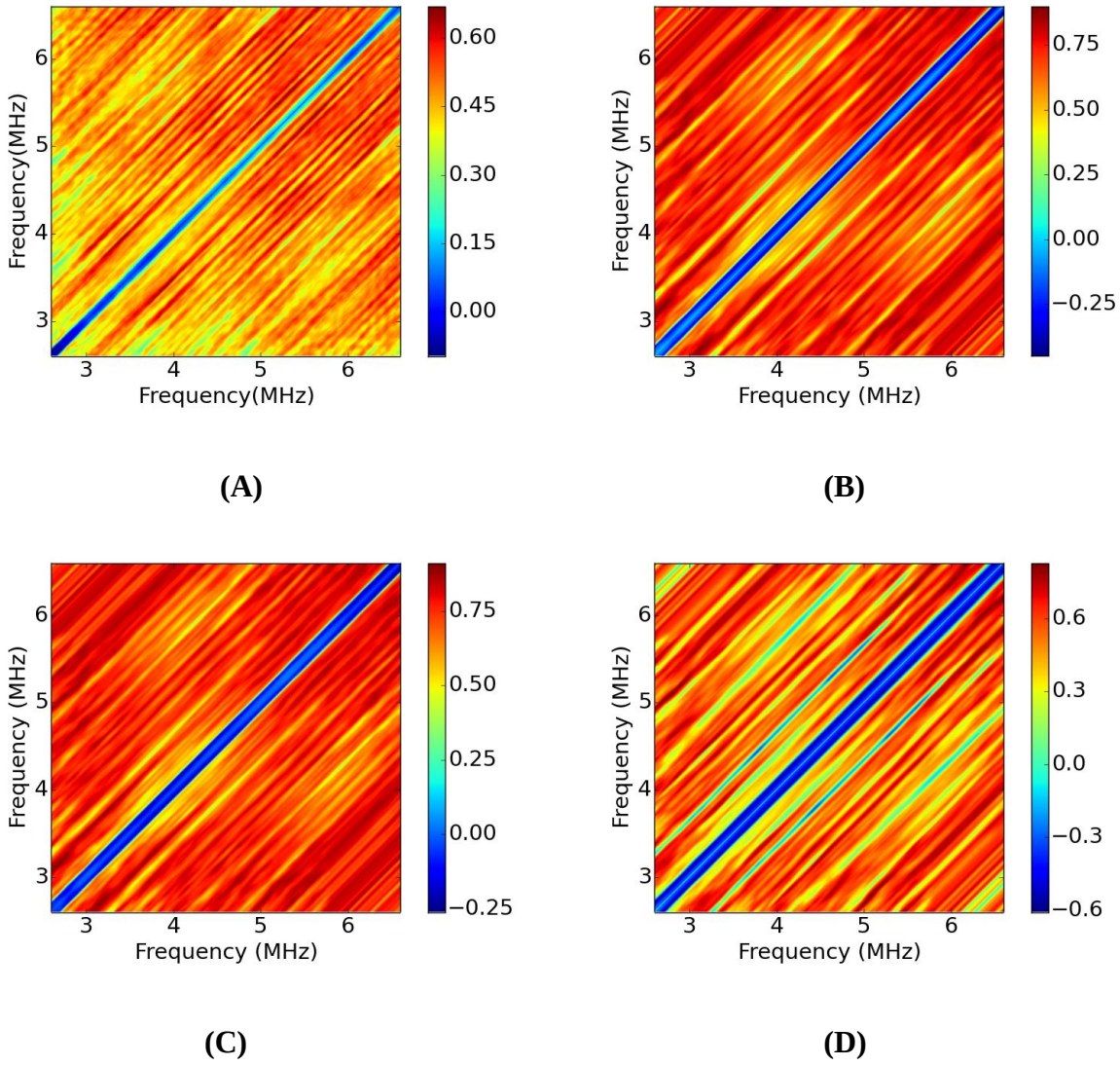

Figure 5.7. Templates created at a gate length of 7 mm by (**A**) MT method (**B**) Hann window (**C**) Hamming window (**D**) Blackman Harris window.

In tables 5.1 and 5.2, we display the minimum classification error achieved by a tissue classifier constructed from each tissue template. Classifiers were generated by varying a threshold on the score computed from equation 5.3, and labeling tissue as positive for liver and negative for ablation. A true positive in this case was liver prior to ablation exhibiting a large amount of coherence. A false positive was thermally ablated liver tissue whose received echoes

possessed a large amount of coherence. The analysis indicates that the MT method has the potential to outperform ST calculations in applications in liver tissue, with a minimum error rate of only 6.5% for the 5 mm gate length and a minimum error rate of 13.0% for the 7 mm gate lengths. We note that increasing the gate length consistently improved the error rate for all ST calculation methods, while the MT calculation showed a slightly worse error rate at a longer gate length. This is probably because at a longer gate length spectral blurring by the Dirichlet kernel is less pronounced, so increasing the gate length lessens the impact of the improvement from multi-tapering, while increasing the chance that the scattering distribution is no longer the same throughout the gate length. When looking at a 7 mm by 5 mm ROI in a very small RF ablation there is a good chance that regions in the ROI near the periphery of the ablation received a smaller thermal dose than regions in the ROI near the center of the ablation.

We note that the tissue templates shown in Figs. 5.6 and 5.7 do not show a single dominant peak and an MSS that can be used to distinguish between thermally coagulated tissue and normal bovine liver. Therefore, we have not demonstrated anything essential about periodicity of thermally ablated tissue and liver in this section. Spectral coherence can result from two kinds of signals: periodic signals and aperiodic signals that result from low scatterer number density tissue. Donohue *et al*. in [165] show that the mean value of spectral coherence increases as the number density of aperiodic scatterers decreases below approximately 10 scatterers per resolution cell. Our templates show that average spectral coherence was elevated in the liver prior to ablation. These results could be interpreted to say that both liver and ablation are aperiodic, but they should be modeled with different scatterer number densities. In the remainder of the sections of this chapter, we will demonstrate that the liver has quasi-periodic scattering while thermally coagulated tissue is better modeled as aperiodic.

Table 5. 1. Minimum classification error for tissue classifiers at a 5 mm gate length.

Method	Ablated Tissue with High Coherence	Unablated Tissue with Low Coherence	Total Errors (%)
Hann	10	4	30.4%
Hamming	4	9	28.2%
Blackman Harris	9	2	23.9%
MT	1	2	6.5%

Table 5.2. Minimum classification error for tissue classifiers at a 7 mm gate length.

Method	Ablated Tissue with High Coherence	Unablated Tissue with Low Coherence	Total Errors (%)
Hann	0	8	17.4%
Hamming	0	6	13.0%
Blackman Harris	5	6	23.9%
MT	2	4	13.0%

5.4. RF Data Acquisition of *Ex Vivo* Tissue Coagulation in a Heated Saline Bath

We also estimated spectral coherence in *ex vivo* beef liver at room temperature and in *ex vivo* beef liver at room temperature following delivery of a uniform thermal dose from saline bath heating. In these experiments, the goal was to establish MSS in *ex vivo* bovine liver and thermally coagulated *ex vivo* bovine liver using large homogeneous sections of tissue. Radiofrequency data were acquired using the VFX 9L4 transducer and the Siemens S2000 system (Siemens Medical Solutions, Mountain View, CA) in five independent *ex vivo* bovine livers and another five independent thermally coagulated *ex vivo* bovine livers. For all *ex vivo* measurements described in this section, we placed the tissue sample in a saline bath maintained

at room temperature, 22° C. The liver tissue was obtained from a slaughterhouse and all measurements were made within 12 hours of animal sacrifice. Within 45 minutes of animal sacrifice, the liver was transported to the laboratory, and was refrigerated until a portion of it was sectioned. The portion of liver was then placed in the saline bath where it was allowed to warm to room temperature. Prior to imaging, tissue was degassed by placing the tissue within the saline bath into a vacuum chamber under a pressure of 25 mm Hg for 15 minutes. In order to thermally coagulate the bovine liver, tissue was placed in an additional saline bath maintained at 80° C for 45 minutes. Over this amount of time, the tissue visibly changed color and became much stiffer as confirmed by manual palpation. The coagulated tissue was returned to its original saline bath at room temperature and degassed prior to imaging.

In these experiments a deeper focus was desired than the shallow focus used in section 5.2 and 5.3. For imaging bovine liver and thermally coagulated tissue, a plastic bag containing an ethylene glycol and water offset was placed between the transducer and the tissue. An ethylene glycol and water solution was used to match the liver sound speed, which we discuss in the following section. The offset was utilized to increase the imaging depth to the point where a second row of elements on the VFX 9L4 transducer activated to assist with elevational focusing. The ethylene glycol concentration was adjusted, along with the beamformer sound speed, until a sound speed of 1600 m/s was achieved for the liver offset, and a sound speed of 1590 m/s was achieved for thermally coagulated liver offset. For a sound speed of 1600 m/s, a volume fraction of 18.2% ethylene glycol was used, and a volume fraction of 16.6% ethylene glycol was used for a sound speed of 1590 m/s. B-mode images of normal and uniformly thermally coagulated liver are shown in figure 5.8. The dark region in the image corresponds to the fluid offset between the tissue and the transducer. For measurements in large homogeneous regions of tissue we fixed the

lateral extent of our ROI at 12 mm. We varied the axial extent of the ROI from 12 to 18 mm. We refer to the axial extent of the ROI as the gate length or window size. The maximum gate length selected was chosen such that a homogenous region could consistently be imaged.

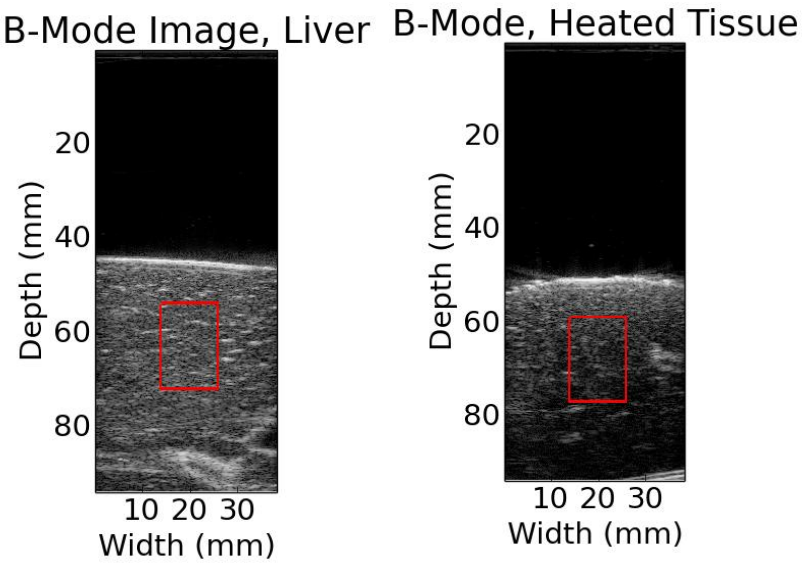

(A) **(B)**

Figure 5.8. B-mode images of **(A)** ex vivo liver and **(B)** uniformly thermally coagulated ex vivo liver. The dark region corresponds to the water/ethylene glycol offset.

5.5. Through Transmission Sound Speed and Attenuation Measurements in *Ex Vivo* Bovine Liver

Sound speed measurements were made using a through transmission substitution method applied to five independent samples of normal liver and five independent samples of thermally coagulated liver tissue. By independent, we mean that each tissue sample came from a separate

animal. All these livers were from separate animals from the livers mentioned in section 5.3. The sound speed of a sample, c_s, was estimated using the following equation:

$$c_s = \frac{c_w}{1 + \frac{c_w \Delta t}{d}} \quad \textbf{(5.5)}$$

In equation 5.5, c_w is the sound speed of water, d is the sample thickness, and Δt is the difference in arrival time with the sample inserted between transmitting and receiving transducers and with the sample absent. The temperature dependent sound speed of water, c_w, was given by the formula of Kaye and Laby [166]*:*

$$c_w = 1402.9 + 4.835T - 0.047016T^2 + 0.00012725T^3 \text{m/s} \quad \textbf{(5.6)}$$

The water in the tank was maintained at room temperature, 22° C. All sample thicknesses, d, were sliced to be equal to 2.6 cm. Three sound speed measurements were made for each sample using three transducers operating at center frequencies of 2.2, 3.2, and 5.20 MHz, respectively. For each transducer, a 5 cycle burst was generated using a function generator. The shift in the location of the third peak in the burst was tracked following insertion of the sample between the transmitting and receiving transducers to compute Δt. Over the 15 measurements (3 frequencies by 5 samples) the sound speed in *ex vivo* bovine liver was estimated to be 1599.9 ± 6.4 m/s and the sound speed in thermally coagulated *ex vivo* bovine liver was estimated to be 1591.6 ± 5.5 m/s. For through transmission measurements, samples were placed into a holder having a hockey puck shape where each face of the hockey puck was made from Saran™ wrap. Tissue density was estimated by weighing the volume of tissue contained in the cylindrical hockey puck container, and dividing that mass by the volume of the hockey puck container.

Table 5.3. Sound speed and density measurements in five ex vivo bovine liver samples.

Sample No	c (m/s), f_c = 2.2 MHz	c (m/s), f_c = 3.2 MHz	c (m/s), f_c = 5.2 MHz	ρ (g/cm^3)
1	1589.9	1589.9	1590.7	1.10
2	1607.6	1601.3	1610.7	1.13
3	1598.1	1597.3	1605.1	1.11
4	1603.0	1592.9	1601.5	1.14
5	1594.7	1592.8	1593.8	1.09

Table 5.4. Sound speed and density measurements in five coagulated ex vivo bovine liver samples.

Sample No	c (m/s), f_c = 2.2 MHz	c (m/s), f_c = 3.2 MHz	c (m/s), f_c = 5.2 MHz	ρ (g/cm^3)
1	1581.6	1584.5	1583.2	1.079
2	1591.9	1597.1	1591.1	1.052
3	1588.9	1589	1590.5	1.042
4	1596.4	1589.8	1596.4	1.102
5	1601.1	1596.0	1596	1.075

Additionally, we estimated a linear attenuation coefficient for each of the five samples. It was assumed for these measurements that the linear attenuation coefficient had an intercept of 0 so that the frequency dependent attenuation was given by: $\alpha(f) = \beta f$. The attenuation coefficient measurements were performed using narrowband transmission of sinusoidal burst pulses (30 cycles) with an unobstructed path in the water tank between transmitter and receiver. The amplitude of the voltage on the receiver was measured before and after insertion of the sample. A frequency dependent correction to the attenuation coefficient for the saran layer covering tissue and keeping it in the holder was given by equation (3) in Wear *et al.* [167]. Measurements were recorded in frequency increments of 0.1 MHz. The same three transducers were used to perform the attenuation measurements. One transducer recorded measurements from 1.7 MHz to

3.2 MHz, a second transducer from 2.4 to 4.2 MHz, and finally the third transducer from 4.0 to 6.3 MHz, respectively. Overlapping measurements were averaged. The results of the attenuation measurements are reported in table 5.5. The average attenuation coefficient in liver was found to be 0.618 dB/cm MHz, and the average attenuation coefficient for thermally coagulated tissue was found to be 1.25 dB/cm MHz. The thermal dose received by the tissue due to the immersion for 45 minutes in high temperature saline solution roughly doubles the ultrasonic attenuation of the liver *ex vivo*.

Table 5. 5. Attenuation measurements in five ex vivo bovine liver samples and five ex vivo coagulated bovine liver sample. All measurements were made following tissue degassing.

Sample No	β (dB/cm MHz), *ex vivo* liver	β (dB/cm MHz), Coagulated liver	R^2, ex vivo liver	R^2, coagulated liver
1	0.54	1.15	0.967	0.986
2	0.68	1.30	0.970	0.953
3	0.67	1.32	0.971	0.972
4	0.64	1.26	0.900	0.967
5	0.56	1.22	0.987	0.979

5.6. Ultrasound Simulation of *Ex Vivo* Untreated Liver and *Ex Vivo* Thermally Coagulated Liver

Based on the measurements presented in section 5.4, we performed frequency domain simulations of quasi-periodic, diffuse, and sparse scattering in order to make comparisons with MSS estimates *ex vivo*. Guided by the results of section 5.2, we hypothesized that thermally coagulated tissue would be better modeled by a strictly aperiodic collection of scatterers, while liver could be modeled as quasi-periodic. For all simulations, we modeled a linear array

transducer having an aperture of 128 elements, each one being 0.2 mm wide laterally and 10 mm wide elevationally. The simulated transducer had a lateral and elevational focus occurring at a depth of 30 mm. We simulated a transmit pulse centered at 5.0 MHz and having a -10 dB bandwidth of 2.0 MHz. For all scatterers, we utilized a frequency dependence of f^2 for the scattering amplitude (yielding a backscatter coefficient with a frequency dependence of f^4).

We simulated two kinds of ROI's to model the liver: diffuse plus periodic scattering, and diffuse plus sparse dominant scattering. To achieve diffuse scattering, a numerical phantom contained 32 uniformly randomly distributed scatterers/mm^3. To simulate periodic scatterers we also included a column of Gamma distributed scatterers along the lateral and elevational center of the simulated beamline as in the simulations of chapter 4. These Gamma distributed scatterers had an MSS of 1.3 mm and a fractional standard deviation in the spacing of 12%. The scattering amplitude for any given periodic scatterer was multiplied by a random constant over all frequencies selected from a Gaussian distribution centered at 300 with a standard deviation of 50. To create sparse dominant scattering, three scatterers were added to a phantom. One was added between a depth of 20 and 50 mm, another between a depth of 30 and 40 mm, and another between a depth of 30 and 50 mm. These scatterers were spatially uniformly distributed and their scattering amplitude was multiplied by a constant value selected from a Gaussian distribution with a mean of 50 and a standard deviation of 10.

We also simulated two kinds of ROI's in ablated tissue: diffuse only, and diffuse plus sparse dominant scatterers. These ROI's were created the same way as in the simulated liver tissue. For the simulations, we neglected the small sound speed difference between thermally coagulated liver tissue and normal liver tissue. We assumed a sound speed of 1600 m/s throughout all simulations. For ROI's representing normal liver, a linear attenuation coefficient

with an attenuation slope of 0.5 dB/cm MHz was assigned to each phantom. For ROI's representing thermally coagulated tissue a linear attenuation coefficient of 1.0 dB/cm MHz was used. These simulations capture the large attenuation differences exhibited between thermally coagulated liver and normal liver we estimated from the through transmission measurements.

5.7. MSS Estimation in *Ex Vivo* Liver Simulations

We simulated 12,000 independent signals from 12,000 numerical liver phantoms. 10,000 of these phantoms contained periodic and diffuse scatterers. 2,000 of these phantoms contained sparse and diffuse scatterers. We also simulated 12,000 independent signals from numerical thermally coagulated phantoms. 10,000 of these phantoms contained diffuse scatterers. 2,000 of these phantoms contained sparse and diffuse scatterers. All signals were gated, centered on a depth of 40 mm. MSS estimates were made by gating 12 or 16 mm of the randomly generated signals, computing spectral coherence, and detecting local maxima between a frequency range of f_1 = 2.8 to 7.0 MHz. Ten independent A-lines were used in each of the spectral coherence calculations. This yielded 1,200 MSS estimates in simulated liver tissue and 1,200 MSS estimates in simulated thermally coagulated tissue. Several examples of randomly generated signals are shown below in figure 5.9.

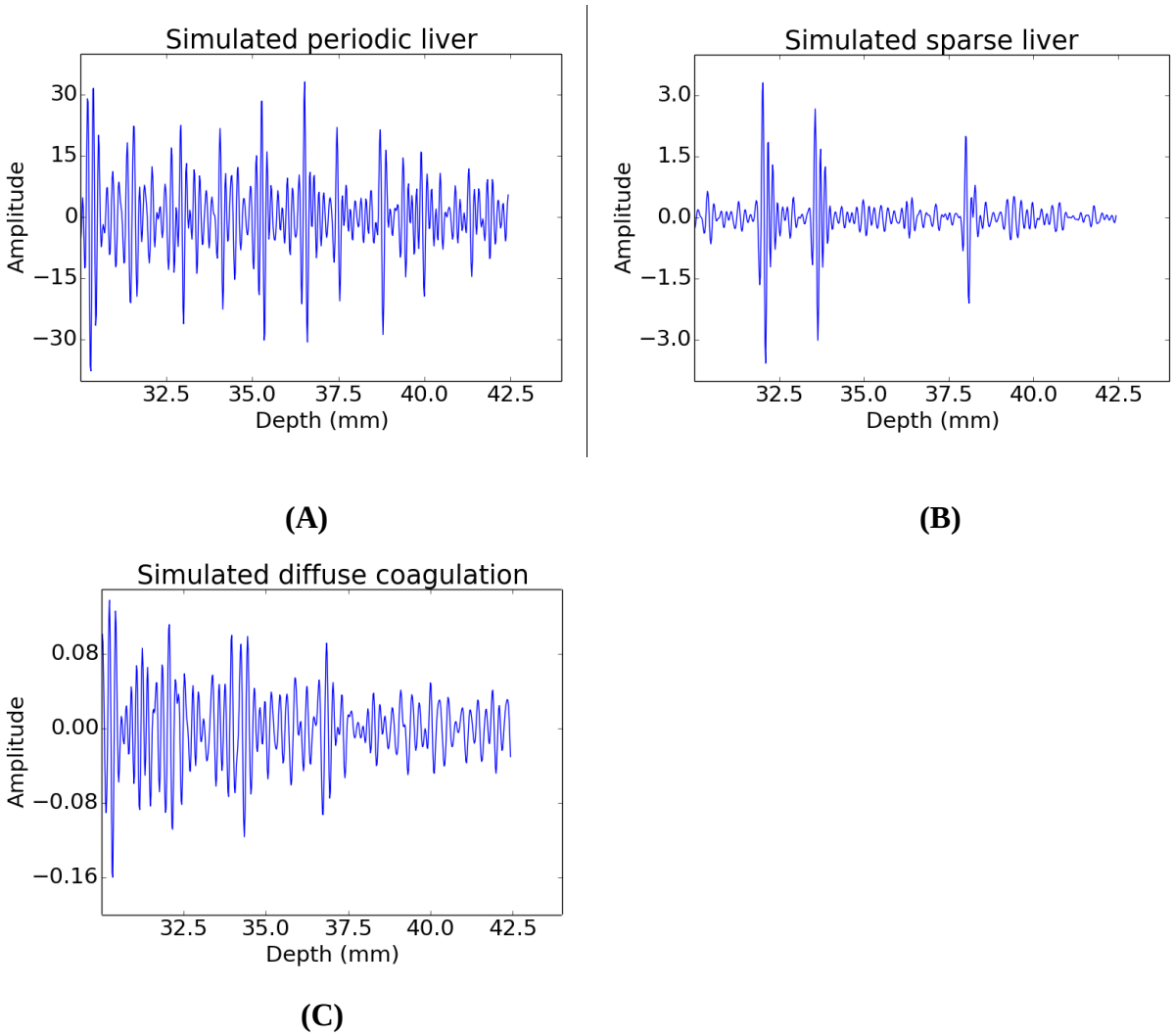

Figure 5.9. (A) A simulated periodic signal from the liver. **(B)** A simulated sparse signal from the liver. **(C)** A simulated diffuse signal from a thermal ablation.

We first consider the effect the inclusion of sparse ROI's has on the MSS estimates. We show histograms of MSS estimates in sparse ROI's in simulated untreated liver in figure 5.10. We note that the MSS estimates in sparse scattering ROI's show a significant probability mass across all possible MSS estimates for a given gate length. The histograms displayed in this chapter are meant to approximate a continuous probability density function, so their y-axes are displayed in units of density. This means that numerically integrating the density assigned to

each bin over all bins in any histogram displayed in this chapter yields a total probability mass of 1.0.

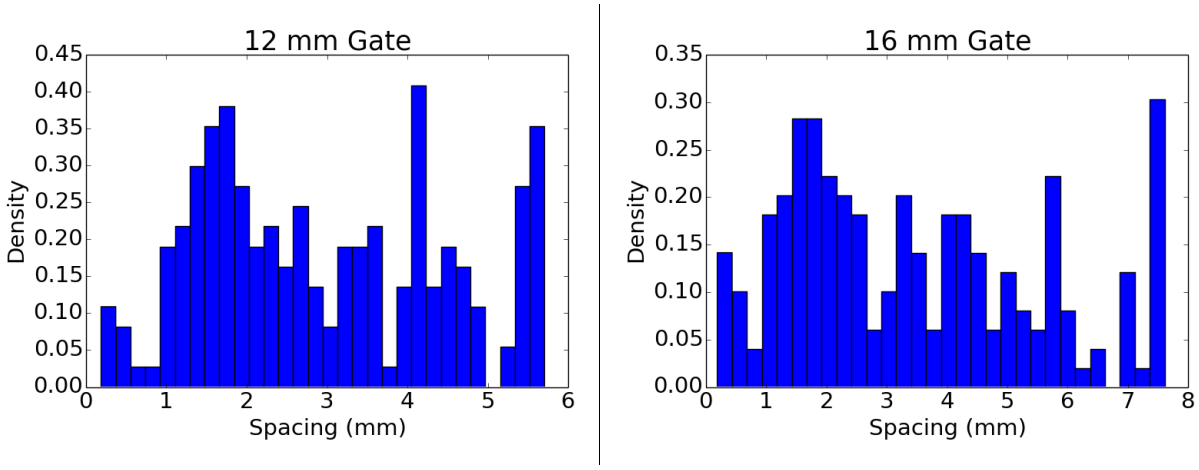

(A) **(B)**

Figure 5.10. Histograms of MSS estimates for sparse scattering ROI's in simulated liver for **(A)** 12 mm and **(B)** 16 mm gate lengths.

We display the results of the MSS estimation in all simulated untreated liver ROI's and all simulated coagulated ROI's as histograms in figure 5.11. We compute the mean, mode, and standard deviation of these measurements and display the results in table 5.6. The central MSS of the histogram bin with the highest number of counts was the initial estimate for the mode of the distribution. A parabolic fit was performed around the maximum peak, and sub-sample estimation was performed to refine the initial estimate of the distribution mode. This procedure is often used in estimating the cross-correlation peak with sub-sample precision in elastography [108], and we employed it with all estimates of histogram modes in this chapter.

Several results stand out. First, it is the mode of the MSS estimates which corresponds to the MSS of the periodic scatterers. Second, the mean of the measured MSS increases with increasing gate length. Finally, the mode of the estimated MSS in the simulated coagulated tissue

is less than one millimeter. The second result is due to the inclusion of the sparse scatterers, and the reason for the third effect will be discussed in a later section.

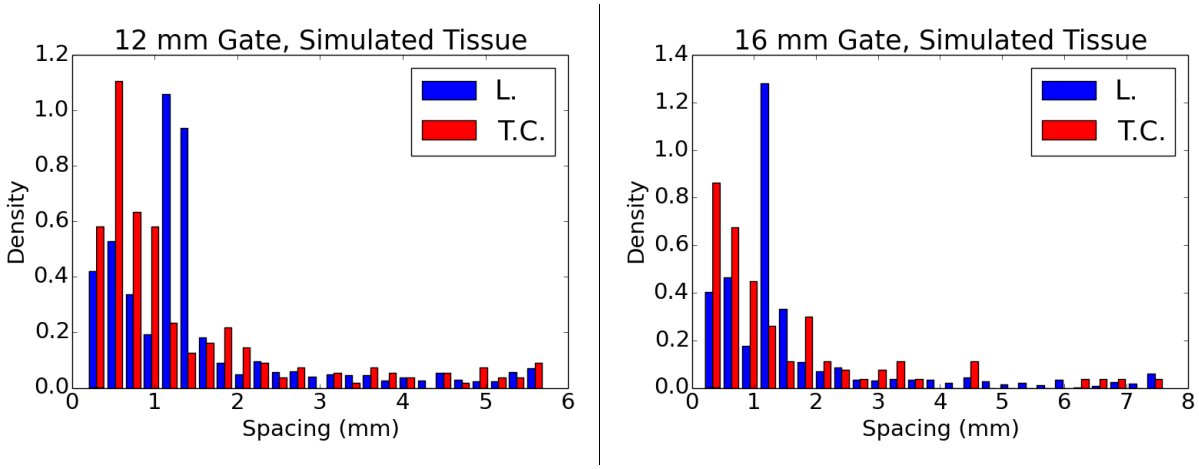

(A) **(B)**

Figure 5.11. Histograms of MSS estimates for simulated liver and thermally coagulated signals. Blue histogram bars represents simulated liver, while red histogram bars represent thermal coagulation. **(a)** 12 mm ROI. **(b)** 16 mm ROI.

Table 5.6. Parameters of estimated MSS distributions in simulated liver and simulated thermally coagulated tissue.

Gate length (mm)	Mean ± Std. Dev. in simulated liver (mm)	Mean ± Std. Dev. in simulated heated tissue (mm)	Mode in simulated liver (mm)	Mode in simulated heated tissue (mm)
12	1.49±1.19	1.25± 1.12	1.27	0.45
16	1.62±1.51	1.47±1.55	1.30	0.43

Note that the sparse scattering ROI's produce many of the spectral peaks corresponding to spacing's greater than 1.3 mm, making up the long tail of the estimated MSS distribution in both

simulated liver and simulated thermal coagulation cases. If the scattering in an ROI was sparse, a spectral peak will occur near the power spectrum, where the frequency difference between the f_1 and f_2 coordinates is almost zero. The MSS associated with these spurious peaks tends to be large, approaching half the gate length. The longer the gate length, the more severe is the effect of this error on shifting the mean of the estimated MSS distribution. This is why the mean MSS measurement is further from the true MSS at a 16 mm gate length than a 12 mm gate length.

5.8. MSS Estimation in *Ex Vivo* Bovine Liver

For the analysis, we estimated the MSS in normal *ex vivo* bovine liver across 1,647 ROI's (391,316,311,333, and 296 ROI's). We estimated MSS across 1,498 ROI's(250,286,317,330, and 315 ROI's) in thermally coagulated *ex vivo* bovine liver. Each ROI was selected from a separate imaging plane, and was separated from adjacent imaging planes by an elevational width of at least one mm. We varied the axial extent of an ROI from 12 mm up to 18 mm, in 2 mm increments. Local maxima were detected between a frequency range of f_1 = 2.8 to 7.0 MHz. In the analysis, we excluded regions containing large vessels with a diameter greater than 1.5 mm. This was done to exclude some specular scattering from the results. However, intermediate size vessels less than this diameter were allowed in the analysis.

An example image containing a vessel traversing the image laterally and having a 1 mm diameter is shown in figure 5.12 (a). Note that this results in specular scattering. We could have attempted to remove all specular scattering from the analysis, but it is not possible to do this just from examining the B-mode image. We demonstrate another ROI in figure 5.12 (c) resulting in a coherence peak near the power spectrum. This ROI is an example of sparse scattering. It contains a small number of aperiodic scatterers dominating the signal, and the MSS estimated from this

ROI is 6.34 mm. However, it would be extremely difficult to tell just from looking at the B-mode image whether this ROI should be labeled as sparse, periodic, or diffuse.

In figure 5.13 (a), we show an example of an ROI in untreated liver we may confidently consider quasi-periodic. Figure 5.13 (a) shows the B-mode image of untreated bovine liver, starting from a depth of 5 cm, and an 18 mm by 12 mm ROI. Figure 5.13 (b) shows the corresponding spectral coherence function. This ROI may be considered periodic because it exhibits a spectral peak corresponding to a scatterer spacing of 1.57 mm, which allows for a large number of scatterer pairs to be contained in the ROI. We contrast this for the sparse and specular cases, where the estimated MSS approaches half the gate length and allows only two scatterer pairs to be contained within the gated A-line segment. In addition to considering an upper limit on what should be considered a true periodicity, the results in thermally coagulated tissue also inform us that a lower limit on periodicity should also be considered. In figure 5.13 (d), we show a spectral coherence peak in thermally coagulated tissue occurring away from the power spectrum, corresponding to an estimated MSS of approximately 0.5 mm. Though we could also consider this ROI in thermally coagulated tissue periodic by the exact same criteria, we recall that an MSS of 0.5 mm was likely in simulated tissue even when no actual periodicity was simulated.

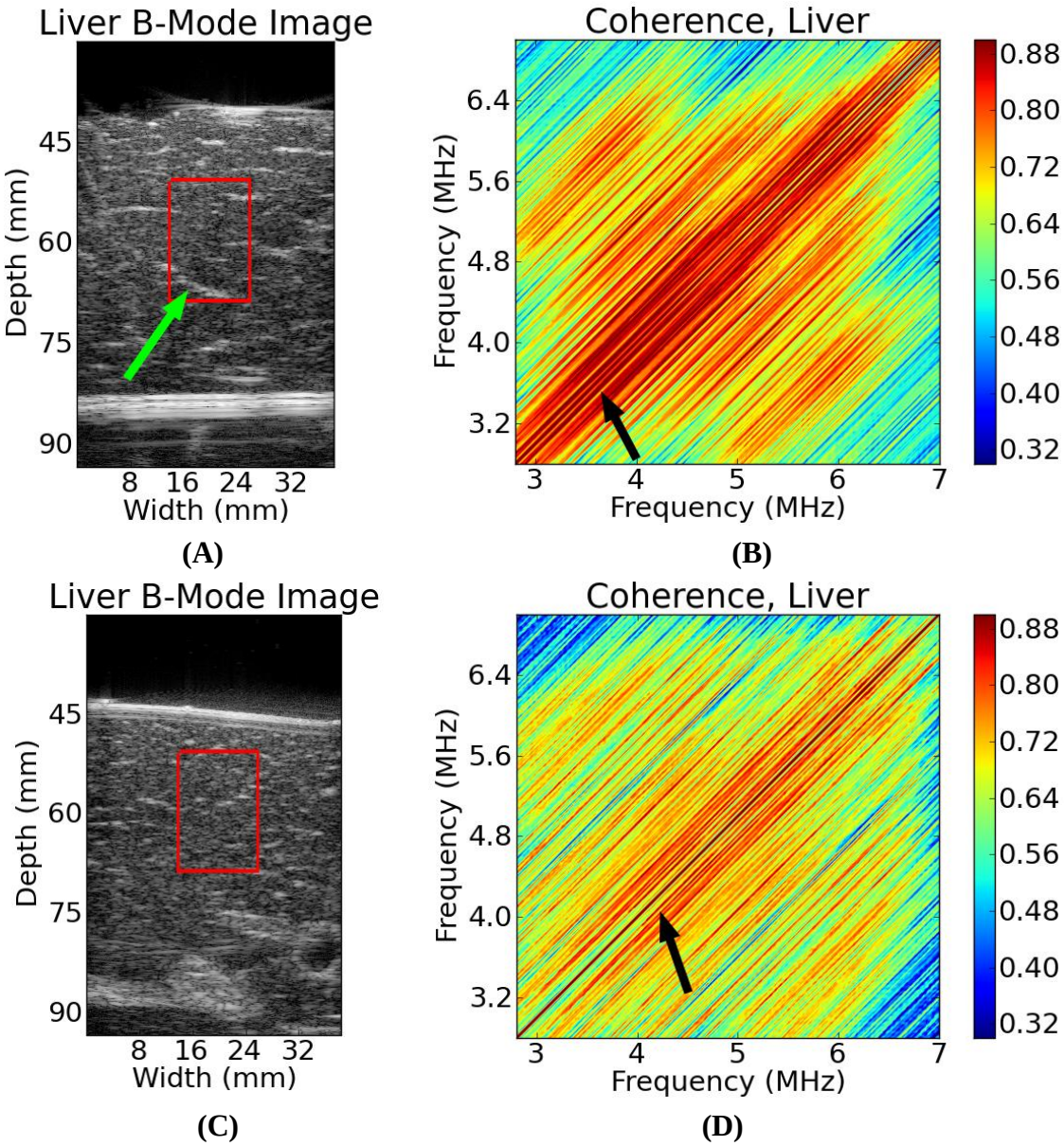

Figure 5.12. (A) B-mode image demonstrating liver tissue exhibiting specular scattering. Green arrow indicates approximate depth of specular scattering surface. Red box indicates analysis ROI. **(B)** Corresponding spectral coherence function with local maximum near power spectrum, denoted by black arrow. **(C)** B-mode image demonstrating sparse scattering. Notice isolated bright points within the ROI. **(D)** Corresponding spectral coherence function with local maximum near power spectrum, corresponding to an MSS of 6.34 mm, denoted by black arrow. Note that this large an MSS is likely not a true periodicity.

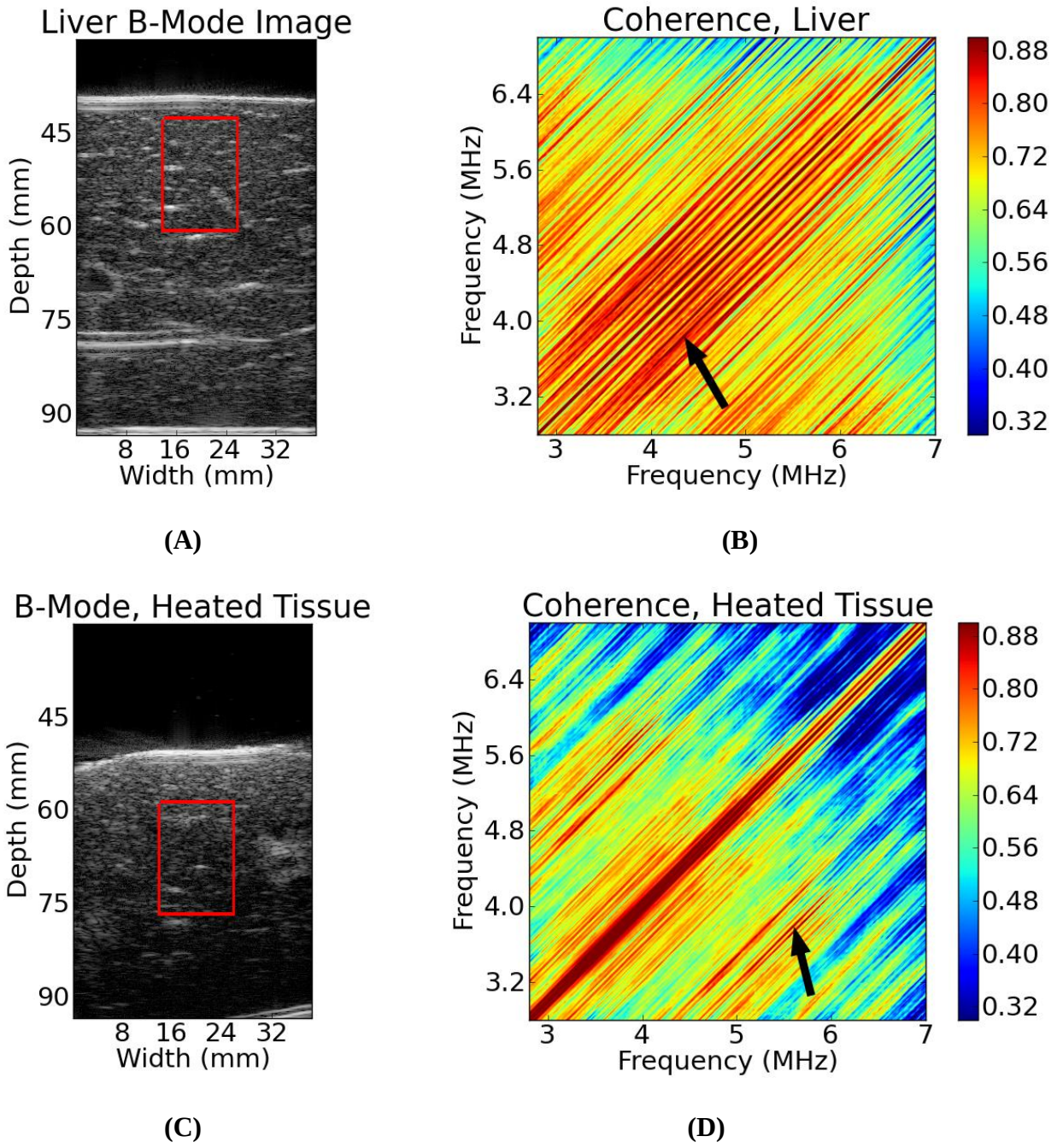

Figure 5.13. (A) 18 mm by 12 mm ROI in ex vivo bovine liver. **(B)** Corresponding spectral coherence function. Arrow identifies a spectral peak corresponding to an MSS of 1.29 mm **(C)** 18 mm by 12 mm ROI in thermally coagulated ex vivo bovine liver. **(D)** Corresponding spectral coherence function. Arrow identifies a spectral peak corresponding to an MSS of 0.5 mm.

Figure 5.14 shows histograms of the resulting MSS estimates in the unheated bovine liver, and the histograms of MSS estimates in the thermally coagulated liver. We present these results in order to show that the estimator for the MSS is biased, and that the bias depends on the gate length. We display the estimated mean, standard deviation, and mode of the estimated MSS in table 5.7. Table 5.7 demonstrates that the mean and standard deviation of the MSS estimates in both liver and thermally coagulated tissue is dependent on the signal processing parameters. At a gate length of 12 mm, the mean of the MSS estimates in the liver was 2.45 mm, while at a gate length of 18 mm the mean of the MSS estimates was 3.06 mm. In the thermally coagulated liver tissue, the mean of the MSS estimates was 2.31 mm at a gate length of 12 mm, and it was 3.01 mm at a gate length of 18 mm. Additionally, the mode of the MSS estimates in the thermally coagulated tissue showed large fluctuations between 0.45 mm and 1.0 mm as the gate length was varied. In the case of the normal liver, the estimated MSS showed a consistent mode varying only between 1.25 mm and 1.37 mm. We demonstrated that in the case of our numerical phantoms the mode was what corresponded to the true MSS of the periodic scatterers.

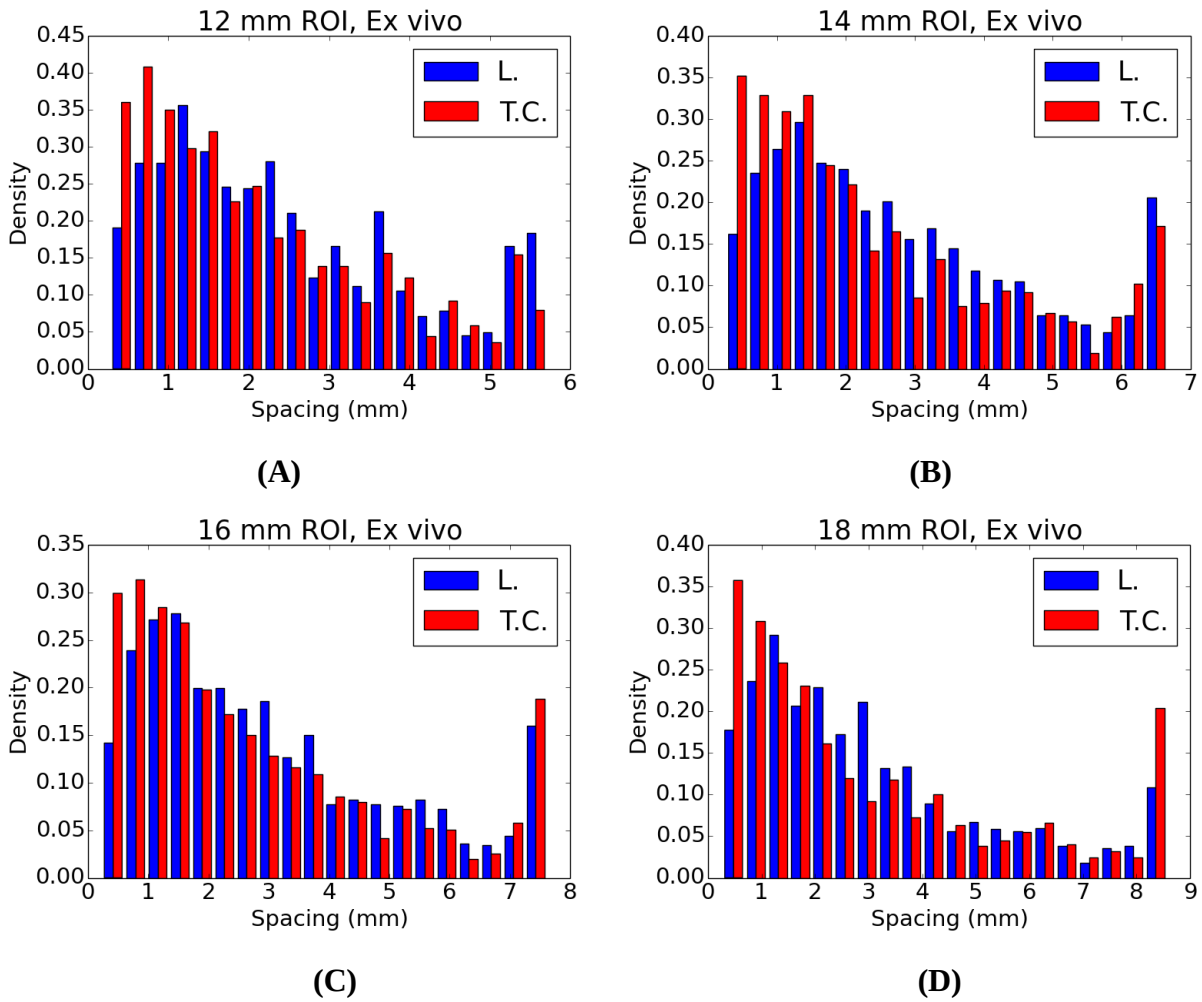

Figure 5.14. Histogram of MSS estimates in liver and thermally coagulated tissue as gate length is varied over **(a)** 12 mm, **(b)** 14 mm, **(c)** 16 mm, **(d)** 18 mm.

Table 5. 7. Parameters of estimated MSS distributions in liver and thermally coagulated tissue.

Gate length (mm)	Mean ± Std. Dev. of MSS estimates in liver (mm)	Mean ± Std. Dev. of MSS Estimates in coagulated tissue (mm)	Mode of MSS estimates in liver (mm)	Mode of MSS estimates in coagulated tissue (mm)
12	2.45±1.51	2.31± 1.63	1.25	0.84
14	2.78±1.75	2.48±1.86	1.35	0.45
16	3.00±2.01	2.74±2.11	1.37	1.00
18	3.06±2.15	3.01±2.50	1.27	0.53

5.9. MSS Estimation and Sampling Effects

This section demonstrates why diffuse scattering tends to result in spectral coherence peaks corresponding to sub-millimeter spacing's. When computing the spectral coherence function, we discretely sample this function over an evenly spaced grid with respect to frequency. This means that larger spacing's are coarsely sampled, while small spacing's are finely sampled. A plot of MSS bin width versus estimated MSS is shown in figure 5.15.

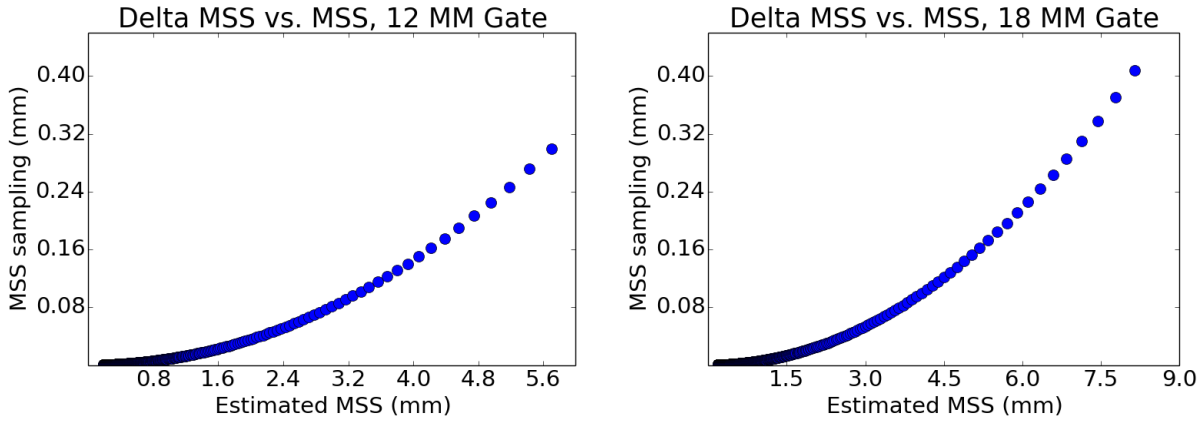

(A) **(B)**

Figure 5.15. Estimated MSS resulting from frequency differences present in the discretely sampled bifrequency plane, assuming a sound speed, 1590 m/s, sampling frequency, 40 MHz, and square region 2.8 MHz to 7.0 MHz. **(A)** 12 mm gate. **(B)** 18 mm gate.

This figure plots the MSS bin width corresponding to spacing's derived from the frequency differences present in the discretely sampled bifrequency plane over the square region from (2.8 MHz, 2.8 MHz) up to (7.0 MHz, 7.0 MHz). We also assume a gate length of 12 mm or 18 mm, a sampling frequency of 40 MHz, and a sound speed of 1590 m/s. These parameters are identical

to the thermally coagulated liver case. With these settings, the smallest possible MSS that could result from a spectral peak in this region of the bifrequency plane corresponds to an MSS of 0.19 mm. The plots demonstrate that there is a much smaller spacing difference between diagonally adjacent peaks corresponding to an MSS under one millimeter than between adjacent spectral peaks corresponding to an MSS over one millimeter. If a spectral coherence function was a random uniformly distributed two-dimensional function this sampling effect would favor the smallest spacing's, tending towards 0.19 mm.

Additionally, the frequency axes are rotated 45 degrees with respect to lines of constant frequency difference and constant scatterer spacing. This means that spectral coherence is calculated over shorter lines of constant scatterer spacing or constant frequency difference as the scatterer spacing gets smaller. If spectral coherence was a uniformly distributed random two-dimensional function the effect of the estimation region shape would be to favor the largest scatterer spacing's.

Now let us consider the expected result if spectral coherence were a uniformly distributed, randomly generated function. In figure 5.16, we show the resulting MSS distribution if the spectral coherence function is a randomly generated function whose pixels are uniformly distributed. This shows that if a spectral peak was equally likely anywhere in the bifrequency plane, with the constraint that no peak may occur too close to the power spectrum, the two competing sampling effects favor a small spacing between 0.5 mm and 1.0 mm.

The actual estimated MSS distribution shown in figure 5.14 demonstrates a heavier tail favoring larger spacing's than what is expected from the considerations in this section. This is because, for diffuse scattering, the spectral coherence function tends to decay as one moves away from the power spectral region of zero frequency difference.

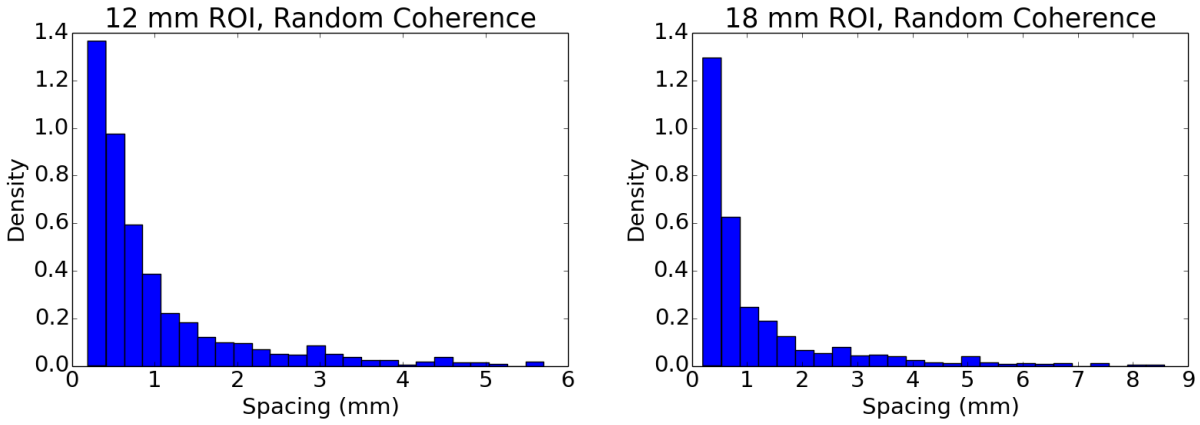

(A) **(B)**

Figure 5.16. Estimated MSS distribution, with each pixel value in the bifrequency plane given by a uniformly distributed random variable. Signal processing parameters were identical to those used when analyzing thermally coagulated tissue. **(A)** 12 mm gate length. **(B)** 18 mm gate length.

5.10. MSS Estimation with Transducers at Different Center Frequencies

In addition to the previously described RF data from the 9L4 transducer, RF data from another 5 independent *ex vivo* bovine livers were recorded with both the 4V1 (315, 312, 295, 340, and 331 imaging planes respectively) and 18L6 transducers (325, 306, 284, 307, and 216 imaging planes respectively). The 4V1 transducer is a phased array transducer operating at a nominal center frequency of 4.0 MHz. The VFX 9L4 transducer is a linear array probe operating at a nominal center frequency of 6.0 MHz and the 18L6 transducer is a linear array probe operating at a nominal center frequency of 10.0 MHz. By the nominal center frequency, it is meant that this is the center frequency that we selected for each of these probes from the center frequency setting on the Siemens S2000 research interface. We show example B-mode images

side-by side in figure 5.17. For the 4V1 transducer the frequency range examined was 1.5 MHz to 4.5 MHz and for the 18L6 transducer the frequency range examined was 4.0 to 8.0 MHz. A histogram of MSS estimates over all ROI's with an 18 mm gate length is pictured in figure 5.18. The mode of our MSS estimates ranges from 0.88 to 1.27 across different center frequencies.

The variability in the MSS estimate across transducers with different center frequencies is higher than it was across different gate lengths with a single transducer. There are several reasons this could be the case. First, MSS may actually vary slightly as the center frequency of the transducer is changed. As discussed in chapter 1, the microvasculature of the liver exists across a range of size scales with slightly different spacing's, and differences in which size vessels reflect the ultrasound beam the most may be significant as the transducer center frequency changes.

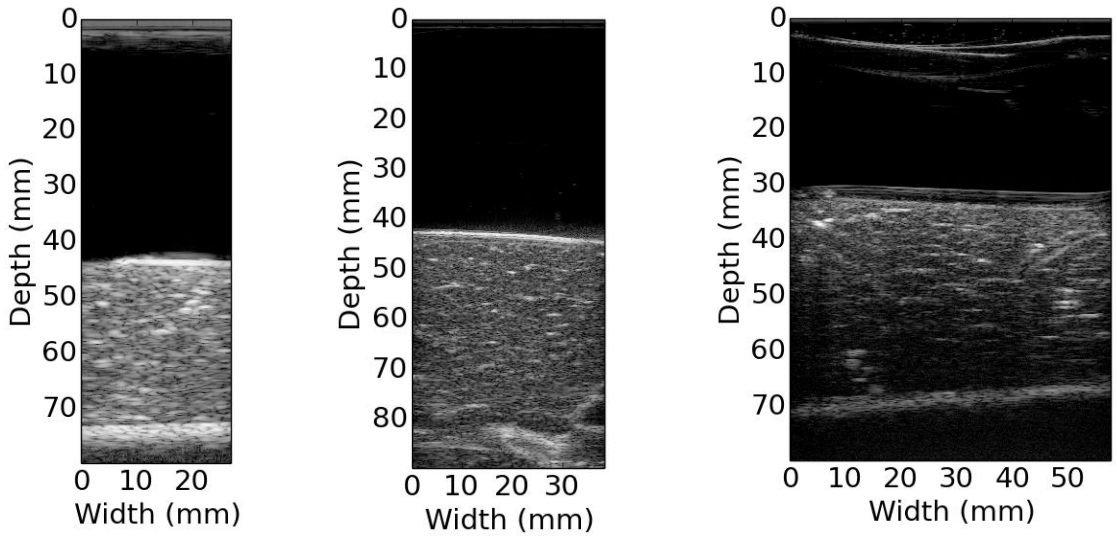

Figure 5.17. B-mode images of normal ex vivo bovine liver produced with RF data recorded from **(A)** 4V1 transducer, **(B)**, 9L4 transducer, **(C)** 18L6 transducer.

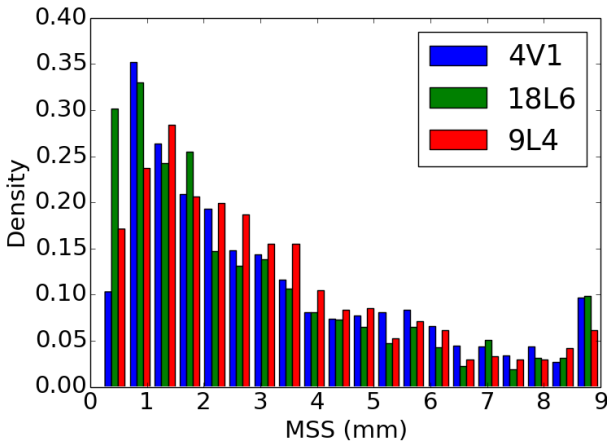

Figure 5.18. Estimated MSS distribution using three different transducers with the same ROI size for each transducer, 18 mm by 12 mm.

Table 5. 8. Parameters of estimated MSS distributions in normal liver across three transducers with a kernel size fixed at 18 mm by 12 mm.

Transducer	Analysis Frequency (MHz)	MSS Mean ± Std. Dev. (mm)	MSS Mode (mm)
4V1	2.0 to 5.0	3.21 ± 2.34	0.94
9L4	2.8 to 7.0	3.06 ± 2.15	1.27
18L6	3.0 to 8.0	2.86 ± 2.39	0.88

The other possibility is that this is an artifact of our estimator for the MSS. While the Slepian sequences are excellent gating functions for estimating the Loève spectrum, we have completely ignored a crucial component in the MSS estimation: the location of the first periodic scatterer in an A-line. Figure 5.19 shows a B-mode image recorded with the 18L6 transducer and the ROI used for calculation. In this image there are several bright points visible throughout the

axial extent of the ROI which are candidates for periodic scattering locations. For the results in this chapter and the previous it was assumed that the brightest periodic scatterer was also the first periodic scatterer. Figure 5.19 illustrates that this may not necessarily be the case, because the second strong scatterer identified would be selected by our algorithm for phase correction. Meanwhile, the first scatterer identified is potentially the true first periodic scatterer along this A-line.

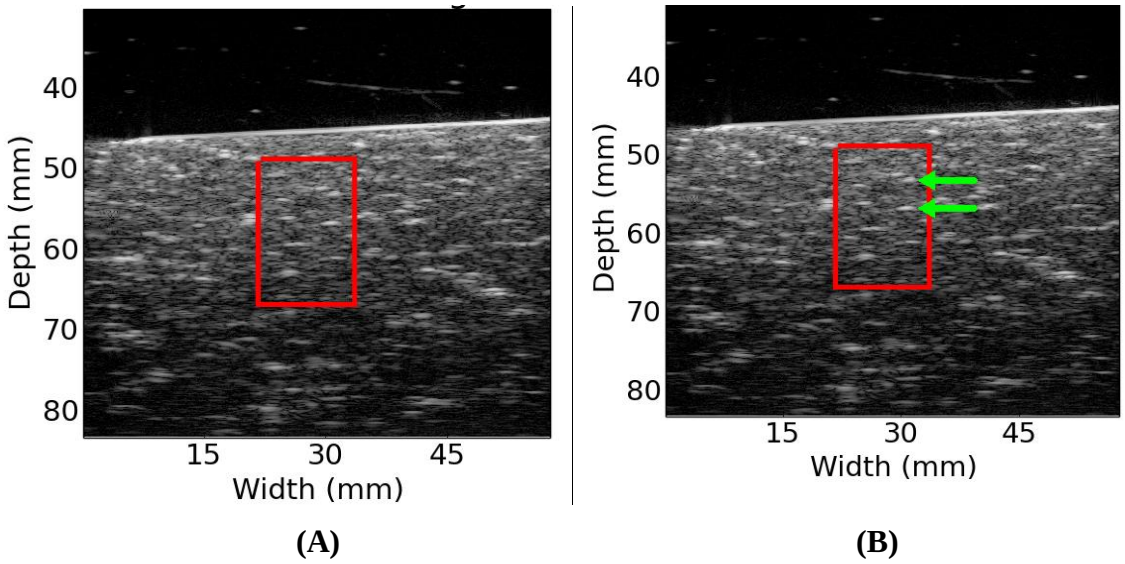

Figure 5.19. (A) B-mode image recorded with 18L6 illustrating ROI where multiple positions are good candidates for periodic scattering locations. **(B)** Two possible periodic scatterer positions identified. The brightest point is not necessarily the shallowest point but would be selected as the first periodic scatterer according to the algorithm used in this chapter.

5.11. Discussion

In this chapter, we first showed that spectral coherence was elevated in the liver when compared to within thermally ablated ROI's when examining small thermal coagulations created using a commercial RF ablation device. We remarked that this result alone leaves two

possibilities for the scattering model in untreated liver. Elevated coherence could be attributed to quasi-periodic scattering or low number density aperiodic scattering. We next looked at large ROI's in homogeneous regions in thermal ablations created using water bath heating. In both *ex vivo* bovine liver and thermally coagulated liver, we found that the distribution of estimated MSS had a mean that steadily increased as we increased the axial extent of our ROI. However, in normal *ex vivo* bovine liver, the mode of the distribution of MSS estimates remained between 1.25 and 1.37 mm. We hypothesize that *ex vivo* bovine liver exhibits a true periodicity at an MSS of approximately 1.3 mm, and that some ROI's in normal liver will fail to be periodic. Based on the simulations of periodic and sparse scattering, we assert that the mode of the estimated MSS distribution should be regarded as the true MSS. The tail of the MSS distribution may be attributed to falsely calculating MSS in regions where no periodicity exists. In the future, our lab will explore parametric images of MSS estimates for delineating thermal ablations. To account for sparse scattering noise, prior information about the expected MSS in untreated liver has to be used to decide on a cut-off spacing above which MSS estimates will be dismissed as sparse scattering noise. This cut-off spacing would be chosen based on prior information about tissue, namely the true MSS in tissue estimated from the mode of an estimated MSS distribution, and not based on the spatial resolution of the MSS estimator. Further studies will be needed to determine the minimum spatial resolution that can be achieved for an MSS estimator while balancing a cut-off spacing chosen independently of the gate length.

There were some small fluctuations in the mode in our MSS estimates in untreated *ex vivo* liver. These fluctuations may be due to the variance inherent in estimating the mode of an unknown probability distribution with only a small number of samples. We also note that the simulations examined in section 5.7 don't create MSS histograms that are exact matches to the

histograms measured *ex vivo* in section 5.8. The peak of the MSS distribution in the simulations is narrower than what was observed *ex vivo*. There may be several reasons for this discrepancy: first, there may be some variance between different animals or between different anatomical sections of the liver within a single animal. Unfortunately, verifying this would require examining a very large number of animals, and we were unable to do this at this time. Second, our periodic scattering model is only a very crude approximation to the actual three-dimensional scatterer arrangement within the liver. In the future, experiments with large numbers of animals and comparisons with data from micro-CT [168] may shed light on this problem. Last, no pathology was performed on the *ex vivo* bovine livers used in the studies in this chapter. All animals were raised to maturity under the same conditions prior to sacrifice for commercial meat production. Therefore, no pathology was expected in any animal, but the lack of pathology is still a source of experimental uncertainty.

While we found a stable mode for the estimated MSS in *ex vivo* bovine liver, the mode of the MSS estimates in coagulated liver ranged between 0.5 and 1.0 mm, with much probability density lying below 1.0 mm. We hypothesize that this is because thermally coagulated liver is better modeled by a diffuse and sparse aperiodic scattering model. While a large difference exists between the MSS estimated in normal liver and MSS estimated in thermally coagulated liver, it must be stressed that an MSS of 0.5 mm in thermally coagulated tissue corresponds to an algorithmic artifact rather than anything physical within the tissue. We note that if thermally coagulated tissue is better modeled as aperiodic, then any value for estimated MSS within this tissue must be regarded as an artifact, and one should avoid estimating MSS within the ROI altogether.

To our knowledge, the only other reported measurements of MSS in *ex vivo* bovine liver is in a paper by Pereira *et al* [139]. In this paper, spacing's of 3.1 to 4.8 mm was found in MSS measurements using SSA in *ex vivo* bovine liver using a transducer with a transmit center frequency of 3.3 MHz. In human liver, measurements of MSS have yielded values of 1 ± 0.16 mm, but this depends on the pathological state of the tissue [131]. We find that the mode of our MSS estimates show better agreement with previously reported MSS values in human liver than the values reported by Pereira *et al.* [139]. Concerning thermal ablation, a study has recently been published which contends that thermal ablation resulted in only a small change in MSS from 0.93 to 1.15 mm in *ex vivo* pig liver [145]. We hypothesize that this result is likely dependent on signal processing parameters, and may not hold if imaging parameters are changed. For example, the authors did not demonstrate that they measure the same MSS if the gate length was changed or the type of wavelet used was altered. All the results presented in this study used an analysis window length fixed at 7 mm [145] and a fifth order bi-orthogonal spline wavelet. It is difficult to say whether algorithmic changes would result in coagulated tissue exhibiting a smaller or larger MSS than normal liver tissue when using a wavelet algorithm, since the tissue may not have a true MSS associated with it to estimate.

Chapter 6. Ultrasound Attenuation Estimation in Normal and Thermally Coagulated Liver

6.1 Introduction

In this chapter we first discuss prior attenuation estimation results in thermally coagulated tissue [169]–[175], followed by the different ultrasound attenuation estimation methods that are utilized [122], [124], [126], [127], [129], [176]–[187]. We then examine the role of the scatterer number density (SND) parameter in attenuation estimation using numerical simulations and tissue-mimicking (TM) phantom experiments. We simulate diffuse scattering phantoms having a variety of scatterer number densities and estimate the envelope signal-to-noise ratio (SNR) of the resulting signals. We demonstrate that reference phantom attenuation estimation is robust to small reductions in envelope SNR, but the variance of attenuation estimates quickly increase as the envelope SNR significantly deviates from 1.91. This limits the spatial resolution that is possible in attenuation imaging with low SNR media. We then provide reference phantom attenuation estimates in TM phantoms containing low SND. Finally, we estimate the attenuation coefficient in *ex vivo* thermally coagulated bovine liver and *ex vivo* untreated normal liver using the reference phantom method [124].

6.2 Review of Attenuation Estimation in Untreated Normal Liver and Thermally Coagulated Tissue

Attenuation coefficient estimation and subsequent imaging has the potential to be a valuable tool for indicating the extent of thermal ablation therapy in the liver and other

abdominal organs. Attenuation in thermally coagulated regions have been shown to be significantly elevated relative to untreated normal liver tissue [169]. In particular, Parmar and Kolios found a relative increase in attenuation by a factor of 2.29 at a transmit center frequency of 5 MHz in *ex vivo* porcine liver following heating to 75° C for 60 minutes [169]. Bush *et al.* estimated changes in attenuation in high-intensity focused ultrasound (HIFU) lesions approximately 10 by 30 mm in cross-section in *ex vivo* pig livers. They estimated increases in attenuation coefficient from 32% to 192% between treated and untreated normal liver using pairs of through transmission, circular single-element transducers operating in the frequency range of 3.0 to 8.5 MHz [170]. On the average, Bush *et al.* found a mean change in sound speed of 0.55 ± 0.25 %, a mean change in backscatter coefficient of -24 ± 38 % and a mean change in attenuation coefficient of 90 ± 63 % [170]. However, these results were for only 4 samples, and all of Bush's experiments were conducted at room temperature [170].

Damianou *et al*. measured both attenuation and absorption in dog muscle, liver, and kidney as a function of temperature and thermal dose [171]. Damianou *et al.* found that the absorption and attenuation coefficient increased with increasing temperature and thermal dose. Additionally, they found that the absorption and attenuation coefficients depended both on the total thermal dose delivered and the delivery rate of the thermal dose [171]. Gertner *et al.* examined the attenuation coefficient over a frequency range of 2.5 to 5.0 MHz in eight store-bought bovine liver samples [172]. They found the attenuation coefficient estimated at 3.5 MHz increased by a factor of over 1.8 following 30 minutes of heating at 70° C in a saline bath [172].

Techavipoo *et al*. examined the temperature dependence of sound speed and attenuation in canine liver tissue. They found that sound speed varied only between 1580 and 1600 m/s over a temperature range of 20° to 90° C [173]. They also found that the attenuation coefficient

showed a slight decrease as tissue was heated up to 50° C, and then liver tissue showed an increase in attenuation as it was heated from 50° to 100° C [173]. Techavipoo *et al*. separately considered the effects of tissue coagulation and temperature by examining the attenuation coefficient in liver tissue at 37° C before and after heating [173]. They found that the effect of tissue coagulation was to increase tissue attenuation, and the effect of low temperature elevation was to decrease tissue attenuation [173]. Worthington and Sherar analyzed the time dependence of increases in the attenuation coefficient over the frequency range of 2.0 to 5.0 MHz in porcine liver tissue [174]. They utilized saline bath heating at various exposure times and temperatures, and found that an exponential model agreed well with their measured data [174].

Kemmerer and Oelze examined the backscatter coefficient, speed of sound, and attenuation coefficient changes in *ex vivo* rat liver following ten minute exposures in heated saline baths at high frequencies [175]. They found that the attenuation slope doubled from 0.2 dB/cm MHz to 0.4 dB/cm MHz over a frequency range of 9 to 25 MHz when rat liver tissue was exposed to a 70° C saline bath [175]. Like the other studies, Kemmerer and Oelze found relatively small changes to the backscatter coefficient and sound speed over the frequency range of 9 to 25 MHz examined in their study.

6.3 Review of Ultrasound Attenuation Estimation

Time domain techniques have been employed to estimate the attenuation coefficient of tissue. He and Greenleaf proposed the envelope peak method, where the ratio of the mean envelope peak to standard deviation of envelope peaks over depth was minimized by adjusting an attenuation-dependent gain function [176]. Jang *et al.* also proposed applying an attenuation and depth dependent gain to the signal envelope in order to determine attenuation [177]. In

Jang's method, the entropy difference between adjacent signal segments was minimized by adjusting the attenuation estimate and an associated depth-dependent gain function [177]. Knipp *et al.* proposed a method for estimating attenuation and backscatter in an unknown sample by comparing B-mode image values with values in a look-up table developed for individual transducers from phantoms with known attenuation and backscatter coefficients [178]. This method had the disadvantage of requiring determination of an effective frequency to assign to the recorded B-mode image to account for frequency dependence of beamforming, backscatter, and attenuation [178]. Ghoshal *et al.* recently proposed a time-domain algorithm where they explicitly modeled the diffraction pattern for a single-element circular transducer and iteratively solved for the attenuation coefficient in an unknown sample [179].

Frequency domain techniques are currently the more popular method for determining the attenuation coefficient in tissue. Frequency domain techniques are frequently described in analogy to two techniques explored by Roman Kuc in [180]: the spectral shift method and the spectral difference method. In Kuc's approach, the ultrasound signal prior to propagating through tissue is modeled by a pulse power spectrum, $P_i(f)$. The effect of traveling through a thickness of tissue, D, is to multiply the pulse power spectrum by an attenuation transfer function, $|H(f)|^2 = \exp(-4\pi\beta f D)$, where the attenuation coefficient is assumed to have a linear frequency dependence. After making a round trip through tissue, the pulse power spectrum is then given by $P_f(f) = P_i(f) \exp(-4\pi\beta f D)$.

In the spectral shift method, $P_i(f)$ is modeled by a Gaussian function, and the effect of attenuation is to shift the center frequency of the Gaussian spectrum by an amount proportional to β. The attenuation coefficient can then be obtained by tracking the center frequency of the

ultrasound pulse with depth. In the spectral difference method, the logarithm of the ratio of the power spectral magnitude is examined. The attenuation slope and the log spectra are related by:

$$ln(P_i(f)) - ln(P_o(f)) = 4\pi\beta fD \quad \textbf{(6.1)}$$

In order to estimate β with the spectral difference method, log spectral ratios are directly computed and no parametric model for the pulse spectrum is necessary. The spectral shift and spectral difference techniques as described by Kuc in [180] fail to account for the effect of transducer beam diffraction and focusing effects. In [181], Insana *et al.* examined correction factors to the spectral difference method to account for beam diffraction when making attenuation measurements in TM phantoms with known attenuation coefficients. In [122], Madsen *et al*. derived a frequency-domain model for the echo signal voltage for measurements of backscatter coefficients. In [122], this model was applied to estimation of backscatter using single element transducers, where beam diffraction was accounted for using the signal spectrum from reflections off a reference planar reflector [122]. Madsen's signal model was later extended to backscatter coefficient and attenuation estimation with clinical array transducers by Yao *et al.* in [124]. In Yao's algorithm, beam diffraction was accounted for by normalizing tissue spectra by spectra acquired from a reference phantom with matched sound speed and the same ultrasound system settings [124].

The reference phantom method developed by Yao *et al.* may be considered a spectral difference method. In this method, amplitude changes in the frequency content of the ultrasound pulse are measured over depth and normalized by a reference spectrum from a well-characterized phantom with known attenuation and backscatter. Attenuation is then estimated from the logarithm of the resulting ratio [124]. Kim and Varghese later implemented a hybrid method by incorporating the reference phantom method for normalizing spectra to reduce system dependent

effects, and then applying a Gaussian filter to the normalized spectra. The frequency shift of the power spectrum with depth was then detected using a cross-correlation algorithm [127]. This algorithm was shown to be less sensitive to artifacts than the reference phantom method when measuring attenuation in regions with inhomogeneous backscatter coefficient under diffuse scattering conditions [127]. Nam *et al.* proposed a reference phantom method where the backscatter coefficient frequency dependence was modeled with a polynomial function and attenuation was assumed to have a linear frequency dependence [129]. In this algorithm, the backscatter and attenuation were estimated simultaneously by minimizing the squared error between the predicted spectral ratio and the measured spectral ratio [129].

The reference phantom method and its variations make several assumptions about the tissue being imaged. First, this method assumes that the tissue being imaged has a sound speed matched to the reference phantom and the assumed sound speed of the beamformer in the ultrasound system. Second, it assumes that scattering occurs from a large number of spatially randomly distributed scatterers and their number density is large enough that the envelope is Rayleigh distributed. The impact of sound speed variations on attenuation estimation has been evaluated previously. Omari et al. examined variations in sound speed from 1480 to 1600 m/s at center frequencies of 4 and 5 MHz and found that sound speed errors led to a bias in the attenuation estimate [182]. Nam *et al.* found that bias in the attenuation estimate due to sound speed errors was worst when examining depths at and around the lateral focal depth [183].

However, little attention was given to the impact of non-Rayleigh scattering conditions on the resulting attenuation estimate. In many of the simulation studies for attenuation estimation, a single scatterer size and an SND greater than 10 per mm is often used [126], [127], [182]–[184], [186]–[188]. This is done to yield Rayleigh scattering statistics. However, non-

Rayleigh scattering statistics commonly occur in ultrasound imaging. For example, cysts and fibroadenoma in the breast have been shown to possess non-Rayleigh statistics and an envelope SNR of less than 1.91 using Nakagami imaging [189]. Ho *et al*. found that the Nakagami m-parameter, estimated from radiofrequency (RF) data recorded with a 6.5 MHz center frequency single-element transducer, increased from 0.55 to 0.83 in rat liver as the Metavir score of that liver increased from 0 to 4 [190]. The Metavir scoring system was developed in France for evaluating fibrosis and cirrhosis of the liver resulting from chronic viral hepatitis [191]. Under this scoring system, a pathologist evaluates the liver for damage and assigns a score of F0 through F4. A score of F0 indicates a healthy liver; F4 indicates cirrhosis; scores in-between F0 and F4, represent varying degrees of fibrosis. The Nakagami imaging study of Ho *et al.* [190] indicate that healthy liver has a low SND, and increasingly severe liver fibrosis tends to increase the SND .

6.4. Reference Phantom Based Attenuation Estimation

The reference phantom method of Yao *et al.* [124] relies on the following equation for attenuation estimation:

$$\frac{P_s(t_0, f)}{P_r(t_0, f)} = \frac{B_s(f)}{B_r(f)} exp((\alpha_s(f) - \alpha_r(f))4z) \qquad \textbf{(6.2)}$$

In **(6.2)**, $P_s(t_0,f)$ denotes a time-varying spectrum of an RF signal from tissue and $P_r(t_0,f)$ is a time-varying spectrum of an RF signal from a reference phantom. By a time-varying spectrum, we mean that RF data may be regarded as approximately stationary over a small time window centered on t_0. Then for fixed t_0, $P_s(t_0,f)$ is the power spectrum estimated over frequency centered on the location t_0. $B_s(f)$ is the backscatter coefficient of a collection of uniformly distributed, monopole scatterers in tissue, and $B_r(f)$ is the same quantity in the reference phantom. $\alpha_s(f)$ is the

attenuation coefficient at frequency f of the unknown sample and $\alpha_r(f)$ is the attenuation coefficient at frequency f of the reference phantom. z is the imaging depth. Imaging depth and time are assumed to be related through a known and constant sound speed, c. In order to compute the attenuation coefficient of the unknown sample at a particular frequency, we take the logarithm of equation 6.2. This yields:

$$\ln\left(\frac{P_s(t_0, f)}{P_r(t_0, f)}\right) = \ln\left(\frac{B_s(f)}{B_r(f)}\right) + (\alpha_s(f) - \alpha_r(f))4z) \quad \textbf{(6.3)}$$

To compute the attenuation coefficient at a particular frequency, we compute a linear fit to equation 6.3 over depth. We then compute the attenuation coefficient from the resulting slope and the known attenuation coefficient of the reference phantom. In this chapter, we have assumed a linear frequency dependence of attenuation with an intercept of 0. Therefore, attenuation in a sample is given by: $\alpha_s = \beta_s f$. To determine attenuation coefficient slope vs. frequency in the sample, we performed a second linear fit to the attenuation coefficient as a function of frequency, fixing the intercept at 0. The estimated attenuation coefficient slope vs. frequency, β_{est}, is then given by:

$$\beta_{est} = \frac{\sum_i \alpha_s(f_i) f_i}{\sum_i f_i^2} \quad \textbf{(6.3)}$$

Equation 6.3 is derived by minimizing the sum of square differences between $\alpha_s(f_i)$ and $\beta_{est}(f_i)$.

To compute the power spectrum, we used Thomson's multi-taper method, previously described in Chapter 4. In this method, an individual power spectrum is computed by averaging multiple power spectra each computed with a separate orthogonal window function. We denote the i^{th} A-line in a 2-D ROI containing M A-lines by x_i. An estimate for the time-varying spectrum is then given by the following expression:

$$S_{k,i}(t_0, f) = \left| \sum_{t=0}^{N-1} h_k(t) x_i(t_0 + t) exp(-i 2\pi f t) \right|^2$$
$$P(t_0, f) = \frac{1}{M} \frac{1}{K} \sum_{i=0}^{M-1} \sum_{k=0}^{K-1} S_{k,i}(t_0, f) \quad \textbf{(6.4)}$$

In equation 6.4, h_k is the k^{th} Slepian sequence. As in previous chapters, all array and FFT operations were carried out using the Python library Numpy [163]. We note that the use of the Slepian multi-tapers has been previously considered by Rosado-Mendez *et al.* [192]. Rosado-Mendez *et al.* found that in general the Slepian multi-tapers provided attenuation estimates with a lower mean square error than attenuation estimates made with single tapers when a small parameter estimation region was used. In the study of Rosado Mendez *et al.*, the frequency dependence of attenuation was modeled with a power law, $\alpha(f) = \beta f^n$, where both β and n were free parameters that were fit. Any further results of that study do not necessarily apply in our situation where we only have a single parameter, the attenuation coefficient slope vs. frequency, to fit.

6.5. Simulation Parameters for Attenuation Estimation

The simulations used were identical to those employed in Chapter 5. Two transducers with different center frequencies (3.5 and 5.5 MHz with 65% bandwidth each) were simulated. Two sets of simulated phantoms with a sound speed of 1600 m/s were created. At this sound speed, the wavelengths corresponding to the transducer center frequencies are 0.457 mm and 0.291 mm. The two sets of numerical phantoms differed in their linear attenuation coefficients. One set had a linear attenuation coefficient of 0.5 dB/cm MHz. The other set of numerical phantoms had a linear attenuation coefficient of 1.0 dB/cm MHz. Numerical phantoms having SND's of 0.2 to 1.0 in 0.1 mm increments, 2 to 128 in dyadic steps, and also 12 and 96 were

simulated for each linear attenuation coefficient value. For each SND, 1,000 A-lines were generated. Each A-line was formed using a completely independent and random realization of the scattering distribution.

6.6. Envelope Statistics, Spectral Coherence, and Scatterer Number Density

Chapters 4 and 5 considered estimating the mean scatterer spacing (MSS) using spectral coherence utilizing the fact that periodically positioned scatterers create local maxima in the bifrequency plane. Spectral coherence may also be affected by uniformly, randomly positioned scatterers if their number density is low enough. If the SND falls to a sufficiently low value, spectral coherence will increase throughout the bifrequency plane. It has also been found that the envelope SNR is related to the SND, where an estimate of the envelope SNR may be obtained using:

$$\begin{aligned} SNR &= \frac{\mu_E}{\sigma_E} \\ \mu_E &= \frac{1}{M}\sum_{i=1}^{M}\frac{1}{T}\sum_{t=1}^{T}E_i(t) \\ \sigma_E^2 &= \frac{1}{M}\sum_{i=1}^{M}\frac{1}{T-1}\sum_{t=1}^{T}(E_i(t)-\mu_E)^2 \end{aligned} \qquad \textbf{(6.5)}$$

In equation 6.5, $E_i(t)$ is the envelope value at the i^{th} A-line in a two-dimensional (2-D) region of interest (ROI) containing M A-lines, at time point t of T discrete points in the axial direction. One of the most widely cited works discussing envelope SNR is an article by Wagner *et al.* [130]. In this article, Wagner *et al.* model the ultrasound signal as an analytic signal whose real and imaginary components are Gaussian distributed. For this case, Wagner *et al.* show that the resulting signal envelope has a Rayleigh distribution. The Rayleigh distribution is characterized

by the ratio of the mean to the standard deviation, i.e. the SNR. For a Rayleigh probability density function (PDF) the SNR is given by $(\pi / (4- \pi))^{1/2}$, which is approximately 1.91.

A Rayleigh PDF is only achieved as a limiting case as the SND becomes large. As the number density of uniform scatterers drops below what is required for a Rayleigh distributed envelope, the envelope SNR of a random signal begins to drop. We plot the envelope SNR as a function of SND for the more highly attenuating simulated signals at both center frequencies in Figure 6.1. We also plot the average value of the spectral coherence over the frequency range 2.0 MHz to 5.0 MHz for the 3.5 MHz center frequency and over the frequency range of 3.5 MHz to 7.0 MHz for the 5.5 MHz center frequency. Both the envelope SNR and mean spectral coherence was computed for a 4 mm and a 12 mm gate length. We note that the longer gate length gives lower overall values for the envelope SNR. In addition, the SNR parameter estimated with a longer gate length is less sensitive to variations in SND when the SND is between 2 and 10. This is because when using longer gate lengths, the signal decays due to attenuation, introducing an additional component to the signal variance and making envelope SNR less dependent on SND. Meanwhile at a short gate length, the mean spectral coherence actually decreases rather than increases when the SND drops below 0.2 scatterers/mm^3. Summarizing, a short gate length performs better when using envelope SNR to determine SND, and a longer gate length has superior performance for distinguishing between different SND based on mean spectral coherence.

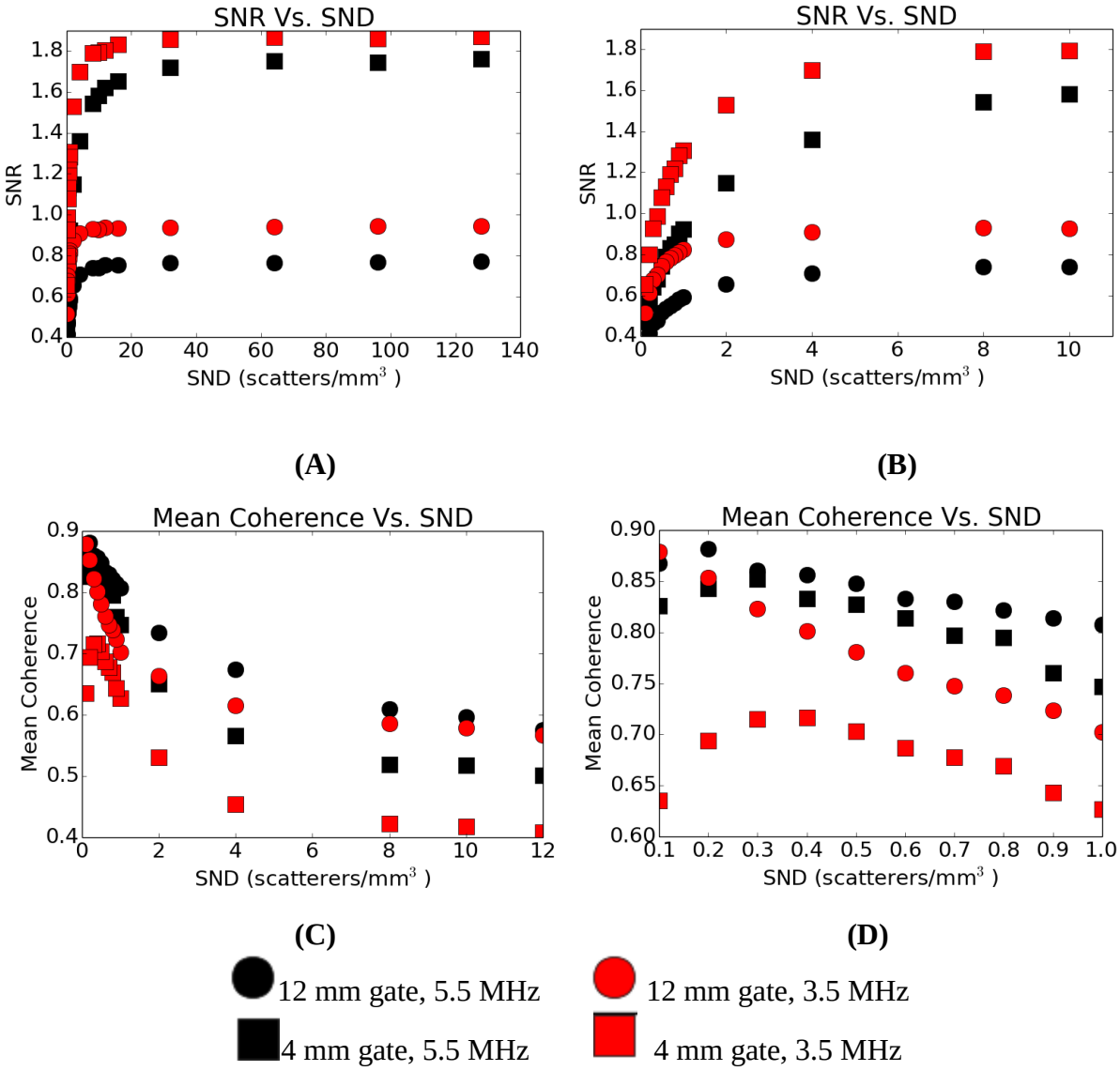

Figure 6. 1. (A) Envelope SNR versus SND calculated with a 4 mm and 8 mm gate starting from a depth of 30 mm in highly attenuating phantoms imaged at 3.5 MHz and 5.5 MHz center frequency. **(B)** Envelope SNR versus SND over a narrower range of SND. **(C)** Mean spectral coherence versus SND over the narrow SND range computed over the same depths from a frequency range of 2.0 to 5.0 MHz and 3.5 to 7.0 MHz also in the highly attenuating phantoms. **(D)** Mean Spectral coherence over an even narrower SND range.

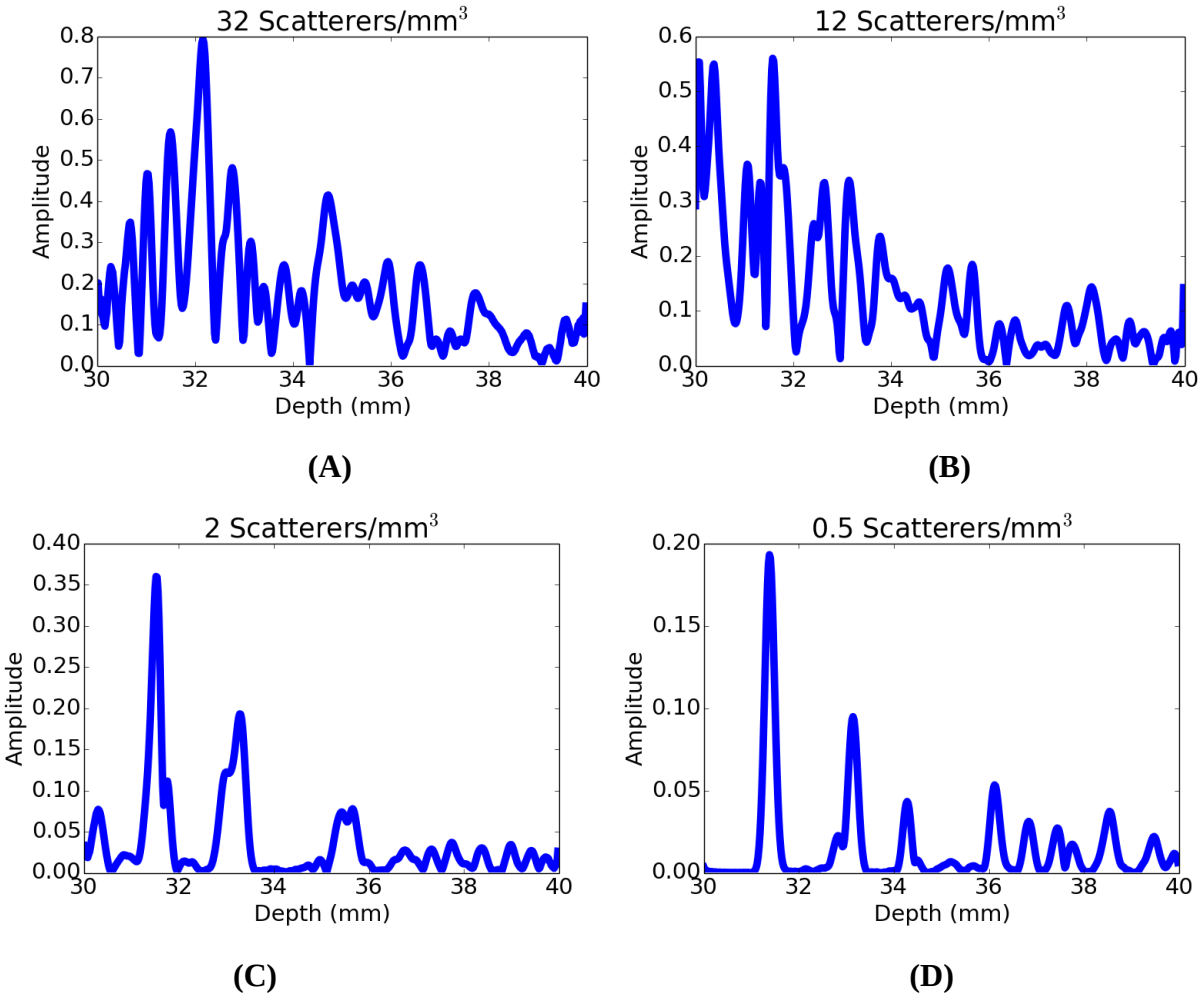

Figure 6.2. Simulated signal envelope from 1.0 dB/cm MHz phantoms imaged at a center frequency of 5.5 MHz. Depth of 25 mm to 35 mm. Scatterer number density of **(A)** 32, **(B)** 12, **(C)** 2, and **(D)** 0.5 per mm^3.

We show signal envelopes for several different values of SND in highly attenuating phantoms in figure 6.2. As shown in the plots of envelope SNR, the signals created with 12 scatterers per mm^3 look similar to the signals created with 32 scatterers per mm^3. The envelope variance shows a clear increase as the number of scatterers drops to 2 scatterers per mm^3. In

figure 6.2 **(C)**, we see that an SND this low leaves the envelope signal with dead spots where the envelope is near zero, over the 10 mm signal length examined.

From figure 6.1, we note that the envelope SNR depends on the simulated center frequency in addition to the SND. This is because the envelope SNR is a function of the number of scatterers per resolution cell, which is a property of both the object being imaged and the imaging device. For the higher center frequency the resolution cell occupies a smaller volume than for the lower transmit frequency, so the number of scatterers per resolution cell changes as we alter the center frequency. We also estimated the dimensions of a resolution cell in our simulations. We assumed that our ultrasound beam could be approximated by a short ellipsoidal cylinder over a small volume. To estimate the axial dimension of a resolution cell, we computed the correlation coefficient between a 4 mm segment of RF data and adjacent data using low attenuation slope, high SND phantoms (0.5 dB/cm MHz, 128 scatterers/mm^3). We estimated the dimension of a resolution cell in the axial direction by the axial shift of the 4 mm data segment which reduced the normalized correlation coefficient below 0.2 when averaging over 100 A-lines. We estimated the lateral resolution by creating 10 numerical phantoms, translating the scatterers in 0.1 mm increments, and measuring the resulting normalized correlation coefficient between 4 mm segments. We estimated the elevational resolution in a similar manner, only shifting the scatterers in the elevational direction. From figure 6.3, the resolution cell occupies a volume of approximately 0.8 mm^3 for the 3.5 MHz simulations and a volume of only approximately 0.4 mm^3 for the 5.5 MHz simulations. It is this difference in resolution cell volume which is responsible for the differences in envelope SNR observed in figure 6.1.

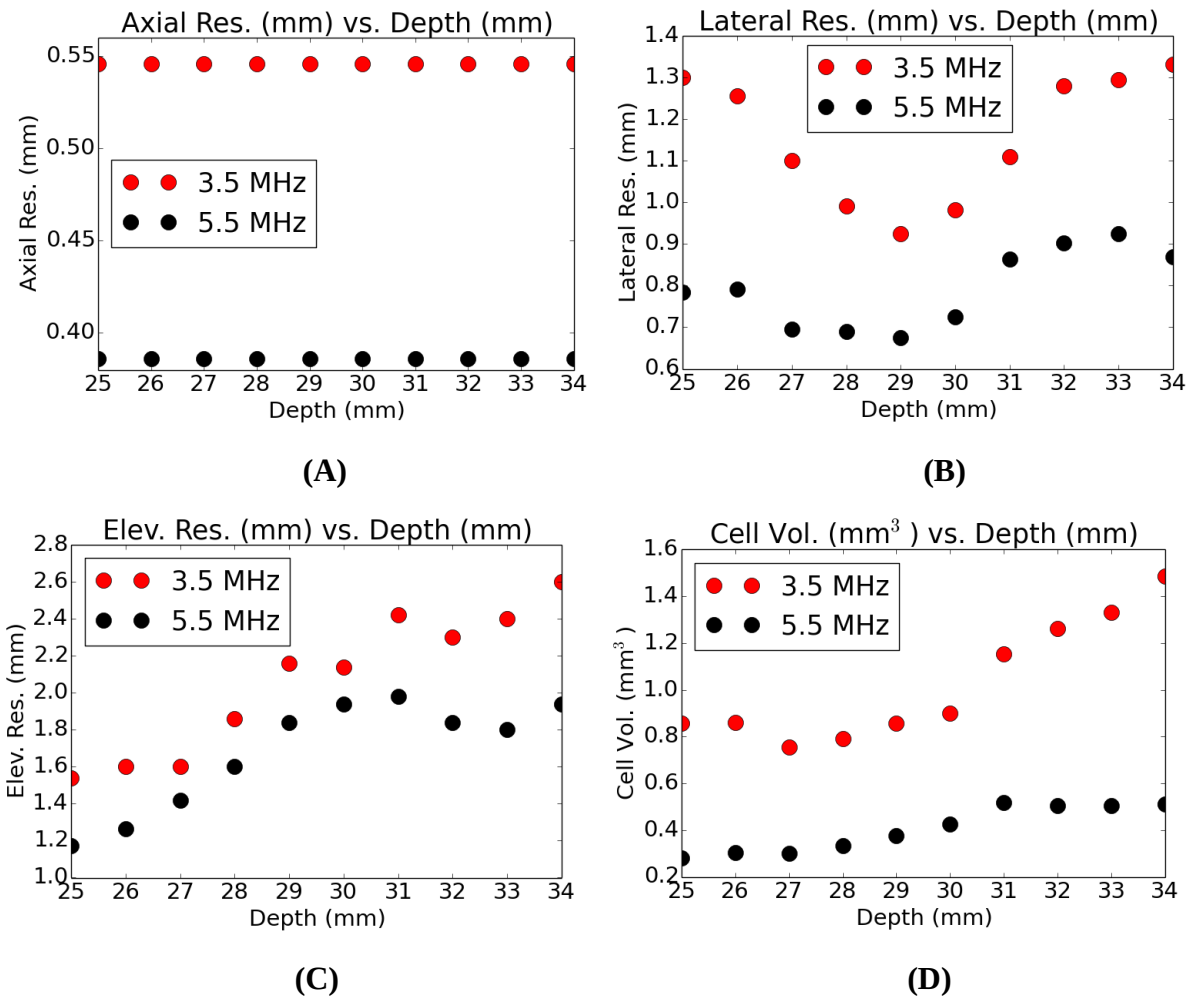

Figure 6.3. (A) Axial resolution of the 3.5 and 5.5 MHz center frequency simulated transducers estimated with a 4 mm data segment and 100 A-lines. **(B)** Lateral and **(C)** elevational **(D)** resolution estimated from examining simulated pressure fields. Resolution cell volume as a function of depth for 3.5 MHz center frequency and 5.5 MHz center frequency. The cell volume was given by π*(elev. res.)/2*(lateral res.)/2*(axial res.)

6.7. Simulation: Attenuation Results

For all attenuation estimates presented, we utilized all 1,000 independent A-lines computed for the 0.5 dB/cm MHz phantom containing 128 scatterers per mm^3 to form the reference power spectrum for a given center frequency. We found that our attenuation results were not dependent on the *W* parameter in the multi-taper method for a choice of W between 0.8 and 1.6. Other values for *W* were not considered. We also found our results were relatively independent of the length of the short-time gate used. Estimating a linear attenuation coefficient by translating 5 mm short-time gates by 5 mm yielded the same bias and coefficient of variation in the attenuation estimate as translating 4 mm short-time gates by 6 mm. With this in mind, we performed all attenuation estimates in these simulations starting at a depth of 25 mm and using a 4 mm short-time window and a smoothing bandwidth, W, equal to 1.0 MHz. We estimate attenuation over the frequency range of 3.5 to 7.0 MHz for the 5.5 MHz center frequency and over the frequency range of 2.0 to 5.0 MHz for the 3.5 MHz center frequency.

We first fixed the total data length at 33 wavelengths, which was 15.1 mm at a center frequency of 3.5 MHz and 9.6 mm at a center frequency of 5.5 MHz. The number of independent A-lines in each sample power spectrum was also fixed to 10 for each attenuation estimate. We plot the result of estimating attenuation in figures 6.4 and 6.5 as the SND and thereby the envelope statistics were varied. figure 6.4 and 6.5 (a) plot the mean value of the attenuation estimates, while Figures 6.4 and 6.5 (b) plot the variance of the attenuation estimates as a function of SND. Figure 6.4 and 6.5 (c) shows the mean attenuation estimate for a narrower range of SND and figure 6.4 and 6.5 (d) shows the variance in the attenuation estimate for the same narrow range of SND. These figures show that at a kernel dimension corresponding to 33 wavelengths the attenuation estimate is unchanged until the envelope SNR is significantly altered

from 1.91. From the previous section, this begins to occur when the SND begins to drop below 10 scatterers per mm^3. The effect that the decreasing SND has on the attenuation estimates is interesting.

The bias of the attenuation estimates shows no trend with decreasing SND. In the highly attenuating phantoms the mean attenuation coefficient slope vs. frequency estimate remains within 16% of the true value of attenuation. In the less attenuating phantoms, the mean attenuation estimate remains within 20% of the true value of the attenuation coefficient slope vs. frequency, except for one outlying point. The reason for the outlying points and some of the apparent attenuation estimation bias may be that as the variance of the attenuation estimates increase we require more attenuation estimates to accurately estimate the attenuation estimator bias. Performing 100 times as many simulations as we have may remove the outlying points and give a more stable mean slope estimate closer to the true slope.

The variance of the attenuation estimates showed no change until we fall below 10 scatterers per mm^3. We then observed only a slight increase in the estimated variance of the attenuation coefficient with decreasing SND of between 2 and 10 scatterers per mm^3. This is seen in both figures 6.4 and 6.5. As the SND drops below 2 scatterers per mm^3, the estimation variance shows a dramatic increase, regardless of whether the sample phantoms have an attenuation coefficient of 0.5 or 1.0 dB/cm MHz and whether the center frequency is 3.5 or 5.5 MHz. Note that this result, indicates that we do not need fully developed speckle in order to obtain a relatively small variance in the attenuation estimate. At an SND as low as 4 scatterers per mm^3, corresponding to an envelope SNR of approximately 1.3 at a center frequency of 5.5 MHz (according to figure 6.1), the standard deviation in the attenuation estimates is still well below 0.2 dB/cm MHz for the highly attenuating phantoms. Figures 6.4 and 6.5 don't show rapid

increases in the variance until the SND drops below 2 scatterers per mm^3, which corresponds to an envelope SNR of approximately 1.2.

From figures 6.4 B and figures 6.5 B, we also note that the variance in the attenuation estimates is roughly comparable when examining fully developed speckle and matching the kernel dimensions of the attenuation estimator in units of wavelengths. The performance of attenuation estimation at different center frequencies diverges as the SND begins to drop and the envelope SNR falls. At low SND, the lower center frequency shows a smaller estimation variance than the higher center frequency for kernels matched axially in wavelengths. This is because of the larger resolution cell exhibited by the lower center frequency simulation. The lower center frequency simulation contains more scatterers per resolution cell and has a higher envelope SNR for the same SND.

We note that the results in figure 6.4. and figure 6.5. are dependent on the spatial resolution of the attenuation estimate that we are attempting to achieve. We next examine two low SND cases and vary the axial kernel dimensions used to obtain the estimate. Figure 6.6 and 6.7 (A) and (B) presents the mean and variance in the attenuation estimates as a function of the axial kernel dimensions when the SND is fixed at 0.6 and 0.3 scatterers per mm^3. From this figure, we see that a low estimation variance may still be achieved even if the SND becomes extremely low as long as resolution is sacrificed. We note that the bias in the attenuation estimate remains relatively small, and it only varies by approximately five to ten percent as the axial kernel dimension is doubled. However, the variance in the estimate shows a large decrease, especially when the SND is 0.3 scatterers per mm^3 and the transducer center frequency is high. From all these simulations, we conclude that the SND is an important parameter in attenuation estimation. When SND becomes extremely low either estimator variance will significantly

increase or estimator kernel dimension must significantly increase to counter the increased variance.

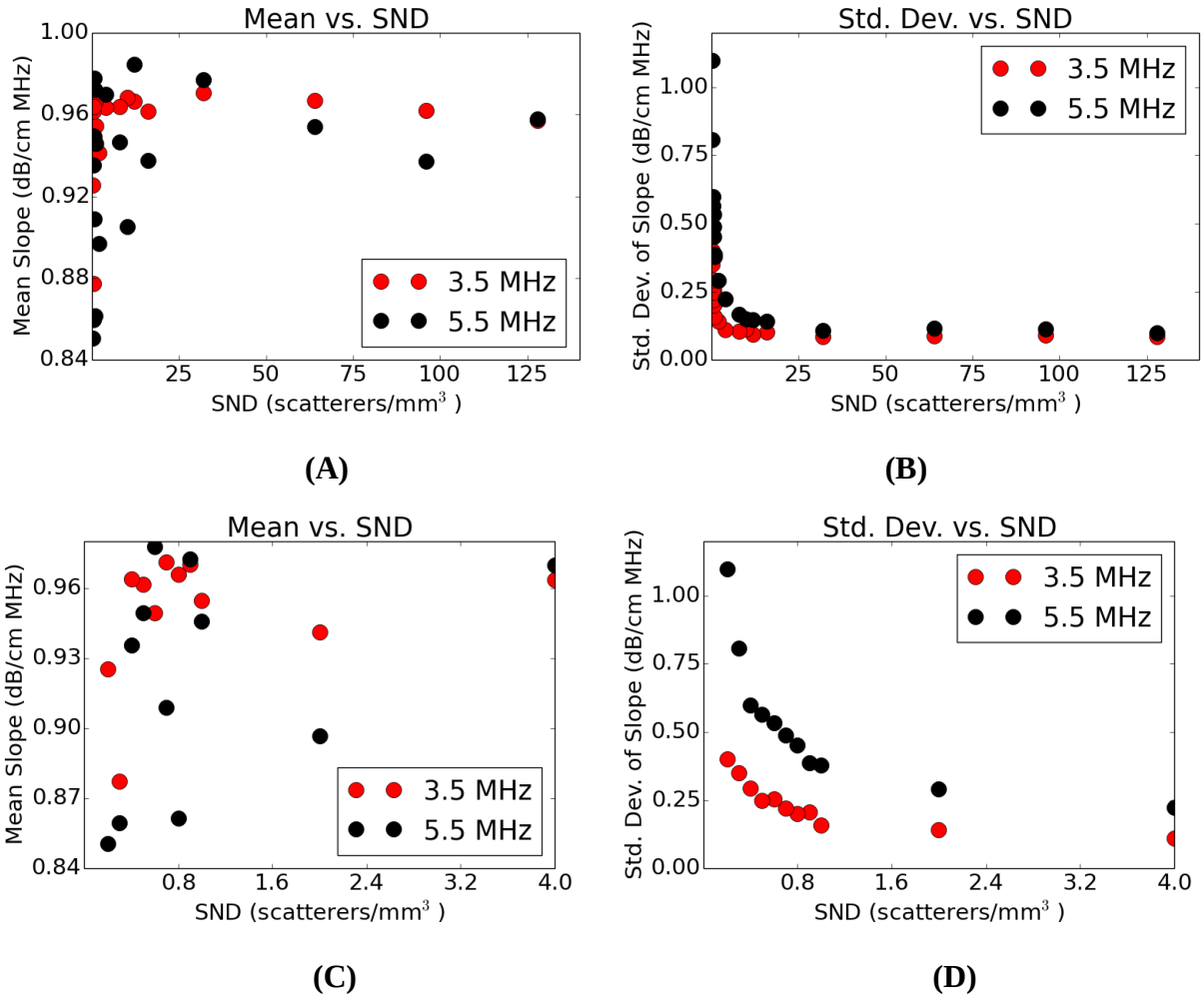

Figure 6.4. (A) Mean and **(B)** variance of attenuation estimate in 1.0 dB/cm MHz phantoms as the SND is varied. For all estimates an axial kernel dimension of 33 wavelengths and 10 independent A-lines were used. **(C),(D)** show the same estimates as in **(A),(B)** but over a narrower range of SND. 33 wavelengths corresponds to 9.6 mm at 5.5 MHz and 15.1 mm at 3.5 MHz.

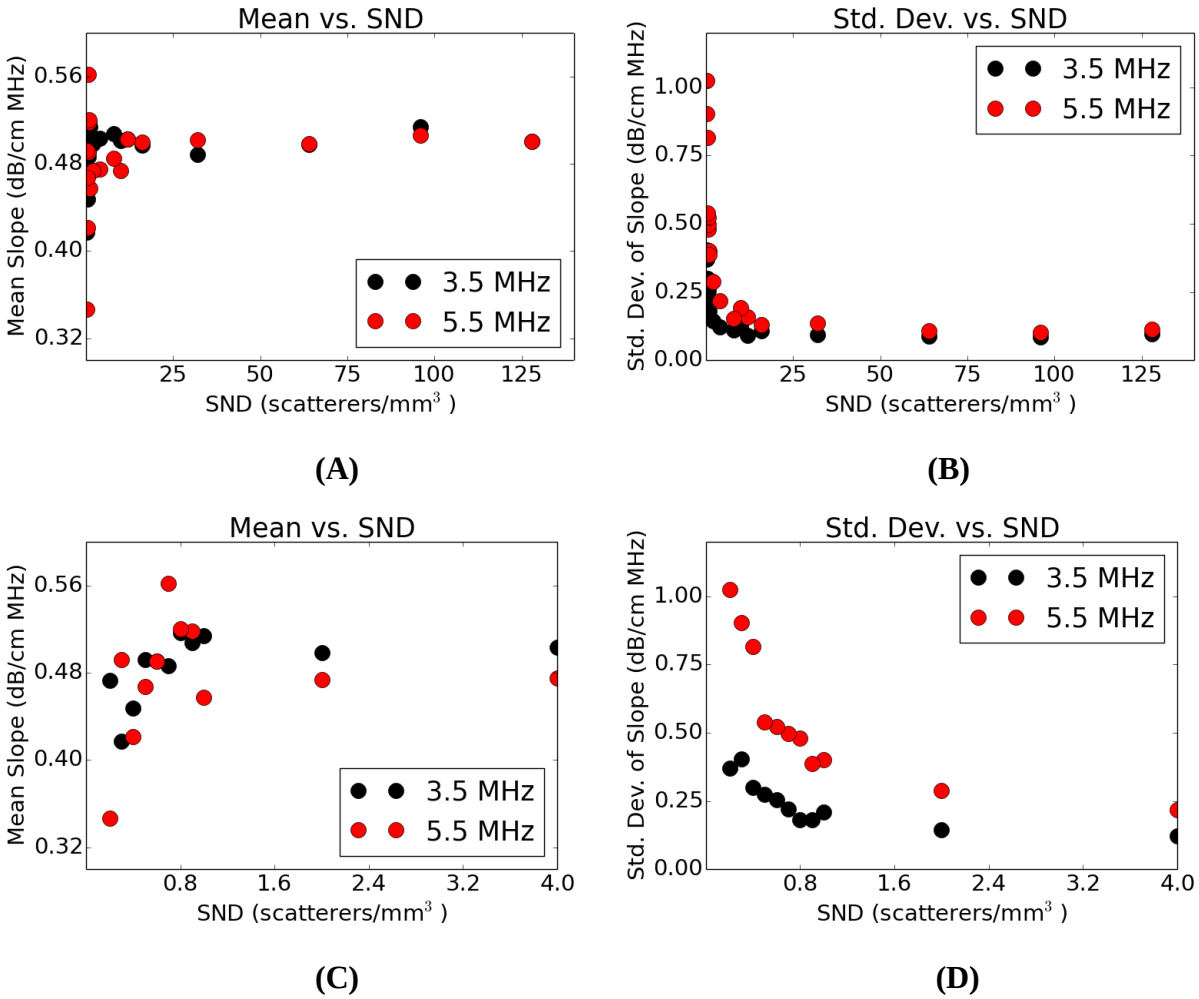

Figure 6.5. (A) Mean and **(B)** variance in attenuation estimate in 0.5 dB/cm MHz phantoms as the SND is varied. For all estimates an axial kernel dimension of 33 wavelengths and 10 independent A-lines were used. **(C),(D)** show the same estimates as in **(A),(B)** but over a narrower range of SND. 33 wavelengths corresponds to 9.6 mm at 5.5 MHz and 15.1 mm at 3.5 MHz.

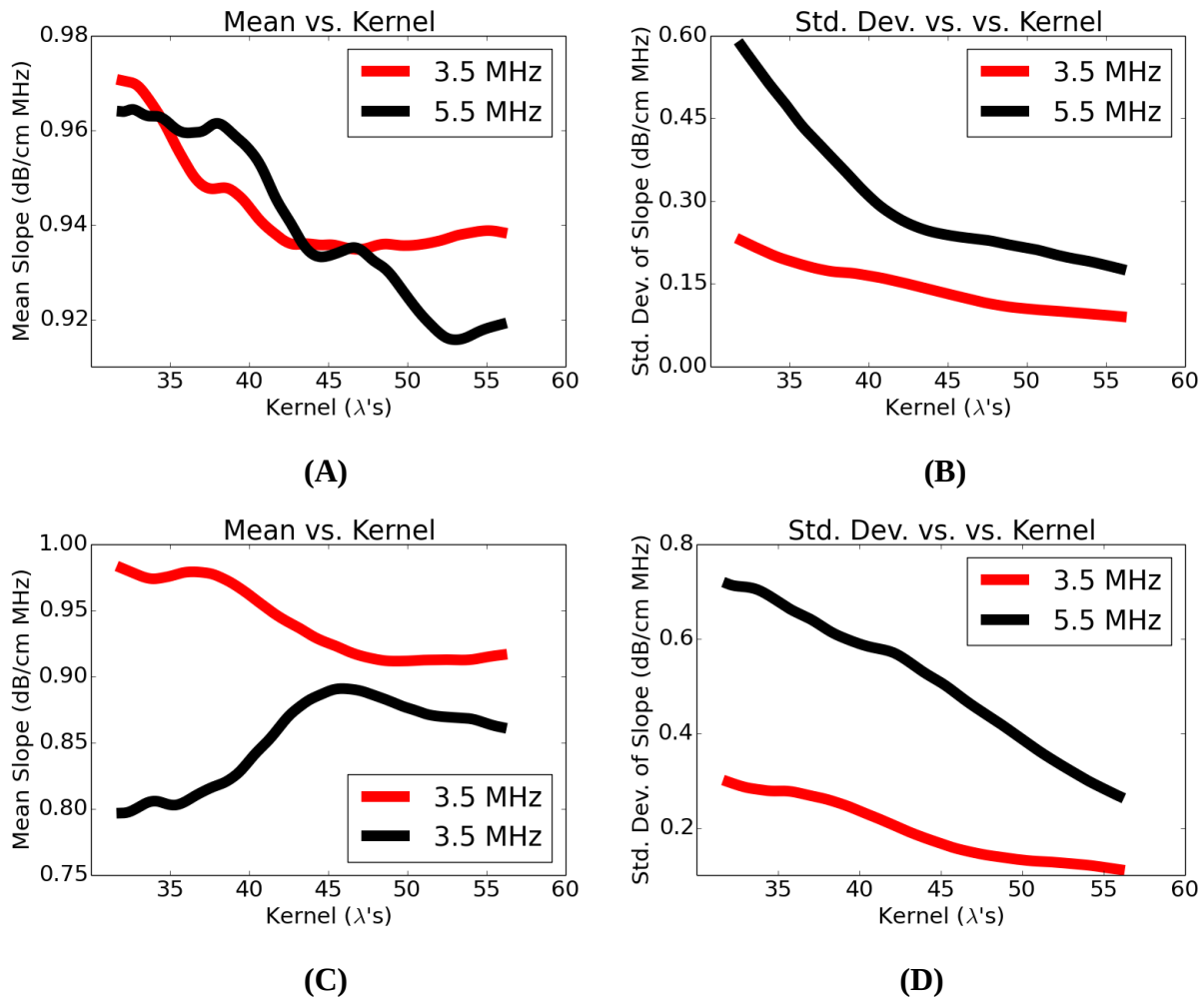

Figure 6.6. (A) Mean and **(B)** variance of attenuation estimates in 1.0 dB/cm MHz phantoms as the axial kernel dimension is varied and the number of A-lines in the estimate is fixed at 10 when the SND is 0.6 scatterers per mm^3. **(C)** Mean and **(D)** variance of attenuation estimates in 1.0 dB/cm MHz phantoms as the axial kernel dimension is varied and the number of A-lines in the estimate is fixed at 10 when the SND is 0.1 scatterers per mm^3.

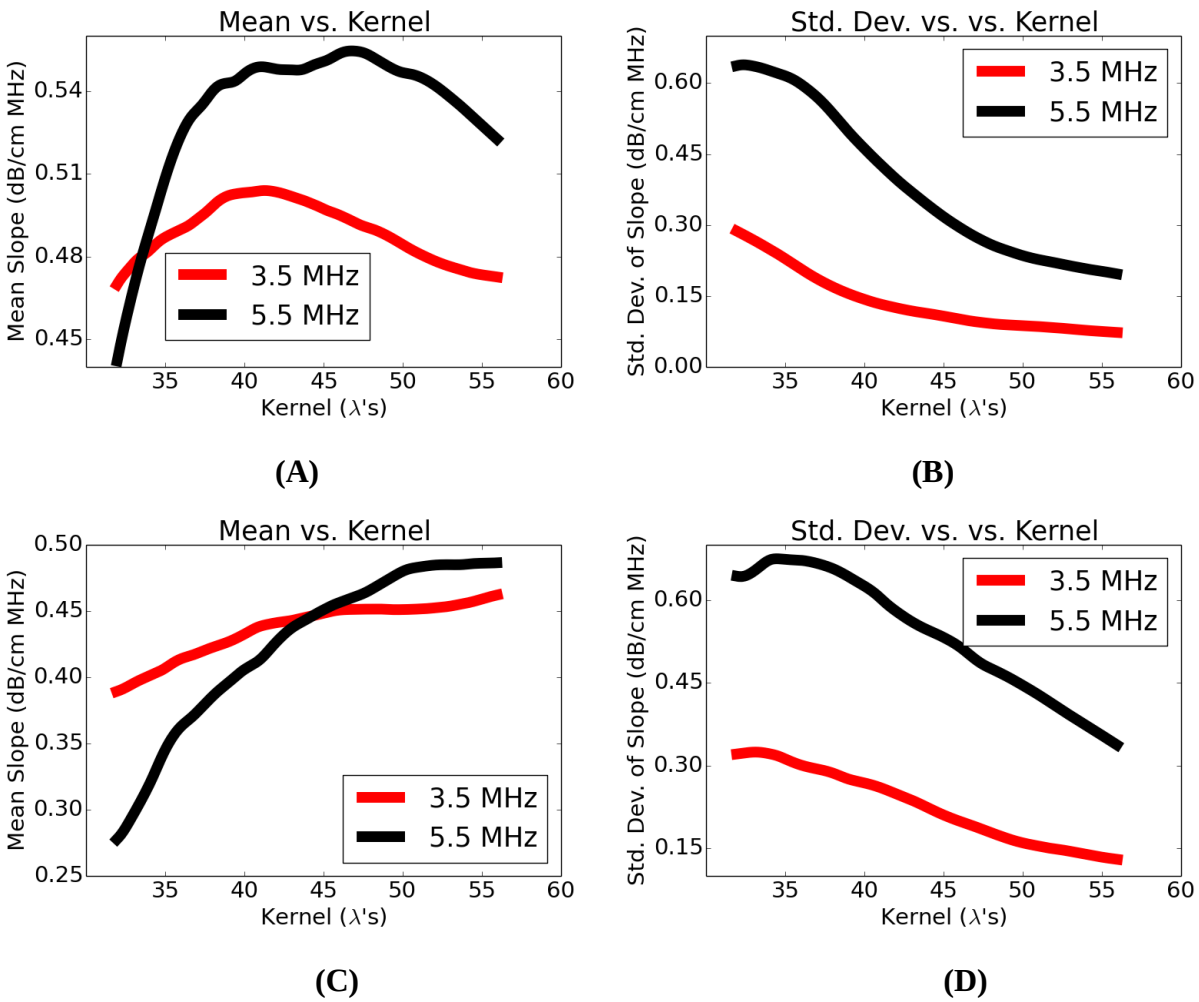

Figure 6.7. (A) Mean and **(B)** variance of attenuation estimates in 0.5 dB/cm MHz phantoms as the axial kernel dimension is varied and the number of A-lines in the estimate is fixed at 10 when the SND is 0.6 scatterers per mm^3. **(C)** Mean and **(D)** variance of attenuation estimates in 0.5 dB/cm MHz phantoms as the axial kernel dimension is varied and the number of A-lines in the estimate is fixed at 10 when the SND is 0.1 scatterers per mm^3.

6.8. Reference Phantom Attenuation Estimates in TM Phantoms.

TM phantoms with low, variable SND's were manufactured in order to compare attenuation estimates made using a clinical linear array transducer (VFX 9L4) and the S2000 ultrasound system, with attenuation estimates obtained using simulated data. Four TM phantoms were manufactured containing agar, glass beads, and graphite powder. Graphite powder was utilized to obtain the desired attenuation coefficient and diffuse scattering, while the glass beads provided scattering with a low SND. Two size distributions of glass beads were utilized: 75 to 90 microns and 125 to 150 microns. All beads were made of soda lime glass and had a mass density of 2.52 g/cm^3. We refer to the phantoms as phantoms A through D in order of the envelope SNR estimated from them. Phantom A contained 1.286 g/liter of 100 to 125 micron glass beads. Phantom B contained 0.278 g/liter of 125 to 150 micron glass beads. Phantom C contained 4 g/liter of 125 to 150 micron glass beads. Phantom D contained 4 g/liter of 75 to 90 micron glass beads. The glass bead diameters, concentrations used in phantom construction, and the estimated number density of glass beads are summarized in table 6.1. We estimated the number density of glass beads by assuming all beads in the distribution had a size equal to the mean of the diameter distribution. Phantom C and D have been previously analyzed by Omari *et al.* in [186]. The estimated sound speed in these phantoms from through transmission measurements was 1533 m/s. At a center frequency of 5.0 MHz, the attenuation coefficient slope vs. frequency estimated in phantom C by through transmission measurements was 0.675 dB/cm MHz, while it was 0.595 dB/cm MHz in phantom D. For the purposes of the analysis in this section we assume sound speeds of 1540 m/s in all TM phantoms.

Through transmission measurements of sound speed and attenuation on phantoms A and B found a sound speed of 1539 and 1541 and attenuation coefficient slopes vs. frequency of

0.495 dB/cm MHz and 0.500 dB/cm MHz with a transducer having a center frequency of 5.00 MHz. RF data was acquired during imaging of each of the TM phantoms on the Siemens S2000 scanner with the VFX 9L4 transducer. B-mode images of the TM phantoms are shown in figure 6.8. 100 sets of RF data were recorded on each of the four TM phantoms with the transducer being translated by at least 2 mm between each image. 15 planes of reference data were acquired from a fifth TM phantom with a large scatterer number density that was used as a reference phantom. The reference phantom also contained agar, graphite powder, and glass bead scatterers. In the reference phantom, the glass beads had a size distribution between 4 and 50 microns. The sound speed and attenuation coefficient of this reference phantom were verified using through transmission measurements. At center frequencies of 2.50 MHz and 5.00 MHz the attenuation coefficient was found to be 0.554 dB/cm MHz and 0.573 dB/cm MHz. The sound speed was found to be 1534 m/s and 1539 m/s.

Estimates of envelope SNR within each phantom are displayed in table 6.2. Envelope SNR estimates were made with 4 mm kernels axially, and were averaged over a 16 mm by 15 mm ROI in the center of each imaging plane. We note that our own results show a simple increase in envelope SNR with increasing glass bead number density. However, the effective SND is not necessarily the same as the estimated number density of glass beads even if our beads have a symmetric Gaussian distribution. This is because scattering is frequency dependent and some sizes will contribute to the signal more than others for a transducer with any given center frequency and bandwidth [193].

Table 6.1. TM Phantom scatterer distributions. The glass bead number density was estimated by assuming each bead in the distribution had a diameter equal to the median of the diameter distribution (137.5 microns and 82.5 microns).

TM Phantom	Glass Bead Diameters (microns)	Glass Bead Concentration (g/liter)	Estimated number density of glass beads (beads/mm^3)
A	125 to 150	0.643	0.25
B	75 to 90	0.278	0.50
C	125 to 150	4	1.55
D	75 to 90	4	7.20
Reference	4 to 50	4	355

Table 6.2. TM Phantom envelope SNR and attenuation coefficient slope vs. frequency estimates with a fixed kernel dimension (16 mm axially by 15 mm laterally).

TM Phantom	Envelope SNR	Through transmission β, 5.0 MHz (dB/cm MHz)	RPM Estimate of β (dB/cm MHz)	β Coefficient of Variation
A	1.01 ± 0.05	0.495	0.50 ± 0.25	50%
B	1.23 ± 0.03	0.500	0.50 ± 0.10	20%
C	1.56 ± 0.03	0.675	0.68 ± 0.08	11.7%
D	1.78 ± 0.02	0.595	0.60 ± 0.07	11.7%
Reference	1.87 ± 0.02	0.573	-	-

We performed attenuation estimation as described in the previous section. An attenuation coefficient slope vs. frequency of 0.56 dB/cm MHz was measured in the reference phantom.

Power spectrum estimates were obtained using Thomson's multi-taper estimator with a short-time gate length of 4 mm and a smoothing bandwidth, *W,* equal to 1.0 MHz. We show results with a fixed axial and lateral kernel dimension in table 6.1. As in the previous section, the bias in the attenuation estimate is relatively independent of the envelope SNR. So, a low SND does not result in biased attenuation estimates. A low SND, however, does result in an increase in the variance of the attenuation estimates. We also estimate attenuation with variable gate lengths and display the results in figure 6.9. As in the simulations, a low SND is not an impediment to achieving an unbiased attenuation estimate and either a small estimation variance or a high spatial resolution. However, a low SND is an impediment to achieving a high spatial resolution and a low estimation variance simultaneously. This is demonstrated in figure 6.9 where the bias in the attenuation estimate changes relatively insignificantly as the kernel dimension is varied, but the variance in the attenuation estimate increases rapidly as the kernel dimension is decreased. This is particularly true of the TM phantom with the lowest SND, denoted by TM A.

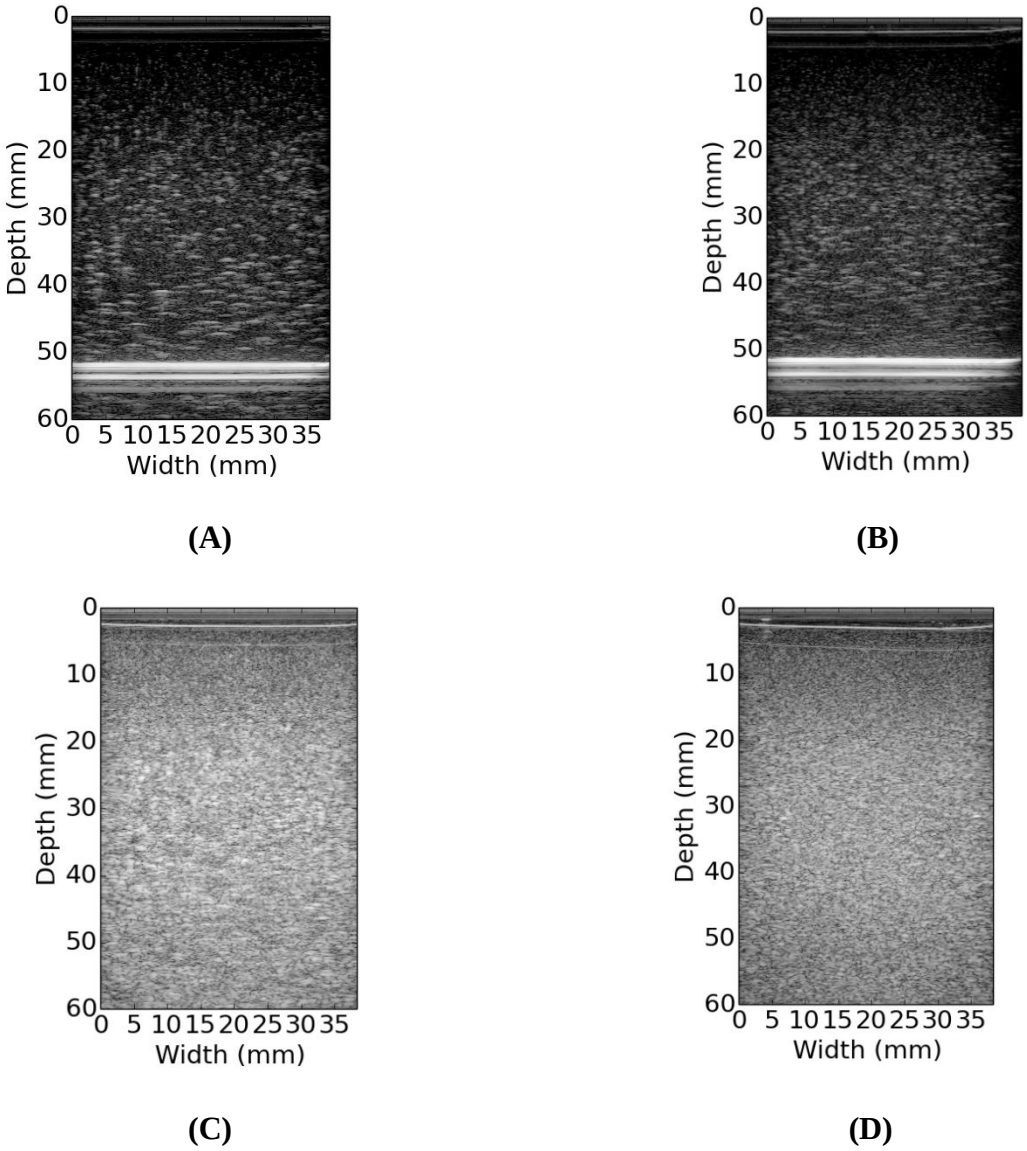

Figure 6. 8. B-mode images of TM phantom labeled **(A)**, **(B), (C),** and **(D)**. Images recorded with a 9L4 transducer on a Siemens S2000, with a transmit focal depth of 3.0 cm. Image **(A)** exhibits the lowest envelope SNR, and Image **(D)** exhibits the highest envelope SNR.

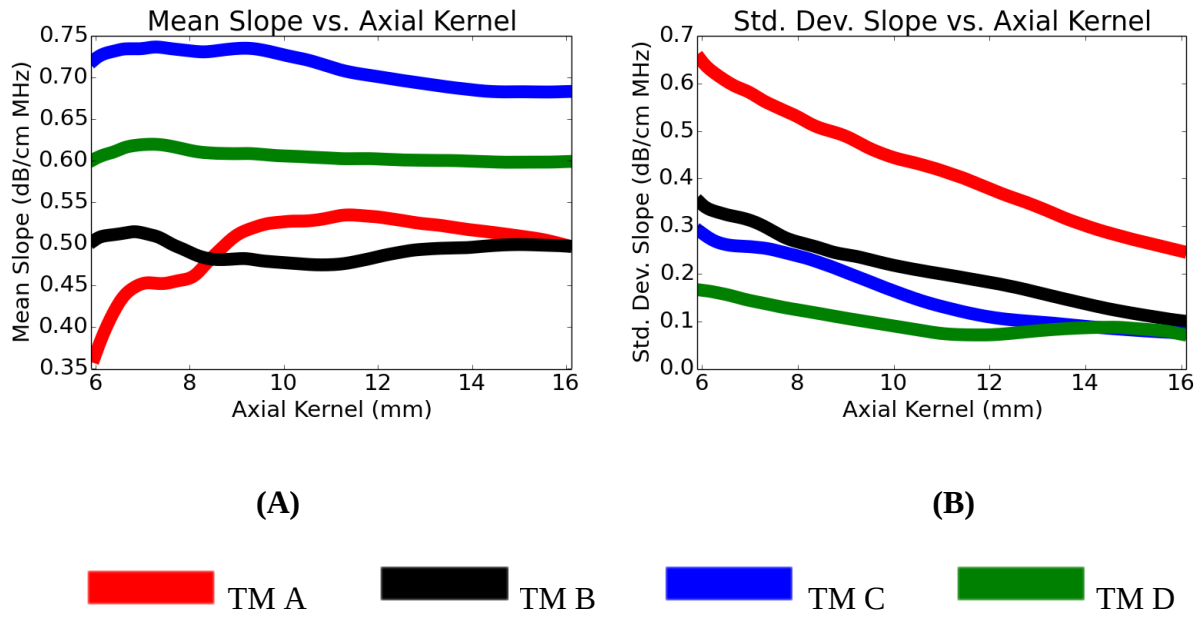

Figure 6.9. Attenuation coefficient slope vs. frequency estimates as a function of axial kernel dimension with the lateral kernel dimension fixed at 15.0 mm. **(A)** Mean estimate vs. axial kernel dimension in TM phantoms. **(B)** Standard deviation of estimates as a function of kernel dimension. Images recorded with a 9L4 transducer on a Siemens S2000 scanner, with a transmit focal depth of 3.0 cm.

6.9. Reference Phantom Attenuation Estimates in *Ex Vivo* Bovine Liver.

We estimated attenuation in the same set of liver samples discussed in the previous chapter in section 5.5. Ten livers were excised from ten separate animals, and five of these livers were thermally coagulated. Reference phantom data was recorded for both thermally coagulated tissue and untreated normal tissue. The reference TM phantom had a sound speed that was found to vary between 1578.73 and 1580.86 m/s when measured at four different center frequencies: 2.5, 5.0, 7.5, and 10.0 MHz. Within the TM phantom, the attenuation coefficient per unit

frequency was found to be 0.569 dB/cm MHz at 2.50 MHz and 0.591 dB/cm MHz at 5.0 MHz. The only construction difference between the reference phantom used in *ex vivo* measurements and the reference phantom used in the measurements with the TM phantoms was a small difference in the amount of propanol added to the phantom to adjust the sound speed. As in chapter 5, we utilized a beamformer sound speed of 1590 m/s for scanning and acquiring RF data recorded within thermally coagulated tissue and a sound speed of 1600 m/s when scanning untreated normal tissue. We note that a sound speed error of 20 m/s is only a 1.26% error relative to a 1600 m/s sound speed. We assumed a linear attenuation coefficient of 0.58 dB/cm MHz in the TM reference phantom for computing attenuation estimates in untreated normal liver tissue and thermally coagulated liver tissue. When collecting reference data, we utilized the same beamformer sound speed as was assumed in the tissue samples. So, a sound speed of 1600 m/s was used when collecting reference RF data from the TM phantom for analyzing untreated liver tissue and a sound speed of 1590 m/s for analyzing thermally ablated bovine liver tissue. For each set of reference data, 15 images were collected from independent imaging planes (separated by 2 mm or more) and power spectra were computed by averaging over all A-lines within an image and all 15 imaging planes. Thomson's multi taper method with a W of 1.0 MHz and a short-time gate length of 4 mm was used for all power spectrum calculations.

We estimated the envelope SNR in thermally coagulated liver and untreated normal *ex vivo* bovine liver. This was done to determine if *ex vivo* bovine liver tissue could be modeled with a high or a low SND, irrespective of periodicity considerations. We found a mean envelope SNR of 1.21 in thermally coagulated tissue, and a slightly lower mean envelope SNR of 1.00 in untreated normal *ex vivo* bovine liver. For the envelope SNR estimates, one 16 mm by 15 mm ROI from each image was subdivided into overlapping 4 mm by 4 mm sub-regions, and the

envelope SNR within a single ROI was taken as the average of the envelope SNR over the sub-regions. Neglecting periodicity, the simulations in combination with table 6.2 inform us that *ex vivo* liver tissue exhibits envelope statistics on the threshold of the low SND regime described in the simulated data.

A large variance in the attenuation estimates obtained in *ex vivo* bovine liver may be expected if we attempt to estimate attenuation with a small kernel dimension, and this large variance is a result of scattering dominated by low SND in liver tissue. We hypothesize that scattering from the liver microvasculature is responsible for the low SND scattering while the hepatocytes provide only a small underlying level of scattering. Recall that the estimation variance could be considerably reduced by giving up on the spatial resolution in the attenuation estimate. We first examine the estimation variance estimated over all liver samples as a function of gate length in both coagulated and untreated liver in fig. 6.10. As in the simulations and TM phantom results, the estimation variance is a strong function of the gate length, and the estimation bias varies much less than the estimation variance. In tissue, the variance in the attenuation estimates obtained was quite large.

We display results of attenuation estimation with a large, fixed kernel dimension within each of the individual livers in figure 6.12 and table 6.2 and table 6.3. Even at a large axial kernel dimension of 16 mm, the standard deviation in the estimates for attenuation in thermally coagulated tissue was approximately 50% of the mean value. This value was even higher in the untreated normal tissue where the coefficient of variation was approximately 100% at a large gate dimension. The lower performance in untreated normal liver could be expected since the envelope SNR was lowest prior to thermal coagulation. A natural question to ask is whether the variance is due to biological variability or estimator variance. The large decrease in estimation

variance with increasing kernel dimensions suggests that a very small variance in the attenuation estimate may be achievable if larger sections of the liver were imaged, degrading the spatial resolution.

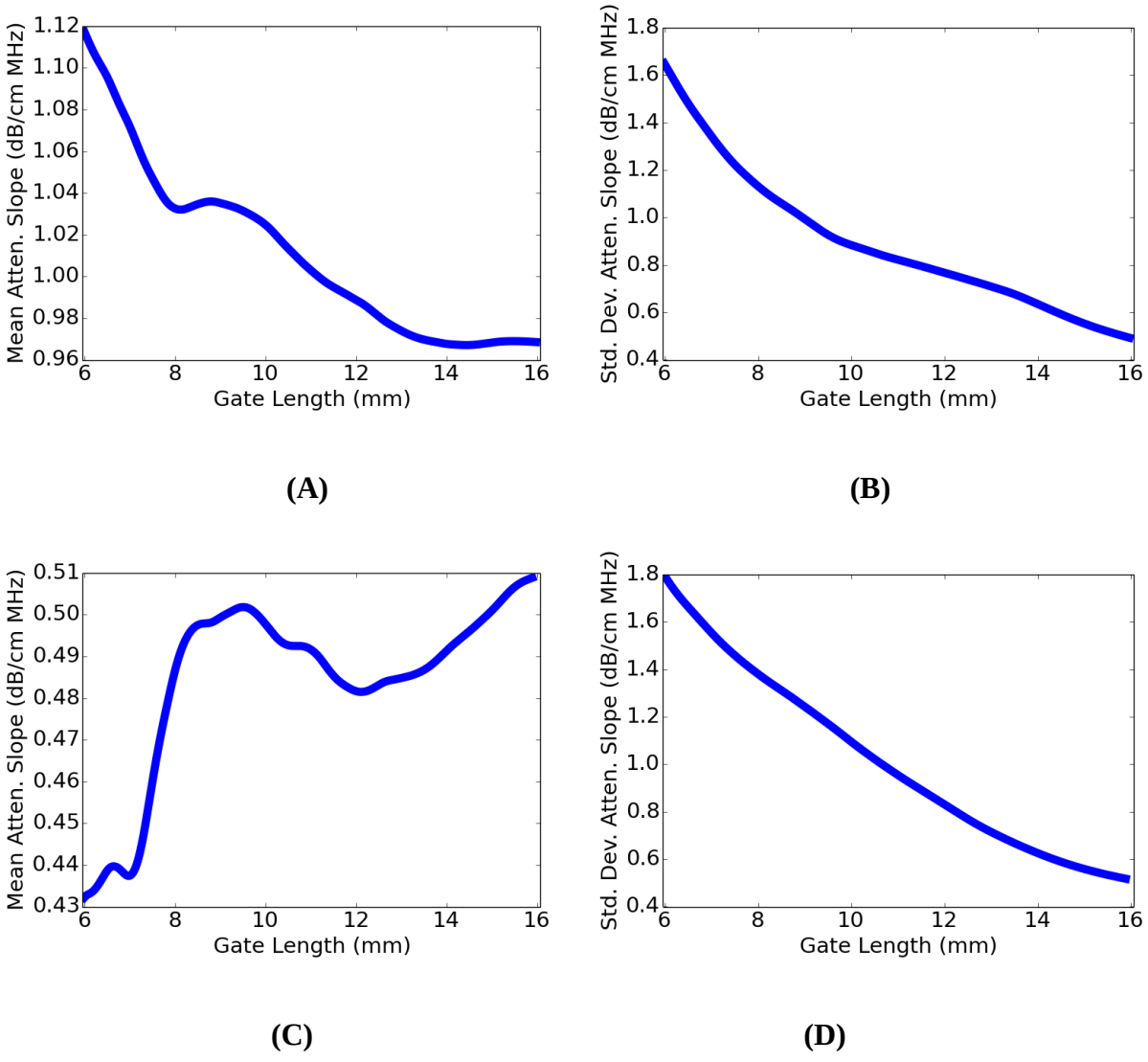

Figure 6.10. (A,C) Mean and **(B,D)** standard deviation of attenuation coefficient slope vs. frequency estimates within all untreated normal liver **(A,B)** and all thermally coagulated liver **(C,D)** as a function of gate length with the lateral extent of the kernel fixed at 15 mm.

The attenuation estimates within a single liver also suggest that the actual biological variability was quite small. We show estimates within individual livers in figure 6.11 (a**)** and **(**b). Over the small sample size (N=5), we don't see large fluctuations in the mean attenuation coefficient slope vs. frequency estimate across each of the untreated livers. We see greater variability in the mean estimates across each of the thermally coagulated liver tissue, but this could be due to differences in tissue heating. There was some variability in the sections of the liver that were heated at one time so smaller pieces would have received a larger thermal dose than larger sections over the same heating time. Making predictions about biological variability is difficult with our data, however. This is because while the number of images we recorded was relatively large (N~1500), the number of livers imaged (N=5) was fairly small.

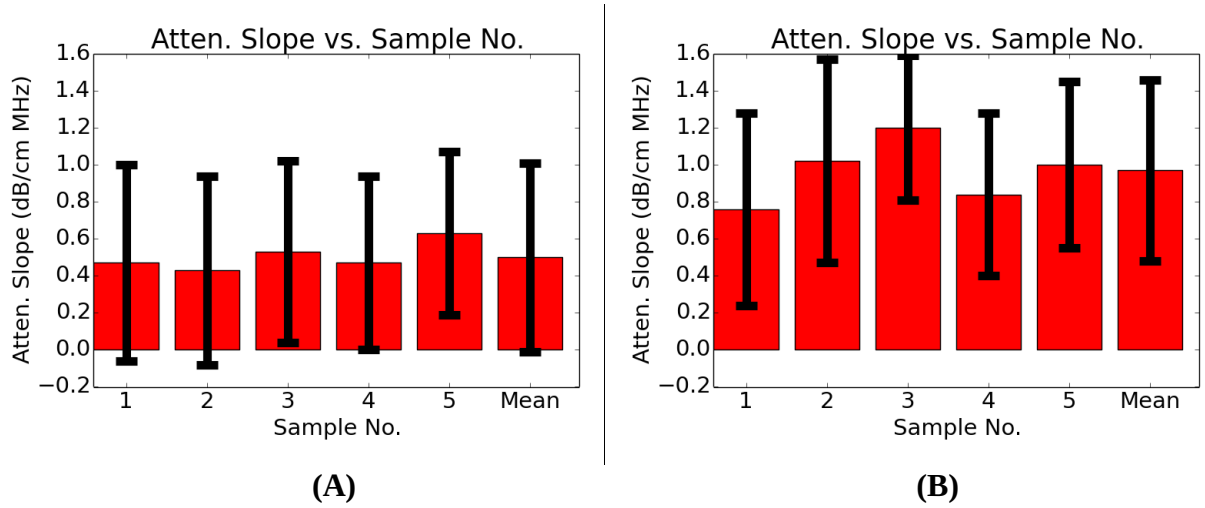

Figure 6. 11. Bar plot showing mean and variance of attenuation coefficient slope vs. frequency estimates in individual **(A)** ex vivo untreated normal bovine livers **(B)** and in individual thermally coagulated livers for a large kernel dimension (16 mm axially by 15 mm laterally). Error bars correspond to one standard deviation.

Table 6. 3. Envelope SNR and attenuation coefficient slope vs. frequency estimates in individual untreated normal bovine livers and all untreated normal bovine liver for a large kernel dimension (16 mm axially by 15 mm laterally).

Sample Number	Envelope SNR	Mean β Estimate (dB/cm MHz)	β Coefficient of Variation
1	1.07 ± 0.12	0.47 ± 0.53	113.0%
2	1.12 ± 0.12	0.43 ± 0.51	118.8%
3	1.04 ± 0.09	0.53 ± 0.49	94.0%
4	1.06 ± 0.10	0.47 ± 0.55	116.3%
5	1.19 ± 0.10	0.63 ± 0.44	70.0%
All	1.10 ± 0.12	0.50 ± 0.51	102.1%

Table 6.4. Envelope SNR and attenuation coefficient slope vs. frequency estimates in individual heated bovine livers and all heated bovine livers for a large kernel dimension (16 mm axially by 15 mm laterally).

Sample Number	Envelope SNR	Mean β Estimate (dB/cm MHz)	β Coefficient of Variation
1	1.35 ± 0.11	0.76 ± 0.52	68.9%
2	1.36 ± 0.13	1.02 ± 0.55	54.4%
3	1.24 ± 0.09	1.20 ± 0.39	32.5%
4	1.21 ± 0.13	0.84 ± 0.44	52.7%
5	1.25 ± 0.10	1.00 ± 0.45	44.5%
All	1.28 ± 0.13	0.97 ± 0.49	50.1%

Based on the results presented in this section, we remark that the error bars are large enough so as to obtain negative values for the attenuation coefficient. While a negative attenuation value is not physically possible, there is no constraint in the reference phantom algorithm that precludes it from obtaining such a result. We show a histogram of all the attenuation estimates in figure 6.12. Observe that the estimates take on an approximately Gaussian, symmetric appearance. Negative attenuation values are then just a logical consequence of the estimation variance being extremely high.

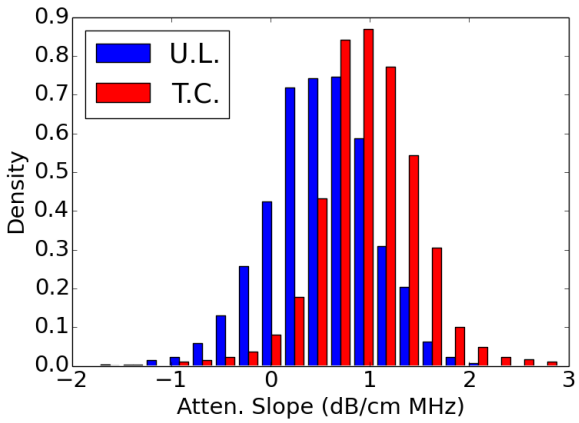

Figure 6.12. Histogram showing approximately symmetric distributions of attenuation coefficient slope vs. frequency estimates in all untreated normal livers and all thermally coagulated livers. The kernel dimension was also 16 mm axially by 15 mm laterally.

6.10. Envelope SNR Estimates in *Ex Vivo* Bovine Liver Across Transducers Operating at Different Center Frequencies.

Note that in figure 6.1 we demonstrated that the envelope SNR is a function of both the SND and the resolution of the US imaging system. Envelope SNR is therefore not an intrinsic property of tissue. In this section we present estimates of envelope SNR in untreated normal liver with the 18L6 and 4V1 transducers. These are the same data sets discussed in the previous chapter. We examine SNR estimates at multiple center frequencies in this section to determine how envelope SNR estimated in the liver changes as the transducer center frequency is changed. If the liver could be characterized by a single set of scatterers at all frequencies, we would expect envelope SNR to be a simple function of the resolution cell volume as it was for the simulations of the previous section. We would estimate the lowest envelope SNR with the 18L6 transducer and the highest envelope SNR with the 4V1 transducer. However, we find that this is not the case.

We first estimate the volume of a resolution cell for these three transducers using the 1580 m/s reference phantom discussed in section 6.9**.** In normal clinical use the 4V1 transducer is a phased array probe. However, we utilized the Siemens Axius Direct research interface to cause the 4V1 to operate as if it were a linear array probe, so a lateral resolution was defined the same way for the 4V1 as for the 9L4 and 18L6 transducers. We estimated the axial, lateral, and elevational resolution of the three transducers in the same way as the resolution estimation was performed in the simulated data. In order to estimate the resolution of a transducer in a given direction we examined the autocorrelation function of RF data recorded from the 1580 m/s reference phantom with the beamformer sound speed set to 1580 m/s. We computed the autocorrelation function using small, 4 mm by 4 mm ROI's, and we defined the half width of the

point spread function in the axial, lateral, or elevational direction to be the point where the correlation coefficient falls below 0.20.

We computed the volume of a resolution cell by approximating it as an ellipsoidal cylinder. We set the focal depths of the probes to 4, 3, and 2 cm on the 4V1, 9L4, and 18L6 transducers. A shallower focal depth was used for the 18L6 to avoid attenuation of the signal at high frequencies. The resolution cell volume is the smallest for the 18L6 transducer and the largest for the 4V1 transducer. The 4V1 has the poorest resolution of the three transducers by far. The reason for the poor resolution of the 4V1 may be that it was intended to be used at a deeper focal depth for abdominal applications and it was also not intended to be used as a linear array transducer.

Table 6.5. Axial resolution, lateral resolution, elevational resolution, and **(D)** resolution cell volume for 4V1, 9L4, and 18L6 transducers with assumed sound speed of 1580 m/s, estimated in 1580 m/s TM phantom. Focal depths were set to 4 CM for the 4V1 and 9L4 transducer and 2 CM for the 18L6 transducer, and measurements were averaged over 1 cm below and above the focal depth.

Transducer	Axial Res. (mm)	Lat. Res. (mm)	Elev. Res. (mm)	Res. Cell Vol. (mm^3)
4V1	0.60	2.43	5.41	9.32
9L4	0.34	1.20	1.75	0.56
18L6	0.28	1.20	1.70	0.44

We present results of envelope SNR estimation in Table 6.6. The envelope SNR is consistently low in *ex vivo* bovine liver tissue, regardless of the transducer used to image tissue.

The envelope SNR estimated with the 18L6 transducer is considerably lower than the envelope SNR estimated with the 4V1 transducer. This is probably because of the considerably smaller resolution cell volume for the 18L6 transducer. We hypothesize that the low SNR observed is due to the presence of periodic and sparse coherent scatterers within the liver. In the previous chapters, we depended upon the diffuse component of the scatterer distribution to be sufficiently weak to estimate MSS. In this chapter, we demonstrate that the periodic and sparse component of the ultrasound signal is a hindrance to estimating an attenuation coefficient with a low variance and high spatial resolution.

Table 6. 6. Envelope SNR estimated across all images of liver using three different transducers. Liver Number 1 imaged with the 4V1 is a distinct liver from liver number 1 imaged with the 9L4 or 18L6 transducer. Envelope SNR was estimated for a large kernel dimension (16 mm axially by 15 mm laterally).

Sample Number	4V1 Envelope SNR	9L4 Envelope SNR	18L6 Envelope SNR
1	1.03 ± 0.11	1.07 ± 0.12	0.875 ± 0.16
2	1.10 ± 0.17	1.12 ± 0.12	1.07 ± 0.17
3	0.98 ± 0.14	1.04 ± 0.09	0.86 ± 0.13
4	1.06 ± 0.19	1.06 ± 0.10	0.78 ± 0.14
5	1.08 ± 0.15	1.19 ± 0.10	0.95 ± 0.18
All Samples	1.05 ± 0.16	1.10 ± 0.12	0.90 ± 0.18

6.11 Discussion

As reported by previous authors, we found that the potential contrast between treated (coagulated) and untreated tissue is high [169]–[175]. Using a linear model for the attenuation coefficient, we found an average attenuation coefficient versus frequency slope of approximately

0.5 dB/cm MHz in *ex vivo* bovine liver prior to thermal coagulation and 1.0 dB/cm MHz following thermal coagulation. In this chapter we demonstrate a reason why it is difficult to obtain attenuation images in the liver with low variance and high spatial resolutions. An *ex vivo* setting is the first step in validating algorithms to be applied to a clinical abdominal ultrasound setting. In an *ex vivo* setting the confounding effects on the imaging of fat and muscle layers intervening between the liver and the transducer may be avoided. However, we find that the coherent scattering we observe in the liver deviates significantly from the scattering model that has been frequently assumed when developing reference phantom and other algorithms for attenuation estimation.

The estimation variance for attenuation coefficient slope versus frequency estimation is highly dependent on the envelope SNR. While our own results in *ex vivo* tissue were not encouraging, we note that the effect of excising liver from an animal on the envelope statistics of an ultrasound image of a liver has not been investigated. We noted that small differences in envelope SNR had a large effect on the attenuation estimation variance once the SNR began to significantly deviate from 1.91. *Ex vivo* porcine [145], [170], bovine ([85], [119], [139], [156], [156], [172], [194], [195]), rat [175], and human [134] liver have all been used for the development of ultrasonic tissue characterization algorithms based on features extracted from RF data. However, we are not aware of any studies comparing estimates of envelope statistics in excised liver with estimates of envelope statistics in an *in vivo* open surgery model using a single transducer. An open surgery model would be necessary to avoid the broadening of a resolution cell that would occur from phase aberration within layers of skin, fat, and abdominal muscle that would be necessary to penetrate when imaging the liver *in vivo*. Additionally, the comparison must be done using the same transducer in order to comment meaningfully on whether SND is

decreased by liver excision and loss of perfusion to the liver. Otherwise, both the volume of the resolution cell and the state of tissue would be changing at the same time and affecting the observed SNR. The effect of the pathological state of tissue and the species under consideration also are likely to have an effect on envelope statistics.

Chapter 7. Summary and Future Research

7.1 Summary

Minimally invasive thermal therapy has great potential to improve the management of both metastatic and primary liver cancer in a large number of patients. The success of this technique is dependent on the ability of clinicians to monitor the extent of the treatment following thermal therapy [196]. It has been well established that thermal ablation treatment results in an increase in the Young's modulus or shear modulus [75], [88], [92] and acoustic attenuation [169]–[175] in the liver. It has also been well established that negligible changes to sound speed and backscatter occur in treated liver following thermal ablation.

In chapter 2 of this thesis we reviewed various elasticity imaging techniques that have been used to image the extent of thermally coagulated liver. In chapter 3, we demonstrated that high quality strain images may be produced in the liver in open surgery, *in vivo* experiments. While elasticity imaging is capable of producing high quality images of thermal ablations, elasticity imaging is usually done over many frames and appropriate frame selection has to be performed in order to delineate the treated region. Therefore, additional parametric imaging of thermal ablations could be useful for delineating the extent of the coagulated region especially for selecting the most accurate strain image from a time series of images. Because of this, we investigated other tissue properties and their suitability for delineating the extent of thermal coagulation.

In chapter 4 we discussed mean scatterer spacing and its estimation. In the past, MSS has been applied to distinguishing between different grades of fibrosis in the liver [134]. It has been estimated through a variety of methods, and we focused on MSS estimation by locating peaks in the spectral coherence function. The estimate of spectral coherence depends upon a gating

function. We applied the discrete prolate spheroidal sequences (DPSS) as gating functions and compared the performance of the DPSS with the Hann, Hamming, and Blackman-Harris windows which are all commonly used in quantitative ultrasound signal processing. We showed that as the signal due to quasi-periodic scattering becomes weak or the variance in the scatterer spacing increases the DPSS outperforms these commonly used windows for estimating MSS.

In chapter 5 we established a novel tissue property for distinguishing thermally coagulated and untreated normal liver. Using a small number of radiofrequency (RF) ablations, we first established that spectral coherence is elevated in the untreated normal liver when compared to thermally coagulated tissue. This result demonstrates that untreated liver should be modeled with a lower scatterer number density than thermally coagulated liver. Since it identifies no local maxima as significant, this result makes no inferences about periodicity in the liver and thermally coagulated tissue. In the rest of chapter 5, we utilized a combination of numerical simulations and a large number of *ex vivo* observations in both thermally coagulated and untreated liver to demonstrate that *ex vivo*, untreated normal bovine tissue may be well modeled by periodically arranged scatterers while thermally coagulated tissue is better modeled by uniformly randomly positioned scatterers.

In chapter 6 we examined reference phantom based attenuation estimation in numerical simulations, TM phantoms, and the same *ex vivo* data sets used in chapter 5. We examined the bias and variance in multi-taper (MT) attenuation estimates as the scatterer number density of tissue was varied. We found that accurate attenuation estimates are obtained when the scatterer number density is high enough to yield a Rayleigh distributed envelope. Small deviation from Rayleigh statistics may occur with only minimal increases to attenuation estimation variance and no effect on attenuation estimation bias. However, for lower values of the envelope SNR,

produced by low SND, we observe large increases in the attenuation estimation variance. We found this was true using numerical simulations at center frequencies of 3.5 and 5.5 MHz and in TM phantoms containing agar, graphite powder to incorporate attenuation, and glass beads for scattering with a low SND. In the numerical simulations we saw attenuation estimation variance increase from 10% to 100% as the envelope SNR dropped from over 1.7 to less than 0.5. Meanwhile, the estimation bias exhibited a maximum value of 16% over the parameters examined. These results were for a transducer with a 5.5 MHz simulated center frequency and an attenuation kernel size of 33 wavelengths (9.6 mm) axially and 10 independent A-lines. In the TM phantoms, there was an increase in the coefficient of variation of attenuation estimates from 11.7% to 50% as the envelope SNR changed from 1.01 to 1.78 and the attenuation estimation region was 16 mm axially by 15 mm laterally.

We then estimated attenuation in both thermally coagulated bovine liver and untreated normal bovine liver *ex vivo* with a reference phantom and found the estimation variance to be quite large. At the largest estimation kernel sizes we found linear attenuation coefficients of approximately 0.5 dB/cm MHz in untreated normal liver and 1.0 dB/cm MHz in thermally coagulated liver. However, we were unable to utilize this result to produce attenuation coefficient images because of large estimation variance. We hypothesize that this large estimation variance is due to low scatterer number density in both treated and untreated *ex vivo* bovine liver.

7.2. Contributions

The contributions of this dissertation may be summarized as follows:

• We demonstrated that electrode displacement elasticity imaging is capable of producing high-quality images delineating thermally coagulated and untreated liver tissue in an open surgery *in vivo* setting.

• We demonstrated that spectral coherence estimates calculated using a multi-taper method instead of a conventional, single-taper provide MSS estimates with lower mean square error.

• We created a novel ultrasound simulation by combining a quasi-periodic scattering model with frequency domain simulations of ultrasound beamforming.

• We introduced a novel tissue property that may be used to produce images of thermal coagulation in the future. Thermally coagulated tissue has an aperiodic arrangement of scatterers, while untreated liver tissue contains a quasi-periodic arrangement of scatterers. Additionally, thermally coagulated tissue has a higher scatterer number density than normal liver tissue.

• We identified a fundamental limitation in attenuation estimation that must be overcome to produce attenuation images delineating thermal coagulations. We showed that the scatterer number density in *ex vivo* untreated bovine liver tissue and in *ex vivo* thermally coagulated liver tissue is lower than required for a Rayleigh distributed envelope. This in turn results in high variance in the attenuation estimates.

7.3. Future Work

There are several directions that future work in this research area can take. First, work should continue to improve upon elasticity imaging. Elasticity imaging is highly dependent on the mechanical boundary conditions experienced by the region of interest at the time of imaging.

This makes real-time feedback during elasticity imaging key to obtaining high-quality displacement and strain images. Currently, our laboratory can only implement real-time algorithms on the Ultrasonix SonicTouch ultrasound scanner. We also have access to an ultrasound system whose transducers have a higher bandwidth and a larger channel count, the Siemens S2000. With these two systems, we must either record ultrasound RF data on a machine whose transducers have a high channel count and a relatively wide bandwidth but a limited amount of programmability. The alternative is to use a highly programmable machine, but the image quality must suffer because of low transducer bandwidth and channel counts. The results in chapter 2 demonstrate a wide range of quality in strain images. These images could be made to have a more uniform quality if real-time imaging with algorithms developed in our own lab could be utilized on a high-end, commercial machine.

The impact of the scatterer number density and MSS variations should continue to be investigated. Variations of these parameters with species and center frequency should be explored. Additionally, differences between *in vivo* and *ex vivo* measurements should be examined. The first question to be addressed is how the scatterer number density and periodicity changes in the liver immediately after it is excised from an animal and blood perfusion ceases. Comparisons between open surgery *in vivo* and *ex vivo* data acquired on the same animal with the same transducer should be made to see if the loss of blood pressure results in an increase or decrease in envelope SNR and any changes to histograms of estimated MSS. An open surgery model is necessary for this comparison to be meaningful so the resolution cell volume is the same. When examining a subject *in vivo,* abdominal ultrasound imaging must usually contend with the abdominal wall. Since the ultrasound beam has to pass through a layer of skin and fat and several layers of muscle before encountering the liver, this increases the volume of the

ultrasound resolution cell compared with the resolution cell volume within *ex vivo* tissue or a TM phantom.

Envelope SNR and spectral coherence provide information useful for tissue classification. Additionally, envelope SNR and mean spectral coherence are useful for predicting how well we can expect to estimate attenuation. A recent article attempted to use parameters derived from spectral coherence and envelope SNR to sort regions within tissue into high SNR and low SNR regions for computing QUS parameters [156]. While an interesting approach, we believe that this is misguided. In *ex vivo* liver we found that ROI to ROI fluctuations in envelope SNR were small and that envelope SNR was characteristic of the entire tissue. Trying to sort tissue into high number density regions and low number density regions is only a good approach if we expect the tissue to contain pathologies that are heterogeneous. Novel approaches to attenuation estimation in the future should be prepared to estimate attenuation in tissue where the envelope SNR may significantly deviate from 1.91 throughout all tissue.

We employed Thomson's multi-taper spectral estimator in this dissertation for our estimation of the power spectrum. However, this spectral estimator was developed for estimating the power spectrum of stationary signals [148]. Reference phantom attenuation estimation theory is currently largely based on the derivations presented by Madsen *et al.* in [122] and Yao *et al.* in [124]. In these papers, the log ratio was explicitly tied to a gating function rather than a mathematically well defined spectrum. A discrete-time, non-stationary, stochastic signal may be characterized in the time domain by the auto-covariance function, in the frequency domain by the Loève spectrum, or in a mixed time-frequency domain by the Rihaczek distribution [197]. In the future, further mathematical development may help relate attenuation to well defined time-varying power spectra and identify better attenuation estimators.

References

[1] A. Jemal, T. Murray, E. Ward, A. Samuels, R. C. Tiwari, A. Ghafoor, E. J. Feuer, and M. J. Thun, "Cancer statistics, 2005," *CA Cancer J. Clin.*, vol. 55, no. 1, pp. 10–30, 2005.

[2] A. Jemal, F. Bray, M. M. Center, J. Ferlay, E. Ward, and D. Forman, "Global cancer statistics," *CA Cancer J. Clin.*, vol. 61, no. 2, pp. 69–90, 2011.

[3] R. Siegel, D. Naishadham, and A. Jemal, "Cancer statistics, 2013," *CA Cancer J. Clin.*, vol. 63, no. 1, pp. 11–30, 2013.

[4] G. C. Kanel, "Liver: Anatomy, Microscopic Structure, and Cell Types," in *Textbook of Gastroenterology*, Blackwell Publishing Ltd., 2009, pp. 2057–2072.

[5] D. E. Malarkey, K. Johnson, L. Ryan, G. Boorman, and R. R. Maronpot, "New insights into functional aspects of liver morphology," *Toxicol. Path.*, vol. 33, no. 1, pp. 27–34, 2005.

[6] J. Weinreb, S. Kumari, G. Phillips, and R. Pochaczevsky, "Portal vein measurements by real-time sonography," *Am. J. Roentgenol.*, vol. 139, no. 3, pp. 497–499, 1982.

[7] P. A. Farazi and R. A. DePinho, "Hepatocellular carcinoma pathogenesis: from genes to environment," *Nat. Rev. Cancer*, vol. 6, no. 9, pp. 674–687, 2006.

[8] Y. H. Shaib, H. B. El-Serag, J. A. Davila, R. Morgan, and K. A. McGlynn, "Risk factors of intrahepatic cholangiocarcinoma in the United States: a case-control study," *Gastroenterology*, vol. 128, no. 3, pp. 620–626, 2005.

[9] F. X. Bosch, J. Ribes, M. Díaz, and R. Cléries, "Primary liver cancer: Worldwide incidence and trends," *Gastroenterology*, vol. 127, no. 5, Supplement 1, pp. S5–S16, Nov. 2004.

[10] B. A. Centeno, "Pathology of liver metastases," *Cancer Control*, vol. 13, no. 1, pp. 13–26, 2006.

[11] L. Solbiati, T. Ierace, M. Tonolini, V. Osti, and L. Cova, "Radiofrequency thermal ablation of hepatic metastases," *Eur. J. Ultrasound*, vol. 13, no. 2, pp. 149–158, 2001.

[12] B. Y. Choi and M. H. Nguyen, "The diagnosis and management of benign hepatic tumors," *J. Clin. Gastroenterol.*, vol. 39, no. 5, pp. 401–412, 2005.

[13] D. Erdogan, O. R. Busch, O. M. Van Delden, R. J. Bennink, F. J. Ten Kate, D. J. Gouma, and T. M. Van Gulik, "Management of liver hemangiomas according to size and symptoms," *J. Gastroenterol. Hepatol.*, vol. 22, no. 11, pp. 1953–1958, 2007.

[14] J. Bruix and M. Sherman, "Management of hepatocellular carcinoma," *Hepatology*, vol. 42, no. 5, pp. 1208–1236, 2005.

[15] S. A. Shah, S. P. Cleary, A. C. Wei, I. Yang, B. R. Taylor, A. W. Hemming, B. Langer, D. R. Grant, P. D. Greig, and S. Gallinger, "Recurrence after liver resection for hepatocellular carcinoma: risk factors, treatment, and outcomes," *Surgery*, vol. 141, no. 3, pp. 330–339, 2007.

[16] E. J. A. Morris, D. Forman, J. D. Thomas, P. Quirke, E. F. Taylor, L. Fairley, B. Cottier, and G. Poston, "Surgical management and outcomes of colorectal cancer liver metastases," *Br. J. Surg.*, vol. 97, no. 7, pp. 1110–1118, 2010.

[17] Y. Fong, D. Carpizo, N. Kemeny, A. M. Covey, C. Willet, and B. G. Czito, "Metastatic Liver Cancer," *Gastrointestinal Oncology: A Critical Multidisciplinary Team Approach*, pp. 469–497.

[18] B. Nordlinger, E. Van Cutsem, T. Gruenberger, B. Glimelius, G. Poston, P. Rougier, A. Sobrero, and M. Ychou, "Combination of surgery and chemotherapy and the role of targeted agents in the treatment of patients with colorectal liver metastases: recommendations from an expert panel," *Ann. Oncol.*, vol. 20, no. 6, pp. 985–992, 2009.

[19] J. C.-H. Cheng, J.-K. Wu, C.-M. Huang, H.-S. Liu, D. Y. Huang, S. H. Cheng, S. Y. Tsai, J. J.-M. Jian, Y.-M. Lin, and T.-I. Cheng, "Radiation-induced liver disease after three-dimensional conformal radiotherapy for patients with hepatocellular carcinoma: dosimetric analysis and implication," *Int. J. Radiat. Oncol. Biol. Phys.*, vol. 54, no. 1, pp. 156–162, 2002.

[20] K. E. Rusthoven, B. D. Kavanagh, H. Cardenes, V. W. Stieber, S. H. Burri, S. J. Feigenberg, M. A. Chidel, T. J. Pugh, W. Franklin, and M. Kane, "Multi-institutional phase I/II trial of stereotactic body radiation therapy for liver metastases," *J. Clin. Oncol.*, vol. 27, no. 10, pp. 1572–1578, 2009.

[21] T. Livraghi, A. Giorgio, G. Marin, A. Salmi, I. de Sio, L. Bolondi, M. Pompili, F. Brunello, S. Lazzaroni, and G. Torzilli, "Hepatocellular carcinoma and cirrhosis in 746 patients: long-term results of percutaneous ethanol injection.," *Radiology*, vol. 197, no. 1, pp. 101–108, Oct. 1995.

[22] T. Mala, "Cryoablation of liver tumours–a review of mechanisms, techniques and clinical outcome," *Minim. Invasive Ther. Allied Technol.*, vol. 15, no. 1, pp. 9–17, 2006.

[23] M. Ahmed, C. L. Brace, F. T. Lee, and S. N. Goldberg, "Principles of and Advances in Percutaneous Ablation," *Radiology*, vol. 258, no. 2, pp. 351–369, 2011.

[24] D. Haemmerich, "Biophysics of Radiofrequency Ablation," *Crit. Rev. Biomed. Eng*, vol. 38, pp. 53–63, 2010.

[25] S. Rossi, M. Di Stasi, E. Buscarini, L. Cavanna, P. Quaretti, E. Squassante, F. Garbagnati, and L. Buscarini, "Percutaneous radiofrequency interstitial thermal ablation in the treatment of small hepatocellular carcinoma.," *Cancer J. Sci. Am.*, vol. 1, no. 1, pp. 73–81, 1995.

[26] L. Solbiati, S. N. Goldberg, T. Ierace, T. Livraghi, F. Meloni, M. Dellanoce, S. Sironi, and G. S. Gazelle, "Hepatic metastases: percutaneous radio-frequency ablation with cooled-tip electrodes," *Radiology*, vol. 205, no. 2, pp. 367–373, 1997.

[27] A. Guglielmi, A. Ruzzenente, M. Sandri, S. Pachera, C. Pedrazzani, S. Tasselli, and C. Iacono, "Radio frequency ablation for hepatocellular carcinoma in cirrhotic patients: prognostic factors for survival," *J. Gastrointest. Surg.*, vol. 11, no. 2, pp. 143–149, 2007.

[28] B. Mensel, "Laser-induced thermotherapy," in *Minimally Invasive Tumor Therapies*, Springer, 2006, pp. 69–75.

[29] G. ter Haar and C. Coussios, "High intensity focused ultrasound: physical principles and devices," *Int. J. Hyperthermia*, vol. 23, no. 2, pp. 89–104, 2007.

[30] J. E. Kennedy, "High-intensity focused ultrasound in the treatment of solid tumours," *Nat. Rev. Cancer*, vol. 5, no. 4, pp. 321–327, 2005.

[31] C. L. Brace, "Microwave Tissue Ablation: Biophysics, Technology and Applications," *Crit. Rev. Biomed. Eng.*, vol. 38, no. 1, pp. 65–78, 2010.

[32] S. Terraz, A. Cernicanu, M. Lepetit-Coiffé, M. Viallon, R. Salomir, G. Mentha, and C. D. Becker, "Radiofrequency ablation of small liver malignancies under magnetic resonance guidance: progress in targeting and preliminary observations with temperature monitoring," *Eur. Radiol.*, vol. 20, no. 4, pp. 886–897, 2010.

[33] B. Quesson, J. A. de Zwart, and C. T. Moonen, “Magnetic resonance temperature imaging for guidance of thermotherapy,” *J. Magn. Reson. Imaging*, vol. 12, no. 4, pp. 525–533, 2000.

[34] L. Crocetti, T. de Baere, and R. Lencioni, “Quality improvement guidelines for radiofrequency ablation of liver tumours,” *Cardiovasc. Intervent. Radiol.*, vol. 33, no. 1, pp. 11–17, 2010.

[35] L. Solbiati, T. Ierace, M. Tonolini, and L. Cova, “Guidance and monitoring of radiofrequency liver tumor ablation with contrast-enhanced ultrasound,” *Eur. J. Radiol.*, vol. 51, pp. S19–S23, 2004.

[36] M. F. Meloni, A. Andreano, E. Franza, M. Passamonti, and S. Lazzaroni, “Contrast enhanced ultrasound: Should it play a role in immediate evaluation of liver tumors following thermal ablation?,” *Eur. J. Radiol.*, vol. 81, pp. e897–e902, 2012.

[37] N. H. Gokhale, P. E. Barbone, and A. A. Oberai, “Solution of the nonlinear elasticity imaging inverse problem: the compressible case,” *Inverse Probl.*, vol. 24, no. 045010, p. 045010, 2008.

[38] J. J. O’Hagan and A. Samani, “Measurement of the hyperelastic properties of 44 pathological ex vivo breast tissue samples,” *Phys. Med. Biol.*, vol. 54, no. 8, pp. 2557–2569, 2009.

[39] J. Ophir, I. Cespedes, H. Ponnekanti, Y. Yazdi, and X. Li, “Elastography: a quantitative method for imaging the elasticity of biological tissues,” *Ultrason. Imaging*, vol. 13, no. 2, pp. 111–134, 1991.

[40] J. Jiang, T. Varghese, C. Brace, E. Madsen, T. Hall, S. Bharat, M. Hobson, J. Zagzebski, and J. F. Lee, “Young’s Modulus Reconstruction for Radio-Frequency Ablation Electrode-Induced Displacement Fields: A Feasibility Study.,” *IEEE Trans. Med. Imaging*, vol. 28, no. 8, pp. 1325–1334, 2009.

[41] S. Bharat, T. Varghese, E. L. Madsen, and J. A. Zagzebski, “Radio-frequency ablation electrode displacement elastography: A phantom study,” *Med. Phys.*, vol. 35, no. 6, pp. 2432–2442, 2008.

[42] T. Varghese, U. Techavipoo, W. Liu, J. A. Zagzebski, Q. Chen, G. Frank, and F. T. Lee Jr, “Elastographic measurement of the area and volume of thermal lesions resulting from radiofrequency ablation: pathologic correlation,” *Am. J. Roentgenol.*, vol. 181, no. 3, pp. 701–707, 2003.

[43] J. Jiang, T. J. Hall, and A. M. Sommer, “A novel image formation method for ultrasonic strain imaging,” *Ultrasound Med. Biol.*, vol. 33, no. 4, pp. 643–652, 2007.

[44] F. Kallel and M. Bertrand, “Tissue elasticity reconstruction using linear perturbation method,” *IEEE Trans. Med. Imaging*, vol. 15, no. 3, pp. 299–313, 1996.

[45] C. Sumi, A. Suzuki, and K. Nakayama, “Estimation of shear modulus distribution in soft tissue from strain distribution,” *IEEE Trans. Biomed. Eng.*, vol. 42, no. 2, pp. 193–202, 1995.

[46] M. M. Doyley, P. M. Mcancy, and J. C. Bamber, “Evaluation of an iterative reconstruction method for quantitative elastography,” *Phys. Med. Biol.*, vol. 45, no. 6, pp. 1521–1540, 2000.

[47] M. A. Lubinski, S. Y. Emelianov, K. R. Raghavan, A. E. Yagle, A. R. Skovoroda, and M. O’Donnell, “Lateral displacement estimation using tissue incompressibility,” *IEEE Trans. Ultrason. Ferroelectr. Freq. Control*, vol. 43, no. 2, pp. 247–256, 1996.

[48] U. Albocher, A. A. Oberai, P. E. Barbone, and I. Harari, "Adjoint-weighted equation for inverse problems of incompressible plane-stress elasticity," *Comput. Method Appl. M.*, vol. 198, no. 30–32, pp. 2412–2420, 2009.

[49] P. E. Barbone and J. C. Bamber, "Quantitative elasticity imaging: what can and cannot be inferred from strain images," *Phys. Med. Biol.*, vol. 47, no. 12, pp. 2147–2164, 2002.

[50] Y. C. Fung, *Biomechanics: Mechanical Properties of Living Tissues*, 2nd ed. Springer-Verlag, 1993.

[51] M. M. Doyley, S. Srinivasan, S. A. Pendergrass, Z. Wu, and J. Ophir, "Comparative evaluation of strain-based and model-based modulus elastography," *Ultrasound Med. Biol*, vol. 31, no. 6, pp. 787–802, 2005.

[52] E. Konofagou and J. Ophir, "A new elastographic method for estimation and imaging of lateral displacements, lateral strains, corrected axial strains and poisson's ratios in tissues," *Ultrasound Med. Biol.*, vol. 24, no. 8, pp. 1183–1199, 1998.

[53] E. E. Konofagou, T. Varghese, and J. Ophir, "Theoretical bounds on the estimation of transverse displacement, transverse strain and Poisson's ratio in elastography," *Ultrason. Imaging*, vol. 22, no. 3, pp. 153–177, 2000.

[54] A. P. Sarvazyan, "Low-frequency acoustic characteristics of biological tissues," *Mech. Polymers*, vol. 11, no. 4, pp. 594–597, 1975.

[55] K. J. Parker, S. R. Huang, R. A. Musulin, and R. M. Lerner, "Tissue response to mechanical vibrations for 'sonoelasticity imaging,'" *Ultrasound Med. Biol.*, vol. 16, no. 3, pp. 241–246, 1990.

[56] L. Sandrin, B. Fourquet, J. M. Hasquenoph, S. Yon, C. Fournier, F. Mal, C. Christidis, M. Ziol, B. Poulet, and F. Kazemi, "Transient elastography: a new noninvasive method for assessment of hepatic fibrosis," *Ultrasound Med. Biol.*, vol. 29, no. 12, pp. 1705–1713, 2003.

[57] J. Lindop, G. Treece, A. Gee, and R. Prager, "The general properties including accuracy and resolution of linear filtering methods for strain estimation," *IEEE Trans. Ultrason. Ferroelectr. Freq. Control*, vol. 55, no. 11, pp. 2363–2368, 2008.

[58] T. Varghese, E. E. Konofagou, J. Ophir, S. K. Alam, and M. Bilgen, "Direct strain estimation in elastography using spectral cross-correlation," *Ultrasound Med. Biol.*, vol. 26, no. 9, pp. 1525–1537, 2000.

[59] T. Varghese and J. Ophir, "A theoretical framework for performance characterization of elastography: the strain filter.," *IEEE Trans. Ultrason. Ferroelectr. Freq. Control*, vol. 44, no. 1, pp. 164–172, 1997.

[60] F. Kallel and J. Ophir, "A least-squares strain estimator for elastography," *Ultrason. Imaging*, vol. 19, no. 3, pp. 195–208, 1997.

[61] T. Varghese, J. A. Zagzebski, and F. T. Lee, "Elastographic imaging of thermal lesions in the liver in vivo following radiofrequency ablation: preliminary results," *Ultrasound Med. Biol.*, vol. 28, no. 11–12, pp. 1467–1473, 2002.

[62] K. R. Raghavan and A. E. Yagle, "Forward and inverse problems in elasticity imaging of soft tissues," *IEEE Trans. Nucl. Sci.*, vol. 41, no. 4 Part 1, pp. 1639–1648, 1994.

[63] Yanning Zhu, T. J. Hall, and Jingfeng Jiang, "A finite-element approach for Young's modulus reconstruction," *IEEE Trans. Med. Imaging*, vol. 22, no. 7, pp. 890–901, 2003.

[64] A. R. Skovoroda, S. Y. Emelianov, and M. O'Donnell, "Tissue elasticity reconstruction based on ultrasonic displacement and strain images," *IEEE Trans. Ultrason. Ferroelectr. Freq. Control*, vol. 42, no. 4, pp. 747–765, 1995.

[65] E. E. W. Van Houten, K. D. Paulsen, M. I. Miga, F. E. Kennedy, and J. B. Weaver, "An overlapping subzone technique for MR-based elastic property reconstruction," *Magn. Reson. Med.*, vol. 42, no. 4, pp. 779–786, 1999.

[66] S. R. Aglyamov, A. R. Skovoroda, H. Xie, K. Kim, J. M. Rubin, M. O'Donnell, T. W. Wakefield, D. Myers, and S. Y. Emelianov, "Model-Based Reconstructive Elasticity Imaging Using Ultrasound," *Int. J. Biomed. Imaging*, vol. 35830, 2007.

[67] P. E. Barbone and N. H. Gokhale, "Elastic modulus imaging: on the uniqueness and nonuniqueness of the elastography inverse problem in two dimensions," *Inverse Probl.*, vol. 20, no. 1, pp. 283–296, 2004.

[68] K. R. Nightingale, M. L. Palmeri, R. W. Nightingale, and G. E. Trahey, "On the feasibility of remote palpation using acoustic radiation force," *J. Acoust. Soc. Am.*, vol. 110, no. 1, pp. 625–634, 2001.

[69] A. P. Sarvazyan, O. V. Rudenko, S. D. Swanson, J. B. Fowlkes, and S. Y. Emelianov, "Shear wave elasticity imaging: a new ultrasonic technology of medical diagnostics," *Ultrasound Med. Biol.*, vol. 24, no. 9, pp. 1419–1435, 1998.

[70] J. Bercoff, M. Tanter, and M. Fink, "Supersonic shear imaging: a new technique for soft tissue elasticity mapping," *IEEE Trans. Ultrason. Ferroelectr. Freq. Control*, vol. 51, no. 4, pp. 396–409, 2004.

[71] L. Sandrin, M. Tanter, S. Catheline, and M. Fink, "Shear modulus imaging with 2-D transient elastography," *IEEE Trans. Ultrason. Ferroelectr. Freq. Control*, vol. 49, no. 4, pp. 426–435, 2002.

[72] L. Gao, K. J. Parker, S. K. Alam, and R. M. Lerner, "Sonoelasticity imaging: theory and experimental verification," *J. Acoust. Soc. Am.*, vol. 97, no. 6, pp. 3875–3886, 1995.

[73] R. Muthupillai, D. J. Lomas, P. J. Rossman, J. F. Greenleaf, A. Manduca, and R. L. Ehman, "Magnetic resonance elastography by direct visualization of propagating acoustic strain waves," *Science*, vol. 269, no. 5232, pp. 1854–1857, 1995.

[74] A. Manduca, T. E. Oliphant, M. A. Dresner, J. L. Mahowald, S. A. Kruse, E. Amromin, J. P. Felmlee, J. F. Greenleaf, and R. L. Ehman, "Magnetic resonance elastography: non-invasive mapping of tissue elasticity," *Med. Image Anal.*, vol. 5, no. 4, pp. 237–254, 2001.

[75] S. Bharat, U. Techavipoo, M. Z. Kiss, W. Liu, and T. Varghese, "Monitoring stiffness changes in lesions after radiofrequency ablation at different temperatures and durations of ablation," *Ultrasound Med. Biol.*, vol. 31, no. 3, pp. 415–422, 2005.

[76] T. Varghese and S. Hairong, "Elastographic imaging of thermal lesions in liver in-vivo using diaphragmatic stimuli," *Ultrason. Imaging*, vol. 26, no. 1, pp. 18–28, 2004.

[77] J. Jiang, T. Varghese, Q. Chen, T. J. Hall, and J. A. Zagzebski, "Finite element analysis of tissue deformation with a radiofrequency ablation electrode for strain imaging," *IEEE Trans. Ultrason. Ferroelectr. Freq. Control*, vol. 54, no. 2, pp. 281–289, 2007.

[78] N. Rubert, S. Bharat, R. J. DeWall, A. Andreano, C. Brace, J. Jiang, L. Sampson, and T. Varghese, "Electrode displacement strain imaging of thermally-ablated liver tissue in an in vivo animal model," *Med Phys*, vol. 37, no. 3, pp. 1075–1082, 2010.

[79] W. Liu, U. Techavipoo, T. Varghese, J. A. Zagzebski, Q. Chen, and J. Lee, "Elastographic versus x-ray CT imaging of radio frequency ablation coagulations: An in vitro study," *Med. Phys.*, vol. 31, no. 6, pp. 1322–1332, 2004.

[80] T. Varghese, U. Techavipoo, J. A. Zagzebski, and F. T. Lee Jr, "Impact of gas bubbles generated during interstitial ablation on elastographic depiction of in vitro thermal lesions," *J. Ultrasound Med.*, vol. 23, no. 4, pp. 535–544, 2004.

[81] S. Bharat and T. Varghese, "Contrast-transfer improvement for electrode displacement elastography," *Phys. Med. Biol.*, vol. 51, no. 24, pp. 6403–6418, 2006.
[82] S. Bharat, T. G. Fisher, T. Varghese, T. J. Hall, J. Jiang, E. L. Madsen, J. A. Zagzebski, and F. T. Lee, "Three-dimensional electrode displacement elastography using the Siemens C7F2 fourSight four-dimensional ultrasound transducer," *Ultrasound Med. Biol.*, vol. 34, no. 8, pp. 1307–1316, 2008.
[83] J. Jiang, C. Brace, A. Andreano, R. J. DeWall, N. Rubert, T. G. Fisher, and T. Varghese, "Ultrasound-based relative elastic modulus imaging for visualizing thermal ablation zones in a porcine model," *Phys. Med. Biol.*, vol. 55, pp. 2281–2306, 2010.
[84] R. J. Dewall and T. Varghese, "Improving thermal ablation delineation with electrode vibration elastography using a bidirectional wave propagation assumption," *IEEE Trans. Ultrason. Ferroelectr. Freq. Control*, vol. 59, no. 1, pp. 168–173, 2012.
[85] R. Dewall, T. Varghese, and E. Madsen, "Shear Wave Velocity Imaging Using Transient Electrode Perturbation: Phantom and ex vivo Validation.," *IEEE Trans. Med. Imag.*, vol. 30, pp. 666–678, 2010.
[86] S. Bharat and T. Varghese, "Radiofrequency electrode vibration-induced shear wave imaging for tissue modulus estimation: A simulation study," *J. Acoust. Soc. Am.*, vol. 128, pp. 1582–1585, 2010.
[87] R. J. DeWall, T. Varghese, and C. L. Brace, "Visualizing ex vivo radiofrequency and microwave ablation zones using electrode vibration elastography," *Med. Phys.*, vol. 39, pp. 6692–6700, 2012.
[88] B. J. Fahey, K. R. Nightingale, D. L. Stutz, and G. E. Trahey, "Acoustic radiation force impulse imaging of thermally-and chemically-induced lesions in soft tissues: preliminary ex vivo results," *Ultrasound Med. Biol.*, vol. 30, no. 3, pp. 321–328, 2004.
[89] B. J. Fahey, K. R. Nightingale, S. A. McAleavey, M. L. Palmeri, P. D. Wolf, and G. E. Trahey, "Acoustic radiation force impulse imaging of myocardial radiofrequency ablation: initial in vivo results," *IEEE Trans. Ultrason. Ferroelectr. Freq. Control*, vol. 52, no. 4, pp. 631–641, 2005.
[90] B. J. Fahey, S. J. Hsu, P. D. Wolf, R. C. Nelson, and G. E. Trahey, "Liver ablation guidance with acoustic radiation force impulse imaging: challenges and opportunities," *Phys. Med. Biol.*, vol. 51, no. 15, pp. 3785–3808, 2006.
[91] B. J. Fahey, R. C. Nelson, S. J. Hsu, D. P. Bradway, D. M. Dumont, and G. E. Trahey, "In vivo guidance and assessment of liver radio-frequency ablation with acoustic radiation force elastography," *Phys. Med. Biol.*, vol. 34, no. 10, pp. 1590–1603, 2008.
[92] J. Bercoff, M. Pernot, M. Tanter, and M. Fink, "Monitoring thermally-induced lesions with supersonic shear imaging," *Ultrason. Imaging*, vol. 26, no. 2, pp. 71–84, 2004.
[93] B. Arnal, M. Pernot, and M. Tanter, "Monitoring of thermal therapy based on shear modulus changes: II. Shear wave imaging of thermal lesions," *IEEE Trans. Ultrason. Ferroelectr. Freq. Control*, vol. 58, no. 8, pp. 1603–1611, 2011.
[94] M. Zhang, B. Castaneda, J. Christensen, W. Saad, K. Bylund, K. Hoyt, J. G. Strang, D. J. Rubens, and K. J. Parker, "Real-time sonoelastography of hepatic thermal lesions in a swine model," *Med. Phys.*, vol. 35, pp. 4132–4141, 2008.
[95] T. Wu, J. P. Felmlee, J. F. Greenleaf, S. J. Riederer, and R. L. Ehman, "Assessment of thermal tissue ablation with MR elastography," *Magn. Reson. Med.*, vol. 45, no. 1, pp. 80–87, 2001.

[96] J. Chen, D. A. Woodrum, K. J. Glaser, M. C. Murphy, K. Gorny, and R. Ehman, "Assessment of in vivo laser ablation using MR elastography with an inertial driver," *Magn. Reson. Med.*, 2013.
[97] F. Viola and W. F. Walker, "A comparison of the performance of time-delay estimators in medical ultrasound," *IEEE Trans. Ultrason. Ferroelectr. Freq. Control*, vol. 50, no. 4, pp. 392–401, 2003.
[98] T. Varghese and J. Ophir, "Characterization of elastographic noise using the envelope of echo signals," *Ultrasound Med. Biol.*, vol. 24, no. 4, pp. 543–555, 1998.
[99] L. Chen, G. M. Treece, J. E. Lindop, A. H. Gee, and R. W. Prager, "A quality-guided displacement tracking algorithm for ultrasonic elasticity imaging," *Med. Image Anal.*, vol. 13, no. 2, pp. 286–296, 2009.
[100] Y. Zhu and T. J. Hall, "A modified block matching method for real-time freehand strain imaging," *Ultrason. Imaging*, vol. 24, no. 3, pp. 161–176, 2002.
[101] A. Pesavento, C. Perrey, M. Krueger, and H. Ermert, "A time-efficient and accurate strain estimation concept for ultrasonic elastography using iterative phase zero estimation," *IEEE Trans. Ultrason. Ferroelectr. Freq. Control*, vol. 46, no. 5, pp. 1057–1067, 1999.
[102] J. Jiang and T. J. Hall, "A Generalized Speckle Tracking Algorithm for Ultrasonic Strain Imaging Using Dynamic Programming," *Ultrasound Med. Biol.*, vol. 35, no. 11, pp. 1863–1879, 2009.
[103] H. Rivaz, E. Boctor, P. Foroughi, R. Zellars, G. Fichtinger, and G. Hager, "Ultrasound elastography: a dynamic programming approach," *IEEE Trans. Med. Imaging*, vol. 27, no. 10, pp. 1373–1377, 2008.
[104] H. Shi and T. Varghese, "Two-dimensional multi-level strain estimation for discontinuous tissue," *Phys. Med. Biol.*, vol. 52, no. 2, pp. 389–402, 2007.
[105] H. Chen, H. Shi, and T. Varghese, "Improvement of elastographic displacement estimation using a two-step cross-correlation method," *Ultrasound Med. Biol.*, vol. 33, no. 1, pp. 48–56, 2007.
[106] F. Yeung, S. F. Levinson, and K. J. Parker, "Multilevel and motion model-based ultrasonic speckle tracking algorithms," *Ultrasound Med. Biol.*, vol. 24, no. 3, pp. 427–442, 1998.
[107] C. Pellot-Barakat, F. Frouin, M. F. Insana, and A. Herment, "Ultrasound elastography based on multiscale estimations of regularized displacement fields," *IEEE Trans. Med. Imaging*, vol. 23, no. 2, pp. 153–163, 2004.
[108] I. Cespedes, Y. Huang, J. Ophir, and S. Spratt, "Methods for estimation of subsample time delays of digitized echo signals.," *Ultrason. Imaging*, vol. 17, no. 2, pp. 142–171, 1995.
[109] M. M. McCormick and T. Varghese, "An Approach to Unbiased Subsample Interpolation for Motion Tracking," *Ultrason. Imaging*, vol. 35, no. 2, pp. 76–89, 2013.
[110] A. Basarab, H. Liebgott, and P. Delachartre, "Analytic estimation of subsample spatial shift using the phases of multidimensional analytic signals," *IEEE Trans. Med. Imaging*, vol. 18, no. 2, pp. 440–447, 2009.
[111] F. Viola and W. F. Walker, "A spline-based algorithm for continuous time-delay estimation using sampled data," *IEEE Trans. Ultrason. Ferroelectr. Freq. Control*, vol. 52, no. 1, pp. 80–93, 2005.
[112] F. Viola, R. L. Coe, K. Owen, D. A. Guenther, and W. F. Walker, "MUlti-Dimensional Spline-Based Estimator (MUSE) for Motion Estimation: Algorithm Development and Initial Results," *Ann. Biomed. Eng.*, vol. 36, no. 12, pp. 1942–1960, 2008.

[113] F. Viola and W. F. Walker, "A spline-based algorithm for continuous time-delay estimation using sampled data," *IEEE Trans. Ultrason. Ferroelectr. Freq. Control*, vol. 52, no. 1, pp. 80–93, 2005.
[114] J. E. Lindop, G. M. Treece, A. H. Gee, and R. W. Prager, "The general properties including accuracy and resolution of linear filtering methods for strain estimation," *IEEE Trans. Ultrason. Ferroelectr. Freq. Control*, vol. 55, no. 11, pp. 2363–2368, 2008.
[115] E. E. Konofagou, T. Varghese, J. Ophir, and S. K. Alam, "Power spectral strain estimators in elastography," *Ultrasound Med. Biol.*, vol. 25, no. 7, pp. 1115–1129, 1999.
[116] H. E. Talhami, L. S. Wilson, and M. L. Neale, "Spectral tissue strain: a new technique for imaging tissue strain using intravascular ultrasound," *Ultrasound Med. Biol.*, vol. 20, no. 8, pp. 759–772, 1994.
[117] T. Nakazawa, S. Kokubu, A. Shibuya, K. Ono, M. Watanabe, H. Hidaka, T. Tsuchihashi, and K. Saigenji, "Radiofrequency ablation of hepatocellular carcinoma: correlation between local tumor progression after ablation and ablative margin," *Am. J. Roentgenol.*, vol. 188, no. 2, pp. 480–488, 2007.
[118] N. Rubert and T. Varghese, "Mean scatterer spacing estimation using multi-taper coherence," *IEEE Trans. Ultrason. Ferroelectr. Freq. Control*, vol. 60, no. 6, pp. 1061–1073, 2013.
[119] K. J. Parker, "Ultrasonic attenuation and absorption in liver tissue," *Ultrasound Med. Biol.*, vol. 9, no. 4, pp. 363–369, 1983.
[120] M. F. Insana and D. G. Brown, "Acoustic Scattering Theory Applied to Soft Biological Tissues," in *Ultrasonic Scattering in Biological Tissues*, CRC Press, 1993, pp. 75–124.
[121] J. A. Campbell and R. C. Waag, "Measurements of calf liver ultrasonic differential and total scattering cross sections," *J. Acoust. Soc. Am.*, vol. 75, pp. 603–611, 1984.
[122] E. L. Madsen, M. F. Insana, and J. A. Zagzebski, "Method of data reduction for accurate determination of acoustic backscatter coefficients," *J. Acoust. Soc. Am.*, vol. 76, pp. 913–923, 1984.
[123] D. K. Nassiri and C. R. Hill, "The use of angular acoustic scattering measurements to estimate structural parameters of human and animal tissues," *J. Acoust. Soc. Am.*, vol. 79, pp. 2048–2054, 1986.
[124] L. X. Yao, J. A. Zagzebski, and E. L. Madsen, "Backscatter coefficient measurements using a reference phantom to extract depth-dependent instrumentation factors," *Ultrason. Imaging*, vol. 12, no. 1, pp. 58–70, 1990.
[125] A. Gerig, J. Zagzebski, and T. Varghese, "Statistics of ultrasonic scatterer size estimation with a reference phantom," *J. Acoust. Soc. Am.*, vol. 113, pp. 3430–3437, 2003.
[126] H. Kim and T. Varghese, "Attenuation estimation using spectral cross-correlation," *IEEE Trans. Ultrason. Ferroelectr. Freq. Control*, vol. 54, no. 3, pp. 510–519, 2007.
[127] H. Kim and T. Varghese, "Hybrid spectral domain method for attenuation slope estimation," *Ultrasound Med. Biol.*, vol. 34, no. 11, pp. 1808–1819, 2008.
[128] W. Liu and J. A. Zagzebski, "Trade-offs in data acquisition and processing parameters for backscatter and scatterer size estimations," *IEEE Trans. Ultrason. Ferroelectr. Freq. Control*, vol. 57, no. 2, pp. 340–352, 2010.
[129] K. Nam, J. A. Zagzebski, and T. J. Hall, "Simultaneous Backscatter and Attenuation Estimation Using a Least Squares Method with Constraints," *Ultrasound Med. Biol.*, vol. 37, no. 12, pp. 2096–2104, 2011.

[130] R. F. Wagner, S. W. Smith, J. M. Sandrik, and H. Lopez, "Statistics of speckle in ultrasound B-scans.," *IEEE Trans. Ultrason. Ferroelectr. Freq. Control*, vol. 30, no. 3, pp. 156–163, 1983.
[131] L. L. Fellingham and F. G. Sommer, "Ultrasonic characterization of tissue structure in the in vivo human liver and spleen," *IEEE Trans. Ultrason. Ferroelectr. Freq. Control*, vol. 31, no. 4, pp. 418–428, 1984.
[132] L. Landini and L. Verrazzani, "Spectral characterization of tissues microstructure by ultrasounds: a stochastic approach," *IEEE Trans. Ultrason. Ferroelectr. Freq. Control*, vol. 37, no. 5, pp. 448–456, 1990.
[133] K. A. Wear, R. F. Wagner, M. F. Insana, and T. J. Hall, "Application of autoregressive spectral analysis to cepstral estimation of mean scatterer spacing," *IEEE Trans. Ultrason. Ferroelectr. Freq. Control*, vol. 40, no. 1, pp. 50–58, 1993.
[134] C. B. Machado, W. C. de Albuquerque Pereira, M. Meziri, and P. Laugier, "Characterization of in vitro healthy and pathological human liver tissue periodicity using backscattered ultrasound signals," *Ultrasound Med. Biol.*, vol. 32, no. 5, pp. 649–657, 2006.
[135] U. R. Abeyratne and X. Tang, "Ultrasound scatter-spacing based diagnosis of focal diseases of the liver," *Biomed. Sig. Proc. Cont.*, vol. 2, no. 1, pp. 9–15, 2007.
[136] R. Kuc, K. Haghkerdar, and M. O'Donnell, "Presence of cepstral peak in random reflected ultrasound signals," *Ultrason. Imaging*, vol. 8, no. 3, pp. 196–212, 1986.
[137] T. Varghese and K. D. Donohue, "Mean-scatterer spacing estimates with spectral correlation," *J. Acoust. Soc. Am*, vol. 96, no. 6, pp. 3504–3515, 1994.
[138] T. Varghese and K. D. Donohue, "Characterization of tissue microstructure scatterer distribution with spectral correlation," *Ultrason. Imaging*, vol. 15, no. 3, pp. 238–254, 1993.
[139] W. C. A. Pereira and C. D. Maciel, "Performance of ultrasound echo decomposition using singular spectrum analysis," *Ultrasound Med. Biol.*, vol. 27, no. 9, pp. 1231–1238, 2001.
[140] W. C. A. Pereira, S. L. Bridal, A. Coron, and P. Laugier, "Singular spectrum analysis applied to backscattered ultrasound signals from in vitro human cancellous bone specimens," *IEEE Trans. Ultrason. Ferroelectr. Freq. Control*, vol. 51, no. 3, pp. 302–312, 2004.
[141] F. S. Cohen, G. Georgiou, and E. J. Halpern, "WOLD decomposition of the backscatter echo in ultrasound images of soft tissue organs," *IEEE Trans. Ultrason. Ferroelectr. Freq. Control*, vol. 44, no. 2, pp. 460–472, 1997.
[142] G. Georgiou and F. S. Cohen, "Tissue characterization using the continuous wavelet transform. I. Decomposition method," *IEEE Trans. Ultrason. Ferroelectr. Freq. Control*, vol. 48, no. 2, pp. 355–363, 2001.
[143] G. Georgiou, F. S. Cohen, C. W. Piccoli, F. Forsberg, and B. B. Goldberg, "Tissue characterization using the continuous wavelet transform. II. Application on breast RF data," *IEEE Trans. Ultrason. Ferroelectr. Freq. Control*, vol. 48, no. 2, pp. 364–373, 2001.
[144] U. R. Abeyratne, A. P. Petropulu, and J. M. Reid, "On modeling the tissue response from ultrasonic B-scan images," *IEEE Trans. Med. Imag.*, vol. 15, no. 4, pp. 479–490, 1996.
[145] Z. Zhou, L. Sheng, S. Wu, C. Yang, and Y. Zeng, "Ultrasonic evaluation of microwave-induced thermal lesions based on wavelet analysis of mean scatterer spacing," *Ultrasonics*, vol. 53, no. 7, pp. 1325–1331, 2013.

[146] K. D. Donohue, F. Forsberg, C. V. Piccoli, and B. B. Goldberg, "Analysis and classification of tissue with scatterer structure templates," *IEEE Trans. Ultrason. Ferroelectr. Freq. Control*, vol. 46, no. 2, pp. 300–310, 1999.
[147] D. B. Percival and A. T. Walden, *Spectral Analysis for Physical Applications: Multitaper and Conventional Univariate Techniques*. Cambridge University Press, 1993.
[148] D. J. Thomson, "Spectrum estimation and harmonic analysis," *Proc. IEEE*, vol. 70, no. 9, pp. 1055–1096, 1982.
[149] M. Loeve, *Probability Theory 1 & 2*, 4th ed. Spring-Verlag, 1978.
[150] L. Gerr Neil and C. Allen Jeffery, "The Generalised Spectrum and Spectral Coherence of a Harmonizable Time Series," *Digit. Signal Process.*, vol. 4, no. 4, pp. 222–238, 1994.
[151] T. Varghese and K. D. Donohue, "Estimating mean scatterer spacing with the frequency-smoothed spectral autocorrelation function," *IEEE Trans. Ultrason. Ferroelectr. Freq. Control*, vol. 42, no. 3, pp. 451–463, 1995.
[152] L. Huang, K. D. Donohue, V. Genis, and F. Forsberg, "Duct detection and wall spacing estimation in breast tissue," *Ultrason. imaging*, vol. 22, no. 3, pp. 137–152, 2000.
[153] K. D. Donohue, L. Huang, T. Burks, F. Forsberg, and C. W. Piccoli, "Tissue classification with generalized spectrum parameters," *Ultrasound Med. Biol.*, vol. 27, no. 11, pp. 1505–1514, 2001.
[154] S. Haykin and D. J. Thomson, "Signal detection in a nonstationary environment reformulated as an adaptive pattern classification problem," *Proc. IEEE*, vol. 86, no. 11, pp. 2325–2344, 1998.
[155] S. Haykin, D. J. Thomson, and J. H. Reed, "Spectrum sensing for cognitive radio," *Proc. IEEE*, vol. 97, no. 5, pp. 849–877, 2009.
[156] A. C. Luchies, G. Ghoshal, W. O'Brien, Jr., and M. L. Oelze, "Quantitative ultrasonic characterization of diffuse scatterers in the presence of structures that produce coherent echoes," *IEEE Trans. Ultrason. Ferroelectr. Freq. Control*, vol. 59, no. 5, pp. 893–904, 2012.
[157] R. Mellors, F. Vernon, and D. Thomson, "Detection of dispersive signals using multitaper dual-frequency coherence," *Geophysical J. Int.*, vol. 135, no. 1, pp. 146–154, 1998.
[158] G. A. Prieto, R. L. Parker, and F. L. Vernon III, "A Fortran 90 library for multitaper spectrum analysis," *Comput. Geosci.*, vol. 35, no. 8, pp. 1701–1710, 2009.
[159] D. J. Thomson, "Quadratic-inverse spectrum estimates: applications to palaeoclimatology," *Phil. Trans. R. Soc. London A*, pp. 539–597, 1990.
[160] Y. Li and J. A. Zagzebski, "A frequency domain model for generating B-mode images with array transducers," *IEEE Trans. Ultrason. Ferroelectr. Freq. Control*, vol. 46, no. 3, pp. 690–699, 1999.
[161] P. Morse and K. Ingard, *Theoretical Acoustics*. Princeton Univ. Press, 1986.
[162] J. J. Faran Jr, "Sound scattering by solid cylinders and spheres," *J. Acoust. Soc. Am*, vol. 23, pp. 405–418, 1951.
[163] T. E. Oliphant, "Python for scientific computing," *Comput. Sci. Eng.*, pp. 10–20, 2007.
[164] N. Rubert and T. Varghese, "Mean scatterer spacing estimation in normal and thermally coagulated ex vivo bovine liver," *Ultrason. Imaging*, In Press.
[165] K. D. Donohue, T. Varghese, and N. M. Bilgutay, "Spectral redundancy in characterizing scatterer structure from ultrasound echoes," *Review of progress in Quantitative Nondestructive Evaluation*, vol. 13, 1994.

[166] G. W. C. Kaye and T. H. Laby, *Table of Physical and Chemical Constants*. London, England: Longman, 1973.
[167] K. A. Wear, T. A. Stiles, G. R. Frank, E. L. Madsen, F. Cheng, E. J. Feleppa, C. S. Hall, B. S. Kim, P. Lee, and W. D. O'Brien, "Interlaboratory comparison of ultrasonic backscatter coefficient measurements from 2 to 9 MHz," *J. Ultrasound Med.*, vol. 24, no. 9, pp. 1235–1250, 2005.
[168] S.-Y. Wan, A. P. Kiraly, E. L. Ritman, and W. E. Higgins, "Extraction of the hepatic vasculature in rats using 3-D micro-CT images," *IEEE Trans Med Imag*, vol. 19, no. 9, pp. 964–971, 2000.
[169] N. Parmar and M. C. Kolios, "An investigation of the use of transmission ultrasound to measure acoustic attenuation changes in thermal therapy," *Med. Biol. Eng. Comput.*, vol. 44, no. 7, pp. 583–591, 2006.
[170] N. L. Bush, I. Rivens, G. R. Ter Haar, and J. C. Bamber, "Acoustic properties of lesions generated with an ultrasound therapy system," *Ultrasound Med. Biol.*, vol. 19, no. 9, pp. 789–801, 1993.
[171] C. A. Damianou, N. T. Sanghvi, F. J. Fry, and R. Maass-Moreno, "Dependence of ultrasonic attenuation and absorption in dog soft tissues on temperature and thermal dose," *J. Acoust. Soc. Am.*, vol. 102, pp. 628–634, 1997.
[172] M. R. Gertner, B. C. Wilson, and M. D. Sherar, "Ultrasound properties of liver tissue during heating," *Ultrasound Med. Biol.*, vol. 23, no. 9, pp. 1395–1403, 1997.
[173] U. Techavipoo, T. Varghese, Q. Chen, T. A. Stiles, J. A. Zagzebski, and G. R. Frank, "Temperature dependence of ultrasonic propagation speed and attenuation in excised canine liver tissue measured using transmitted and reflected pulses," *J. Acoust. Soc. Am.*, vol. 115, pp. 2859–2865, 2004.
[174] A. E. Worthington and M. D. Sherar, "Changes in ultrasound properties of porcine kidney tissue during heating," *Ultrasound Med. Biol.*, vol. 27, no. 5, pp. 673–682, 2001.
[175] J. P. Kemmerer and M. L. Oelze, "Ultrasonic Assessment of Thermal Therapy in Rat Liver," *Ultrasound Med Biol*, vol. 38, no. 12, pp. 2130–2137, 2012.
[176] P. He and J. F. Greenleaf, "Attenuation estimation on phantoms—A stability test," *Ultrason. Imaging*, vol. 8, no. 1, pp. 1–10, 1986.
[177] H. S. Jang, T. K. Song, and S. B. Park, "Ultrasound attenuation estimation in soft tissue using the entropy difference of pulsed echoes between two adjacent envelope segments," *Ultrason. Imaging*, vol. 10, no. 4, pp. 248–264, 1988.
[178] B. S. Knipp, J. A. Zagzebski, T. A. Wilson, F. Dong, and E. L. Madsen, "Attenuation and backscatter estimation using video signal analysis applied to B-mode images," *Ultrason. Imaging*, vol. 19, no. 3, pp. 221–233, 1997.
[179] G. Ghoshal and M. L. Oelze, "Time domain attenuation estimation method from ultrasonic backscattered signals," *J. Acoust. Soc. Am.*, vol. 132, pp. 533–543, 2012.
[180] R. Kuc, "Estimating acoustic attenuation from reflected ultrasound signals: Comparison of spectral-shift and spectral-difference approaches," *IEEE Trans. Acoust., Speech, Signal Process.*, vol. 32, no. 1, pp. 1–6, 1984.
[181] M. Insana, J. Zagzebski, and E. Madsen, "Improvements in the spectral difference method for measuring ultrasonic attenuation," *Ultrason. Imaging*, vol. 5, no. 4, pp. 331–345, 1983.
[182] E. Omari, H. Lee, and T. Varghese, "Theoretical and phantom based investigation of the impact of sound speed and backscatter variations on attenuation slope estimation," *Ultrasonics*, vol. 51, no. 6, pp. 758–767, 2011.

[183] K. Nam, I. M. Rosado-Mendez, N. C. Rubert, E. L. Madsen, J. A. Zagzebski, and T. J. Hall, "Ultrasound attenuation measurements using a reference phantom with sound speed mismatch.," *Ultrason. Imaging*, vol. 33, no. 4, pp. 251–263, 2011.

[184] H. Kim, J. A. Zagzebski, and T. Varghese, "Estimation of ultrasound attenuation from broadband echo-signals using bandpass filtering," *IEEE Trans. Ultrason. Ferroelectr. Freq. Control*, vol. 55, no. 5, pp. 1153–1159, 2008.

[185] H. Kim and S. W. Heo, "Time-domain calculation of spectral centroid from backscattered ultrasound signals," *IEEE Trans. Ultrason. Ferroelectr. Freq. Control*, vol. 59, no. 6, pp. 1193–1200, 2012.

[186] E. A. Omari, T. Varghese, E. L. Madsen, and G. Frank, "Evaluation of the impact of backscatter intensity variations on ultrasound attenuation estimation," *Med Phys*, vol. 40, no. 8, p. 082904, 2013.

[187] Y. Labyed and T. A. Bigelow, "A theoretical comparison of attenuation measurement techniques from backscattered ultrasound echoes," *J. Acoust. Soc. Am.*, vol. 129, pp. 2316–2324, 2011.

[188] Kim, H. and Heo, S.W., "Time-domain calculation of spectral centroid from backscattered ultrasound signals," *IEEE Trans. Ultrason. Ferroelectr. Freq. Control*, vol. 59, no. 6, pp. 1193–1200, 2012.

[189] P.-H. Tsui, C.-K. Yeh, C.-C. Chang, and Y.-Y. Liao, "Classification of breast masses by ultrasonic Nakagami imaging: a feasibility study," *Phys. Med. Biol.*, vol. 53, no. 21, pp. 6027–6044, 2008.

[190] M.-C. Ho, J.-J. Lin, Y.-C. Shu, C.-N. Chen, K.-J. Chang, C.-C. Chang, and P.-H. Tsui, "Using ultrasound Nakagami imaging to assess liver fibrosis in rats," *Ultrasonics*, vol. 52, no. 2, pp. 215–222, 2012.

[191] P. Bedossa and T. Poynard, "An algorithm for the grading of activity in chronic hepatitis C," *Hepatology*, vol. 24, no. 2, pp. 289–293, 1996.

[192] I. M. Rosado-Mendez, K. Nam, T. J. Hall, and J. A. Zagzebski, "Task-Oriented Comparison of Power Spectral Density Estimation Methods for Quantifying Acoustic Attenuation in Diagnostic Ultrasound Using a Reference Phantom Method," *Ultrason. Imaging*, vol. 35, no. 3, pp. 214–234, 2013.

[193] J.-F. Chen, E. L. Madsen, and J. A. Zagzebski, "A method for determination of frequency-dependent effective scatterer number density," *J. Acoust. Soc. Am.*, vol. 95, pp. 77–85, 1994.

[194] P. D. Bevan and M. D. Sherar, "B-scan ultrasound imaging of thermal coagulation in bovine liver: frequency shift attenuation mapping," *Ultrasound Med. Biol.*, vol. 27, no. 6, pp. 809–817, 2001.

[195] P. D. Bevan and M. D. Sherar, "B-scan ultrasound imaging of thermal coagulation in bovine liver: log envelope slope attenuation mapping," *Ultrasound Med. Biol.*, vol. 27, no. 3, pp. 379–387, 2001.

[196] S. N. Goldberg and D. E. Dupuy, "Image-guided radiofrequency tumor ablation: challenges and opportunities—part I," *J. Vasc. Interv. Radiol.*, vol. 12, no. 9, pp. 1021–1032, 2001.

[197] L. L. Scharf and B. Friedlander, "Toeplitz and Hankel kernels for estimating time-varying spectra of discrete-time random processes," *IEEE Trans. Signal Process.*, vol. 49, no. 1, pp. 179–189, 2001.